



UNIL | Université de Lausanne

Unicentre

CH-1015 Lausanne

<http://serval.unil.ch>

Year : 2023

UNRAVELLING THE HEAT BUDGET OF THE LEPONTINE DOME: INTERDISCIPLINARY GEOLOGICAL, ETROLOGICAL, THERMODYNAMIC AND GEOCHRONOLOGICAL STUDY OF SHEAR ZONES

Tagliaferri Alessia

Tagliaferri Alessia, 2023, UNRAVELLING THE HEAT BUDGET OF THE LEPONTINE DOME:
INTERDISCIPLINARY GEOLOGICAL, ETROLOGICAL, THERMODYNAMIC AND
GEOCHRONOLOGICAL STUDY OF SHEAR ZONES

Originally published at : Thesis, University of Lausanne

Posted at the University of Lausanne Open Archive <http://serval.unil.ch>
Document URN : urn:nbn:ch:serval-BIB_61F5B9AED5125

Droits d'auteur

L'Université de Lausanne attire expressément l'attention des utilisateurs sur le fait que tous les documents publiés dans l'Archive SERVAL sont protégés par le droit d'auteur, conformément à la loi fédérale sur le droit d'auteur et les droits voisins (LDA). A ce titre, il est indispensable d'obtenir le consentement préalable de l'auteur et/ou de l'éditeur avant toute utilisation d'une oeuvre ou d'une partie d'une oeuvre ne relevant pas d'une utilisation à des fins personnelles au sens de la LDA (art. 19, al. 1 lettre a). A défaut, tout contrevenant s'expose aux sanctions prévues par cette loi. Nous déclinons toute responsabilité en la matière.

Copyright

The University of Lausanne expressly draws the attention of users to the fact that all documents published in the SERVAL Archive are protected by copyright in accordance with federal law on copyright and similar rights (LDA). Accordingly it is indispensable to obtain prior consent from the author and/or publisher before any use of a work or part of a work for purposes other than personal use within the meaning of LDA (art. 19, para. 1 letter a). Failure to do so will expose offenders to the sanctions laid down by this law. We accept no liability in this respect.



UNIL | Université de Lausanne

Institut des sciences
de la Terre

Faculté des géosciences et de l'environnement

Institut des sciences de la Terre

Doctorat en Sciences de la Terre

UNRAVELLING THE HEAT BUDGET OF THE LEPONTINE DOME:
INTERDISCIPLINARY GEOLOGICAL, PETROLOGICAL, THERMODYNAMIC
AND GEOCHRONOLOGICAL STUDY OF SHEAR ZONES

THÈSE DE DOCTORAT

présentée à la Faculté des géosciences et de l'environnement de l'Université de Lausanne par

ALESSIA TAGLIAFERRI

Maîtrise ès Sciences de la Terre de l'Università degli Studi di Milano Statale

Jury

Prof. Dr. Stefan M. Schmalholz	Université de Lausanne	Directeur de thèse
Dr. Filippo L. Schenker	Scuola universitaria professionale della Svizzera italiana	Co-directeur de thèse
Dr. Alexey Ulianov	Université de Lausanne	Expert interne
Prof. Dr. Claudio L. Rosenberg	Sorbonne Université	Expert externe
Prof. Dr. Whitney M. Behr	ETH Zürich	Expert externe
Prof. Dr. Michel Jaboyedoff	Université de Lausanne	Président du jury

Lausanne, 2023

IMPRIMATUR

Vu le rapport présenté par le jury d'examen, composé de

Président de la séance publique :	M. le Professeur Michel Jaboyedoff
Président du colloque :	M. le Professeur Michel Jaboyedoff
Directeur de thèse :	M. le Professeur Stefan Schmalholz
Co-directeur de thèse :	M. le Docteur Filippo Schenker
Expert interne :	M. le Docteur Alexey Ulianov
Expert externe :	M. le Professeur Claudio Rosenberg
Expert externe :	Mme la Professeure Whitney Behr

Le Doyen de la Faculté des géosciences et de l'environnement autorise l'impression de la thèse de

Madame Alessia TAGLIAFERRI

*Titulaire d'un
Master Sciences de la Terre
de l'Université de Milan*

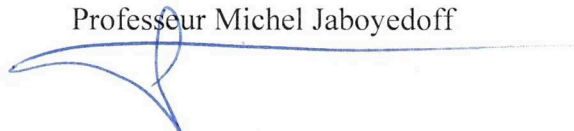
intitulée

UNRAVELLING THE HEAT BUDGET OF THE LEPONTINE DOME: INTERDISCIPLINARY GEOLOGICAL, PETROLOGICAL, THERMODYNAMIC AND GEOCHRONOLOGICAL STUDY OF SHEAR ZONES

Lausanne, le 06 décembre 2023

Pour le Doyen de la Faculté des géosciences et de
l'environnement

Professeur Michel Jaboyedoff



Die Tektonik der penninischen Decken in den Westalpen darf heute in ihren grossen Zügen als gelöst betrachtet werden (Jenny, 1923).

Ai miei genitori.



Contents

Abstract	vi
Résumé	ix
<u>Chapter 1</u>	
GENERAL INTRODUCTION	
1.1 Aim of the project	2
1.2 The heat budget problem	3
1.3 Shear zones and heat transfer	5
1.3.1 An overview on shear zones	6
1.3.2 Rationale of shear zone formation: insights into the thermo-mechanical aspects	7
1.4 The Lepontine dome case study	8
1.4.1 The Lepontine nappes	10
1.4.2 Barrovian metamorphism in the Lepontine dome	11
1.4.3 Heat sources and geodynamic scenarios	13
1.4.4 Why the Lepontine dome?	16
1.5 Thesis synopsis	17
<u>Chapter 2</u>	
QUANTIFICATION OF HEAT TRANSFER IN SHEAR ZONES THROUGH 2D THERMO-KINEMATIC NUMERICAL MODELLING	
2.1 Introduction	20
2.2 Methodology	21
2.2.1 Quantification of dimensionless parameters	22
2.2.2 2D thermo-kinematic numerical model configuration	23
2.3 Results	25
2.3.1 Dimensional analysis	25
2.3.2 2D thermo-kinematic numerical model results	27
2.4 Discussion and conclusions	30

IMPLICATIONS OF NEW GEOLOGICAL MAPPING AND U-Pb ZIRCON DATING
FOR THE BARROVIAN TECTONO-METAMORPHIC EVOLUTION
OF THE LEPONTINE DOME (CENTRAL EUROPEAN ALPS)

Abstract	36
3.1 Introduction	37
3.2 Geological overview	39
3.2.1 Tectonic overview and formation of the Lepontine dome	39
3.2.2 The Lepontine nappes	41
3.2.2.1 The Simano nappe	41
3.2.2.2 The Cima Lunga unit	41
3.2.2.3 The Maggia nappe	42
3.2.2.4 The Adula nappe	42
3.2.3 The Barrovian metamorphism	43
3.2.4 Structures	44
3.2.4.1 Migmatites	44
3.3 Sampling and dating methodology	45
3.3.1 Sample collection and preparation	45
3.3.2 Analytical techniques	48
3.4 Geological results and zircon growth: structural position, sample description, zircon CL-images, U-Pb ages, and geochemistry	50
3.4.1 The Cima di Gagnone area	50
3.4.2 The Cima di Precastello area	54
3.4.3 The San Vittore-Giova area	57
3.5 Discussion	65
3.5.1 Methodological considerations on zircon U-Pb dating	65
3.5.2 Combining geological mapping and pre-Alpine zircon U-Pb ages	67
3.5.2.1 The Cima Lunga unit as a pre-Variscan sedimentary basin	67
3.5.2.2 The Cima Lunga unit embedded in the Simano nappe	68
3.5.2.3 The Maggia-Adula nappe system	69
3.5.3 Combining geological mapping and results on Alpine zircon growth	72
3.5.3.1 Syn-tectonic migmatites on the sole of the Maggia-Adula nappe	72
3.5.3.1.1 Migmatites occurrence	72
3.5.3.1.2 Migmatization age	72

3.5.3.1.3	Post-migmatization ages	73
3.5.3.2	Timing of the regional Barrovian metamorphism: peak T conditions at 31 Ma	74
3.5.4	Geodynamic implications	77
3.5.4.1	Geodynamic reconstruction	77
3.5.4.2	Heat transfer mechanisms	78
3.6	Conclusions	82
	Acknowledgements	84

Chapter 4 **85**

FAST AND SPATIALLY HETEROGENEOUS COOLING RATES AT AMPHIBOLITE-FACIES CONDITIONS REVEAL THE SIGNIFICANCE OF LOCAL HEAT SOURCES: A CASE STUDY FROM THE LEPONTINE ALPS (SWITZERLAND)

	Abstract	86
4.1	Introduction	87
4.1.1	Geological overview	88
4.1.2	Application of inverse multicomponent-diffusion modelling in garnet	91
4.2	Methodology	92
4.3	Results	96
4.3.1	Sample description and mineral chemistry	96
4.3.2	Geothermometry and cooling rate estimates	98
4.3.3	Thermal models	100
4.4	Discussion	104
4.4.1	The T and CR pattern through the nappe pile	104
4.4.2	CR and 1D thermal model results	105
4.4.2.1	Higher tectonic levels: the Maggia-Adula shear zone	106
4.4.2.2	Footwall of the Maggia-Adula thrust	107
4.4.2.3	The Southern Steep Belt	108
4.4.3	Relation between U-Pb zircon dating and obtained CR	108
4.5	Conclusion	109
	Acknowledgements	110

<u>Chapter 5</u>	111
DISCUSSION AND CONCLUSIONS	
5.1 Redefinition of nappe boundaries in the Lepontine dome	114
5.2 Peak conditions in the field	115
5.3 The “problem” of cross-cutting isotherms and the numerical model solution	116
5.4 The importance of local heat sources	117
5.4.1 Shear heating vs. Fluids	118
5.4.2 Timing of shear heating	118
5.5 Possible outlooks	120
5.5.1 Geodynamic scenarios and numerical models	120
5.5.2 The geochronology of the Cima Lunga unit	121
<u>Appendix</u>	123
A – ANALYTICAL METHODS AND EVALUATION OF UNCERTAINTY IN LA-ICP-MS	123
B – CODE FOR DIMENSIONAL ANALYSIS	137
C – CODE FOR 2D THERMO-KINEMATIC MODELS AND NUMERICAL MODEL RESULTS	141
D – METHODOLOGY (CHAPTER 3)	151
E – GEOLOGICAL MAPS	157
F – LA-ICP-MS AND SIMS ANALYSES	163
G – DESCRIPTION OF THIN SECTIONS	169
H – MICROPROBE ANALYSES AND GEOTHERMOBAROMETRIC CALCULATIONS	203
I – MICROPROBE CHEMICAL PROFILES AND RESULTS OF DIFFUSION MODELLING IN GARNET	205
J – CODE FOR 1D THERMAL MODELS AND NUMERICAL MODEL RESULTS	231
Bibliography	239
Curriculum vitae	269

Abstract

This thesis aims to disclose the origin of the Barrovian metamorphism of the Lepontine dome. The Lepontine dome is a metamorphic and structural dome located in the Penninic domain of the Central European Alps. It was formed during the Alpine collision due to the accretion of crystalline-basement nappes which belonged to the subducting European plate. The area is characterized by a regional Barrovian metamorphism, which is expressed by isograds indicative of peak temperature conditions and by a pervasive mineral and stretching lineation in amphibolite facies. The Barrovian isograds intersect the tectonic nappe contacts, which is frequently interpreted as evidence of metamorphism that occurred after nappe emplacement. Differently, the lineation is associated with NNW-SSE directed shearing, which suggests that peak Barrovian conditions are coeval with nappe accretion. This study was tackled by combined geological mapping, U-Pb zircon dating, major and minor elements chemical analyses, petrography and petrology, two-dimensional thermo-kinematic numerical modelling at the crustal scale, one-dimensional thermal models, and inverse diffusion modelling in garnets to study the geological and thermo-mechanical evolution of the Lepontine dome and their relation to nappe overthrusting.

Geological and structural mapping combined with U-Pb dating permitted to define a crustal-scale shear zone, that we named “Maggia-Adula shear zone”. This tectonic contact is marked by syn-kinematic migmatites in which metamorphic zircon rims are dated at 31-33 Ma. Locally, a younger population of metamorphic zircon rim ages at 22-24 Ma is recorded in post-migmatization dikes and associated metasomatism. These intrusions likely sourced from the Southern Steep Belt (SSB) migmatitic complex bordering the Lepontine dome to the south.

The Maggia-Adula shear zone is located at the top of the Simano nappe and comprises the Cima Lunga unit. In the paragneisses of the Cima Lunga unit, magmatic and detrital zircon cores suggest that this unit was a pre-Variscan metasedimentary sequence and it is not an Alpine tectonic mélange constituted by Mesozoic fragments as commonly assumed. During Permian, this sequence was intruded by granitic sills, that are now continuous orthogneissic horizons. The Cima Lunga unit was strongly deformed during the overthrusting of a rock pile that is here named “Maggia-Adula nappe”.

The regional lineation in amphibolite facies formed during the emplacement of the Maggia-Adula nappe, until peak amphibolite-facies conditions at 31-33 Ma. During overthrusting heat was dominantly advected, as suggested by Péclet number (1–10) and Brinkman number (0.002–1.8) estimations. Also, our thermo-kinematic numerical models show that shear heating represented an additional local heat source on the Maggia-Adula shear zone and together with advection contributed

to the development of inverted metamorphism around the thrust. Moreover, heat conduction during thrusting promoted the smoothing of the temperature profiles and intersection relationships between isograds and the main thrust.

To study the cooling history after the temperature peak, we analyzed amphibolite-facies garnet-paragneisses at different structural levels within the Lepontine nappe pile. These rocks contain garnets with Alpine rims that grew coevally with the amphibolite-facies metamorphic foliation. At close-to-peak temperature conditions, these rims were compositionally re-equilibrated through retrograde reactions, displayed in Mn-increase and Mg-decrease at the garnet border. Applying geothermobarometry, we estimated the post-peak temperatures of re-equilibration to range between 577 and 661 °C at pressures between 0.5 and 1.3 GPa. Multicomponent diffusion modelling applied to garnet rim profiles revealed a thermal quenching on the thrust after peak temperatures at ca. 31 Ma. This fast cooling at close-to-peak conditions of 635 °C and 0.8 GPa is quantified by apparent cooling rates of 100-400 °C/Myr within the shear zone, which are indicative of shear heating active during peak. Indeed, these cooling rate values cannot be explained by regional exhumation processes, even when high exhumation velocities are considered. Shear heating contributed to the heat transfer equilibrium generating high-grade rocks within the Maggia-Adula shear zone and migmatites in its high-strain locations.

Differently, the footwall of the Maggia-Adula thrust at the base of the Simano nappe cooled at a rate of 2 °C/Myr, which agrees with cooling rates predicted by one-dimensional thermal models simulating a regional exhumation of ca. 1 mm/yr for specific rock markers. This exhumation velocity is coherent with the typical values of a regional exhumation scenario. Differently, the apparent cooling rates within the SSB are 20-50 °C/Myr, likely due to the combination of spasmodic melt/fluid advection and diapirism in the migmatitic body which kept the temperature high within the migmatitic complex.

In summary, our results suggest that the Barrovian metamorphism of the Lepontine dome is the expression of the emplacement of the Maggia-Adula nappe, testified in the field by isograds, lineation and migmatites of 31 Ma age. The Barrovian metamorphism is mainly due to heat advected with the overthrusting of this main nappe and coeval conduction of heat. Shear heating was also effective within the Maggia-Adula shear zone during thrusting. Spatially heterogeneous cooling followed at close-to-peak conditions, possibly generating a later heating event in the frontal domains of the Penninic nappes.

Résumé

Cette thèse a pour but de révéler l'origine du métamorphisme barrovien du dôme Lépontin. Le dôme Lépontin est un dôme métamorphique et structural situé dans le domaine Pennique des Alpes d'Europe centrale. Il s'est formé lors de la collision alpine dû à l'accrétion des nappes du socle cristallin qui appartenaient à la plaque Européenne subductée. La région est caractérisée par un métamorphisme barrovien régional, qui s'exprime par des isogrades indiquant des conditions de température maximale et par une linéation minérale et d'étirement omniprésente dans le faciès amphibolite. Les isogrades barroviennes croisent les contacts tectoniques des nappes, ce qui est souvent interprété comme la preuve d'un métamorphisme survenu après la mise en place des nappes. En revanche, la linéation est associée à un cisaillement orienté NNW-SSE, ce qui suggère que les conditions barroviennes maximales coïncident avec l'accrétion des nappes. Cette étude a été réalisée en combinant la cartographie géologique, la datation U-Pb des cristaux de zircon, les analyses chimiques des éléments majeurs et mineurs, la pétrographie et la pétrologie, la modélisation numérique thermo-cinématique en 2-dimension à l'échelle de la croûte, les modèles thermiques en 1-dimension et la modélisation de la diffusion des éléments majeurs dans les grenats afin d'étudier l'évolution géologique et thermo-mécanique du dôme Lépontin et de leur relation avec le chevauchement des nappes.

La cartographie géologique et structurale combinée à la datation U-Pb a permis de définir une zone de cisaillement à l'échelle de la croûte, que nous avons nommée "zone de cisaillement Maggia-Adula". Ce contact tectonique est marqué par des migmatites syn-cinématiques dans lesquelles les bordures métamorphiques de zircon sont datées à 31-33 Ma. Localement, une population de bordures métamorphiques de zircon plus jeune, datés à 22-24 Ma, est enregistrée dans des filons postérieurs à la migmatisation et dans le métasomatisme qui leur est associé. Ces intrusions sont probablement originaires du complexe migmatitique de la Southern Steep Belt (SSB) qui borde le dôme Lépontin au sud.

La zone de cisaillement Maggia-Adula est située au sommet de la nappe de Simano et comprend l'unité de la Cima Lunga. Dans les paragneiss de la Cima Lunga, des cœurs de zircon magmatique et détritique suggèrent que cette unité était une séquence métasédimentaire pré-varisque et qu'il ne s'agit pas d'un mélange tectonique alpin constitué de fragments mésozoïques, contrairement à ce qui est généralement supposé. Pendant le Permien, cette séquence a été intrudée par des filons-couches granitiques, qui constituent aujourd'hui des horizons orthogneissiques continus. La Cima Lunga a été fortement déformée pendant le chevauchement d'une pile de roches appelée ici "nappe de la Maggia-Adula".

La linéation régionale dans le faciès amphibolite s'est formée pendant la mise en place de la nappe Maggia-Adula, jusqu'aux conditions maximales du faciès amphibolite à 31-33 Ma. Pendant le chevauchement, la chaleur a été principalement transportée par advection, comme le suggèrent les estimations du nombre de Péclet (1-10) et du nombre de Brinkman (0.002-1.8). En outre, nos modèles numériques thermo-cinématiques montrent que le chauffage par cisaillement a représenté une source de chaleur locale supplémentaire dans la zone de cisaillement Maggia-Adula et a contribué, avec l'advection, au développement du métamorphisme inversé autour du cisaillement. En plus, la conduction de la chaleur pendant le chevauchement a favorisé le lissage des profils de température et les relations d'intersection entre les isogrades et la zone de cisaillement Maggia-Adula.

Pour étudier l'histoire du refroidissement après le pic de température, nous avons analysé des paragneiss à faciès amphibolite contenant des grenats à différents niveaux structuraux dans les nappes Lépontines. Ces roches contiennent des grenats à bordures alpines qui se sont développés en même temps que la foliation métamorphique du faciès amphibolite. Dans des conditions de température proches du maximum, la composition de ces bordures a été rééquilibrée par des réactions rétrogrades, ce qui se manifeste par une augmentation de manganèse et une diminution de magnésium à la marge du grenat. En appliquant la géothermobarométrie, nous avons estimé que les températures de rééquilibration après le pic thermique se situaient entre 577 et 661 °C à des pressions comprises entre 0.5 et 1.3 GPa. La modélisation de la diffusion multicomposante appliquée aux profils des bords des grenats a révélé une trempe thermique dans la zone de cisaillement après le pic de température à environ 31 Ma. Ce refroidissement rapide dans des conditions proches du pic à 635 °C et 0.8 GPa est quantifié par des taux de refroidissement apparents de 100-400 °C/Ma dans la zone de cisaillement, qui indiquent un chauffage par cisaillement actif pendant le pic. En effet, ces taux de refroidissement ne peuvent pas être expliqués par des processus d'exhumation régionaux, même si on considère des vitesses d'exhumation élevées. Le chauffage par cisaillement a contribué à l'équilibre du transfert de chaleur générant des roches à haute degré de métamorphisme dans la zone de cisaillement Maggia-Adula et des migmatites dans les zones de forte déformation.

Par contre, sous le chevauchement Maggia-Adula, à la base de la nappe de Simano, le refroidissement s'est produit à une vitesse de 2 °C/Ma, ce qui correspond aux vitesses de refroidissement prévues par les modèles thermiques à 1-dimension simulant une exhumation régionale d'environ 1 mm/a pour des marqueurs rocheux spécifiques. Cette vitesse d'exhumation est cohérente avec les valeurs typiques d'un scénario d'exhumation régionale. Différemment, les taux de refroidissement apparents à l'intérieur du SSB sont de 20-50 °C/Ma, probablement en raison de la combinaison de l'advection

spasmodique de roches fondues ou des fluides et du diapirisme dans le corps migmatitique qui a maintenu la température élevée à l'intérieur du complexe migmatitique.

En résumé, nos résultats suggèrent que le métamorphisme barrovien du dôme Lépontin est l'expression de la mise en place de la nappe de Maggia-Adula, attestée sur le terrain par des isogrades, une linéation constante et des migmatites d'un âge de 31 Ma. Le métamorphisme barrovien est principalement dû à la chaleur advectée par le chevauchement de cette nappe principale et à la conduction simultanée de la chaleur. Le chauffage par cisaillement a également été efficace dans la zone de cisaillement Maggia-Adula pendant le chevauchement. Un refroidissement hétérogène dans l'espace a suivi dans des conditions proches du maximum, générant peut-être un réchauffement ultérieur dans les domaines frontaux des nappes Penniques.

Chapter 1

GENERAL INTRODUCTION

1.1 Aim of the project

The main goal of this thesis is to unravel the heat budget in an area located in the heart of the Alpine chain with the focus on the quantification of metamorphic heat sources in crustal-scale shear zones.

The case study is the crystalline basement of the Lepontine dome (Central Swiss Alps), which exposes the tectonostratigraphy of the Penninic Central Alps. The Penninic domain is formed by a sequence of gneissic nappes derived from the European post-Variscan crust and stacked during the Alpine cycle thanks to the movement over crustal-scale shear zones.

The structural and thermal anomaly of the Lepontine Alps has been the center of a longstanding debate on the relation between nappe formation and collisional heat budget. The collisional heat budget can be divided in two heat sources end-members: allochthonous heat sources (conduction or advection) and in-situ heat sources (production from radiogenic heating or mechanical work). Quantifying the relative importance of these end-members is crucial for the analysis of deformation and the relevant heat budget in crustal processes. Therefore, this study deals with a geodynamic problem intrinsic to most orogens.

Specific aims of this study include:

- Geological survey for the realization of the new Swiss National Maps 1:25.000 for the Federal Office of Topography swisstopo.
- Geological and structural analysis on the tectonic contacts to determine the geometry and thickness of the shear zones.
- Geological and structural analysis within the Lepontine nappes to investigate their internal deformation.
- Tackling the timing between major tectonic events and metamorphism, i.e., timing between nappe emplacement and peak Barrovian conditions.
- Assessing the controlling parameters of heat transfer in shear zones and applying this analysis to the Lepontine dome heat budget.

1.2 The heat budget problem

All modern collisional orogens are characterized by a regional metamorphic sequence of (greenschist to amphibolite) conditions called Barrovian metamorphism, in honor of George Barrow who first described the association between regional metamorphism and poly-deformed rocks (Barrow, 1893; 1912). Barrovian conditions characterize continent-continent collisions and correspond to temperatures (T) of ca. 450-750 °C and pressures (P) of ca. 0.5-1 GPa. These conditions are hotter than typical subduction zone geotherms (geothermal gradient of 6-10 °C/km) and the temperatures are ca. 100-300 °C higher than the estimates for the surrounding regions. The origin of this heat surplus has been explained with different models.

The main factors controlling collisional heat budget (*figure 1.1*) are identified in: (i) heat conduction from the mantle, (ii) heat advection from the emplacement of hotter crustal slices or percolation of hot fluids/magma, and (iii) heat production through mechanical work dissipation or from in-situ radioactive processes.

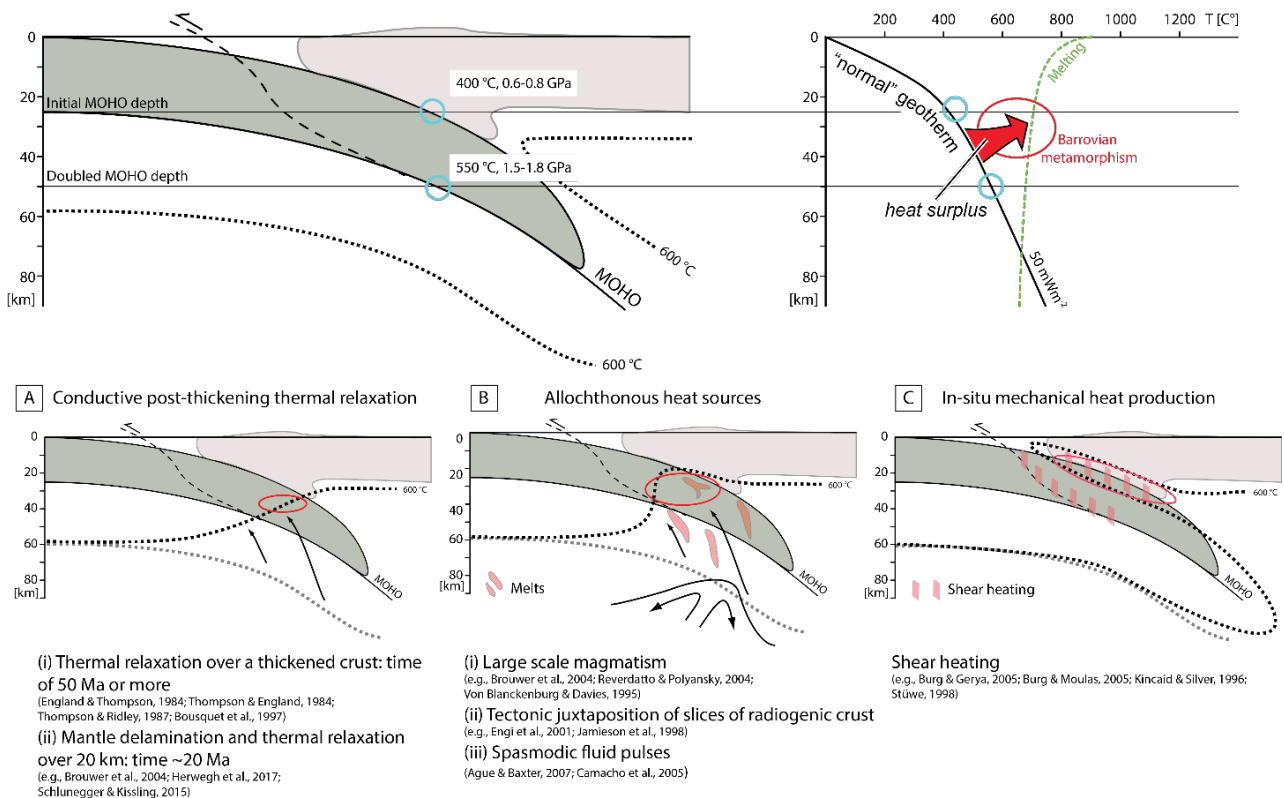


Figure 1.1. Visualization of the mechanisms proposed in the literature as possible solutions for explaining collisional heat budget (from Schenker, 2013). See further details in the main text. Subducting and overriding slabs are represented with different colors and depth is indicated to the left of each plot. Depth is calculated assuming pressure-to-depth. Dashed lines with the upside-pointing arrow within the subducting slab represent the development of a possible thrust surface. Black dashed lines show the evolution of the isotherms, related to heat-induced mechanisms (direction of temperature rise indicated by black arrows). The red circles mark the location of the Barrovian metamorphic imprint.

The first models describing the thermal evolution of Barrovian metamorphism proposed the process of thermal relaxation through conductive heating (*figure 1.1A*), acting from the base of the lithosphere after a rapid phase of crustal thickening (England & Thompson, 1984; Thompson & England, 1984; Thompson & Ridley, 1987; Bousquet et al., 1997). These models predict a metamorphic cycle lasting ca. 50 Ma or more, depending on the considered erosion rate. However, these values do not correspond to the duration of most orogens' metamorphism, which is less than 10-20 Ma (e.g., Ague & Baxter, 2007; Camacho et al., 2005; Dewey, 2005). Therefore, a faster heat source accounting for asthenospheric mantle uprise was proposed. Models which explain mantle uprise invoke mechanical processes such as slab breakoff, slab rollback, and lower crust delamination (e.g., Brouwer et al., 2004; Herwegh et al., 2017; Schlunegger & Kissling, 2015).

A second group of models is represented by the advection models, which consider allochthonous heat sources of diverse nature (*figure 1.1B*). Magmatic or fluid pulses are the first type of source which can contribute to a localized heat surplus in the crust. Extensive magmatism has been correlated with slab breakoff (Von Blanckenburg & Davies, 1995) and linked to elevated horizontal thermal gradients in the middle crust (ca. 14 °C/km; Reverdatto & Polyansky, 2004). Magmas can also be associated to hot fluid flow occurring spasmodically in the crust. The hot fluids advection would cause short timescales heat pulses (Ague & Baxter, 2007; Camacho et al., 2005), but it would also be responsible for the Barrovian regional metamorphic heating itself (Viète et al., 2011). Furthermore, another type of heat advection mechanism at the crustal scale is the tectonic redistribution and accretion of radiogenic crust slices, which are brought at mantle depth through subduction (e.g., Jamieson et al., 1998) or exhumed from mantle depth after subduction (e.g., Engi et al., 2001).

The third category of heat transfer models considers in-situ heat production, which can be radiogenic or through mechanical work dissipation (*figure 1.1C*). Radiogenic heating requires too long time periods (order of tens of Ma) to reproduce the required Barrovian temperatures (Brouwer et al., 2004). While, heat produced through mechanical work (shear heating or viscous heating) has been the center of discussion in multiple publications (e.g., Burg & Gerya 2005; Duretz et al., 2015; Hartz & Podladchikov, 2008; Kincaid & Silver, 1996; Leloup et al., 1999; Maino et al., 2015; Souche et al., 2013; Stüwe, 1998; Thielmann et al., 2015). Shear heating is considered by some authors as an essential mechanism in the formation and development of crustal-scale shear zones, capable of affecting both temperature distribution and the deforming crust structure (e.g., Burg & Gerya 2005; Burg & Schmalholz, 2008; Thielmann et al., 2015). Some authors even support the thesis that shear heating accounts for an increase in metamorphic crustal temperatures between 25 °C and 200 °C and can generate inverted metamorphic zonation and partial melting (e.g., Burg & Gerya 2005; Cioldi, 2017; Nabelek et al., 2010; Schmalholz & Duretz, 2015). However, others deny that crustal

temperature increase due to shear heating can exceed 80 °C and can produce either change in metamorphic grade, inverted metamorphism or even partial melting (Platt, 2015; Kidder et al., 2013). In general, the scientific debate resolves around the extent to which mechanical deformation can elevate the temperatures of deforming metamorphic systems (e.g., Mako & Caddick, 2018).

As a conclusion, we can state that each of the heat transfer processes presented above can explain one or more aspects characterizing the Barrovian terrains. However, the interplay between these endmembers, when they act contemporaneously within deforming rocks, remains cryptic to decipher. With this contribution we aim to fill this gap quantifying the relative impact of the conduction, advection, production terms that describe the heat transfer in any large-scale crustal process.

1.3 Shear zones and heat transfer

Barrovian terrains are always associated with deformation, and can generate in diverse tectonic settings, either in compressional or extensional systems. Some examples of coupled metamorphism and deformation are found in the Main Central Thrust of Himalaya, Nestos Thrust Zone in Rhodope (Greece and Bulgaria), Alpine fault (New Zealand), Grampian terrane (Scotland). In all these geodynamic contexts crustal-scale shear zones accommodate and, at the same time, induce a large part of deformation. Therefore, in the case of collisional orogens, the study of Barrovian metamorphism cannot be dissociated from shear zones.

Viète (2008) observed that peak metamorphism in the Barrovian metamorphic series of Scotland occurred during a shearing episode on large-scale extensional shear zones. These shear zones concentrated episodic heat sources and the duration of their activation controlled the one of regional metamorphism. According to these observations, the movement on mid-crustal shear zones may influence the thermal behavior during orogenesis. As a consequence, the impact of shear zone development within a collisional orogen may affect the nature and origin of regional metamorphic terrains and must be investigated to solve the ongoing debate of collisional heat budget.

1.3.1 An overview on shear zones

Crustal-scale shear zones are regions in the lithosphere where strain localizes, they occur in diverse geodynamic settings and permit the exhumation of rocks which were deeper in the Earth (Fossen, 2016). One example are the large-scale shear zones forming within a collisional orogen, capable of juxtaposing different crustal slices in the process of mountain building.

In an ideal case, strain localization is maximum in the center of the shear zone, where following rocks markers becomes more difficult due to their change in shape, orientation and thickness (figure 1.2). The ideal shear zone develops in a simple shear regime (Ramsay, 1980) but most of them form in conditions when both pure and simple shear act on the same plane.

Shear zones grow in length and thickness and can organize in anastomosing or conjugate arrays (Fossen & Cavalcante, 2017). The anastomosing array consists of a zone of shear formed by multiple high-strain planar zones with non-coaxial deformation which together define a composite shear zone, whereas in the conjugate array a pattern of multiple conjugated shear zones characterized by coaxial deformation dissects low-strain domains.

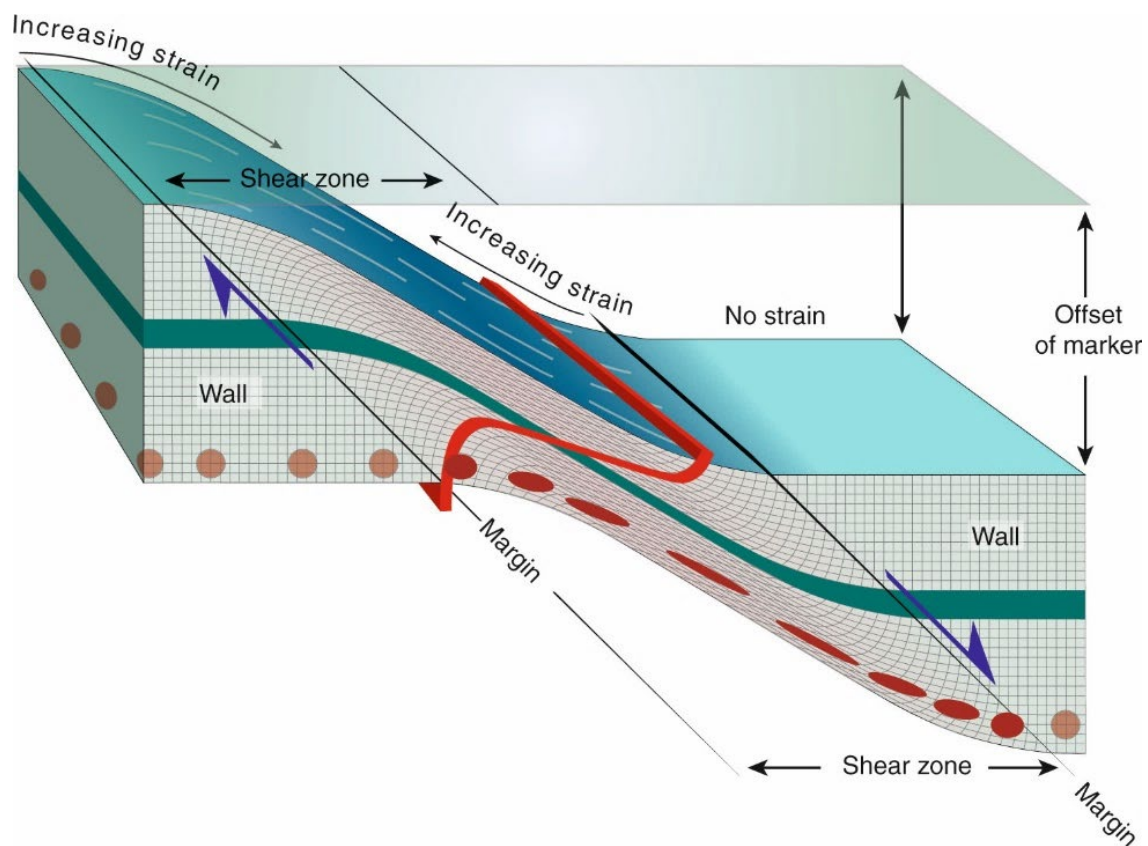


Figure 1.2. 3D model of an ideal shear zone (from Fossen, 2016). Shear zone deformation is illustrated on a grid, with two planar perpendicular markers (in red and teal colors) and with circular strain markers. The grid and the markers change shape, orientation and thickness across the shear zone. The maximum strain is at the center of the shear zone. Blue arrows indicate the sense of shear. Parallel light blue lines at the bottom of the 3D model are stretching lineations developing on the foliation plane.

Shear zones classification can also be made according to their dominant micro-scale deformation mechanism: in plastic shear zones intra-crystalline deformation dominates (dislocation creep, dislocation glide, twinning; [Passchier & Trouw, 2005](#)), while frictional shear zones are governed by brittle deformation mechanisms (e.g., grain fracture or rotation). Furthermore, the deformation style can be continuous or discontinuous depending on whether rock markers can be followed continuously across the shear zone (ductile shear zone) or not (brittle shear zone; [Fossen & Cavalcante, 2017](#)).

In ductile shear zones, a foliation and a stretching lineation can develop in initially isotropic rocks. The lineation lies on the foliation plane and it is stretched in the direction of the X-axis of the strain ellipsoid, its projection on the shear plane indicates the shear direction ([Fossen, 2016](#)). Consequently, the development of a stretching lineation permits to detect the strain regime orientation active during shearing. This feature becomes fundamental, for example, when analyzing the effects on rock geometries produced by shear zones moving with different velocities along the shear plane. Complex foliation geometries can indeed originate due to flow perturbations folding ([Alsop & Holdsworth, 2007](#)) making difficult the reconstruction of movement direction along the shear zone.

1.3.2 Rationale of shear zone formation: insights into the thermo-mechanical aspects

Shear zones can generate from several different processes. Strain localization is coupled with rock's strength decrease and can be achieved by: (i) geometric softening, involving slip on mineral crystallographic planes and minerals reorientation ([Etchecopar, 1977](#); [Ji et al., 2004](#); [Passchier & Trouw, 2005](#)); (ii) grain size reduction, producing new fine-size strain-free weaker grains (e.g., [Braun et al., 1999](#); [Platt & Behr, 2011](#); [Rutter & Brodie, 1988](#)); (iii) reaction softening, which can promote a loss of cohesion between grain boundaries, growth of new weaker phases or new minerals aligned with the shear plane (e.g., [Gueydan et al., 2003](#); [Newman et al., 1999](#); [Oliot et al., 2010](#); [Passchier & Trouw, 2005](#); [Steffen et al., 2001](#)); (iv) fluid-related softening, causing grain dissolution, retrograde hydration reactions, or introduction of water into the crystal lattice (e.g., [Finch et al., 2016](#); [Mancktelow & Pennacchioni, 2004](#)); (v) thermal softening, where temperature determines a decrease in rocks' viscosity (e.g., [Brun & Cobbold, 1980](#); [Kiss et al., 2019](#)).

In general, the initiation of a ductile shear zone progresses with the rapid build of strain concentration. At the micro-scale, the strain accumulation leads to continuous recrystallization, which in turn enhances the formation of small grains that weaken the rock. Some shear zones develop as a consequence of thermal softening, which leads to strain localization (e.g., [Duretz et al., 2015](#); [Kiss et al., 2019](#)). Once deformation is confined, heat starts dissipating and in the shear zone it develops a thermal peak which decreases with time (e.g., [Fleitout & Froidevaux, 1980](#)). Shear zones are related

to thermal perturbations and both their lifetime and width partially depend on the amount of heat produced within them.

The thermal evolution within lithospheric-scale shear zones is determined by the balance between three end-members: diffusion of heat, advection of heat and production of heat (Duprat-Oualid et al., 2015). Advection refers to transport of heat caused by the juxtaposition of hot and cold rock units and it is more efficient when velocities are higher. When considering advection alone, the resulting isotherms after thrusting are displaced on one side and the other of the thrust, creating a temperature jump. However, also diffusion acts as a heat transport mechanism during thrusting with the effect of smoothing thermal gradients over time (e.g., Thompson & Ridley, 1987). Finally, if production of heat is considered, the mechanical work can create through shear heating an inverted distribution of isotherms with the core of the thrust hotter than the wall rocks. The main parameters controlling the extent of heat produced by shear heating are strain rate and rocks' viscosity. The interplay of these three terms can lead to different configurations depending on the importance of each of them, which can be assessed only by a quantitative study.

Our testing strategy will focus on the quantification of the relative impact of advection, diffusion and production. Indeed, these end-members are directly linked to the three types of mechanisms controlling the collisional heat budget (see previous *section 1.2*).

1.4 The Lepontine dome case study

The Lepontine dome belongs to the Penninic domain of the Central European Alps, which includes portions of the European plate subducted and accreted during the Alpine collision (Cretaceous-Paleogene Period). The foliation and thrusts attitudes define a dome shape, thus the name “Lepontine dome”. The dome is structurally divided in two culminations: the Simplon (or Toce) subdome to the west and the Ticino subdome to the east (Merle et al., 1989), divided by a steep zone called “Querzone” (Preiswerk, 1918). In this contribution we focus on the Ticino subdome.

The Lepontine dome is internally formed by crystalline basement nappes (Lepontine nappes) deriving from the distal margin of the European plate (*figure 1.3*). The basement nappes of the Lepontine dome are, from bottom to top: Leventina, Simano, Adula-Cima Lunga, Maggia. These units consist mainly of gneisses (both orthogneiss and paragneiss), with a minor occurrence of carbonates and ultramafic rocks. To the south, the Lepontine nappes are bordered by a belt of migmatites with steep attitudes, named Southern Steep Belt (SSB).

Metamorphic structure of the Lepontine dome

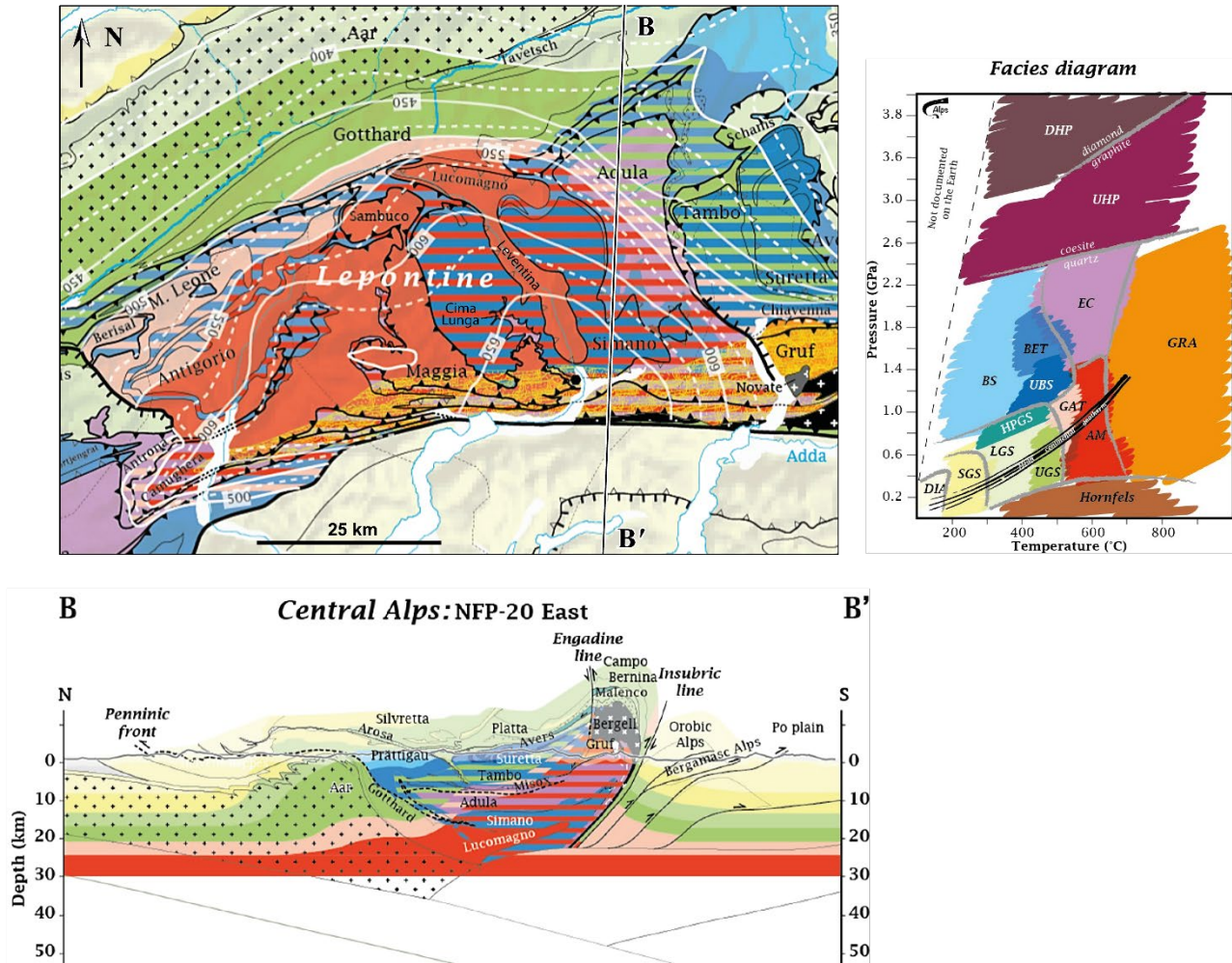


Figure 1.3. Metamorphic-structural map of the Lepontine dome and tectonic section B-B' of the Central Alps, extracted from the Metamorphic framework of the Alps (Bousquet et al., 2012). The colors are indicative of the different metamorphic facies, as shown in the facies diagram to the right. Abbreviations indicate: diagenesis/sub-anchizone (DIA), sub-greenschist facies (SGS), lower greenschist facies (LGS), upper greenschist facies (UGS), high-pressure greenschist facies (HPGS), blueschist facies (BS), upper blueschist facies (UBS), blueschist-eclogite transition (BET), eclogite facies (EC), ultra high-pressure facies (UHP), ultra high-pressure facies II (DHP), greenschist-amphibolite transition (GAT), amphibolite facies (AM), granulite facies (GRA). The black line in the facies diagram is the mean continental geotherm. White lines in the metamorphic-structural map are isograds with relevant temperature values indicated upside-down.

1.4.1 The Lepontine nappes

In this section we describe the geology and peak P-T conditions of each nappe within the Ticino culmination of the Lepontine dome (*figure 1.4*). Geochronological estimates are given for the main metamorphic events relevant to nappe emplacement.

The Leventina nappe is predominantly formed by leucocratic gneisses containing small volumes of paragneisses, amphibolites and calcsilicate rocks (Casasopra, 1940; Codoni, 1981). The metamorphic conditions are constrained between 550-650 °C and 0.5-1 GPa (Rütti et al., 2008). The gneissic foliation decreases in intensity to the south, together with a mineralogical change and a rise in temperatures attributed to the vicinity to the SSB (Burri et al., 2005; Casasopra, 1940; Todd & Engi, 1997).

The Simano nappe is constituted by several generations of orthogneisses, paragneisses, minor mafic dikes, ultramafic lenses, and marbles. The thrusting of the Simano nappe on top of the Leventina happened at ca. 31 Ma, at around 550 °C (Boston et al., 2017; Gieré et al., 2011; Janots et al., 2009). Peak Alpine P-T conditions are recorded at 625 °C and 0.6 GPa (e.g., Allaz et al., 2005; Rütti, 2001; Rütti et al., 2005).

Upsection, the Adula and Cima Lunga units are traditionally considered as one nappe that dies out to the west, emplaced above the Simano (e.g., Dal Vesco, 1953). The Adula-Cima Lunga nappe exhibits orthogneisses and paragneisses with subordinate volumes of marbles and mafic-ultramafic rocks recording (U)HP conditions. It is the only nappe containing a large distribution of (U)HP relics, with peak P recorded at 2-3 GPa (Evans et al., 1979; Heinrich, 1982; Nimis & Trommsdorff, 2001; Pfiffner, 1999; Scambelluri et al., 2014), that are the evidence of the deep burial of the unit (Brouwer et al., 2005; Engi et al., 2001; Froitzheim et al., 2003; Nagel et al., 2002b; Schmid et al., 2004). The HP of the Adula-Cima Lunga nappe is commonly placed at ca. 38-40 Ma (Becker, 1993; Brouwer et al., 2005; Gebauer, 1996; Herwartz et al., 2011; Sandmann et al., 2014). Later, at ca. 32 (e.g., Galli et al., 2012; Gebauer, 1996), the nappe decompressed and experienced peak amphibolite conditions of 650-700 °C at ca. 0.8 GPa (e.g., Brouwer et al., 2004; Herwartz et al., 2011; Liati et al., 2009; Nagel, 2008; Sandmann et al., 2014).

The Maggia nappe lies above the Cima Lunga and the Simano nappe in the central part of the Ticino culmination and above the Mergoscia zone and the Antigorio nappe more to the west (e.g., Steck et al., 2019). This nappe is formed by orthogneisses, paragneisses and banded mafic rocks. The maximum T-P conditions reached 600-700 °C at 0.8-0.9 GPa (Allaz et al., 2005; Boston et al., 2017; Brower et al., 2005; Burri et al., 2005; Todd & Engi, 1997). The Maggia nappe and the adjacent units

have undergone polyphase deformation (e.g., [Maxelon & Mancktelow, 2005](#)) which makes complex the interpretation of their relationships.

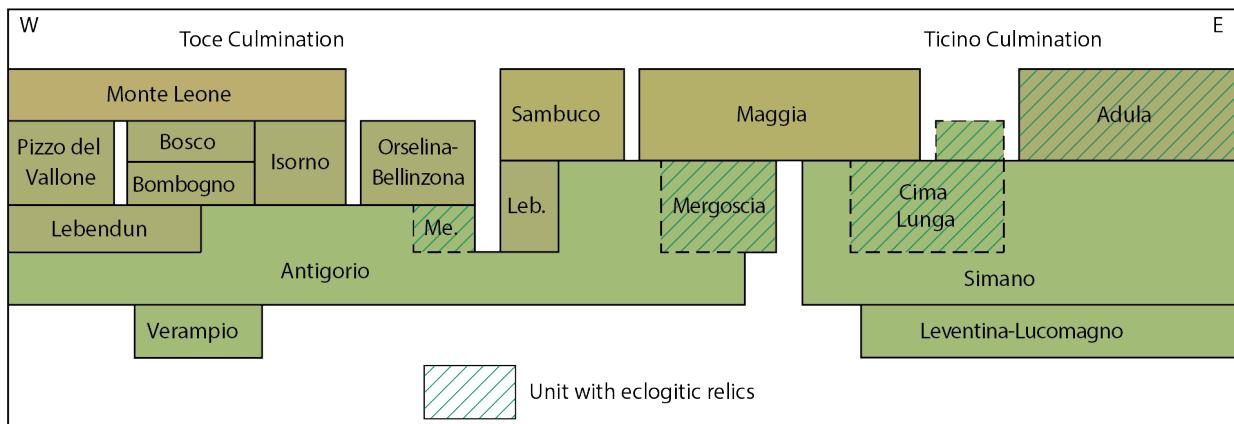


Figure 1.4. E-W schematic structural asset of the Lepontine dome, modified after [Gouffon \(in review\)](#). Nappes are represented as rectangles and the relations between them in the Ticino and Toce culminations are shown. Abbreviations “Leb.” And “Me.” indicate Lebendun and Mergoscia respectively. The position of the Maggia nappe with respect to the surrounding units is highly debated.

Lastly, the roots of these nappes have been destroyed and reworked during the continuous melting between 22-32 Ma of the migmatites of the SSB ([Boston et al., 2017](#); [Gregory et al., 2012](#); [Rubatto et al., 2009](#)). The peak conditions registered by these migmatites are ca. 620-750 °C and 0.7-0.8 GPa (e.g., [Berger et al., 2008](#); [Burri et al., 2005](#); [Rubatto et al., 2009](#)).

1.4.2 Barrovian metamorphism in the Lepontine dome

As described in the previous *section 1.4.1*, the Lepontine dome is characterized by a widespread Barrovian metamorphic imprint. This imprint is recorded in the concentric distribution of metamorphic isograds ([Todd & Engi, 1997](#); [Wenk & Keller, 1969](#); [figure 1.3](#)) and in a constant NW-SE directed mineral and stretching lineation at peak amphibolite conditions ([Wenk, 1955](#)). From north to south, the peak T conditions increase from 500-550 °C at the northern margin of the dome (e.g., [Frey, 1969](#); [Janots et al., 2008](#)) to ca. 650-700 °C at its southern margin ([Burri et al., 2005](#)).

In general, the Barrovian imprint is constrained somewhere after the main episode of nappe emplacement between 35-38 Ma and 20 Ma (e.g., [Merle et al., 1989](#) and references therein; [Boston et al., 2017](#)). Afterwards, thermal relaxation took place and the Lepontine dome cooled down rather homogeneously ([Hurford, 1986](#); [Janots et al., 2009](#)). Nevertheless, the timing of the metamorphic events is still controversial. The ages at 35-38 Ma (muscovite-phengite Rb-Sr; [Hunziker, 1970](#); [Steinitz & Jäger, 1981](#)) were initially interpreted as the peak of Lepontine metamorphism ([Jäger, 1973](#)). However, ubiquitous younger ages around 20-25 Ma have been proposed to record peak amphibolite conditions (monazite U-Pb and amphibolite K-Ar; [Boston et al., 2017](#); [Deutsch &](#)

Steiger, 1985; Hännly et al., 1975; Köppel et al., 1981; Köppel & Grünenfelder, 1975; Köppel & Grünenfelder, 1978; Monié, 1985). Therefore, a more complex thermal history for the Lepontine dome was suggested (e.g., Huber et al., 1980; Klaper, 1982; Merle et al., 1989), and the youngest ages until 20 Ma were identified as a second episode of mineral growth (e.g., micas Rb-Sr; Steiger, 1983; Steiger & Bucher, 1978). Accordingly, many authors proposed a second thermal event within the Lepontine dome postdating the nappe pile formation. This popular hypothesis of a post-nappe emplacement heating was justified by the cross-cutting field relationship between isograds and main tectonic contacts (e.g., Berger et al., 2011; Frey et al., 1999; Nagel, 2008; Todd & Engi, 1997; Trommsdorff, 1974; Wenk & Keller, 1969; Wiederkehr, 2009). Also, in some regions, mineral crystal growth after the main syn-thrusting foliation have been observed (Klaper, 1982; Wiederkehr et al., 2008).

Nevertheless, within the basement nappes the presence of a constantly oriented lineation at amphibolite conditions (see *figure 1.5*) suggests that the peak Barrovian conditions may be related and be coeval to the nappe stacking. This controversy leaves the debate on the evolution of the Lepontine Barrovian metamorphism unresolved. Both the thermal (metamorphic isograds and peak amphibolite conditions) and mechanical (nappe emplacement over crustal-scale shear zones) aspects must be considered when analyzing the complex metamorphic history of the Lepontine dome. Therefore, a study attempting to unravel the thermal history of the Lepontine is not complete without considering the thermo-mechanical implications of shear zones development (ref. to *section 1.3.2*).



Figure 1.5. Example of lineation marked by biotite and elongate quartz-feldspar aggregates in a gneiss from Val Maggia (Ticino, Switzerland).

1.4.3 Heat sources and geodynamic scenarios

The main tectonic event of the Lepontine dome is represented by the formation of the nappe stack. The most pervasive metamorphic event within the basement nappes is related to the development of the Barrovian conditions. The Barrovian conditions that were reached during the formation of the main mineral and stretching lineation suggest a coeval genesis of these two tectonic and metamorphic processes. Their combined analysis can be achieved by considering the heat transport mechanisms within the geodynamic context.

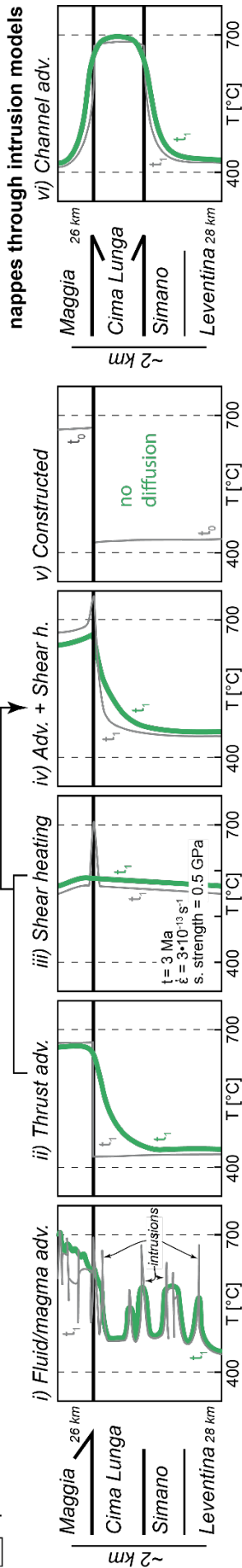
Two models have been proposed to explain the emplacement of the Lepontine nappes: the orogenic wedge model, and the buoyancy-driven exhumation models. The orogenic wedge model describes a northward nappe accretion in front of Adria plate (Platt, 1986). Within this model, rocks are not buried to great depth, and the presence of (U)HP rocks is explained by local pressure variations deviating from lithostatic conditions (e.g., Schmalholz et al., 2014). Alternatively, (U)HP rocks have been justified with a second type of models. These models explain nappe emplacement through buoyancy-driven exhumation which can be controlled by return flow in the subduction channel or Stokes flow, both possibly associated with slab rollback (e.g., Beltrando et al., 2010; Burov et al., 2001; England & Holland, 1979; Froitzheim et al., 2003; Schenker et al., 2015; Schmalholz & Schenker, 2016; Schmid et al., 1996; Stöckhert & Gerya, 2005).

Within these exhumation models, nappe emplacement can be achieved through thrusting or intrusion. The combination of emplacement mode, heat transfer mechanisms and possible heat sources can lead to diverse scenarios of recorded peak T metamorphism with depth. In *figure 1.6* we illustrate our working hypotheses which try to explain the current peak T metamorphic record in the Lepontine dome with different possible scenarios.

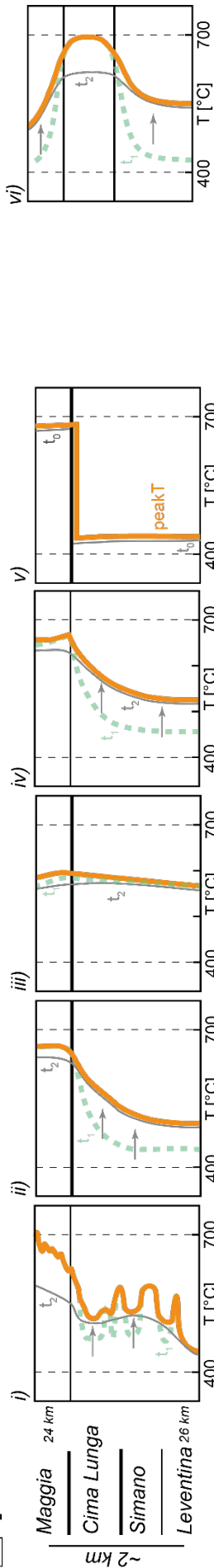
Figure 1.6. Possible T-evolution with depth in the nappes of the Lepontine dome (tectonic section at the center of the dome) according to different geodynamic scenarios. See detailed description in the main text. The initial depth at the onset of thrusting is set to 26 km, based on figure 1.1. Gray lines are the transient temperature distribution at time $t_{0,1,2}$. The thick green lines are the transient temperature distribution during nappe emplacement (t_1) when diffusion is considered with advection/production. The thick orange lines are the distribution of the peak temperature record after nappe emplacement and thermal relaxation at t_2 within a normal geotherm. Thick blue and red lines are peak temperature records when a heat source from the asthenosphere (ca. 1300 °C at 60 or 50 km depth) is considered at $t_{3C,H}$. Thick dashed lines represent the precedent thermal state (light green) or peak temperature record (light orange) which has been modified by successive thermal events. Gray lines in panel (C) point to the temperature increase due to thermal relaxation of the dome. Thermal profiles are qualitatively constrained, except for shear heating with diffusion (green thick line in B-iii) and panel (D) where t_{3C} and t_{3H} are quantitatively constrained with the one-dimensional models of Nabelek et al. (2010). In panel B-iii, t is time, $\dot{\epsilon}$ is strain rate, “s. strength” indicates the shear strength of rocks considered for the calculation of the shear heating contribution.

A $t_0 = 40-38$ Ma: initiation of Adula nappe emplacement

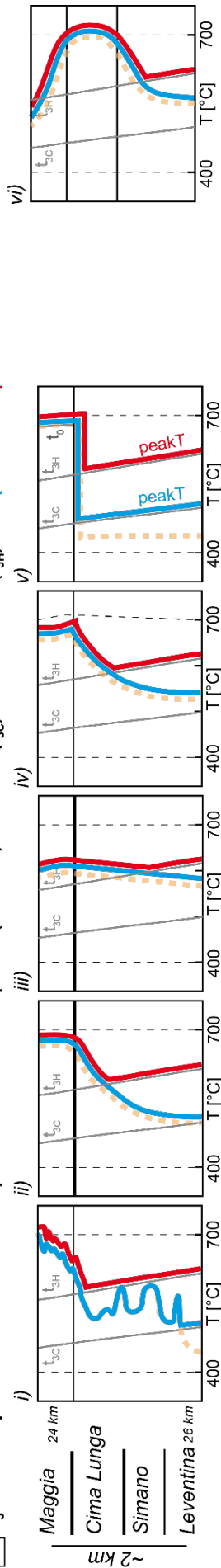
B $t_1 = 33-32$ Ma: final stages of Adula nappe emplacement



C $t_2 = 32-20$ Ma: thermal relaxation within a normal geotherm → peakT record



D $t_3 = 20$ Ma: peak of second thermal pulse with asthenosphere (1300 °C) at 60 km (t_{3C}) and at 50 km (t_{3H}) → peakT and peakT record



When we consider nappe thrusting, we can discern between four principal end-members. The first case corresponds to hot fluids injections or magma intrusions which can origin as continuous and long-lived spasmodic pulses prior, during or post-nappe emplacement (*figure 1.6B-i*). The magmatism would produce a regional metamorphism lasting for 10-20 Ma (Camacho et al., 2005; Viète et al., 2011). The temperature-depth distribution recorded by the metamorphism would show a sawtooth profile. These local variations of the temperature profiles are then smoothed during the following thermal relaxation (*figure 1.6C-i*).

A second case is represented by advection of heat during overthrusting, where heat is transported by the overriding nappe. The exhuming nappe heats the nappe below and the temperature profile shows an inverted configuration with a quasi-constant temperature within the hanging wall and an exponential decrease in the footwall (*figure 1.6B-ii*). The subsequent thermal relaxation in normal geotherm conditions determines an increase in footwall temperature and the recorded peak T will be higher than the temperature experienced during thrusting (*figure 1.6C-ii*).

A less marked inverted pattern arises in the case of shear heating acting on the thrust surface when conduction is also considered. In the shear heating case, a temperature increase is recorded in correspondence of the thrust, whereas hangingwall and footwall temperatures decrease far from the shear zone (*figure 1.6B-iii*). The amount of temperature increase on the thrust surface is controlled by viscosity (within the “shear strength” term) and strain rate. Isograd’s configuration after thermal relaxation records the transient temperature increase on the thrust during nappe emplacement (*figure 1.6C-iii*).

Shear heating in natural shear zones is strongly connected with advection and conduction. A combination of advection and shear heating produces a temperature increase in correspondence of the thrust and a decrease both upwards and downwards. The decrease in the footwall is exponential, while in the hangingwall is less marked (*figure 1.6B-iv*). The final peak T record is similar to the advection case; however, the highest metamorphic temperatures are recorded at the thrust interface (*figure 1.6C-iv*).

Finally, if metamorphism occurs prior to nappe emplacement (t_0 in *figure 1.6B-v*) and it is subsequently transposed, a sharp jump will result in the recorded temperature profile. This configuration will remain the same also during the following thermal relaxation (*figure 1.6C-v*).

Another possibility of explaining nappe emplacement is through an intrusion model. In this kind of model, one nappe intrudes in the nappe stack and transports its heat through advection (*figure 1.6B-vi*). In this case, the internal temperature of the advecting nappe is maintained and the exponential

decay seen in the advection due to thrusting repeats both in the nappes above and below the intruding unit. With thermal relaxation, the temperature profile diffuses equally in hangingwall and footwall (*figure 1.6C-vi*).

In general, conduction during thermal relaxation smooths temperature profiles with time. The thermal assets resulting from thermal relaxation after nappe emplacement (*figure 1.6C*) changes configuration when a second thermal peak event at ca. 20 Ma is considered (*figure 1.6D*). Previous authors proposed heating of the nappes from below due to wedging and underthrusting (Berger et al., 2011) or due to slab breakoff or lower crustal/mantle delamination (Herwegh et al., 2017). We simulated these scenarios by placing the asthenosphere (ca. 1300 °C) at shallow levels of 50 and 60 km depth (calculated with the one-dimensional models of Nabelek et al. (2010)). Even at these extreme conditions, the relaxation of the system would shift the peak T record only in the lowermost structural levels of the nappe pile, leaving the uppermost peak T record unchanged. This shows that even with a second extreme heat conductive event, it is likely that the metamorphic record of the nappe emplacement would be preserved.

In conclusion, multiple possibilities can be proposed to explain the Lepontine dome thermal evolution but there is still no agreement on which is the most feasible one(s). The aim of this thesis is to test and verify these geodynamic scenarios applying multiple disciplines from fieldwork to geochronology to numerical modelling.

1.4.4 Why the Lepontine dome?

The Lepontine dome is only one example of Barrovian conditions recorded within a collisional orogen. For this reason, one could ask why is the Lepontine metamorphism so different and why does this area merit particular study?

The Alps are probably the most studied collisional orogen but there are still unresolved issues, the Lepontine metamorphism is one of those. The characteristic components of this area are the structural dome shape, the internal tectonic subdivision in nappes separated by shear zones, the concentric isograds that intersect the tectonic contacts, the presence of inverted metamorphic gradients, the constant lineation at peak conditions. The combination of these features is peculiar to the Lepontine dome.

We try to unravel this complexity through a multidisciplinary approach investigating both large-scale and small-scale processes. The Lepontine dome is a unique area where this kind of analysis can be achieved. The exposure of different structural levels within few kilometers distance permits to test the hypotheses concerning the possible geodynamic scenarios (see previous *section 1.4.3*) together

with specific mechanisms acting at the scale of a single shear zone (see *section 1.3.2*). Finally, these are the reasons why understanding the Lepontine metamorphism is crucial for the advance of our comprehension of collisional orogens' heat budget.

1.5 Thesis synopsis

This thesis is structured in five chapters.

- Chapter 1: *General introduction.*
- Chapter 2: *Quantification of heat transfer in shear zones through 2D thermo-kinematic numerical modelling.*
- Chapter 3: *Implications of new geological mapping and U-Pb zircon dating for the Barrovian tectono-metamorphic evolution of the Lepontine dome (Central European Alps).*
- Chapter 4: *Fast and spatially heterogeneous cooling rates at amphibolite-facies conditions reveal the significance of local heat sources: a case study from the Lepontine Alps (Switzerland).*
- Chapter 5: *Discussion and Conclusions.*

The central chapters (*Chapters 3 and 4*) have been written as standalone journal articles, which contain the background information relative to them. *Chapter 3* has been published in *Geochemistry, Geophysics, Geosystems* journal. *Chapter 4* is under review for the *American Journal of Science*.

In addition to these papers, I have also co-authored a paper which is under review for the *International Journal of Geosciences*: Corvò, S., Maino, M., Langone, A., Schenker F. L., Tagliaferri, A., Perozzo, M., Casini, L., and Seno, S. (in review) *Monazite and zircon U-(Th-)Pb dating reveal multiple episodes of HT metamorphism in the Cima Lunga unit (Central Alps): implications for the exhumation of high-pressure rocks.*

Moreover, I have co-authored the new Swiss National geological maps 1:25.000 n°1273 Biasca, 1294 Grono, 1274 Mesocco, 1254 Hinterrhein, which will be published by swisstopo in the next years.

The final section of this thesis consists in multiple appendixes which contain a brief description of the applied analytical methods and a detailed description of uncertainty evaluation for ICP-MS analyses (*Appendix A*), the supplementary material relevant to *Chapter 2* (*Appendix B and C*), to *Chapter 3* (*Appendix C, D, E, F, G*) and to *Chapter 4* (*Appendix G, H, I, J*). Excel tables, Matlab codes, movies and some figures have been uploaded onto the general-purpose open-access repository Zenodo: <https://zenodo.org/record/8399771>.

This thesis is the result of my own work, in collaboration with other researchers. Throughout the thesis, I use the pronoun “we” to acknowledge the researchers who contributed in shaping methods and approaches adopted in my PhD project and in developing the ideas presented in my thesis.

Chapter 2

QUANTIFICATION OF HEAT TRANSFER IN SHEAR ZONES
THROUGH 2D THERMO-KINEMATIC NUMERICAL MODELLING

2.1 Introduction

Numerical models are a useful tool to understand geological processes. Computer-based numerical solutions implement the physics of kinematic, thermal, mechanical, chemical natural scenarios in order to quantify the variables involved. In general, kinematic numerical models implement the laws of physics describing the movement of points or elements in space, thermal models permit to compute processes involving temperature changes, mechanical models simulate the behavior in response to stress and strain, and chemical models describe the change in chemical and mineralogical characteristics of a material. Simple models implement only one or two of these aspects, and they have the power to give exhaustive and didactic results. The complexity becomes greater with the increase in the controlling parameters when a problem is described from multiple perspectives.

The aim here is to quantify the relative importance of the different heat transfer mechanisms acting within a shear zone (see *section 1.3.2* in *Chapter 1*). To describe the thermal asset of a shear zone during its movement, the minimal configuration needs to couple both thermal and kinematic processes. Therefore, we opt for a thermo-kinematic model which can be easily adapted to the geometry of our case study. In addition, the thermo-kinematic models were proven to be a powerful tool to solve first-order thermal problems in shear zones ([Duprat-Oualid et al., 2015](#); [Herman et al., 2010](#)).

The thermal part of these models implements the temperature variation with time through the heat flow equation, controlled by the combination of three end-members. The heat flow equation is expressed by (in one-dimension; [Spear, 1993](#)):

$$\frac{dT}{dt} = D \cdot \frac{\partial^2 T}{\partial z^2} + \frac{H}{\rho c} - v \cdot \frac{dT}{dz} \quad (1)$$

Where the term $D \cdot \frac{\partial^2 T}{\partial z^2}$ is the expression governing heat conduction, $\frac{H}{\rho c}$ heat production, and $v \cdot \frac{dT}{dz}$ heat advection. D is the thermal diffusivity, T is the temperature, z unit length, H internal heat production (e.g., radiogenic heating or shear heating), ρ density, c specific heat, v velocity.

The temperature variations are linked to the movement of elements, hence to their velocity. Velocities are computed in the kinematic part of these models and contribute to the advection and production terms of the heat equation. The heat production comprises both the radiogenic heating and the shear heating components, this latter computed as:

$$H_{sh} = \tau \cdot \dot{\epsilon} \quad (2)$$

Shear heating depends on the strain rate $\dot{\epsilon}$ and on the shear strength $\tau = 2 \cdot \eta \cdot \dot{\epsilon}$, with η viscosity.

In this chapter we present simple thermo-kinematic numerical models which we used to assess the influence of diffusion, advection, production of heat during thrusting. Our results will try to explain physically some of the thermal features observed in the Lepontine dome (see *section 1.4.2* in *Chapter 1*).

2.2 Methodology

We consider a scenario where the overthrusting of a crustal slice on top of another happens on a prescribed thrust surface. The aim is to reproduce the geodynamic scenario of the Lepontine nappe emplacement during Alpine subduction, with a focus on the Adula nappe. We consider a low-angle (α) ramp thrust of 15 degrees, and a ramp height (h) of 5 km corresponding to the maximum thickness of the Adula nappe (e.g., [Cavargna-Sani et al., 2014b](#)). The reference temperature at the thrust height above the ramp (T) is set to 500 °C, which approximately corresponds to the temperature at the top of the Simano nappe during the prograde phase before reaching peak conditions (e.g., [Janots et al., 2009](#); [Rütti, 2003](#)). The adopted physical parameters used in the numerical simulations are displayed in *table 2.1*.

Physical parameters		Value	SI unit	Reference
$grad$	geothermal gradient	0.01	$K \cdot m^{-1}$	Subduction-zone geotherm conditions: 10°C/km
k	thermal conductivity	2.5	$W \cdot m^{-1} \cdot K^{-1}$	Mean value for gneiss (Cermak & Rybach, 1982)
C	heat capacity	1000	$J \cdot kg^{-1} \cdot K^{-1}$	Value for quartz and feldspar is ca. 700 $J \cdot kg^{-1} \cdot K^{-1}$ (Cermak & Rybach, 1982)
ρ	density	2700	$kg \cdot m^{-3}$	Average density for gneiss/granite
D	thermal diffusivity	$0.9 \cdot 10^{-6}$	$m^2 \cdot s^{-1}$	Typical values for the crust: $0.6-1.2 \cdot 10^{-6} m^2 \cdot s^{-1}$ (Spear, 1993)
η	Effective rock viscosity	$10^{19}-10^{22}$	$Pa \cdot s$	Viscosity variation in exhuming rock units (Vaughan-Hammon et al., 2022)
Q	activation energy	$200 \cdot 10^3$	$J \cdot mol^{-1}$	(Candioti et al., 2022)
R	gas constant	8.314	$J \cdot K^{-1} \cdot mol^{-1}$	
$H0$	surface radiogenic heat production	$5 \cdot 10^{-7}$	$W \cdot m^{-3}$	(Hacker et al., 2015)
α	Ramp angle	15°		
h	Height of the ramp	$5 \cdot 10^3$	m	Maximum thickness of the Adula nappe (Cavargna-Sani et al., 2014b)
$T(h)$	Temperature at h	773	K	Temperature at the top of the Simano nappe before peak (Janots et al., 2009 ; Rütti, 2003)

Table 2.1. Physical parameters used in numerical simulations.

2.2.1 Quantification of dimensionless parameters

We applied dimensional analysis following the approach of Duprat-Oualid et al. (2015). With this simple analysis, we quantitatively describe the relative contribution of each term of the heat equation using two dimensionless parameters: Péclet (Pe) and Brinkman (Br) numbers.

The Péclet number quantifies the effectiveness of heat transport by advection versus diffusion. In general, for the case of nappe overthrusting, the Péclet number is calculated with the formula (England & Thompson, 1984; Molnar & England, 1990):

$$Pe = \frac{(h \cdot v)}{D} \quad (3)$$

In the numerator, h is the thickness of the overthrusting nappe and v is the velocity of emplacement. The Brinkman number measures instead the relative importance of production versus diffusion of heat, where heat production refers to shear heating on the thrust surface. Various definitions of the Brinkman number have been formulated. For our analysis, we calculate the Brinkman number as (Brinkman, 1951; Kiss et al., 2019; Yuen et al., 1978):

$$Br = \frac{\eta \cdot v^2}{k \cdot T(h)} \quad (4)$$

In the numerator, η is the effective rock viscosity and the emplacement velocity v is considered constant. In the denominator, k is the thermal conductivity and $T(h)$ is the representative ambient temperature at the ramp height.

Moreover, from Pe and Br values we calculated three more non-dimensional parameters (Duprat-Oualid et al., 2015) which directly express the relative percentage of advection (R_{adv}), diffusion (R_{diff}) and production (R_{pro}) of heat:

$$R_{adv} = \frac{Pe}{Pe + 1 + Br} \quad (5a)$$

$$R_{diff} = \frac{1}{Pe + 1 + Br} \quad (5b)$$

$$R_{pro} = \frac{Br}{Pe + 1 + Br} \quad (5c)$$

For the estimate of all these dimensionless parameters, we set a constant viscosity and constant velocity. The calculation is performed by the Matlab code *Dimensional_Analysis.m* in Appendix B.

2.2.2 2D thermo-kinematic numerical model configuration

The temperature variation within a thrust system was computed through the implementation of a thermo-kinematic numerical model in two-dimensions.

The model's initial conditions are shown in [figure 2.1](#). The model domain is defined by two independent grids. The variation of the shortening velocity is computed on the outer bigger Lagrangian kinematic grid (i.e., it deforms with the movement of points), on which the ramp height and angle are fixed. While the thermal advection, diffusion, and production (shear heating and radiogenic heat) are computed on the inner Eulerian (i.e., fixed mesh grid) temperature grid. The emplacement velocity v is controlled by a prescribed background velocity of 2 cm/yr (for intra-continental shear zones, relative velocities are usually < 3 cm/yr; e.g., [Burg & Gerya, 2005](#); [Hilley et al., 2005](#); [Malusà et al., 2015](#)). This velocity field is interpolated on the temperature grid for the computation of the temperature-advection term (red arrows in [figure 2.1](#)).

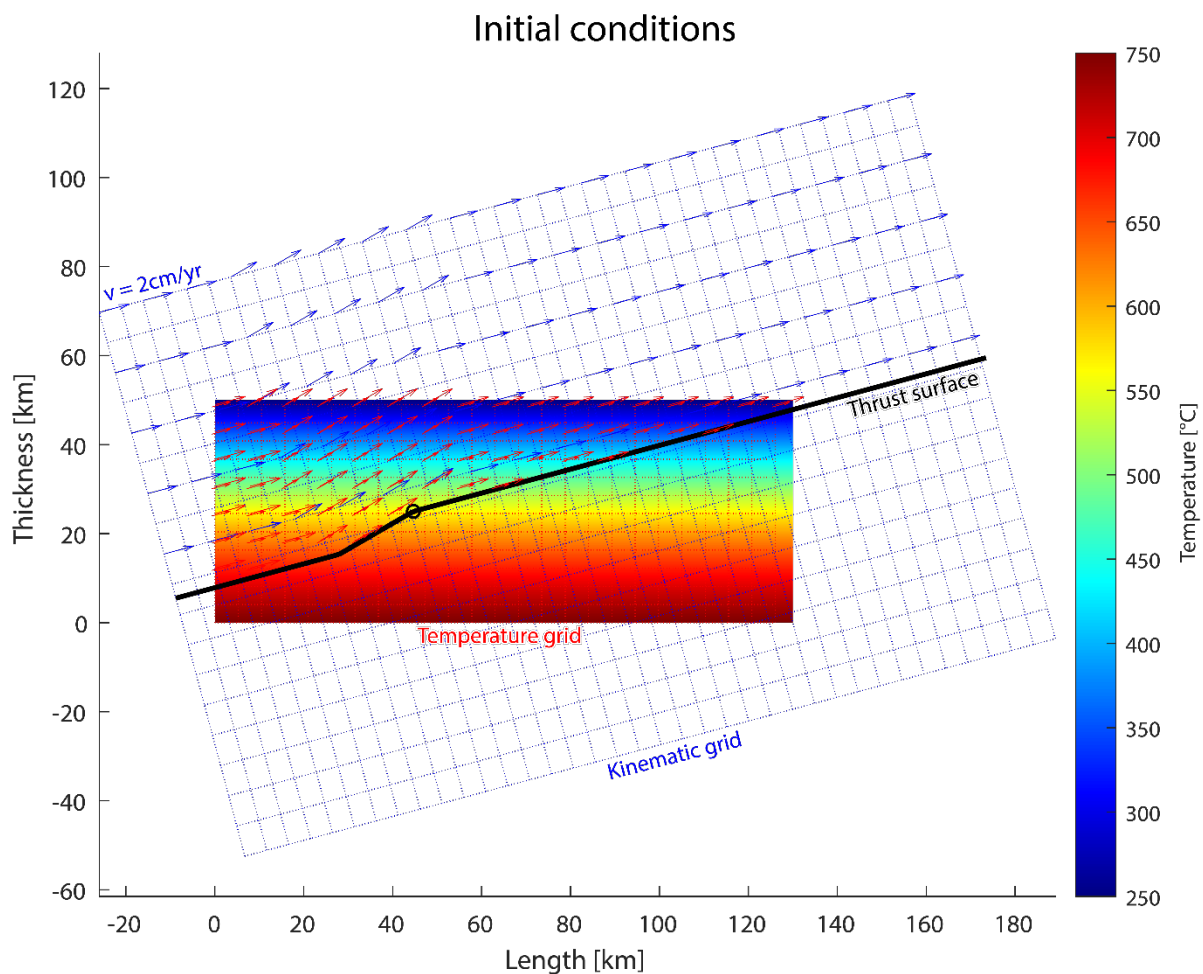


Figure 2.1. Configuration of the 2D thermo-kinematic numerical model at time-step 1. Kinematic grid with relevant velocities (blue), and temperature grid with relevant interpolated velocities (red) are shown. The thick black line indicates the thrust surface and the black circle is the reference point. The rotation angle between the two grids is 15° and the ramp angle is 15° from the base of the thrust. The prescribed shortening velocity v is 2 cm/yr. Horizontal and vertical axes show the length and thickness of the numerical model.

The kinematic part of the model is based on the function *FaultBendFold* of [Allmendinger et al. \(2011\)](#) and no assumption is made for the driving force (buoyancy or compression). The initial temperature distribution is defined relatively to the reference point on the upper tip of the thrust ramp (see [figure 2.1](#)) whose initial temperature is fixed at 500 °C. We consider a geothermal gradient of 10 °C/km and a constant radiogenic heat production (see [table 2.1](#)). All the simulations ran for 5 Ma, which corresponds to the time elapsed between the initiation and the final stages of Adula nappe emplacement (eclogitization at 38-40 Ma and peak Barrovian metamorphism at 32-33 Ma; [Herwartz et al., 2011](#); [Liati et al., 2009](#); [Nagel, 2008](#); [Sandmann et al., 2014](#)).

We ran thermo-kinematic models with a T-independent viscosity, fixed at $\eta=10^{21}$ Pa·s, and models with T-dependent viscosity. This temperature-dependency could not be considered when applying the simple dimensional analysis. In this case, we set an initial viscosity of $\eta_0=10^{21}$ Pa·s, since we consider rock deformation dominated by feldspar minerals. This initial value changes over time together with temperature and it is computed through the relation:

$$\eta(T) = \eta_0 \cdot \exp\left(\frac{Q}{R \cdot T}\right) \quad (6)$$

The code for the 2D thermo-kinematic numerical model written in Matlab (*TK_code.m*) is in [Appendix C](#).

2.3 Results

2.3.1 Dimensional analysis

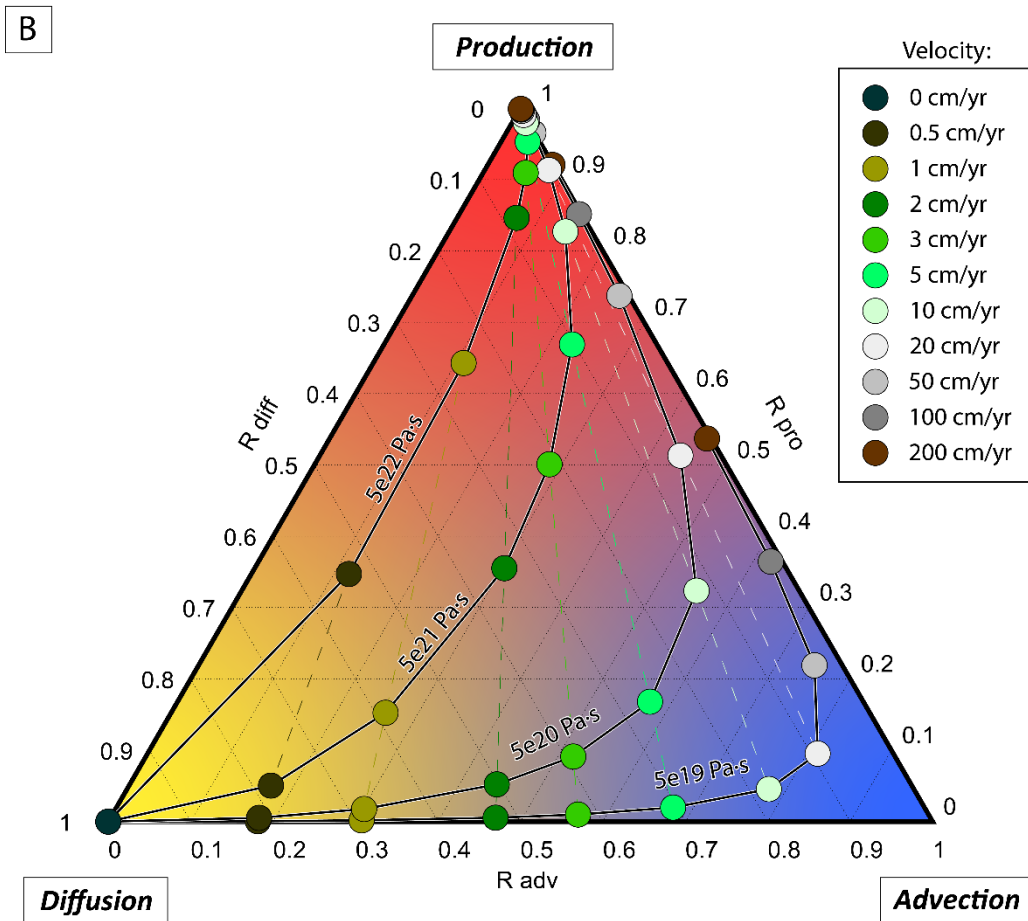
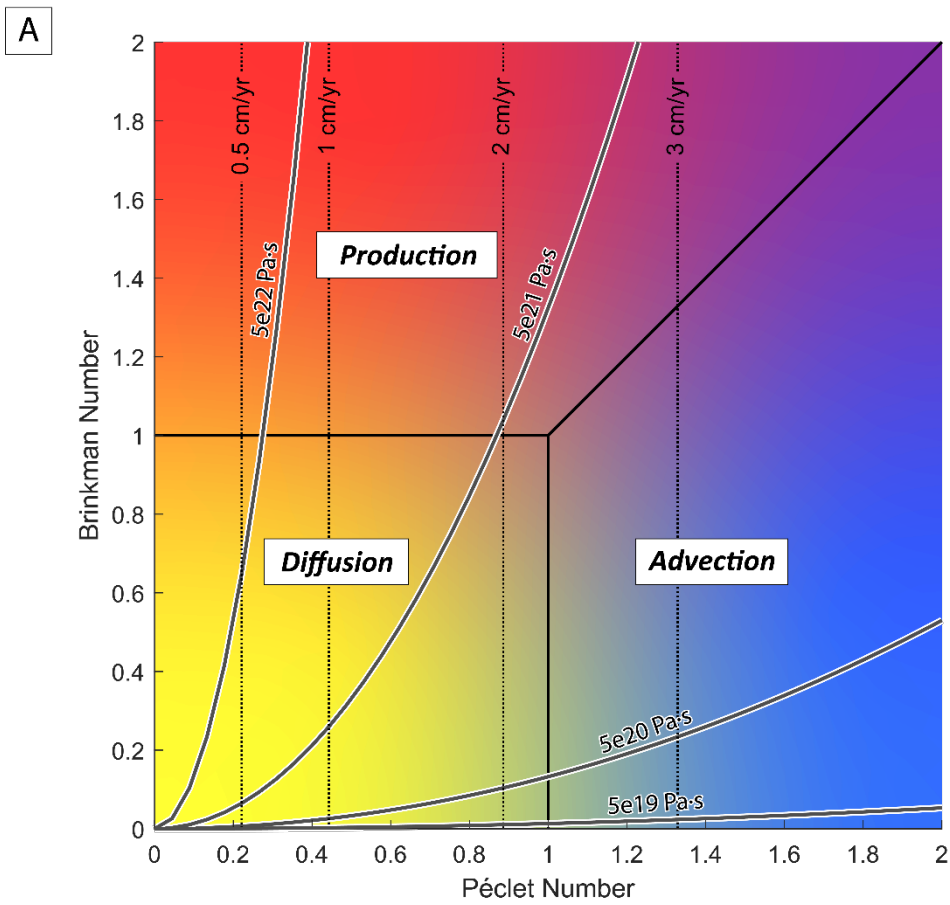
The results of dimensional analysis show the impact of velocity on Péclet and Brinkman numbers, for different constant viscosities (*figure 2.2*).

In *figures 2.2A* and *B* the three end-members are indicated by different colors: diffusion in yellow, advection in blue and production in red. The transitions between them are qualitatively represented by a smooth color transition. In both *figures 2.2A* and *B*, the static (zero/low velocity) conditions are characterized by the dominance of the diffusion term. *Figure 2.2A* shows that for progressive increments in velocity, the dominant mechanism shifts directly to either production or advection. When viscosity is high ($5 \cdot 10^{21}$ - 10^{22} Pa·s), the dominating heat transfer becomes production. Indeed, the production term increases considerably with small velocity increments. Whereas, using smaller viscosities ($5 \cdot 10^{19}$ - 10^{20} Pa·s) results in a more important effect of advection. These same velocity- and viscosity-dependent evolutions can also be recognized in a ternary diagram (see *figure 2.2B*). *Figure 2.2B* reveals that a continuous velocity increase leading to very high velocities (above ca. 20 cm/yr) determines a shift from the advection to the production term even for low viscosities. Indeed, the velocity-dependent Br-increase is squared with respect to the Pe-increase, which means that incrementing the velocity leads to an even more conspicuous increment of the viscous heat-producing term.

When we consider a scenario where the emplacement velocity stays constant (points computed with same velocity are linked by dashed colored lines in *figure 2.2B*), the shift between end-members depends on the viscosity. Hence, we can discern between two extreme behaviors: (i) for low velocities, the heat transfer is governed mainly by the interaction diffusion-production, (ii) for high velocities, the shift happens between advection and production. The passage between diffusion and advection is usually seen when a change in velocity is considered.

Figure 2.2. (A) Brinkman vs. Péclet number plot showing the relative importance of the diffusion, advection and production terms according to the dimensional analysis from Duprat-Oualid et al. (2015). Gray thick lines are calculated using the Matlab code *Dimensional_Analysis.m* (Appendix B). Each line is computed for a specific viscosity value ($5 \cdot 10^{19}$, $5 \cdot 10^{20}$, $5 \cdot 10^{21}$, $5 \cdot 10^{22}$ Pa·s) and indicates the variation of Péclet and Brinkman numbers while velocity changes. Note that radiogenic heat production is implemented within the code, hence “Production” end-member refers only to other sources (e.g., shear heating). (B) Dimensional analysis in a ternary diagram, modified after Duprat-Oualid et al. (2015). The quantification of advection, diffusion, production end-members is done by calculating R_{adv} , R_{diff} , R_{pro} . The same viscosity values as in panel A are considered and selected velocities are represented by different color shades. Iso-velocity dashed lines of the same colors connect points in the ternary diagram.

Dimensional analysis



2.3.2 2D thermo-kinematic numerical model results

We compared thermo-kinematic models both with and without T-dependent viscosity to constrain its importance on the thermal asset of the crust during nappe formation.

The model with shear heating (SH) and a constant viscosity of 10^{21} Pa·s generated very high temperatures, with the highest temperature on the thrust ramp reaching values above 1600 °C (see [figure 2.3](#)). The final configuration of the isotherms shows a strong inverted temperature distribution around the thrust.

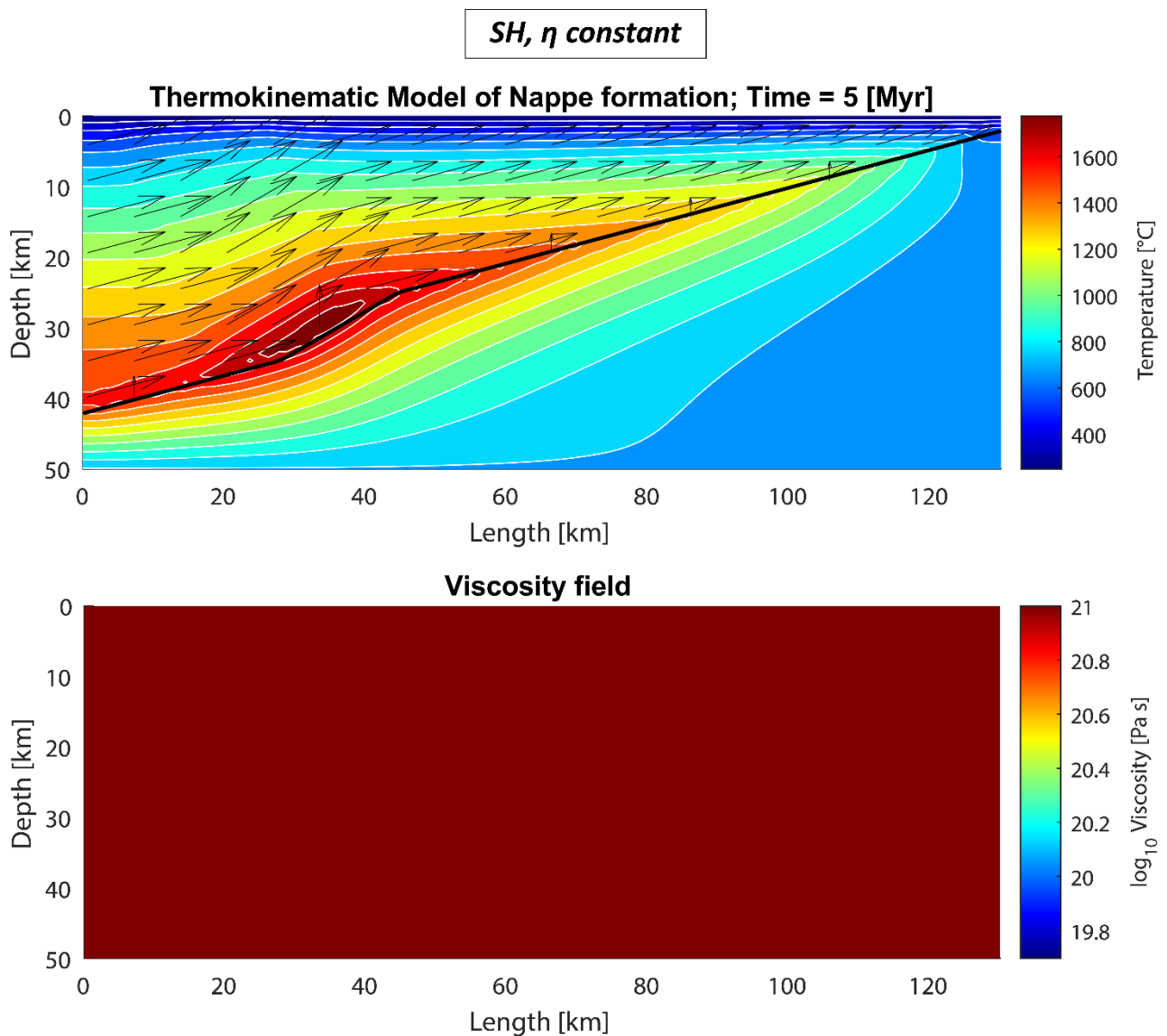


Figure 2.3. Results of the thermo-kinematic numerical simulation with shear heating (SH), constant viscosity $\eta=10^{21}$ Pa·s, velocity $v=2\text{cm/yr}$, constant radiogenic heat production $H_{rad}=5\cdot 10^{-7}$ W·m⁻³.

The simulation with T-dependent viscosity and an initial viscosity η_0 of 10^{21} Pa·s produced maximum temperatures at ca. 750 °C (*figure 2.4*). Isotherms are overturned around the thrust, especially in correspondence of the ramp. The viscosity immediately drops on the thrust plane from 10^{21} to $5 \cdot 10^{19}$ Pa·s at the onset of overthrusting (*figure 2.4*). The same amount of decrease is recorded for a higher initial viscosity η_0 of 10^{22} Pa·s. When the background velocity is reduced to 1 cm/yr the viscosity drop is lower, from 10^{21} to $1.6 \cdot 10^{20}$ Pa·s.

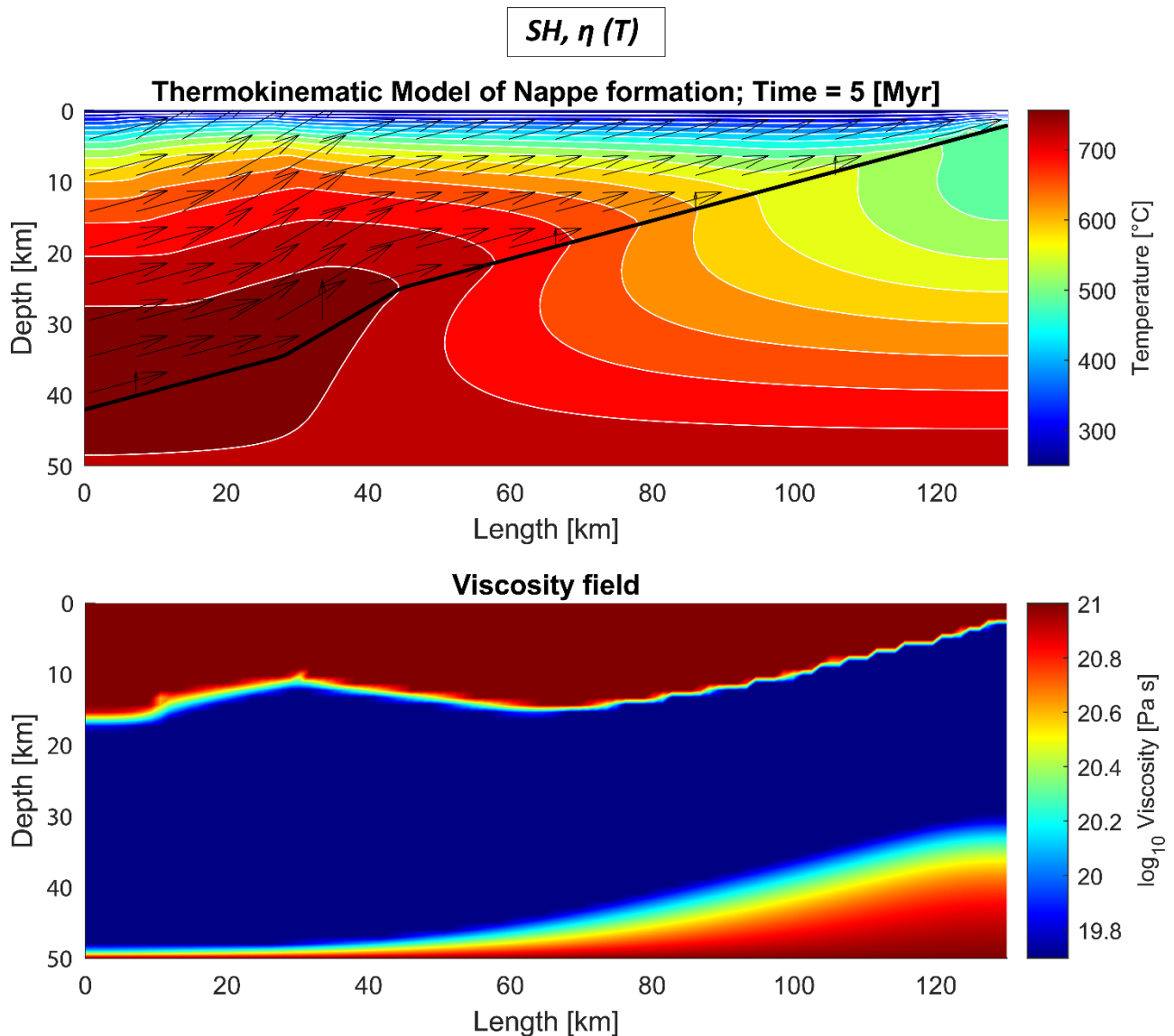


Figure 2.4. Results of the thermo-kinematic numerical simulation with shear heating (SH), initial viscosity $\eta_0=10^{21}$ Pa·s, velocity $v=2$ cm/yr, constant radiogenic heat production $H_{rad}=5 \cdot 10^{-7}$ W·m⁻³. Viscosity is T-dependent and its value drops by 1.5 orders of magnitude in the center of the model.

Finally, we compared the results obtained without shear heating and T-dependent viscosity. When only advection and diffusion are considered, maximum temperatures are a bit lower, at ca. 700 °C (*figure 2.5*). Here, the final configuration shows the isotherms cross-cutting the main thrust even though they are slightly less overturned along thrust plane compared to the shear heating model (*figure 2.4*).

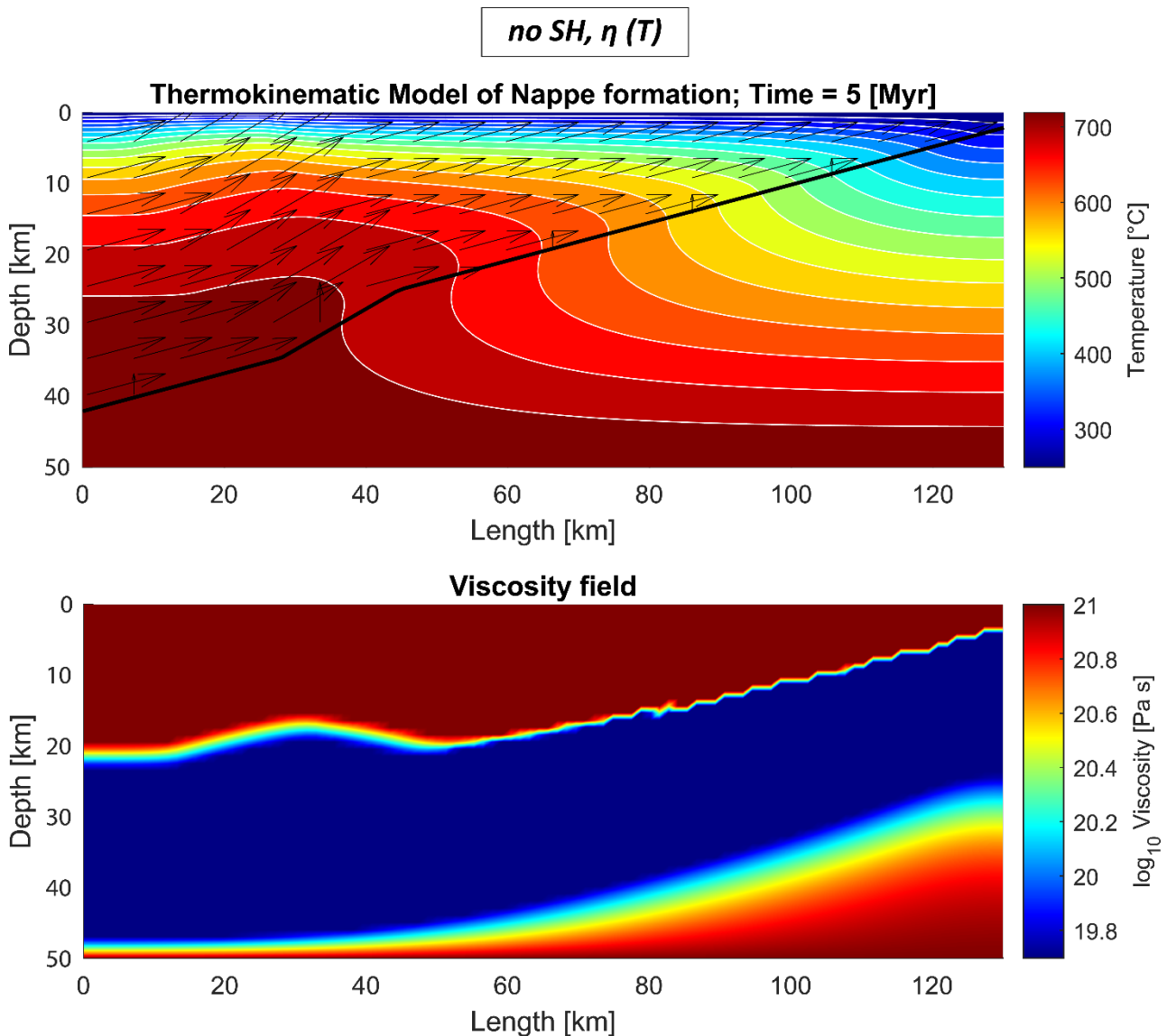


Figure 2.5. Results of the thermo-kinematic numerical simulation without shear heating (no SH), initial viscosity $\eta_0=10^{21}$ Pa·s, velocity $v=2$ cm/yr, constant radiogenic heat production $H_{rad}=5\cdot 10^{-7}$ W·m⁻³. Viscosity is T-dependent and its value drops in the center of the model in an area that is slightly narrower than the final configuration with shear heating (c.f. with figure 2.4).

2.4 Discussion and conclusions

In this section we briefly discuss the results and relevant implications of our thermo-kinematic numerical models.

When a constant rock viscosity is adopted, dimensional analysis permits to investigate the velocity-dependent shift between the three heat transfer end-members. The velocity increase is normally associated to a higher advection impact in producing overturned isotherms (see instantaneous thrusting models of [England & Thompson \(1984\)](#)). This is generally true for viscosities of 10^{19} - 10^{20} and velocities until ca. 10-20 cm/yr. However, [figure 2.2B](#) shows that faster velocities shift the heat transfer contribution towards the production term. Alternatively, when high viscosities of 10^{21} - 10^{22} are considered, small velocity increases are sufficient to enhance the production contribution. Therefore, our dimensional analysis reveals that the shear heating effect is amplified when a constant rock viscosity is adopted. The results of η -constant thermo-kinematic model with shear heating display indeed an unrealistic temperature distribution ([figure 2.3](#)). Consequently, adopting a constant viscosity overestimates shear heating and temperature increase.

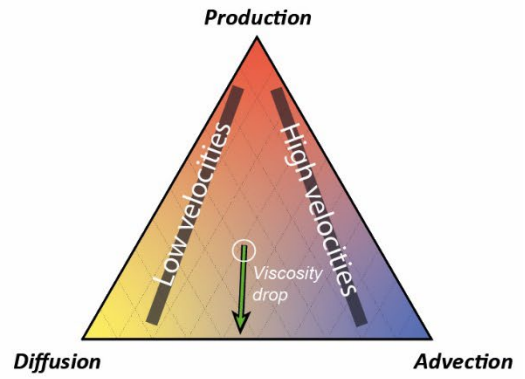
Since viscosity variations play a key role, we applied a T-dependent viscosity in the thermo-kinematic model with shear heating in order to avoid the overestimation of the production term. The $\eta(T)$ -model supports inverted isotherms configuration and isotherms intersecting the thrust surface. This is seen also in thermo-mechanical numerical models (e.g., [Candioti et al., 2021](#); [Vaughan-Hammon et al., 2022](#)), where thrusting is coupled with inverted isotherms configuration and shear heating between 20 and 40 km depth in the upper crust. These considerations show that it is possible to generate inverted metamorphism with both advection and shear heating.

Considering all the above-mentioned observations, we can imagine three hypothetical geodynamic scenarios of collision and exhumation (see [figure 2.6](#)). During collision we assume that the boundary condition is a prescribed, fixed background velocity. The first collision scenario corresponds to our thermo-kinematic model, where overthrusting of a nappe happens on a planar, linear thrust surface with no thickness ([figure 2.6A](#)). If we consider an initial η of 10^{21} Pa·s and an average velocity of 2 cm/yr, in the early stage of thrusting diffusion, advection and production end-members are quite balanced (see position of the white circle representing the ternary point in the triangle of [figure 2.6A](#)). The increase of temperature expected in a later stage of thrusting reduces the viscosity and moves the ternary point away from the production end-member. This means that during the evolution of a natural shear zone, we expect that the shear heating impact is maximal in the early stages of thrusting. The absolute value and consequent decrease of the production term depends on the initial η and the background velocity.

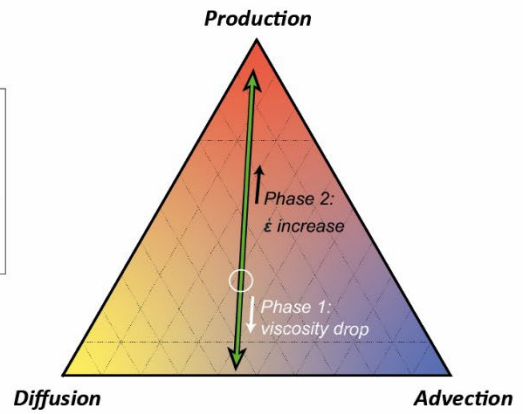
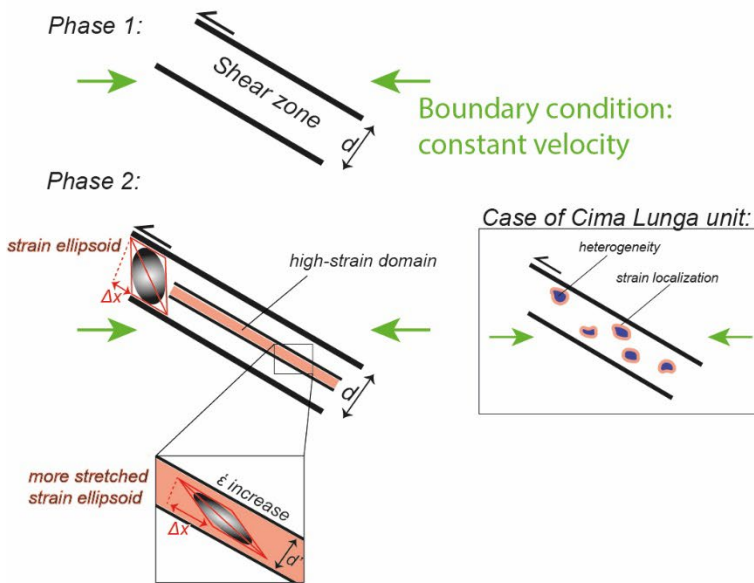
A more realistic natural scenario would be a shear zone with a thickness d subjected to a constant background shortening velocity (*figure 2.6A'*). The initial behavior is the same as a simple thrust surface configuration where the production endmember decreases with the temperature rise during thrusting (*Phase 1 in figure 2.6A'*). However, at some point, the strain might concentrate in smaller domains within the shear zone volume (*Phase 2 in figure 2.6A'*). Such a domain can be a single planar elongated surface with thickness $d' < d$ close to the center of the shear zone. In this case, strain concentration could be due to processes like grain size reduction, chemical reactions or migmatization. In alternative, strain might localize close to original rock heterogeneities (see the case of Cima Lunga unit in *figure 2.6A'*). In both scenarios, the concentration of deformation causes a distribution of the strain acting on the shear zone over a smaller volume, hence the strain ellipsoid becomes more stretched (zoom of *Phase 2 in figure 2.6A'*). The localization of deformation with a constant background velocity would lead to an increase in the strain rate ($\dot{\epsilon}$) and consequently promote shear heating. The quantification of these competing effects is not trivial and more complex numerical models are required. Furthermore, in this scenario, for the calculation of the Brinkman number (*equation 4*), a formulation which accounts for the thickness changes of the deforming shear zone volume would be more suitable (Gruntfest number; e.g., [Kiss et al., 2019](#)).

A third scenario corresponds to a buoyancy-driven exhumation of a nappe along a basal shear zone (*figure 2.6B*). In this case, velocity depends on the resistance of the material to move upwards and changes during the exhumation history. If the initial conditions of the shear zone correspond to η of 10^{21} Pa·s and the velocity to 2 cm/yr (white circle in the ternary plots), the viscosity then decreases with rising temperatures similarly to what described in *figure 2.6A* and *A'* (*I in figure 2.6B*). When viscosity is low, a reduction in velocity values can happen only due to the resistance of the material external to the nappe body (e.g., external body blocking the upward movement of the nappe). When this velocity reduction happens, the contribution shifts towards the diffusion end-member (*II in figure 2.6B*). In a more feasible scenario, the viscosity drop lowers the resistance of the upward flow of the nappe. Therefore, the exhumation velocity of the nappe will increase and the ternary point will move in the direction of the advection endmember. A further increase in velocity will bring the tertiary point towards the production endmember as shown in *figure 2.6B* (*III*). Since migmatization can enhance a viscosity drop of one or two orders of magnitude, partial melting can be considered a process that further enhances this positive feedback between viscosity-drop and velocity-increase.

A Collision - Linear (confined) thrust surface



A' Collision - Shear zone with a thickness d



B Buoyancy-driven nappe exhumation

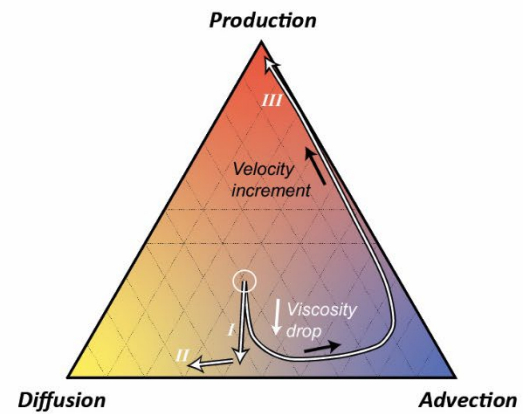
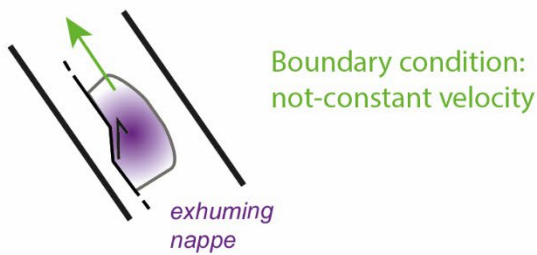


Figure 2.6. Schematic representation of three possible scenarios involving nappe overthrusting and its effects on the balance between diffusion, advection and production of heat. Black arrows on top of the thrust planes in the cartoons indicate the shear sense. Green arrows in the cartoons indicate the considered boundary conditions: compression with a constant velocity in (A) and (A') or spasmodic velocity variations in (B). Δx is the length variation due to deformation during shearing, $\dot{\epsilon}$ is strain rate, d and d' are the initial and reduced shear zone's thicknesses. The colored triangles are taken from the ternary plot in figure 2.2B. The white circles in the ternary plots (ternary points) indicate the initial conditions of the shear zones with a velocity of 2 cm/yr and viscosity of 10^{21} Pa·s. In (A) and (A'): the thick green arrow within the triangle shows the moving directions for points having the same velocity and different viscosities; in (A), also the relevant end-members for low and high velocities are displayed with transparent black thick lines. In (A'): a first phase of viscosity decrease is followed by a strain rate increase due to a reduction of the shear zone thickness ($d' < d$). In (B): the white curved arrow follows an increasing velocity path after the viscosity drop. Three scenarios are shown, which correspond to a constant (I), a decreasing (II) and a continuous increment in velocity (III). See the complete description in the main text.

In conclusion, if we apply our model results to the Lepontine dome we can state that:

- Cross-cutting isograds can be the record of peak T isotherms developed during nappe emplacement. Our thermo-kinematic models with T-dependent viscosity produce indeed a thermal configuration where isotherms intersect the thrust surface and temperatures higher than 650 °C develop in the vicinity and on the thrust ramp.
- Local inverted isotherm configuration can be produced either by advection and/or shear heating.
- The final Lepontine thermal configuration can be the result of variations in time of both viscosity and velocity. Therefore, the relative amounts of heat diffused, advected and produced changed over time during the Barrovian history.

Chapter 3

IMPLICATIONS OF NEW GEOLOGICAL MAPPING AND U-Pb ZIRCON DATING FOR THE BARROVIAN TECTONO- METAMORPHIC EVOLUTION OF THE LEPONTINE DOME (CENTRAL EUROPEAN ALPS)

A. Tagliaferri^{1,2}, F. L. Schenker¹, A. Ulianov², M. Maino³ and S. M. Schmalholz²

¹*Institute of Earth Sciences, University of Applied Sciences and Arts of Southern Switzerland (SUPSI), CH-6850 Mendrisio, Ticino, Switzerland.*

²*Institute of Earth Sciences, University of Lausanne (UNIL), CH-1015 Lausanne, Vaud, Switzerland.*

³*Department of Earth and Environmental Sciences, University of Pavia (UNIPV), IT-27100 Pavia, Italy.*

This chapter is published in:
Geochemistry, Geophysics, Geosystems, 24, e2022GC010772.
<https://doi.org/10.1029/2022GC010772>

Abstract

The Barrovian metamorphism of the Lepontine dome is manifested by isograds that cross-cut tectonic nappe contacts, which is commonly interpreted as metamorphism that occurred after nappe emplacement. However, the pervasive mineral and stretching lineation in amphibolite facies, associated with top-to-foreland shearing, suggests that peak Barrovian conditions are coeval with nappe-overthrusting. Here, we combine mapping and U-Pb zircon dating to better constrain the relation between metamorphism and overthrusting. Metamorphic zircon rims show two age populations at 31-33 and 22-24 Ma. The younger population is locally observed in post-foliation dikes (and associated metasomatism) likely sourced from deep-migmatites exhuming along the Alpine backstop. The older population occurs regionally and is found in syn-kinematic migmatites which occur along a crustal-scale shear zone. Below this shear zone, magmatic and detrital zircon cores suggest that the Cima Lunga unit, previously interpreted as a tectonic mélange with Mesozoic fragments, was a pre-Variscan metasedimentary sequence intruded by Permian granitic sills, now orthogneisses. This unit was strongly sheared along the top of the Simano nappe during overthrusting of a rock pile here-termed Maggia-Adula nappe. This large-scale nappe emplacement imprinted the regional lineation and peak temperatures until 31-33 Ma. Péclet (1-10) and Brinkman (0.002-1.8) numbers, estimated for the overthrusting, suggest an advection-dominated heat transfer caused by rock exhumation, with some diffusion (conduction) during nappe emplacement. Diffusion contributed to Barrovian isograds discordant to the thrust. Shear heating was important if stress times shearing rate $> \sim 5 \cdot 10^{-6} \text{ W} \cdot \text{m}^{-3}$ within the nappe. The thermal evolution after overthrusting was spatially heterogeneous until ca. 22 Ma.

3.1 Introduction

Barrovian metamorphism is characterized by a sequence of mineral assemblages associated with increasing metamorphic conditions, from chlorite through biotite, garnet, staurolite, kyanite to sillimanite-bearing (Barrow, 1893, 1912; Jamieson et al., 1998; Tilley, 1925). A Barrovian metamorphic overprint is common in most collisional orogens and in many occurs as concentric metamorphic mineral zones (e.g., Miyashiro, 2012; Winter, 2013). Typical Barrovian temperature (T) and pressure (P) conditions correspond to ca. 450-750 °C and ca. 0.5 up to 1 GPa (ca. 20-40 km lithostatic depth), respectively (e.g., Jamieson et al., 1998). However, the geodynamic interpretation of such temperatures, which are higher than typical subduction zone geotherm conditions, remains debated. The main reason for this debate is that the relative importance of the controlling heat sources, such as radiogenic heat production or shear heating, and of the associated heat transfer processes, such as heat diffusion (in this work equivalent to heat conduction) and heat advection by kilometer-scale exhuming rock units, as well as the heat transport associated with fluid and melt migration, is still unclear (e.g., Burg & Gerya, 2005; Jamieson et al., 1998; Thompson & Ridley, 1987).

In the Lepontine dome of the Central Alps, Barrovian metamorphism is associated with a dome structure that comprises a pile of tectonic nappes, including the Adula, Maggia and Simano nappes (*figure 3.1*), which are separated by major shear zones (e.g., Berger et al., 2005; Frey & Ferreiro Mählmann, 1999; Nagel, 2008; Rosenberg et al., 2021; Todd & Engi, 1997; Trommsdorff, 1974; Wenk & Keller, 1969; *figure 3.1*). In the Lepontine area, the metamorphic isograds cross-cut the tectonic nappe boundaries (e.g., Frey & Ferreiro Mählmann, 1999; Nagel, 2008; Todd & Engi, 1997; Trommsdorff, 1974; Wenk & Keller, 1969; *figure 3.1*). This observation is frequently interpreted as evidence for a Barrovian overprint that occurred after nappe emplacement, defining the Barrovian metamorphism as post-nappe or post-tectonic (e.g., Frey et al., 1999; Nagel, 2008; Todd & Engi, 1997; Trommsdorff, 1974; Wenk & Keller, 1969). However, Barrovian metamorphism had already begun by ca. 32 Ma (e.g., SHRIMP II U-Pb zircon dating in Galli et al. (2012); SHRIMP U-Pb dating in Gebauer (1996)), which corresponds to the late stage of nappe emplacement, that is between 31 and 33 Ma for the Adula nappe (e.g., Herwartz et al., 2011; SHRIMP U-Pb zircon dating in Liati et al. (2009); Nagel, 2008). In principle, it is possible that nappe emplacement contributed significantly to the heat transfer responsible for the regional Barrovian metamorphism. Heat is indeed advected and produced during nappe exhumation and overthrusting. Furthermore, heat can be transferred by diffusion to the colder units adjacent to the overthrusting nappe (e.g., England & Molnar, 1993; Huerta et al., 1998; Oxburgh & Turcotte, 1974; Thigpen et al., 2017), hence, it can generate metamorphic isograds that cross-cut nappe boundaries (e.g., Huerta et al., 1998; Thigpen et al., 2017,

2021). Therefore, the evidence of cross-cutting relationships between isograds and tectonic boundaries does not exclude a syn-tectonic origin of the Barrovian metamorphism.

In addition to the timing, the tectonic processes responsible for the Barrovian metamorphism are also debated. Several interpretations and models have been proposed, such as: (i) post-tectonic (after nappe emplacement) thermal relaxation through far-field conductive heating (e.g., Bousquet et al., 1997), (ii) post-tectonic heating related to deeper processes such as slab breakoff, slab retreat, or lower crust delamination (e.g., Brouwer et al., 2004; Herwegh et al., 2017; Schlunegger & Kissling, 2015), (iii) tectonic juxtaposition of slices of highly radiogenic crust and associated radiogenic heating (e.g., Engi et al., 2001), (iv) syn-tectonic in situ heat production by shear heating during orogenic wedge formation (e.g., Burg & Gerya, 2005), or (v) superposition of different processes at different stages, such as accretion of hot middle crust material within a subduction channel and underplating of hot material during continental lower plate accretion (e.g., Berger et al., 2011). In order to test such models and unravel the tectono-metamorphic processes responsible for the Barrovian metamorphism, detailed geological maps and cross sections, structural analysis as well as geochronological data are necessary. Without an improved knowledge of the current nappe geometries and kinematic evolution of the Lepontine nappes, the interpretation of the Barrovian metamorphism remains difficult. This is true also for the rest of the Alps, which have been studied for more than a century, but they are still arguably one of the most controversially interpreted orogens. For example, in the Lepontine area both the paleogeographic origin and the current structural position of the Maggia nappe within the Lepontine nappe pile are debated (e.g., Maxelon & Mancktelow, 2005; Schmid et al., 2004; Steck et al., 2019; see also next section 3.2.2.3). In addition, the Cima Lunga has recently been the center of a renewed debate concerning the origin of its high-pressure rocks, either formed during the deep burial history of the unit or at shallower depths with pressures deviating from lithostatic conditions (c.f. Corvò et al., 2021; Maino et al., 2021; Piccoli et al., 2021). Therefore, we present here the results of a tectono-metamorphic study comprising: (i) detailed geological mapping and structural analysis (macro-, meso-, and micro-scale) built on the new large-scale geological maps of Osogna n°1293, Biasca n°1273, Grono n°1294 of the Swiss National Map 1:25.000 (mapping at scale 1:10.000), which we produced at the University of Applied Sciences and Arts of Southern Switzerland (SUPSI) for swisstopo, (ii) collection and description of representative samples (e.g., syn-tectonic migmatites) in specific localities (at tectonic contacts and inside the nappes) and (iii) Laser Ablation Inductively-Coupled Plasma Mass Spectrometry (LA-ICP-MS) and Secondary Ion Mass Spectrometry (SwissSIMS) U-Pb geochronology and geochemistry (LA-ICP-MS trace element analyses) on zircon crystals. Specific aims of our study are: (i) to pinpoint the age of the peak T metamorphism characterizing the Lepontine area with U-Pb zircon dating, by

investigating the ages of syn-kinematic migmatites observed along major tectonic nappe boundaries, (ii) to investigate the structural style (coherent vs. tectonic mélangé) and age of the Cima Lunga unit as well as its structural relation with the Simano and Adula nappes, (iii) to discuss the paleogeographic and tectonic relationship between the major tectonic nappes in the Lepontine dome, namely the Simano nappe, the Cima Lunga unit and the Maggia and Adula nappes and hence (iv) to propose a revised geodynamic interpretation for peak Barrovian metamorphism in the Lepontine dome.

We start with a geological overview of the Lepontine dome, followed by a description of sampling and dating methodology. Afterward, due to the large amount of new data from several localities, we present together the results and interpretation of data from mapping, sample description, and dating for each locality. Finally, we integrate information from all the studied areas, providing a general discussion about the timing and mechanisms of the Barrovian metamorphism in the Lepontine dome.

3.2 Geological overview

3.2.1 Tectonic overview and formation of the Lepontine dome

The Central Alps formed as a consequence of the closure of the Mesozoic Ligure-Piemontese basin(s) (e.g., Handy et al., 2010; Stampfli et al., 1998; Trümpy, 1973). This closure involved the south-verging subduction of the Ligure-Piemontese unit and the European passive margin under the Adriatic (African) plate, which started in the middle Cretaceous (e.g., Handy et al., 2010; Rosenbaum & Lister, 2005; Stampfli et al., 1998; Trümpy, 1973; Zanchetta et al., 2012). In the more proximal domains of the extended paleo-European passive margin, nappe stacking started in the vanishing stage of oceanic subduction and continued during continental collision (e.g., Coward & Dietrich, 1989; Hurford, 1986; Schmid et al., 1996). In the Penninic domain of the Central Alps, the transition from oceanic subduction to continent-continent collision occurred between the Eocene and Early Oligocene (e.g., Gebauer, 1996; Schmid et al., 1990, 1996; Wiederkehr et al., 2009). In the frontal Penninic domain, $^{40}\text{Ar}/^{39}\text{Ar}$ dating of biotite and white mica constrains the Eocene sediment accretion and subduction at 40-42 Ma, and the nappe stacking at 33-36 Ma (Wiederkehr et al., 2008, 2009). The basement nappes were stacked from south to north forming a crustal nappe stack, which was later up-arched to form the Lepontine dome (Merle et al., 1989; Steck & Hunziker, 1994; Steck et al., 2013). Its architecture is subdivided in two sub-domes: the so-called Toce culmination to the west and the Ticino culmination to the east (*figure 3.1A*). The Ticino culmination, subject of this study, exposes in its core the Leventina and Simano nappes that are flanked to the east by the Adula nappe and to

the west by the Cima Lunga unit and the Maggia nappe (*figure 3.1*; e.g., Dal Vesco, 1953; Maxelon & Mancktelow, 2005; Steck et al., 2013).

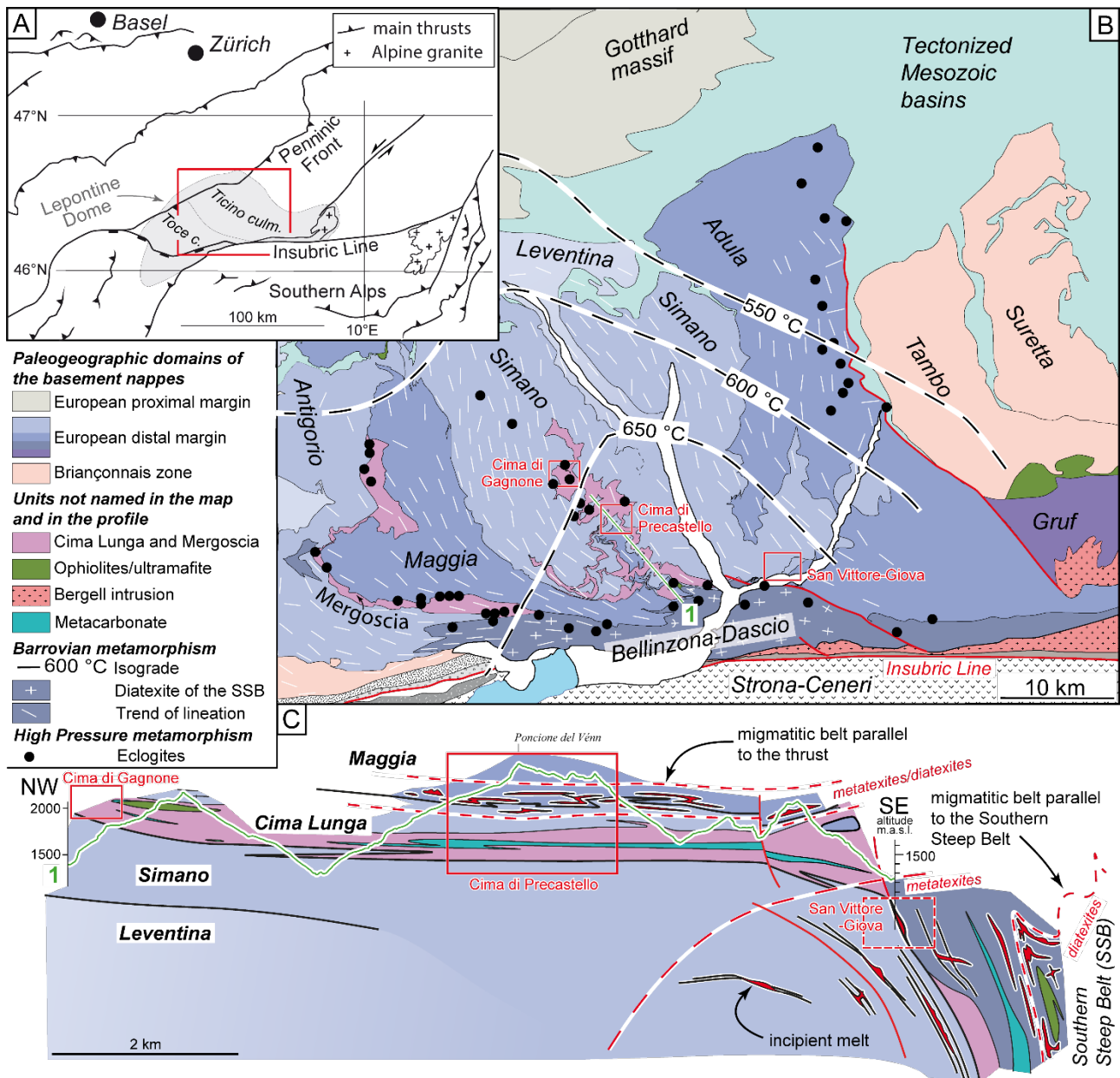


Figure 3.1. Tectonic overview of the Lepontine area. (A) Location of the Lepontine dome in the Central European Alps context (modified after Burg & Gerya (2005)). (B) Tectonic map of the Ticino culmination of the Lepontine dome (modified after Brouwer et al. (2005); Cavargna-Sani et al. (2014b); Corvò et al. (2021); Maino et al. (2021); Steck et al. (2013); Todd & Engi (1997); Wenk (1955)). (C) Simplified tectonic profile (Profile 1) through the central domain of the Ticino culmination. The red boxes indicate the studied areas (Cima di Gagnone, Cima di Precastello, San Vittore-Giova).

3.2.2 The Lepontine nappes

3.2.2.1 The Simano nappe

The lower tectonic units in our study area are the Leventina and Simano nappes (*figure 3.1B* and *3.1C*). The Simano nappe is a metamorphosed intrusive complex formed by several Ordovician and Carboniferous magmatic bodies (Köppel et al., 1981), the latter intruding pre-Mesozoic paragneisses (Jenny, 1923; Wenk & Keller, 1969). To the north, the Simano nappe was thrust over the Leventina nappe, forming a fold nappe. Based on multiple-equilibrium thermobarometry, Alpine metamorphism peaked at ca. 0.6 GPa and 625 °C without preserved evidence of an Alpine eclogitic precursor (e.g., Allaz et al., 2005; Rützi, 2001; Rützi et al., 2005, 2008).

3.2.2.2 The Cima Lunga unit

To the west, the Simano nappe is overlaid by the Cima Lunga unit that comprises paragneisses, orthogneisses, sheets of marble and calcschist, as well as mafic and ultramafic rocks (*figure 3.1B* and *3.1C*). The latter outcrop as lenses or boudinaged layers due to the intense deformation (e.g., Becker, 1993; Corvò et al., 2021; Evans et al., 1979; Maino et al., 2021; Pfeiffer, 1981). The Cima Lunga unit differs lithologically from the other Penninic nappes (Leventina, Simano and Maggia) in the more frequent occurrence of ultramafic bodies and eclogites. Eclogitic metarodingites within ultramafic lenses testify metasomatism and serpentization prior to the Alpine eclogitic metamorphism and deformation (Evans & Trommsdorff, 1978; Evans et al., 1979; Pfiffner & Trommsdorff, 1997, 1998). Eclogitic conditions occurred at ca. 40 Ma (Becker, 1993) before decompression until ca. 32 Ma (Becker, 1993; Berger et al., 2011; Brouwer & Engi, 2005; Corvò et al., 2021; Gebauer, 1994, 1996, 1999). The peak pressure condition reached 2.0-3.0 GPa at 650-850 °C in the ultramafic lenses (Evans et al., 1979; Heinrich, 1982; Nimis & Trommsdorff, 2001; Pfiffner, 1999; Scambelluri et al., 2014) and 1.5-2.5 GPa at 600-700 °C in the eclogites (Heinrich, 1986). It was even proposed that peak pressures may have reached extreme conditions of at least ca. 5.9 GPa at ca. 1180 °C in the garnet peridotite lens at Alpe Arami (e.g., Dobrzhinetskaya et al., 1996; Paquin & Altherr, 2001). However, these extreme conditions are disputed (e.g., Nimis & Trommsdorff, 2001).

The bulk of the Cima Lunga unit is made of paragneisses characterized by dominant amphibolite-facies conditions (peak P of 0.6-0.8 GPa and peak T of 600-675 °C) with local evidence of high-pressure (HP) and high-temperature (HT) mineral assemblages (up to 2.7 GPa and 850°C; Corvò et al., 2021; Grond et al., 1995; Heinrich, 1982; Piccoli et al., 2021; Pfiffner, 1999). HP-HT conditions are attributed to either extreme depth reached by the whole unit during subduction (Piccoli et al., 2021) or local coexisting heterogeneous metamorphic equilibria driven by deformation (Corvò et al., 2021).

The Cima Lunga unit is commonly interpreted to connect to the east with the Adula nappe (e.g., [Dal Vesco, 1953](#); [Trommsdorff et al., 2000](#)). To the west, [Steck et al. \(2013\)](#) proposed its tectonic correlation with the Mergoscia zone, which is an eclogitic HP unit at the top of the Antigorio nappe and enveloping the bottom of the Maggia nappe. To the south, the Cima Lunga unit is tectonically overlaid by the Maggia nappe ([Steck et al., 2013](#)).

3.2.2.3 The Maggia nappe

The Maggia nappe is dominated by orthogneisses with (mostly) Permian intrusion ages ([Bussien et al., 2011](#); [Köppel et al., 1981](#); [Steiner, 1984](#)), which are enveloped by polymetamorphic sedimentary rocks ([Günthert et al., 1996](#)). Some of these meta-sedimentary rocks show pre-Silurian sedimentation ages ([Köppel et al., 1981](#)). Amphibolitic zones are also present, and ultramafic lenses are sparsely scattered (e.g., [Buchmann, 1953](#); [Della Torre et al., 2015](#); [Preiswerk, 1918](#)). The frontal part of the Maggia nappe is in contact with the Simano and the Antigorio gneisses and the Mesozoic sedimentary cover. There, the structures remain controversial due to the complex superposed folding along the “Maggia-querzone” that locally reverses the tectonostratigraphy along the NW–SE directed fold axes. Accordingly, different interpretations have been suggested for the paleogeographic origin of the Maggia nappe. The Maggia nappe has been attributed to (from the distal to the proximal domains): (i) the Briançonnais domain ([Froitzheim et al., 1996](#); [Schmid et al., 2004](#)), (ii) the Lower Penninic domain ([Grujic & Mancktelow, 1996](#); [Steck, 1998](#); [Steck et al., 2013](#)), (iii) the Helvetic domain ([Debelmas & Lemoine, 1970](#); [Rütti et al., 2005](#); [Steck et al., 2019](#)), or (iv) both the Briançonnais (the southern part) and Helvetic (the northern part) domains (Sambuco lobe, [Berger et al., 2005](#)).

3.2.2.4 The Adula nappe

On the eastern flanks of the dome, the Simano nappe was overthrust by the Adula nappe, which is dominated by orthogneisses and paragneisses, quartzite sheets, calcitic and dolomitic marbles, calcschists, and lenses of eclogitic mafic and ultramafic rocks ([Cavargna-Sani et al., 2014a](#); [Jenny, 1923](#); [Nagel, 2008](#)). Here, peak P metamorphism (eclogitic) is restricted to mafics, ultramafics and whiteschist lenses, and to minor volumes of paragneisses ([Brouwer & Engi, 2005](#); [Heinrich, 1982](#); [Meyre et al., 1998](#)) reaching up to ca. 3 GPa at 800 °C ([Dale & Holland, 2003](#); [Nimis & Trommsdorff, 2001](#); [Tumiati et al., 2018](#)). The activity of the Adula thrust is bracketed between the eclogitization at 38-40 Ma and the peak of Barrovian metamorphism at ca. 32-33 Ma ([Herwartz et al., 2011](#); [Liati et al., 2009](#); [Nagel, 2008](#); [Sandmann et al., 2014](#)). The Adula nappe and the Cima Lunga unit are generally interpreted in the literature as parts of the same tectonic nappe (e.g., [Dal Vesco, 1953](#)).

3.2.3 The Barrovian metamorphism

The Lepontine dome exposes IP (Intermediate Pressure)-HT (High Temperature) rocks, indicative of Barrovian metamorphic conditions, ranging from migmatites to lower amphibolite-greenschist facies. Minor volumes of (ultra-)HP rocks are also present within the rocks of the Barrovian sequence. The overall metamorphic trend of the Lepontine dome shows high-grade (upper amphibolite facies) migmatites at the southern margin, along the Southern Steep Belt (SSB), and lower amphibolite-greenschist facies rocks in the dome carapace (*figure 3.1*, northern and eastern parts). Peak T increases from 500 to 550 °C at the northern margin of the dome, defined by the Northern Steep Belt (NSB; Frey, 1969; Janots et al., 2008), to ca. 700 ± 50 °C at its southern margin along the SSB (Burri et al., 2005). The mineral-zone boundaries and the isograds of this Tertiary metamorphism show an asymmetric zonation. This zonation does not coincide with the dome shape, which is defined by the regional attitudes of foliation and thrust sheets (e.g., Maxelon & Mancktelow, 2005; Merle et al., 1989; Todd & Engi, 1997; Wenk, 1955; Wenk & Keller, 1969). In fact, the Barrovian isograds depict concentric shells locally dissecting the tectonic nappe contacts (*figure 3.1*). Most P-T paths for the Lepontine nappes show a single clockwise path with the amphibolitic climax reached at close to peak P or during decompression from HP (e.g., Brouwer et al., 2004; Nagel, 2008; Rütti et al., 2008). The final isothermal decompression of the (U)HP units (Adula nappe and Cima Lunga unit, e.g., Brouwer et al., 2004; Nagel, 2008) at amphibolitic condition of 650-700 °C at ca. 0.8 GPa occurred at or before 32 Ma (zircon U-Pb SHRIMP; Galli et al., 2012; Gebauer, 1996). Some rocks in the SSB and NSB record instead a two-stage thermal event articulated in an isobaric heating to peak T after decompression from HP (e.g., Bousquet et al., 2008; Wiederkehr et al., 2008). The peak T metamorphism in the SSB lasted from 32 to 22 Ma within a long-lasting episodic migmatitic event, as constrained by different geochronometers (allanite U-Th-Pb SHRIMP in Gregory et al. (2012); zircon U-Pb SHRIMP in Rubatto et al. (2009)). In the NSB, prograde syn-tectonic garnets nucleated and grew during the Alpine metamorphism and were dated at 25.4 Ma (Lu-Hf garnet-rutile; Berg et al., 2013). Along the NSB, peak T metamorphism started later between 25 and 19 Ma at lower temperatures than the southern units (Berg et al., 2013; Janots et al., 2009; Wiederkehr et al., 2011).

Across the Lepontine dome, Boston et al. (2017) reported allanite U-Th-Pb age data, providing evidence that nappe stacking at prograde amphibolite facies conditions and refolding occurred between 32 and 27 Ma. Younger U-Th-Pb monazite ages (until ca. 19 Ma) are interpreted as post-collisional mineral growth close to peak T (Boston et al., 2017). After ca. 19 Ma, the Lepontine dome cooled from 500 °C to 120 °C (zircon fission track) relatively homogeneously until ca. 6 Ma as shown by low-T geochronometers (Hurford, 1986; Janots et al., 2009). Within this diachronous metamorphic

history, the discordant metamorphic isograds are considered to form during late conductive heating at ca. 19 Ma (e.g., Berger et al., 2011).

3.2.4 Structures

Regionally, all lithologies show a sub-horizontal penetrative foliation, formed at peak T condition (*figure 3.2*). This foliation dips gently along the dome flanks forming a bell-shaped architecture. The foliation intensity varies with rock-type (see *figure 3.2*) and structural position. The alternation of lithotypes is mostly parallel to the nappe boundaries, and constant over its kilometer-scale length (Swiss National Map no. 1293 - Osogna (1:25.000)). Intra-foliation folds with axial planes sub-parallel to the foliation and fold axes oriented close to NW-SE trend are common. Furthermore, sheath folds are common in some units (e.g., in gneissic rocks enveloping ultramafics of the Cima Lunga unit; Maino et al., 2021; Steck et al., 2019) and show complex deformation patterns in the field.

On the foliation, an extremely pervasive NW-SE directed mineral and stretching lineation points to non-coaxial deformation at peak Barrovian metamorphic conditions. The orientation of the lineation is independent of the foliation attitude. Independently of the position within the concentric dome isograds, the ubiquitous linear fabric is defined by minerals of the peak T assemblage, such as biotite flakes, amphiboles and kyanite, as well as stretched lithons (Maino et al., 2021; Swiss National Map no. 1293 - Osogna (1:25.000); Wenk & Keller, 1969). The penetrative character of the linear fabric within the dome core (see *figure 3.1*) suggests that the constrictional (axes of the strain ellipsoid: $X > Y = Z$) deformation event likely occurred during shearing coeval with nappe emplacement and regional amphibolite facies metamorphism. However, the absolute timing of the upper-amphibolitic, non-coaxial deformation along the tectonic contacts is still poorly constrained.

3.2.4.1 Migmatites

Alpine migmatites have been observed in the SSB trending E-W parallel to the Insubric Line (*figure 3.1*, Burri et al., 2005; Gebauer, 1994, 1996; Rubatto et al., 2009), and within the Cima Lunga paragneisses (Corvò et al., 2021; Pfiffner, 1999). Wenk & Keller (1969) also mapped migmatites further north of the SSB, although these are generally interpreted as pre-Alpine (e.g., Burri et al., 2005). Burri et al. (2005) suggested that some of these migmatites (15 km north of the SSB, Maggia Valley) could have an Alpine age, however there is no chronometric data confirming this hypothesis. In the migmatites of the SSB, U-Pb ages on metamorphic zircon rims and allanite bracket the peak T conditions after the HP event between 32 Ma and 22 Ma (Gebauer, 1999; Gregory et al., 2012; Rubatto et al., 2009). These ages and the relative distribution of zircon overgrowths were interpreted as repeated melting events within a single Barrovian metamorphic cycle. This melting was due to a

combination of water-assisted and muscovite-dehydration partial melting, which occurred at roughly constant T and minimal P variations (700 ± 50 °C and 0.6-0.8 GPa; Berger et al., 2008; Burri et al., 2005; Rubatto et al., 2009).

The Cima Lunga migmatites around an ultramafic HP lens dated by Corvò et al. (2021) at ca. 36 Ma were instead considered as melts formed during decompression from 2.5 to 1.5 GPa at ca. 750-850°C.

Most syn-tectonic migmatites reported in this study (*figure 3.2*) were not previously reported in the literature or were considered as pre-Alpine. The overall timing of this partial melting is important to correlate the close-to-peak T conditions that the migmatites are thought to have formed at, with deformation along the nappe boundaries.

3.3 Sampling and dating methodology

3.3.1 Sample collection and preparation

We performed detailed geological mapping coupled with structural analysis in three key areas of the central-southern Lepontine dome to study the upper-amphibolitic deformation at different tectonostratigraphic levels of the nappe pile and at different horizontal distances with respect to the migmatites of the SSB (*figure 3.1*): (i) the Cima di Gagnone area of the Cima Lunga unit, located in the center of the dome and at a distance of ca. 15 km from the SSB (*figure 3.3*), (ii) the Cima di Precastello area at the Cima Lunga-Simano-Maggia nappe boundary, at ca. 8 km distance from the SSB (*figure 3.4*), and (iii) the San Vittore-Giova area located at the Simano-Adula nappe contact at the northern margin of the SSB (*figure 3.5*). The geological maps relevant to these three areas are the result of our own original geological mapping at the scale 1:10.000 and structural data measured in the field. The map of the Cima di Gagnone area was already published by Maino et al. (2021) and Corvò et al. (2021). Overall, thirteen samples were collected at different tectonic levels for U-Pb zircon dating (*table 3.1*).

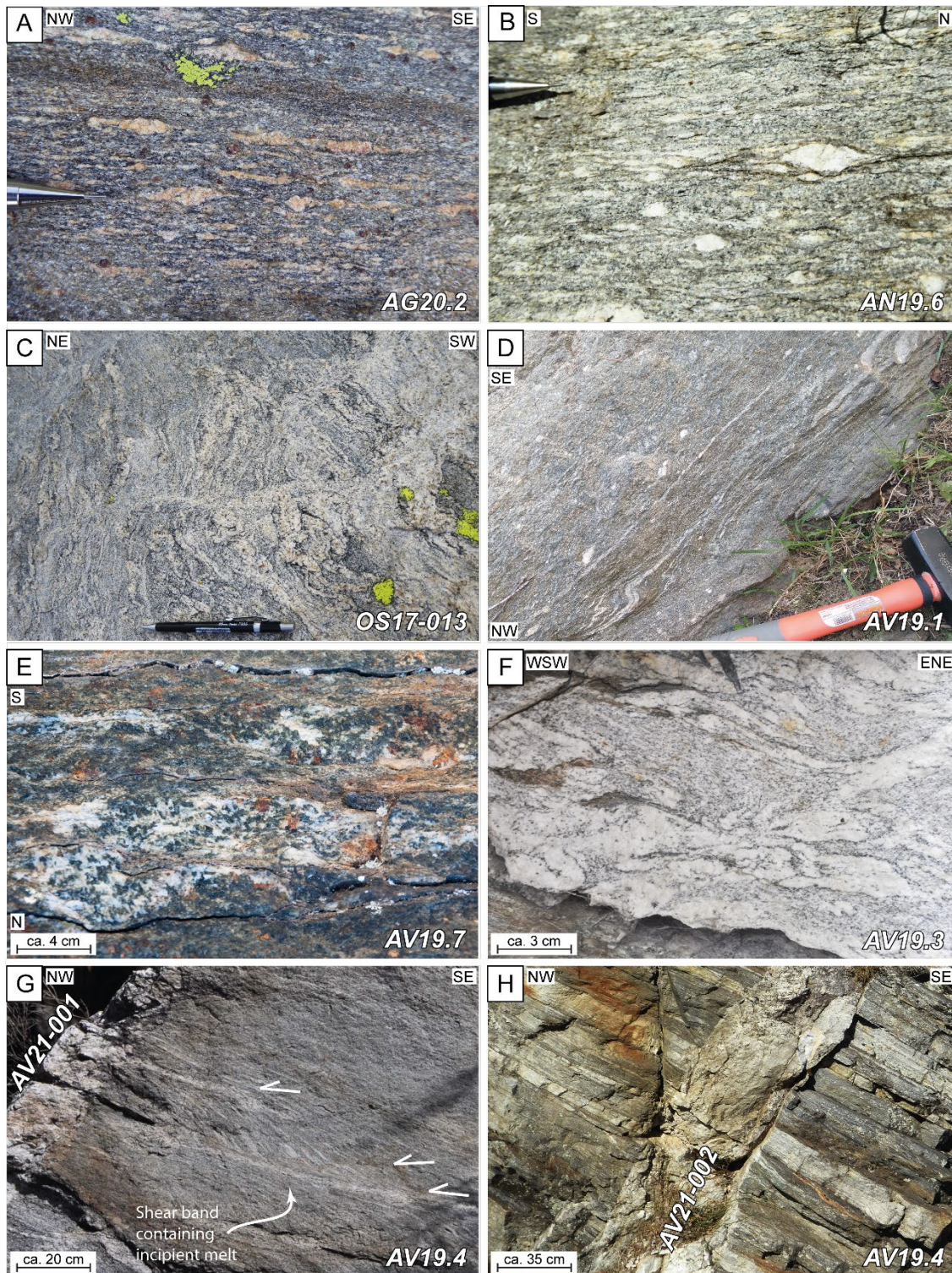


Figure 3.2. Field occurrence of the analyzed lithotypes. **(A)** Leucocratic pods in the (partially) migmatitic garnet-paragneiss AG20.2 in Cima di Gagnone (Cima Lunga unit). **(B)** Feldspar augen in the foliation of the leucocratic orthogneiss AN19.6 in Cima di Precastello (Cima Lunga unit). **(C)** Diffuse leucosomes in OS17-013 migmatitic orthogneiss in Cima di Precastello (base of Maggia nappe). **(D)** Sheared quartz veins in the AV19.1 metaconglomerate in San Vittore (Simano-Adula nappe contact). **(E)** Detail of the migmatitic garnet-paragneiss AV19.7 in San Vittore (Simano-Adula nappe contact). **(F)** Detail of a deformed leucosome network in the syn-tectonic migmatites AV19.3 in San Vittore (Simano-Adula nappe contact). **(G)** Syn-tectonic migmatites AV19.4 in Giova (base of Simano nappe) with leucosomes within shear bands. The migmatitic foliation is sharply cut by the AV21-001 pegmatitic dike. **(H)** The m-scale aplitic to pegmatitic dike AV21-002 cuts the migmatitic and mylonitic foliation of AV19.4 in Giova.

Tectonic nappe	Study area	Sample Rock type	Mineral assemblage*	Zircon main textural features	Interpreted zircon origin and Th/U ratio			Swiss grid coordinates (CH1903+/LV95)		
					Origin	Th/U ratio: range median (n)	Age (Ma) (2σ error)	E	N	
Cima Lunga	Cima di Gagnone	AG19.5 <i>Quartzofeldspathic gneiss</i>	qtz, feld, bt, wm, chl, st, zr, ep	125-250 μ m Anhedral to subhedral Uneven edges Micro-cracks	DR	0.097 (1)	276.76 \pm 3.56	2708973	1132336	
						0.128-0.291 (5)				
						0.345-1.87 (11)				
		AN20.1 <i>Quartzofeldspathic gneiss</i>	qtz, feld, bt, wm, chl, zr, ep, ox	125-200 μ m Anhedral to subhedral Uneven edges	DR	0.189 (1)	282.87 \pm 5.50	2708891	1135441	
						0.414-0.613 (2)				
						0.448-1.110 0.840 (3) [CORE] 0.016-0.052 0.031 (5) [RIM]				
	AG19.6 <i>Grt-paragneiss</i>	qtz, feld, grt, bt, wm, chl, ky, st, zr, ep, rt, ap, ox	200 μ m Anhedral	DR	0.002 (1)	322.9 \pm 30.4	2708804	1132391		
					0.161-0.231(2) 0.507-1.330 (3)					
	AG20.1 <i>Migmatitic grt-paragneiss</i>	qtz, feld, grt, bt, wm, chl, zr, ep, rt, ttn, ox	60-150 μ m Anhedral to subhedral	DR	0.094-0.974 0.620 (3)	687.09 \pm 23.82	2708333	1131210		
					0.005-0.007 0.006 (5)					
	AG20.2 <i>Migmatitic grt-paragneiss</i>	qtz, feld, grt, bt, chl, zr, rt, cld, ox	125-250 μ m Anhedral to subhedral Uneven edges	DR	0.219-0.284 (2) 0.378-0.870 (14)	548.76 \pm 10.57	2708337	1131193		
					0.002-0.003 (2)					
0.001-0.010 0.004 (41)										
Maggia	Cima di Precastello	AN19.6 <i>Quartzofeldspathic gneiss</i>	qtz, feld, bt, chl, wm, zr, rt, ox	100-250 μ m Anhedral to subhedral Uneven edges	MG	0.154-0.717 0.278 (28)	277.74 \pm 2.82	2713614	1127870	
	OS17-013 <i>Migmatitic orthogneiss</i>	qtz, feld, bt, wm, chl, zr, ap	100-250 μ m Anhedral to subhedral Uneven edges	MG	0.056-0.334 0.147 (13)	281.01 \pm 2.86	2712677	1126237		
					0.0006-0.009 0.002 (40)					
	Simano-Adula	San Vittore-Giova	AV19.1 <i>(Migmatitic) Meta-conglomerate</i>	qtz, feld, bt, wm, chl, zr, ep, ap, ox	90-250 μ m Idiomorphic to anhedral	DR	0.002-0.080 (13)	31.15 \pm 0.32	2728908	1122413
							0.164-0.269 (12)			
							0.322-1.735 (54)			
			AV19.7 <i>Migmatitic grt-paragneiss</i>	qtz, feld, grt, bt, wm, chl, ky, st, zr, ep, rt, ap, amph, cld, ox	200 μ m Anhedral, some idiomorphic	DR	0.048-0.064 (2)	34.75 \pm 0.83 31.53 \pm 0.68	2728838	1122423
							0.200-0.278 (8)			
							0.309-1.210 (17)			
		AV19.3 <i>Migmatitic orthogneiss</i>	feld, qtz, bt, wm, chl, zirc, ep, ox, amph	125-250 μ m Subhedral to anhedral Uneven edges	MG	0.001-0.015 0.004 (26)	282.07 \pm 1.79	2728407	1122398	
						0.0005-0.016 0.0039 (13)				
						0.001-0.114 0.006 (16)				
AV19.4 <i>Migmatitic orthogneiss</i>		feld, qtz, bt, wm, chl, zirc, ep, ap, ox	125-250 μ m Subhedral to anhedral Uneven edges	MG	0.013- 0.661 0.450 (8)	278.41 \pm 4.99	2728425	1123530		
					0.002-0.016 0.006 (9)					
AV21-001 <i>Pegmatitic dike</i>		feld, wm, qtz, grt, zirc	100-150 μ m Sub-idiomorphic Uneven edges	MG	0.003-0.013 0.006 (20)	23.00 \pm 0.14	2728422	1123526		
AV21-002 <i>Granitic dike</i>	feld, qtz, wm, bt, chl, zirc, rt, ep, ox	50-100 μ m Anhedral to subidiomorphic	MG	0.003-0.004 0.004 (6)	22.57 \pm 0.31	2728187	1123488			
				0.064-0.066 (2)						

Table 3.1. *Samples, locations and zircon characteristics. Mineral abbreviations* are reported in Appendix G. Zircon origin is indicated as: DR=detrital, MG=magmatic, ME_V=metamorphic (Variscan), ME_A=metamorphic (Alpine). Th/U ratios are reported with their range and median value, n=number of analyses. Detrital zircon crystals are subdivided according to Teipel et al. (2004). Th/U is calculated from LA-ICP-MS data (see LA-ICP-MS U-Pb analyses in Appendix F – folder UPb_LAICPMS online) and ages are LA-ICP-MS Concordia ages with 2σ error (only one SIMS Pb²⁰⁶/U²³⁸ age with its relevant Th/U is reported in italics: single data from Appendix F – UPb_SIMS.xlsx online). The distribution of dates for detrital zircon grains is in figures F.1 and F.2 in Appendix F.*

Zircon grains were separated at the University of Lausanne by standard grinding followed by sieving (125-250 μm fraction was selected), panning, magnetic separation and heavy liquid procedures. For some samples (*Sample OS17-013; AV21-001; AV21-002; AN20.1; AG20.1; AG20.2*), a Wilfley table at ETH Zurich was used for zircon extraction. Zircon grains were subsequently cast in epoxy resin to form mounts which were polished down to expose grain centers.

3.3.2 Analytical techniques

Cathodoluminescence (CL) imaging was carried out at the Scanning Electron Microscope laboratory of the University of Lausanne using a CamScan MV2300 electron microscope. CL-images were used to set point analyses on the target zircon domains.

Analyses were performed using LA-ICP-MS (Laser Ablation Inductively-Coupled Plasma Mass Spectrometry) and SwissSIMS ion probe (Secondary Ion Mass Spectrometry) facilities at the University of Lausanne. Laser spot diameter for U-Pb dating by LA-ICP-MS was set to 20 μm (30 μm pre-ablation), using the GJ-1 reference zircon (Boekhout et al., 2012; Ulianov et al., 2012) for the standardization of relative sensitivity factors and Plešovice (Sláma et al., 2008) as a secondary standard for accuracy control. The SIMS was operated at a beam size of 10x8 μm, using Temora (Black et al., 2004) and Plešovice (Sláma et al., 2008) standards. Trace elements were analyzed for selected samples by LA-ICP-MS, setting different spot diameters depending on the size of the target zircon domain (50, 38, or 30 μm), and using the SMR612 and BCR-2G glass standards.

Data reduction for LA-ICP-MS analyses was performed using Lamtrace software (Jackson, 2008). As an additional control of the spot positions, zircon populations were subjected to an *a posteriori* CL-check. The craters ablated on more than one growth zone, on densely fractured spots, or with inclusions were not further considered. Finally, the data were plotted on a Wetherill Concordia diagram using IsoplotR (Vermeesch, 2018). All the graphically discordant analyses were avoided from the Concordia age calculations. Zircon dates in the text are LA-ICP-MS dates, indicated as Concordia ages with a 2σ confidence interval, unless otherwise specified (e.g., SIMS dates).

The complete description of the applied methodology is reported in *Appendix D*.

Furthermore, in *Appendix E* there are the extended versions of [figures 3.3](#), [3.4](#) and [3.5](#) with geological maps and sections, together with the relevant stereographic projections of structural data. The detailed mineralogy of all sampled rocks is summarized in [table 3.1](#) and the relevant detailed thin section descriptions can be found in *Appendix G*. The measured U-Pb zircon data for LA-ICP-MS and SIMS analyses and the results of geochemical analyses are reported in *Appendix F – UPb_LAICPMS folder*, *UPb_SIMS.xlsx* and *Trace_LAICPMS.xlsx online*. LA-ICP-MS data distribution for all samples is represented in Kernel Density Estimates in [figures F.1](#) and [F.2](#) of *Appendix F*, computed with IsoplotR ([Vermeesch, 2018](#)). Discordia lower intercepts for SIMS analyses calculated in the Tera-Wasserburg diagram are in [figure F.3](#) of *Appendix F*, also computed with IsoplotR (Discordia Model-1; [Vermeesch, 2018](#)). Analytical results and Concordia diagrams for reference materials adopted in LA-ICP-MS analyses are in *Appendix F – Stds_LAICPMS.xlsx online*.

3.4 Geological results and zircon growth: structural position, sample description, zircon CL-images, U-Pb ages, and geochemistry

3.4.1 The Cima di Gagnone area

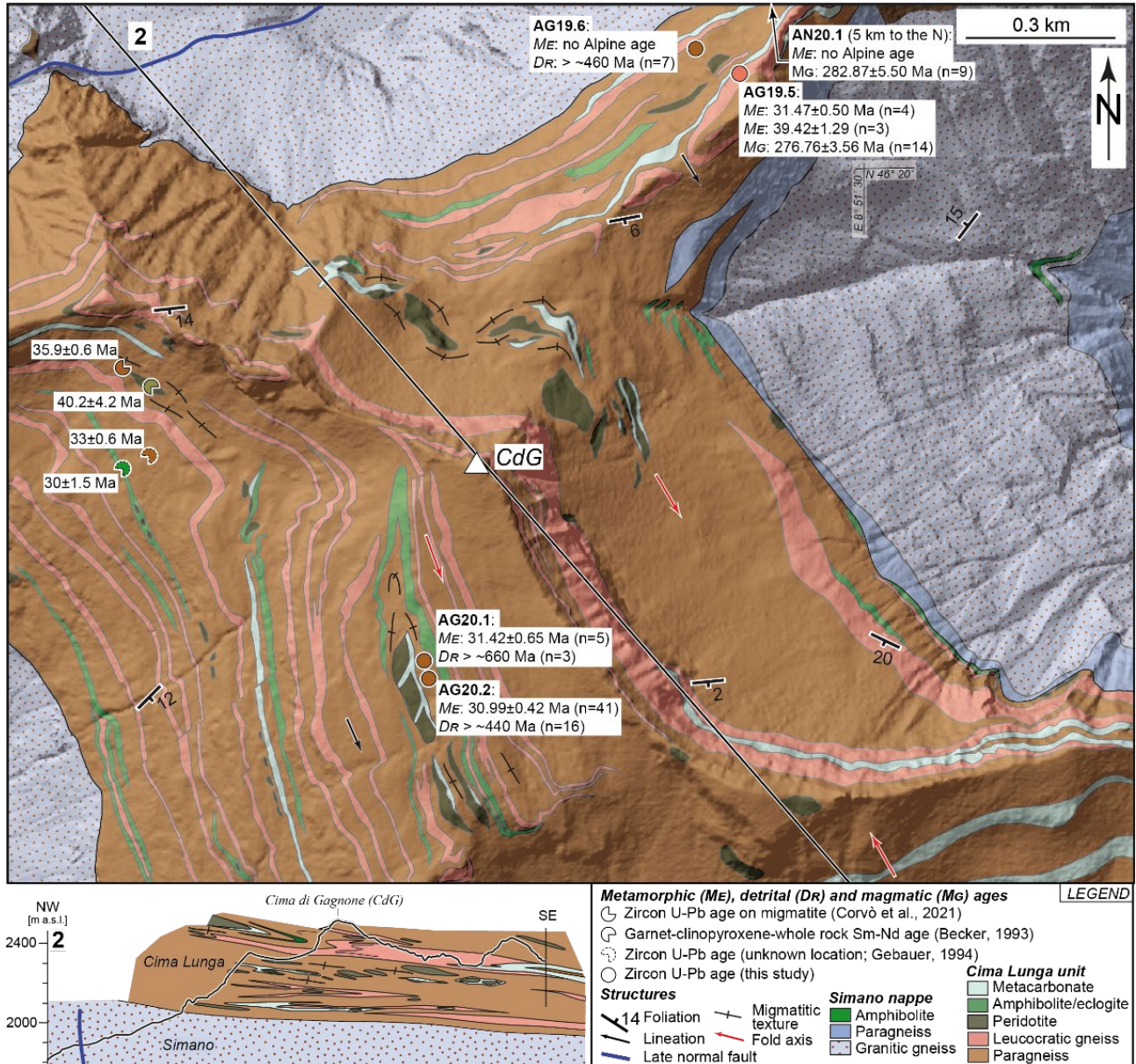


Figure 3.3. Geological-structural map of the first studied area, Cima di Gagnone, with the relevant geological section (Profile 2) (with minor modifications after Corvò et al. (2021) and Pfiffner & Trommsdorff (1997)). The ages of samples from this study and literature data are indicated in the map. Notice the continuity of lithotypes and the boudinage of ultramafics in the Cima Lunga unit. The zircon U-Pb ages from this study indicated in this map are LA-ICP-MS ages. An extended version of this figure is in Appendix E.

In the mapped area (*figure 3.3*), the Cima Lunga unit lies above orthogneisses, minor paragneisses and amphibolites of the Simano nappe. The Cima Lunga unit consists of biotite-muscovite paragneisses and micaschists, locally garnet-bearing, that wrap lenses of garnet peridotite and chlorite harzburgite. The metasedimentary stratigraphy is locally interlayered with amphibolites, which are locally boudinaged, and by quartzo-feldspathic gneisses (*figure 3.3*; *AG19.5*) of unknown protolith. Ultramafics are typically structurally linked with metacarbonates, being wrapped by and deformed together with them, and include basaltic amphibolites, eclogites, metarodingites and eclogitic metarodingites.

In the Cima Lunga unit, the presence of sheath folds documents highly sheared zones within a general top-to-NW shearing sense, as also previously documented by asymmetric sigmoids and garnet rotation (see also structural details in [Maino et al. \(2021\)](#)). The transition from the Simano nappe up to the contact with the Cima Lunga unit is marked by an overall progressive (but locally not linear) change in the gneiss texture, parallel to the regional foliation. The fabric is more developed toward the top of the sequence over ca. 200 m (e.g., decreased grain size, elongated lithons), suggesting an upward strain increase in the direction of the Cima Lunga unit. On the regional foliation plane the penetrative lineation trends NW-SE.

The HP/HT assemblages of mafic/ultramafic lenses are largely overprinted by amphibolite facies assemblages, which also dominate the enveloping paragneiss host rocks. Migmatitic structures occur around the ultramafic bodies as stromatic leucosomes and locally in the paragneisses as leucocratic intrafoliation pockets boarded by a melanocratic rim (*figure 3.2A* and *3.3*; *AG20.1*, *AG20.2*). This sporadic incipient melting is more prominent around the ultramafic inclusions and the volume of partial melting in the Cima Lunga unit is visually estimated in the field to maximal 2-3 vol%. Syn- to post- (Alpine) foliation veins containing quartz, kyanite and andalusite suggest that a release of fluids from the paragneisses occurred late in the decompression history (at $P \leq 0.4$ GPa), but still at 600-675 °C, as also previously noted and computed by [Allaz et al. \(2005\)](#).

Quartzo-feldspathic gneiss AG19.5 was sampled in the Cima Lunga unit from a continuous gneissic horizon located above metacarbonates and ultramafic lenses, and below paragneisses (*figure 3.3*). The rock texture is granoblastic with sparse feldspar augen. Foliation is defined by the preferred orientation of quartz, feldspar, biotite and white mica. Elongated mica flakes and quartz and feldspar aggregates define the lineation. At the micro-scale, grain boundary migration, subgrain rotation and myrmekites of feldspars and quartz suggest dynamic recrystallization at temperatures above 500 °C ([Passchier & Trouw, 2005](#); [Stipp et al., 2002](#)).

Rimmed zircon cores display a non-unique appearance in CL images (*figure 3.6*), reflected in a wide range of dates. Zircon core dates are spread along the Concordia line (total number of concordant analyses is $n=31$): the oldest are ca. 1000 Ma ($n=2$), a population is between 700 Ma and 400 Ma ($n=15$), and the highest density cluster is at 276.76 ± 3.56 Ma (Concordia age; $n=14$; MSWD=1.3; *figure 3.7A*). This Permian population is composed of both oscillatory cores and faint oscillatory rims around older cores (*figure 3.6*), and it shows Th/U ratios tendentially higher than 0.1 (median value: 0.339; *table 3.1*), indicative of magmatic zircon (Hoskin & Schaltegger, 2003; Teipel et al., 2004). The magmatic Th/U ratios, the oscillatory growth around older zircon grains, and the orthogneissic texture of the rock advocate a Permian magmatic age of the rock. Finally, rare homogeneous CL-gray rims wrap the zircon grains, giving dates split in two groups at 39.42 ± 1.29 Ma (Concordia age; $n=3$; MSWD=12) and 31.47 ± 0.50 Ma (Concordia age; $n=4$; MSWD=9.6) (*figure 3.8A*). Their Th/U is between 0.001 and 0.040 (*table 3.1*), typical of metamorphic zircon (Teipel et al., 2004).

Quartzo-feldspathic gneiss AN20.1 was sampled in Val Nédro (north of *figure 3.3*), at the base of the Cima Lunga unit. Foliation is defined by biotite, partially replaced with chlorite, and there is a large variability in lithons' composition: facies having feldspar augen and quartz-rich facies can both be found at the meso-scale. In thin section we observed that pre-existing feldspar augen can be replaced by newly-formed plagioclase grains and myrmekites along their boundaries, pointing to recrystallization temperatures above 500 °C (Passchier & Trouw, 2005).

Cathodoluminescence images depict zircon cores with oscillatory or sector zoning rimmed by a discordant oscillatory zone. Three cores resulted in dates between ca. 420 and 590 Ma, whereas nine other cores and oscillatory rims formed a cluster at 282.87 ± 5.50 Ma (Concordia age; $n=9$; MSWD=0.63; *figure 3.7B*). Zircon cores have $\text{Th/U} > 0.45$, and zircon rims $\text{Th/U} < 0.05$ (*table 3.1*) in the range of metamorphic zircon (Teipel et al., 2004). The within-error coeval magmatic cores and magmatic/metamorphic oscillatory rims coupled with the overall texture of the rock hint at a quartz-rich magmatic protolith of 282.87 ± 5.50 Ma age.

Garnet-paragneiss AG19.6 was sampled above calcschists and leucogneisses, and below ultramafic lenses (*figure 3.3*). It is characterized by cm-scale pre- to syn-tectonic snowball garnets and a tectonic fabric defined by kyanite and biotite with a preferred orientation, also defining the mineral lineation. Grain boundary migration microstructures indicate quartz and feldspar dynamic recrystallisation.

Two main groups of dates at ca. 585 Ma and ca. 460 Ma were detected for magmatic oscillatory and sector-zoned cores (*figure 3.6*). SIMS gave a date of 468.4 ± 13.4 Ma ($n=1$; $\text{Pb}^{206}/\text{U}^{238}$ age; error 2δ ; see *Appendix F – UPb_SIMS.xlsx online*) for a magmatic core ($\text{Th/U}=0.38$). A thin metamorphic rim

(Th/U=0.02), homogeneous, CL-gray in color and sub-idiomorphic, yields an age of 322.9 ± 30.4 Ma ($n=1$; Pb^{206}/U^{238} age; error 2σ ; *Appendix F – UPb_SIMS.xlsx online*), indicative of Carboniferous metamorphism. Therefore, the magmatic dates likely belong to detrital zircon grains and the deposition age of these metasediments predates the Variscan orogeny.

Migmatitic garnet-paragneiss AG20.1 was sampled above an HP ultramafic lens at Cima di Gagnone (*figure 3.3*). At the meso-scale, the rock has leucocratic migmatitic intra-foliation layers. The thin section shows that both biotite and white mica define the foliation and garnets are pre- to syn-kinematic. Some garnets are at the borders of the leucocratic domains.

Zircon cores display oscillatory zoning, dated at 687.09 ± 23.82 Ma (Concordia age; $n=3$; MSWD=3.3) and a Th/U between 0.09 and 1.00 (*table 3.1*). CL-gray rims, usually thick, with a smooth zoning pattern, wrap the zircon (*figure 3.6*). Their dates are clustered at 31.42 ± 0.65 Ma (Concordia age; $n=5$; MSWD=3.7; *figure 3.8B*) and they have a metamorphic Th/U imprint (0.005-0.007; *table 3.1*; [Teipel et al., 2004](#)). In these rims, the positive Ce-anomaly, the absence of the Eu-anomaly and the flat HREE profile (*figure 3.9*) together suggest zircon growth from incipient anatectic melt ([Sawyer, 2008](#)) in the presence of garnet (e.g., [Rubatto, 2002](#)), placing the migmatization at 31.42 ± 0.65 Ma.

Migmatitic garnet-paragneiss AG20.2 was collected in a rock portion with leucocratic cm-scale pockets (*figure 3.2A*). Leucosomes boarded by melanosomes also occur as boudinaged intrafoliation lenses, locally folded. Garnets are pre- to syn-kinematic, and quartz is more abundant with respect to feldspar. Undulose extinction of feldspars and quartz, coupled with the preferred orientation of quartz aggregates, indicate dynamic recrystallization.

Zircon cores have magmatic oscillatory or sector zoning, sometimes with rounded or zoning-parallel inclusions (*figure 3.6*). Their Concordia age is 548.76 ± 10.57 Ma ($n=16$; MSWD=4.5), associated with magmatic Th/U of 0.22-0.87 (*table 3.1*). Abundant metamorphic layers with chaotic zonation and ubiquitous rounded inclusions (generally $< ca. 10 \mu m$, up to ca. $20 \mu m$ in diameter) grew outside the cores (*figure 3.6*). Two inclusion-free spots gave concordant dates at 315.30 ± 16.71 Ma (Concordia age; $n=2$; MSWD=1.0). Finally, thick metamorphic rims (up to ca. $30-35 \mu m$) with low Th/U ratios (0.001-0.010; *table 3.1*) wrapping the zircon have an age of 30.99 ± 0.42 Ma (Concordia age; $n=41$; MSWD=17; *figure 3.8C*). Similar to *AG20.1*, the absence of the Eu-anomaly accompanied by a positive Ce-anomaly and a flat HREE profile indicate zircon growth while garnet and incipient anatectic melt coexisted (*figure 3.9*), pointing to a partial melting event at 30.99 ± 0.42 Ma.

3.4.2 The Cima di Precastello area

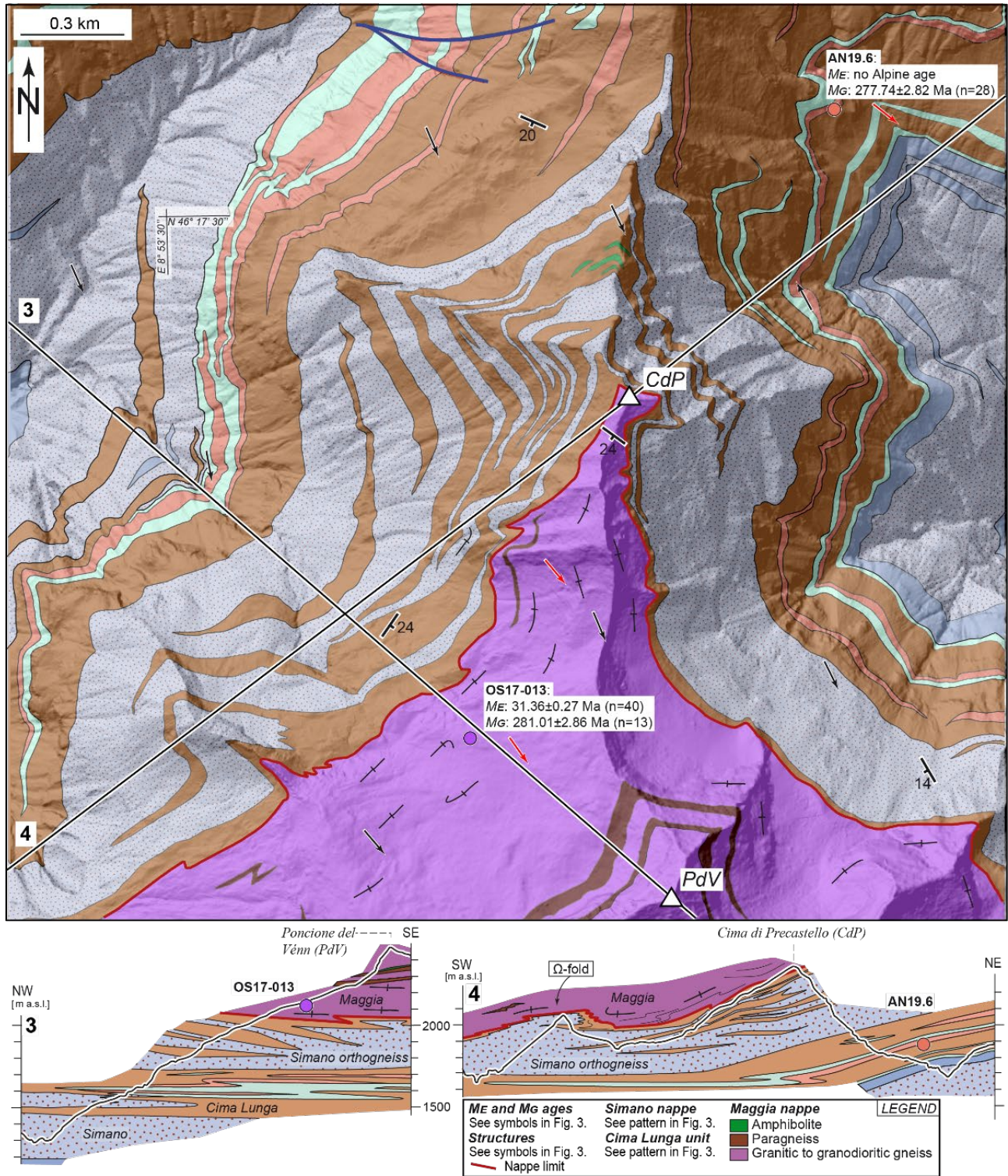


Figure 3.4. Geological-structural map of the second studied area, Cima di Precastello, with the relevant geological sections (Profile 3, 4). Own samples and LA-ICP-MS U-Pb zircon ages are indicated in the map. An extended version of this figure is in Appendix E.

In this mapped area (*figure 3.4*) the Cima Lunga unit is sandwiched between orthogneisses that are attributed to the Simano nappe. The Cima Lunga unit is constituted by an intensely folded sequence of paragneisses, leucocratic gneisses and metacarbonates, mainly calcschists. East of the mountain ridge of Cima di Precastello, these calcschists can be continuously followed over 6-10 km to the south (*figure 3.1C*). The stratigraphy of the bottom part of the Cima Lunga unit alternates calcschists with amphibolitic paragneisses, and local layers of a quartzo-feldspathic gneiss whose protolith nature and age are unknown (*AN19.6*). At the top of the Cima Lunga unit, paragneisses are interfingering by Simano orthogneisses, that are locally folded (*figure 3.4*). Here, the orthogneisses show sporadic migmatitic textures. The whole package is overlaid by granitic to dioritic orthogneisses that are diagnostic for the Maggia nappe (Rüscada and Cocco gneisses; [Bussien et al., 2011](#)). At the base of the Maggia nappe, migmatites with stromatic patches and a complex deformed network of leucosomes (*figure 3.2C*; *OS17-013*) testify partial melting during deformation. The contact is folded, having a fold axis parallel to the NW-SE directed lineation. On planes orthogonal to the lineation, these folds depict concentric- or Ω -shapes typical of sheath folds (see *Profiles 3 and 4* in *figure 3.4*), reflecting a high non-coaxial strain along the tectonic contact at the base of the Maggia nappe.

According to the mineral assemblages, we consider the metamorphic conditions in this area similar to those described in the Cima di Gagnone area, even though no eclogite was found and no detailed petrological study has been published.

Quartzo-feldspathic gneiss AN19.6 was sampled at the base of the Cima Lunga unit to the east (*figure 3.4*), in between metacarbonate layers. The tectonite fabric is defined by quartz-feldspar lithons and films of biotite and white micas. In the foliation, abundant feldspathic millimetric to centimetric augen with elliptical shape (*figure 3.2B*) indicate a magmatic protolith. The thin sections show evidence of crystal lattice distortion and dynamic recrystallization in the rock such as undulose extinction, subgrain rotation in quartz and feldspars, and grain boundary migration in quartz (only a few cases in feldspar), but also myrmekites which indicate temperatures above ca. 500 °C ([Passchier & Trouw, 2005](#)).

Zircon crystals are formed by an outer irregular, extremely thin (ca. 5 μm) rim wrapping the cores. Only in a few cases were these rims wide enough to analyze, although they yielded discordant dates. The inner part of the zircon cores is mostly idiomorphic, with oscillatory zoning, typical of magmatic zircon. However, the outermost layers of the core are typically damaged or resorbed, resulting in a porous aspect, or sometimes show damage trend parallel to the oscillatory zoning (*figure 3.6*). The U^{238} content of the porous zircon zones is higher than that of the pristine cores (5535 ppm and 1053 ppm respectively; see *Appendix F – Trace_LAICPMS.xlsx online*). In some cases, the boundary

between the apparently undamaged and the damaged zircon portions is gradational. Spot analyses of damaged zones resulted in discordant dates. On the same oscillatory cores, we could observe younger dates from the innermost portion of the zircon at 277.74 ± 2.82 Ma (Concordia age; $n=28$; $MSWD=1.6$; [figure 3.7C](#)) to the parts closer to the damaged zones (until ca. 220 Ma old; see distribution in [figures F.1](#) and [F.2](#) in *Appendix F*), with Th/U ratios for the pristine cores between 0.15 and 0.72 ([table 3.1](#)). These considerations and the orthogneissic texture of the rock point to a magmatic protolith, whose intrusion age is close to the age of the inner undamaged zircon at 277.74 ± 2.82 Ma.

Migmatitic orthogneiss OS17-013 was sampled from a leucosome-rich fraction of the migmatitic portion (metatexite to diatexite) of the Ruscada orthogneiss along the contact between the Maggia nappe with the lower rocks of the Cima Lunga unit and Simano nappe ([figure 3.4](#)). At the outcrop scale ([figure 3.2C](#)), the structures of the migmatites can be variable ranging from a layer-structured (in most cases) to local net-structured metatexites where both in situ and in-source leucosomes can be seen (see [Sawyer, 2008](#) as reference for migmatites' description). Some leucocratic portions are folded, and in a few cases a local patchy morphology can be seen. The rock consists of biotite, white mica, elongated and platy quartz and feldspar aggregates forming the foliation, with evidence of incipient melting at the micro scale which is testified by for example, polysynthetic twinning in plagioclase ([Vance, 1961](#)), and possibly indicated by tartan pattern in feldspars ([Winter, 2013](#)).

The oscillatory and sector-zoned zircon cores ([figure 3.6](#)) are dated at 281.01 ± 2.86 Ma (Concordia age; $n=13$, $MSWD=2$; [figure 3.7D](#)) with most Th/U ratios in the magmatic range (0.06-0.33; [table 3.1](#)). The cores are surrounded by outer layers that are not considered for magmatic age calculation being resorbed or with complex zoning patterns. The outermost layer has a very low Th/U (0.0006-0.009; [table 3.1](#)) pointing to a metamorphic origin ([Teipel et al., 2004](#)) and migmatization age at 31.36 ± 0.27 Ma (Concordia age; $n=40$, $MSWD= 0.71$; [figure 3.8D](#)).

3.4.3 The San Vittore-Giova area

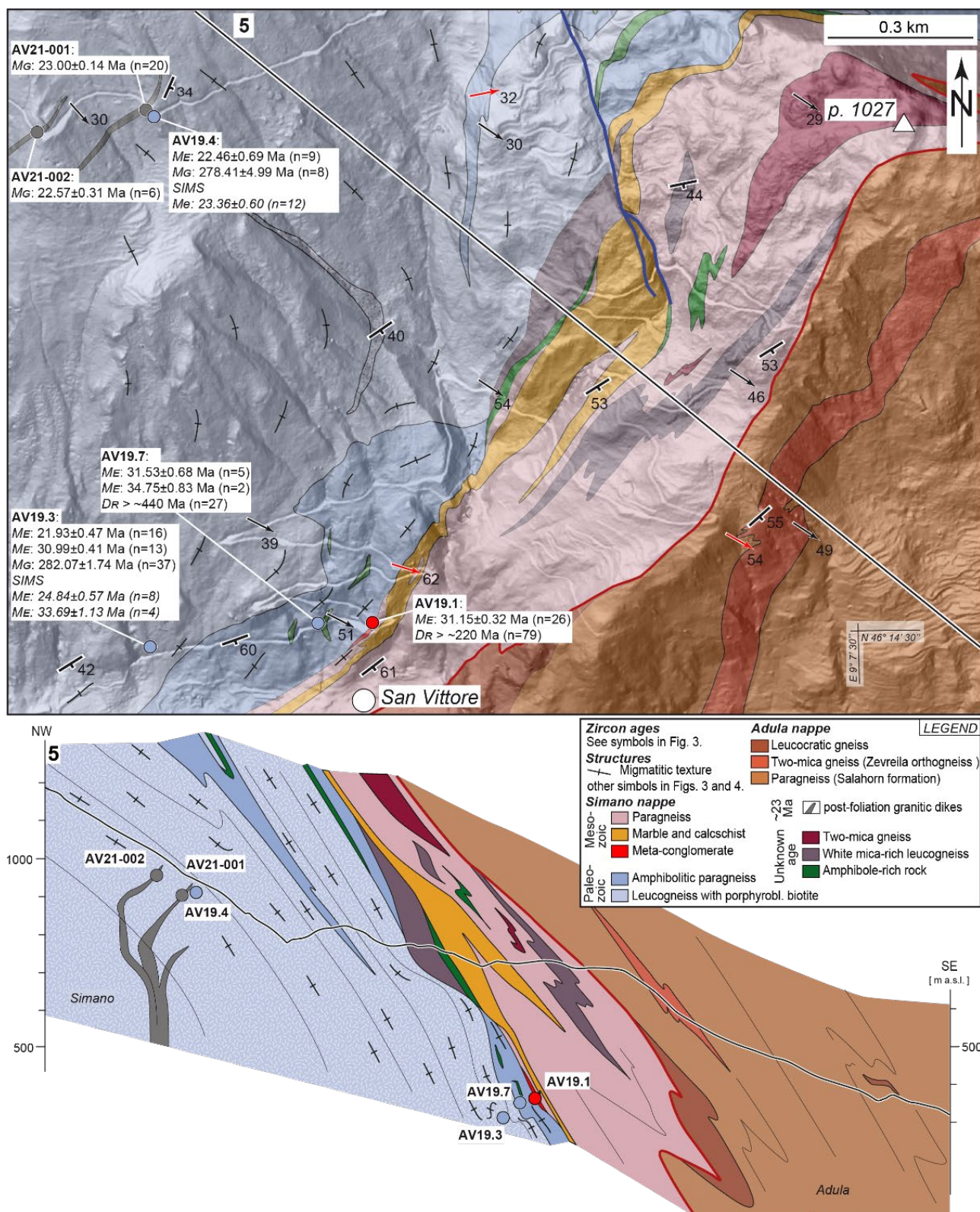


Figure 3.5. Geological-structural map of the third studied area, San Vittore-Giova, with the relevant geological section (Profile 5). Own samples and U-Pb zircon ages are indicated in the map. If not specified, zircon U-Pb ages are LA-ICP-MS ages. An extended version of this figure is in Appendix E.

In the San Vittore-Giova area (*figure 3.5*), the Adula nappe rests above the Simano nappe. The Simano nappe consists of leucocratic orthogneisses with porphyroblastic biotite, forming a large body that extends for several kilometers to the north and to the east. Minor volumes of paragneisses, locally containing garnets, and amphibolite lenses crop out above and inside this body. All along the upper tectonic contact of the Simano nappe with the Adula nappe, the orthogneisses and paragneisses show diffuse migmatitic textures (*figure 3.2E-G*; *AV19.7*, *AV19.3*, *AV19.4*) which are locally transected by granitic dikes (*figure 3.2G* and *3.2H*; *AV21-001*, *AV21-002*). The migmatitic texture disappears downsection in the tectonostratigraphy. The base of the Adula nappe is dominated by paragneisses and micaschists of the Salahorn formation (*Cavargna-Sani et al., 2014b*) and minor layers of orthogneisses. These rocks contain abundant stretched and folded intra-foliation quartz-veins. During deformation, the fluids that precipitated within these veins increased the mica content of the rocks which makes the macroscopic distinction between ortho- and para-gneisses difficult. In these gneisses, we do not observe migmatitic textures.

The roof of the Simano nappe is formed by a 200-400 m thick sequence that alternates paragneisses, micaschists, marbles, metaconglomerates and leucogneisses. The paragneisses and quartzofeldspathic gneisses show (at least at the base) migmatitic textures. The origin and the tectonic attribution of this folded and stretched sequence are unknown. The planes of alternating lithotypes and rock foliation dip to the southeast with an angle that gradually changes southwards from ca. 30° to ca. 60°, depicting the bending of the tectonostratigraphy in the SSB (*Profile 5* in *figure 3.5*). In this sequence of San Vittore, south-vergent asymmetric folds have SE plunging fold axis parallel to the mineral and stretching lineation (*figure 3.5*). The upper limbs are often sheared in a top-to-NW direction. This shearing occurred close to peak T metamorphic conditions and was the dominant deformation regime, as deduced from shear bands containing migmatitic leucosomes (*figure 3.2F* and *3.2G*; *AV19.3*, *AV19.4*), sigma clasts (*figure 3.2D*; *AV19.1*) and rotated garnets (*figure 3.2E*; *AV19.7*) all over the studied area.

In the studied area, the metamorphism of the Simano nappe reached partial melting conditions (\geq ca. 650 °C). Structurally below the migmatites, 5 km to the north, the peak conditions of the Simano nappe were computed at ca. 600 °C and 0.4 GPa (*Rütti, 2001*), whereas peak T conditions in the Adula nappe were estimated around 700 °C during decompression until 0.6-0.8 GPa (*Nagel et al., 2002a*; *Rütti et al., 2008*).

Quartzofeldspathic gneiss AV19.1 is a metaconglomerate, with centimetric, elliptical augen made of quartz and feldspar (*figure 3.2D*). Folded veins, locally quartz-rich, lay within the foliation, defined by the preferred orientation of biotite. At the micro-scale, polysynthetic twinning in plagioclase and

growth of fine-sized lobate quartz crystals from plagioclase borders testify incipient partial melting (Paterson et al., 1989). Zircon grains have a heterogeneous morphology and internal zonation (*figure 3.6*). Zircon cores also show variability in the inclusion content (*figure 3.6*): (i) CL-dark gray inclusion-rich inner cores surrounded by a CL-gray layer, and (ii) CL-light gray to gray inclusion-free cores. Their dates are spread along the Concordia over 1000 Ma, with the highest density of analyses around 300 Ma (*figure 3.7E*) and the second highest at 600-650 Ma. Th/U is usually higher than 0.1 (max. 1.73; *table 3.1*), even though some Permo-Carboniferous cores show lower values (min. 0.002; *table 3.1*). The distribution of concordant dates ranges from Precambrian to Permian-Triassic (*figure 3.7E*; see *figures F.1* and *F.2* in *Appendix F*). Finally, zircon cores are wrapped by CL-dark gray metamorphic rims, dated at 31.15 ± 0.32 Ma (Concordia age; n=26; MSWD=24; *figure 3.8E*), and having low Th/U ratios (0.001-0.015; *table 3.1*). We attribute this age to the beginning of partial melting at the micro-scale, hence to the migmatization stage. The morphological-heterogeneous population of the detrital cores (*figure 3.6*) and the spreading of concordant dates down to ca. 180 Ma (*figure 3.10*) suggest a Mesozoic deposition age.

Migmatitic garnet-paragneiss AV19.7 has cm-scale pre- to syn-tectonic garnets and shows mylonitic to migmatitic fabric (*figure 3.2E*) identified by the preferred orientation of biotite, which also defines the mineral lineation. Locally, at the meso-scale, asymmetric leucocratic pockets show a top-to-NW shear sense and migmatization. At the micro-scale, two main stages of garnet fabric evolution can be identified: (i) nucleation and growth prior to the development of the main tectonic foliation, and (ii) growth within the biotite + quartz + feldspar + kyanite foliation, associated with partial melting (see thin sections description in *Appendix G*).

Zircon grains have magmatic oscillatory or sector-zoned cores, anhedral in shape, sometimes eroded (*figure 3.6*), with dates spanning between ca. 475-625 Ma. Metamorphic rims are present. Some of them have dates around ca. 300 Ma. The outermost metamorphic rims with low Th/U ratios (0.002-0.009; *table 3.1*) cluster at 34.75 ± 0.83 Ma (Concordia age; n=2; MSWD=0.86) and 31.53 ± 0.68 Ma (Concordia age; n=5; MSWD=0.46) (*figure 3.8F*). Similar to the Cima Lunga migmatitic paragneisses (AG20.1, AG20.2), the Ce-anomaly, the absence of Eu-anomaly, and flat HREE profile (*figure 3.9*) reflect zircon crystallization in coexistence of incipient anatectic melt and garnet growth (Sawyer, 2008), prior to plagioclase crystallization (e.g., Rubatto et al., 2009) or with Eu-depleted plagioclase (e.g., Gregory et al., 2009). The 34.75 ± 0.83 Ma zircon rims have slightly lower HREE hinting at a metamorphic/migmatitic precursor involving garnet growth coeval with zircon formation. SIMS analyses gave one concordant date at 32.9 ± 1.0 Ma (n=1; Pb²⁰⁶/U²³⁸ age; error 2 δ ; *figure 3.8F*).

Migmatitic orthogneiss AV19.3 was sampled from a leucocratic portion of the rock. The rock texture is formed by mica films (biotite and white mica) and quartz-feldspar lithons, many of which gradually transition into leucocratic melt pockets, which locally accumulate in stromatic leucosomes parallel to the foliation, or within shear bands, or in veins cutting the foliation. Leucosomes may be locally folded, giving an overall picture of a syn-tectonic migmatite ([figure 3.2F](#)).

Zircon grains have inclusion-rich magmatic cores with oscillatory or sector zoning, their age is 282.07 ± 1.79 Ma (Concordia age; $n=37$; MSWD=1; [figure 3.7F](#)) and Th/U ratios cluster at ca. 0.4 ([table 3.1](#)). The cores are wrapped by partially resorbed layers showing a pattern of porous, convoluted zones, CL-black, frequently with cavities filled by later CL-gray zircon growth ([figure 3.6](#)). Finally, the outermost layers are metamorphic rims showing multiple growths. The inner ones are typically CL-gray and thick, with low Th/U ratios (median value: 0.004; [table 3.1](#)) and an age of 30.99 ± 0.41 Ma (Concordia age; $n=13$; MSWD=5.1; [figure 3.8G](#)). Outside, several thin layers (inner CL-light gray, outer CL-black) yielded an age of 21.93 ± 0.47 Ma (Concordia age; $n=16$; MSWD=1.1; [figure 3.8G](#)), having also low Th/U ratios (0.001-0.114; [table 3.1](#)). We also analyzed the zircon rims using SIMS, and they were dated at 33.69 ± 1.13 Ma (Concordia age; $n=4$; MSWD=3.7) and 24.84 ± 0.57 Ma (Concordia age; $n=8$; MSWD=0.46) respectively ([figure 3.8G'](#)). The REE profile of the 30.99 ± 0.41 Ma zircon population has a positive slope with high HREE contents and Eu-negative and Ce-positive anomalies ([figure 3.9](#)), possibly formed during zircon crystallization in the absence of garnet in evolved melts where a substantial amount of plagioclase was already crystallized (Sawyer, 2008). Trace element measurements were not performed on the outer younger rims because of their insufficient thickness.

Migmatitic orthogneiss AV19.4 was sampled from leucocratic portions of the rock along the same migmatitic belt of AV19.3. Its morphology is predominantly stromatic with veins or pockets cutting the foliation. Frequent dm-scale shear zones with melt in the shear plane ([figure 3.2G](#)), coupled with the asymmetric shape of some cm-scale melt pockets, indicate a top-to-NW shear sense parallel to the pervasive mineral lineation visible on the foliation planes.

Zircon internal stratigraphy is analogous to AV19.3. CL-gray cores provide an age of 278.41 ± 4.99 Ma (Concordia age; $n=8$; MSWD=0.013; [figure 3.7G](#)). These inner cores transition to damaged or resorbed layers with porous structure toward the external portions of the zircon, which are ultimately wrapped by metamorphic rims ([figure 3.6](#)). The outermost layer of rims we already identified in sample AV19.3, the CL-light gray and CL-black rims, is more developed in this sample. The age of these rims resulted in 22.46 ± 0.69 Ma (Concordia age; $n=9$; MSWD=0.0079) for LA-ICP-MS and 23.36 ± 0.60 Ma (Concordia age; $n=12$; MSWD=10) for SIMS analyses ([figure 3.8H](#) and [3.8H'](#)).

Th/U ratios cluster at ca. 0.5 for inner cores, whereas they are lower for the rims (median value: 0.006; [table 3.1](#)). Rims' REE pattern is marked by a positive slope with low MREE, no Eu-negative anomaly and a less pronounced Ce-anomaly compared to the analyzed metamorphic rims of sample *AV19.3*. These pieces of evidence suggest zircon rim crystallization during metasomatism or hydrothermalism (e.g., [Fu et al., 2008](#); [Geisler et al., 2003, 2007](#); [Hoskin, 2005](#); [Hoskin & Black, 2000](#)).

Granitic dike (pegmatite) AV21-001 was sampled from a pegmatitic dike cutting sharply across the migmatitic foliation of sample *AV19.4* ([figure 3.2G](#)). It contains quartz, feldspar, porphyroblastic biotite, and locally (unzoned, Ca-poor) garnet. Zircon grains have complex internal stratigraphy showing convoluted zoning and patchy patterns of CL-black and CL-gray zones ([figure 3.6](#)). Their age is 23.00 ± 0.14 Ma (Concordia age; n=20; MSWD=11; [figure 3.8I](#)). The low Th/U ratios are unusual for magmatic zircon crystals (0.0003-0.013; [table 3.1](#)). The U content is high (average of 19866.24 ppm for ^{238}U ; see [Appendix F – Trace_LAICPMS.xlsx online](#)). REE contents are high, reaching values of 10^3 - 10^4 higher than chondritic for Lu, with Eu-negative anomaly but not always showing a Ce-positive anomaly ([figure 3.9](#)), hence suggesting zircon crystallization in variable oxygen fugacity conditions ([Hoskin & Schaltegger, 2003](#)).

Granitic dike (aplite to pegmatite) AV21-002 is an approximately 40 cm thick dike showing both pegmatitic (central part) and aplitic portions ([figure 3.2H](#)). It contains quartz, feldspar with porphyroblastic biotite, and locally garnet. At the micro-scale, the fabric is magmatic. However, also small deformation signs can be observed, such as deformation lamellae in plagioclase or local slight kinking of white mica. Zircon grains show patchy CL-patterns ([figure 3.6](#)). Their age is 22.57 ± 0.31 Ma (Concordia age; n=6; MSWD=0.22; [figure 3.8J](#)), they have low Th/U ratios (0.003-0.004; [table 3.1](#)), and REE content covering a wide range, with Lu abundances 10^4 - 10^5 higher than chondritic ([figure 3.9](#)). The flat HREE profile, the Eu-negative anomaly, and the absence of Ce-anomaly ([figure 3.9](#)) hint at zircon crystallization under reducing conditions ([Hoskin & Schaltegger, 2003](#)). Late zircon overgrowths, CL-dark gray to black in color, appear as a triangular protuberance grown on top of a pre-existing zircon ([figure 3.6](#)), and have an age of 21.56 ± 0.62 Ma (Concordia age; n=2; MSWD=0.75; [figure 3.8J](#)). These overgrowths also have low Th/U ratios (ca. 0.06; [table 3.1](#)) and the REE trend is similar to that of the other zircons, although at higher abundances, reaching values of 10^6 higher than chondritic for Lu ([figure 3.9](#)). For this sample, from the REE evolution and from the aplitic to pegmatitic texture, we can suggest that the dike intruded at 22.57 ± 0.31 Ma and that around 21.56 ± 0.62 Ma late fluids/melts were still percolating within it.

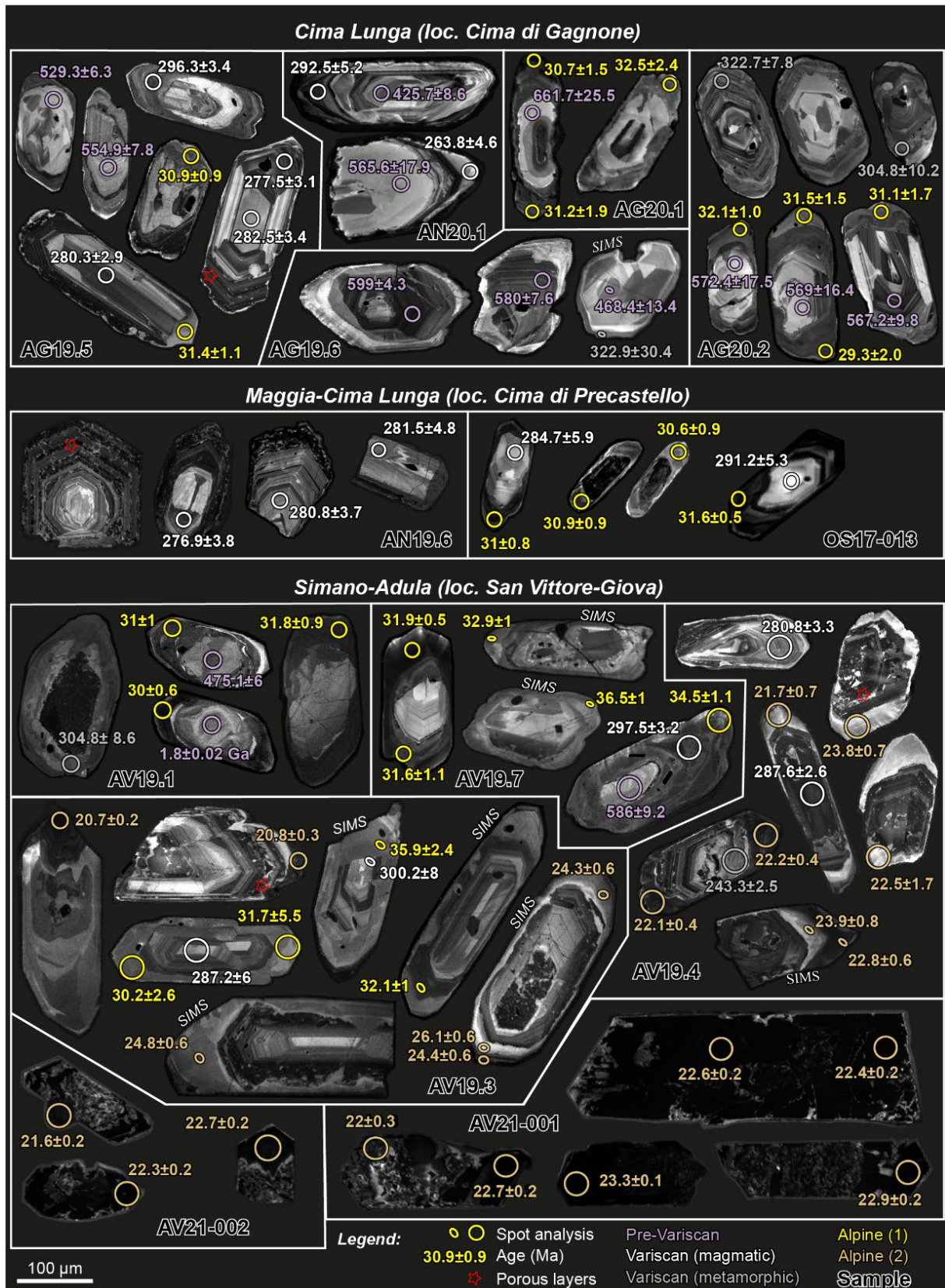


Figure 3.6. Cathodoluminescence (CL) images of representative zircon crystals. The big circles represent the LA-ICP-MS spot analyses (20 or 30 μm diameter), whereas the smaller elliptical ones indicate the SIMS spots (8x10 μm). The reported dates are ²⁰⁶Pb/²³⁸U (Ma) ± 2 sigma error. See the text for discussion on zircon internal stratigraphy and relevant ages.

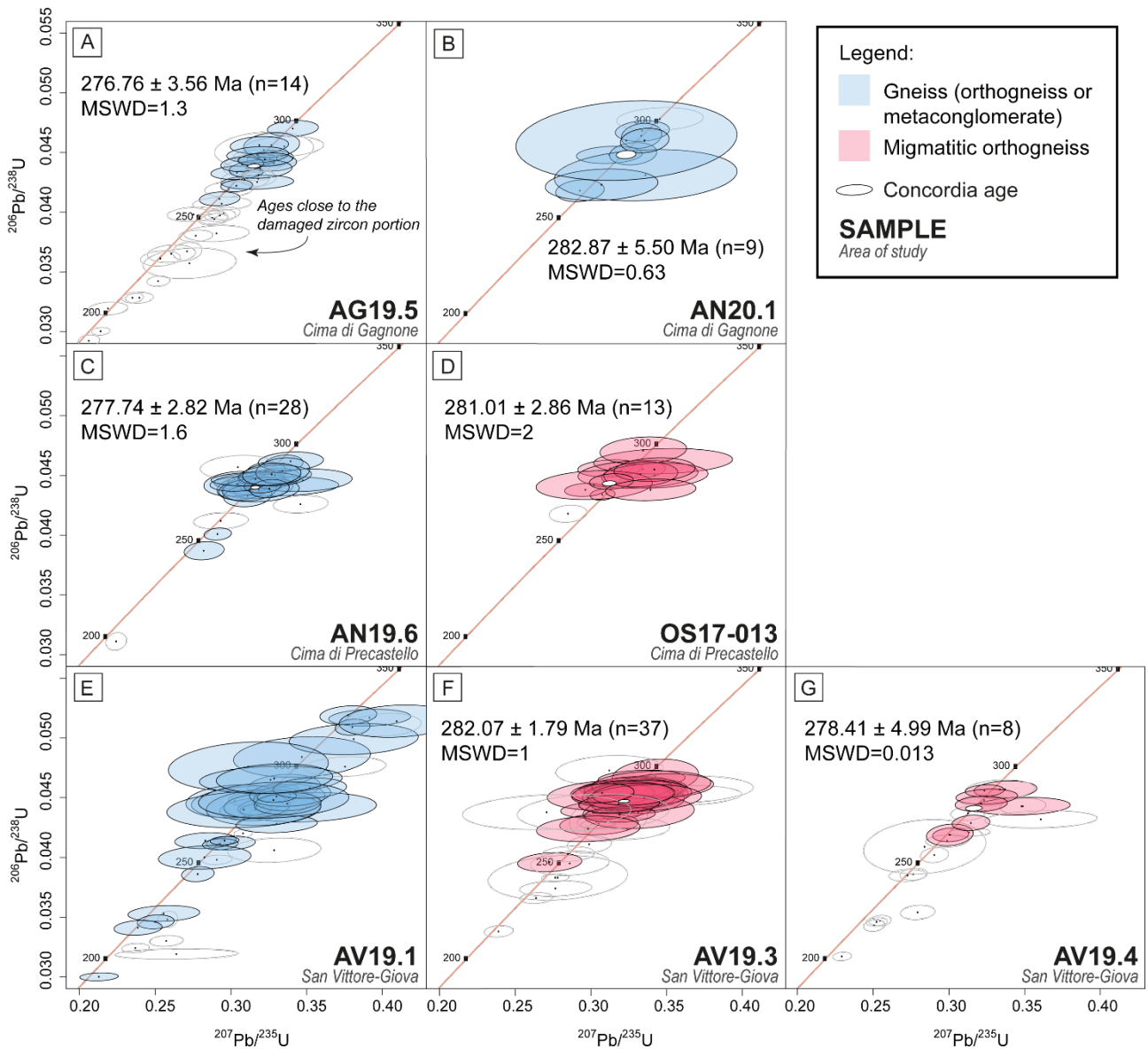


Figure 3.7. Wetherill Concordia plots for Permian ages. The age estimates are Concordia ages computed using IsoplotR (Vermeesch, 2018), and the mean square of weighted deviation (MSWD) is also calculated (both are absent in panel (E)). The number of concordant analyses considered for the calculation is indicated in brackets (n). Colorless ellipses represent discarded data. In panel (E): zoom of data distribution for detrital zircon grains in sample AV19.1, no age is computed.

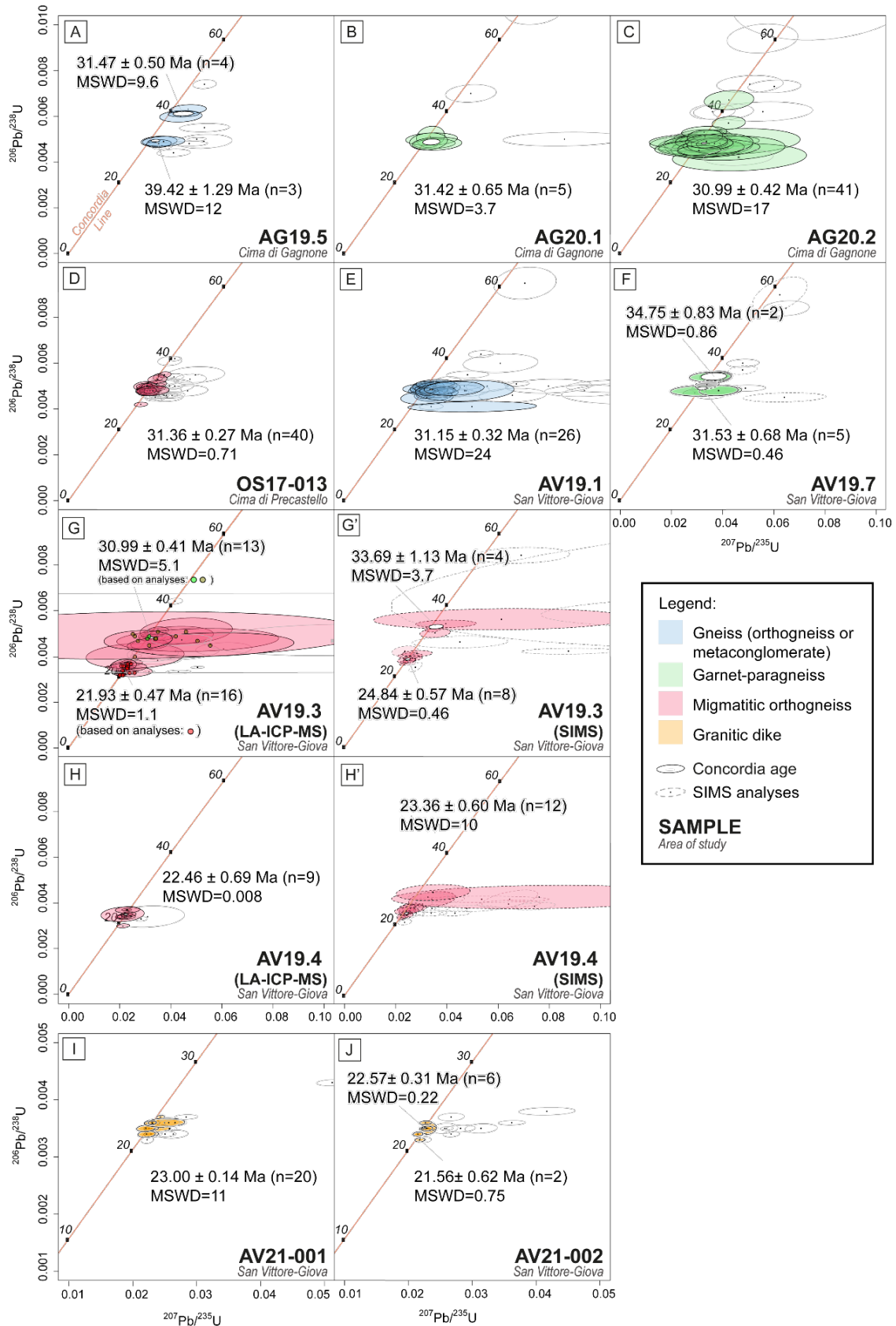


Figure 3.8. Wetherill Concordia plots for Alpine ages. Concordia ages are computed using IsoplotR (Vermeesch, 2018); the number of concordant analyses considered for the calculation is indicated in brackets (*n*) and is represented by color-filled ellipses. LA-ICP-MS data points are indicated with solid lines and SIMS results with dashed lines. For comparison, SIMS data computed with IsoplotR Discordia Model-1 (Vermeesch, 2018) in the Tera-Wasserburg diagram are reported in figure F.3 of Appendix F.

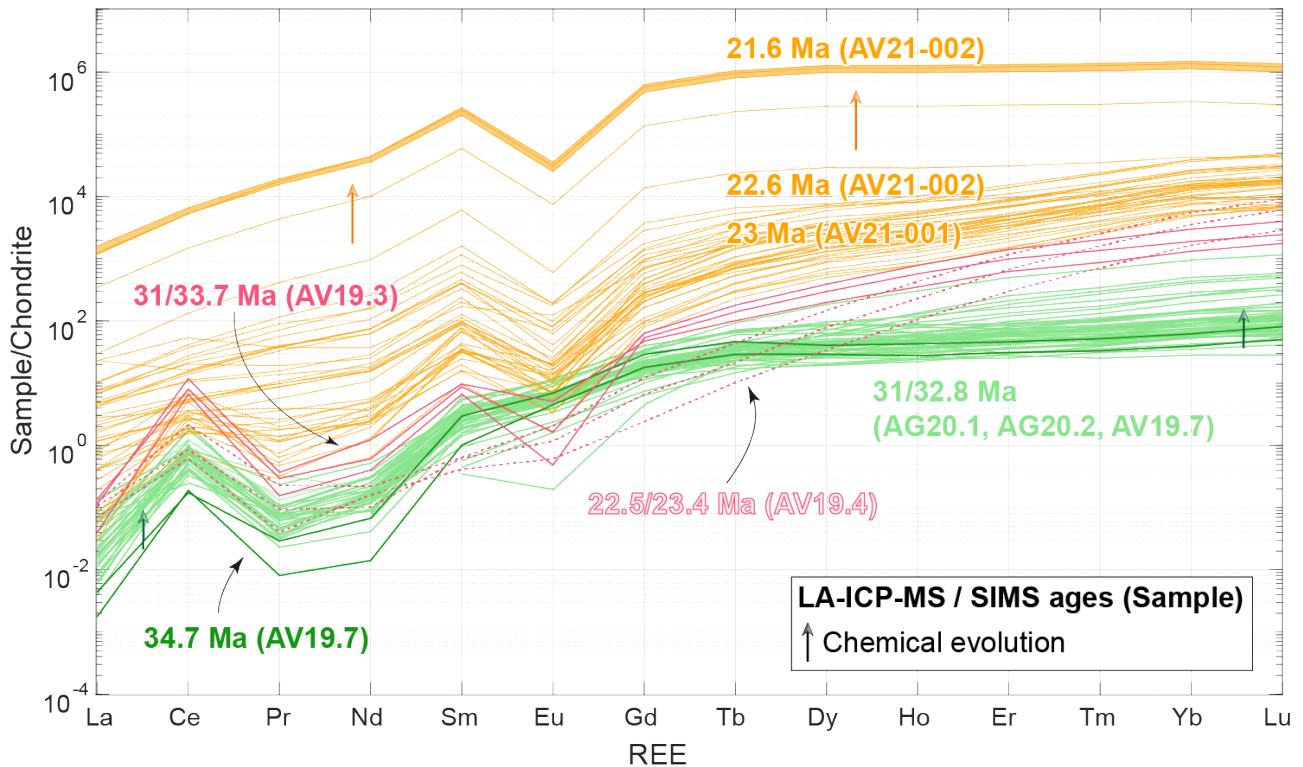


Figure 3.9. REE chondrite-normalized patterns for different samples (the same colors used in the precedent figures correspond to the different lithotypes). Trace element abundances were measured with LA-ICP-MS in the same zircon domains analyzed for U-Pb zircon dating (see main text for discussion). All the analyses are reported in Appendix F – Trace_LAICPMS.xlsx online.

3.5 Discussion

3.5.1 Methodological considerations on zircon U-Pb dating

We recognized three main zircon domains (*figure 3.6*) in the lithotypes of the Lepontine dome (*figure 3.10*): (i) pre-Permian detrital or Permian magmatic cores (*figure 3.7*), (ii) intermediate porous layers, and (iii) Cenozoic metamorphic rims (*figure 3.8* and *3.11*). Zircon layers are generally interpreted as magmatic when $\text{Th/U} > 0.3$, whereas low ratios ($\text{Th/U} < 0.1$) are indicative of metamorphic or near-solidus growth (Teipel et al., 2004; Vavra et al., 1999; Yakymchuk et al., 2018). The porous layers between the core and the outermost rims (*figure 3.6* and *3.10*) show Th/U around $0.1 (\pm 0.09)$. They appear as convoluted zones, black in the CL images, frequently with cavities (see AV19.3 in *figure 3.6*), and sometimes characterized by an “oscillatory damage” (see AN19.6 in *figure 3.6*). We analyzed these layers in migmatitic orthogneisses of the Simano nappe in San Vittore (AV19.3, AV19.4) and in the orthogneisses of the Cima Lunga unit (AG19.5, AN19.6). They usually show Jurassic-Cretaceous ages mostly discordant, hence not considered for U-Pb dating calculations. The high frequency of discordant dates within such porous layers can be due to radioactive damage

(metamictization) linked to initial high U-abundance, possibly accompanied by fluid leaching and/or bringing elements into the opened zircon system (Geisler et al., 2007; Harley et al., 2007). These zircon layers indeed show higher REE contents (particularly LREE) with respect to the older cores (average of ^{238}U : 609 ppm for porous layers, 3884 ppm for inner cores; average of ΣREE : 1630 ppm for porous layers, 982 ppm for inner cores; see *Appendix F – Trace_LAICPMS.xlsx online*), and they can contain inclusions.

In addition, these intermediate rims are often damaged by fractures (frequently very thin) which spread into the outer portions of the magmatic Permian cores (*figure 3.6; AN19.6*). These tiny fractures likely served as pathways for selective Pb or U removal, as manifested by the slightly younger dates with respect to the corresponding inner layers of the core. For this reason, in order to get a robust magmatic age for samples *AG19.5*, *AV19.3* and *AV19.4*, the results from spot analyses positioned in the outer portions of the zircon cores and/or close to cracks were not considered for the calculation of the Concordia age (*figure 3.7*).

The results of SIMS analyses provided age populations comparable to LA-ICP-MS, giving dates that are within-error to 1-2 Ma older (*figure 3.8*). This difference is reduced if a discordia computation approach is applied to SIMS data. The ages computed with ‘Discordia Model-1’ of IsoplotR in the Tera-Wasserburg diagram (see *figure F.3 in Appendix F*) are younger than the ones we calculated using our ‘concordant’ approach. The results are 0.2-0.4 Ma younger in sample *AV19.3*, while 2.5 Ma younger in *AV19.4*, however with a higher 2σ error (± 3.44 Ma). This may be due to a higher common Pb present in the latter sample, in which a higher number of discordant data was indeed obtained.

The partial lack of accuracy between methods can be attributed to the difference in the ablated material (SIMS: $8 \times 10 \mu\text{m}$ vs. LA-ICP-MS: $20\text{-}30 \mu\text{m}$). A larger spot may include more unrecognized damaged zones that could have suffered Pb or U loss. Alternatively, the age gap may be explained by the lower number of concordant SIMS analyses. However, the within-error overlap of LA-ICP-MS U-Pb dates at 31 Ma on metamorphic rims over seven samples suggests that a non-systematic effect of zircon damage zones cannot have significantly influenced the final ages and confirms the robustness of our data.

3.5.2 Combining geological mapping and pre-Alpine zircon U-Pb ages

3.5.2.1 The Cima Lunga unit as a pre-Variscan sedimentary basin

Our geological mapping of the Cima Lunga unit shows a metamorphic unit which apparently still preserves its sedimentary stratigraphy even though it is highly sheared and folded, particularly around the mafic and ultramafic lenses (Maino et al., 2021). In the Cima Lunga unit, we mapped approximately 20 m thick calcschist layers, which are continuous over a distance of 6-10 km (*figure 3.1, 3.3, and 3.4, Cima di Gagnone, Cima di Precastello*). These layers occur together with quartzofeldspathic layers that we identified as orthogneisses (see results; *AG19.5, AN20.1, AN19.6*). This continuity of both calcschist and orthogneiss layers contrasts with the spotted arrangement of the mafic and ultramafic rocks, which are more abundant in the upper part of the unit.

The spotted arrangement of mafic and ultramafic rocks was previously interpreted as the result of an Alpine tectonic *mélange* and the metasediments of the Cima Lunga unit were interpreted to derive from a Mesozoic Tethyan oceanic basin (Engi et al., 2001; Trommsdorff, 1990; Trommsdorff et al., 2000). However, our U-Pb zircon ages disagree with a Mesozoic origin of the Cima Lunga metasediments since the detrital zircon cores record only pre-Devonian ages and these cores are rimmed by Variscan metamorphic rims (ca. 300-315 Ma, sample *AG20.2*; and 323 Ma, sample *AG19.6*; *figure 3.6*). As already mentioned by Gebauer (1994), the detrital zircon cores from the Cima Lunga paragneisses (*AG19.6, AG20.1, AG20.2*) have a wide range of ages spanning from Precambrian to Cambro-Ordovician, and the youngest detrital zircon grains are ca. 400 Ma (*figure 3.10*).

A Cambro-Ordovician age for the Cima Lunga basin is also in line with the protolith ages of the dismembered ophiolitic fragments (528 ± 6 Ma age; zircon U-Pb SHRIMP on a mafic eclogite; Gebauer, 1994). The ages obtained for the ophiolitic fragments are similar to the ages of pre-Variscan ophiolitic rocks that are found within the gneissic basement nappes of both the external massifs and the Central Alps (Schaltegger et al., 2002). Hence, these ophiolitic rocks cannot be correlated with any Tethyan ophiolite.

We infer that also the continuous calcschist layers, which belong to the same pre-Variscan metasedimentary sequence of the Cima Lunga paragneisses, cannot be ascribed to a Mesozoic origin. The calcschist layers occur together with orthogneisses. The protolith ages of orthogneisses at 277-283 Ma (*AG19.5, AN20.1, AN19.6, OS17-013, AV19.3, AV19.4*) reflect the late Variscan magmatism of the pre-Alpine European basement units. Since these Permian magmatic events are well-documented in both margins of the Alpine Tethys (e.g., Beltrán-Triviño et al., 2013), it is unlikely that a Mesozoic basin within the Penninic domain would not contain any detritism of these Permian

events. The pre-Carboniferous ages of a small number of old zircon cores detected in these orthogneisses with Permian protolith would belong to fragments inherited from the surrounding paragneissic country rocks during intrusion, or to remnants of older molten precursors.

This Permian protolith age answers to a long-standing debate whether the origin of the quartzofeldspathic gneisses is magmatic or sedimentary (Dal Vesco, 1953; Pfeifer, 1987; Swiss National Map no. 1293 - Osogna (1:25.000) – Note esplicative). Their intra-layer appearance without an evident discordance with the outer paragneissic rocks (e.g., *figure 3.3*) infers that they represented sill-like intrusions in the pre-existing metasedimentary sequence (*figure 3.12B*), being subsequently metamorphosed and sheared with it during the Alpine cycle (*figure 3.12C-E*). Finally, the continuity over several kilometers of these 10-30 m thick orthogneissic layers (sample AN20.1; *figure 3.3*) within calcschists suggests that these layers are not imbricated fragments derived from the Simano nappe.

3.5.2.2 The Cima Lunga unit embedded in the Simano nappe

The transition from the Simano nappe to the Cima Lunga unit up to the Maggia nappe is marked by a non-linear increase in strain (see also Maino et al., 2021). In places, the attribution of the gneissic rocks to either the Simano nappe or the Cima Lunga unit is difficult, suggesting that these lithotypes may belong to the same original tectonostratigraphic sequence. Indeed, as discussed in *section 3.4*, the Permian protoliths of the migmatitic leucogneisses of the Simano nappe (AV19.3 and AV19.4) have magmatic ages contemporaneous within-error to the orthogneissic protolith of the Cima Lunga unit (AG19.5, AN20.1, AN19.6; *figure 3.7*). In addition, in the Simano basement of the San Vittore sequence, the Pre-Alpine garnet-paragneiss (sample AV19.7) shows a distribution of ages (older than 500 Ma; see *figures F.1* and *F.2* in *Appendix F*) similar to the detritism of the Cima Lunga garnet-paragneisses.

In agreement with these data, in the Cima di Precastello region (*figure 3.4*), the upper part of the Cima Lunga unit is interfingering by locally folded Simano orthogneisses. Below the tectonic contact with the overthrust Maggia nappe (see *profiles* in *figure 3.4*), this deformed geometry of interfingering gneisses recalls the intrusion of magmas into paragneisses.

Within a shear zone like the Maggia-Simano tectonic contact, it is difficult to exclude *a priori* that the Cima Lunga unit may be an independent tectonic slice detached from the Simano nappe or alternatively from the Maggia nappe. However, the actual geometry of the upper Simano nappe and the Cima Lunga unit suggests a coherent inherited large-scale (Permian) magmatic edifice, sheared and folded below the Maggia nappe during nappe emplacement. Similar magmatic relationships can be observed in other parts of the Simano nappe (e.g., the famous Lavertezzo outcrops; Sharma, 1969).

Rütti et al. (2005) suggested that the geometry of the upper Simano nappe may be explained by post-nappe emplacement folding (deformation phase D2) in which the Cima Lunga unit represents the fold core. However, the parasitic folds along the thrust are at odds with this explanation, and at the lower boundary of the Maggia nappe, they depict Ω -folds (*figure 3.4*). The Ω -folds occurred during extensive partial melting (Sample *OS17-013*) that likely accommodated part of the deformation during overthrusting. This syn-migmatitic deformation depicts a tectonic boundary that defines the base of the Maggia nappe.

3.5.2.3 The Maggia-Adula nappe system

Based on our observations, the Maggia nappe rests above the Simano nappe (which includes the Cima Lunga unit) and is on the same tectonostratigraphic level as the Adula nappe further to the east. Both contacts, Maggia-Simano and Adula-Simano, are prominent shear zones that are marked by syn-kinematic migmatitic belts, and where the upper block moved in the same kinematic direction and at the same time (see *sections 3.5.3 and 3.5.4*).

Along the Adula-Simano nappe contact, a Mesozoic nappe-divider was mapped in the San Vittore region (*figure 3.5*). Inside this sequence, according to the detrital dates, the metaconglomerate *AV19.1* is interpreted as a Mesozoic sediment, metamorphosed and deformed within the shear zone. Directly above it, calcschists, marbles and an amphibolite suggest a Triassic sequence of Helvetic affinity in a normal stratigraphic position (Beltrán-Triviño et al., 2013; Gisler et al., 2007), likely belonging to the parautochthonous cover of the Simano nappe. Alternatively, the intense deformation may have put these lithotypes together in Alpine times. This explanation is suggested by the presence of folded lenses of possible Adula origin (*lithologies of unknown age in figure 3.5*) in the upper part of the sequence.

Along the Maggia-Simano nappe contact, the shear zone comprises the Cima-Lunga unit (see *section 3.5.2.2*). Further to the west, the Maggia nappe rests above the Antigorio nappe and the Mergoscia zone (*figure 3.1B*). The Mergoscia zone can be considered a shear zone at the base of the Maggia nappe, comparable in metamorphism and in deformation to the Cima Lunga unit (e.g., Steck et al., 2013, 2019). We therefore consider the Maggia-Simano, Adula-Simano, and Maggia-Antigorio contacts to all form part of the same shear zone.

Hence, the architecture of the Lepontine nappes (*figure 3.12*) supports a large-scale Alpine Maggia-Adula nappe that was thrust over the Simano and Antigorio nappes, as already proposed in the early work of Jenny (1923). The geometry of the Maggia-Adula nappe depicts a mirror-like symmetry along the NW-SE central axis of the Ticino culmination (*figure 3.12A*). In the western and northern parts, our reconstruction agrees with the sheath fold model of the Maggia nappe of Steck et al. (2019).

However, to the south the Maggia-Adula nappe was disrupted and folded by the migmatites of the SSB and, as a consequence, it appears rootless. Before the intense reworking of the migmatitic belt, the nowadays spatially separated Maggia and Adula nappes presumably formed a laterally continuous Maggia-Adula nappe which was bent in the SSB (*figure 3.12D* and *3.12E*).

The ages of the Permian protolith of the orthogneisses constituting the Maggia and Adula nappes are comparable (*figure 3.12B*). The Cocco and Ruscada orthogneisses in the Maggia nappe mostly show ages at ca. 300-310 Ma (Bussien et al., 2011), and the Zervreila orthogneiss in the Adula nappe at 288-297 Ma (Cavargna-Sani et al., 2014a). The orthogneisses in the Simano nappe (orthogneisses AV19.3, AV19.4 in this study) show younger ages at 278-282 Ma (*figure 3.7*). Therefore, the similar ages of orthogneisses in the Maggia and Adula sectors of the nappe may also support lateral paleogeographic continuity.

A challenge for the interpretation of a large-scale Maggia-Adula nappe is the absence of HP rocks in its western region, the current Maggia nappe. Schmid et al. (2004) mention that Engi et al. (2001) report eclogitic slices found at the base of the Maggia nappe, but their location is to our knowledge uncertain. Eclogitic mafic rocks are documented only within the Adula nappe, being mostly concentrated on its upper part (see *figures 3.1B* and *3.12A*). However, neither the Adula ortho- nor para-gneisses show evidence of HP mineral assemblages, except for a whiteschist lens (Meyre et al., 1999). Therefore, it cannot be excluded that the orthogneisses of the current Maggia nappe have experienced a similar P-T evolution as the orthogneisses of the current Adula nappe.

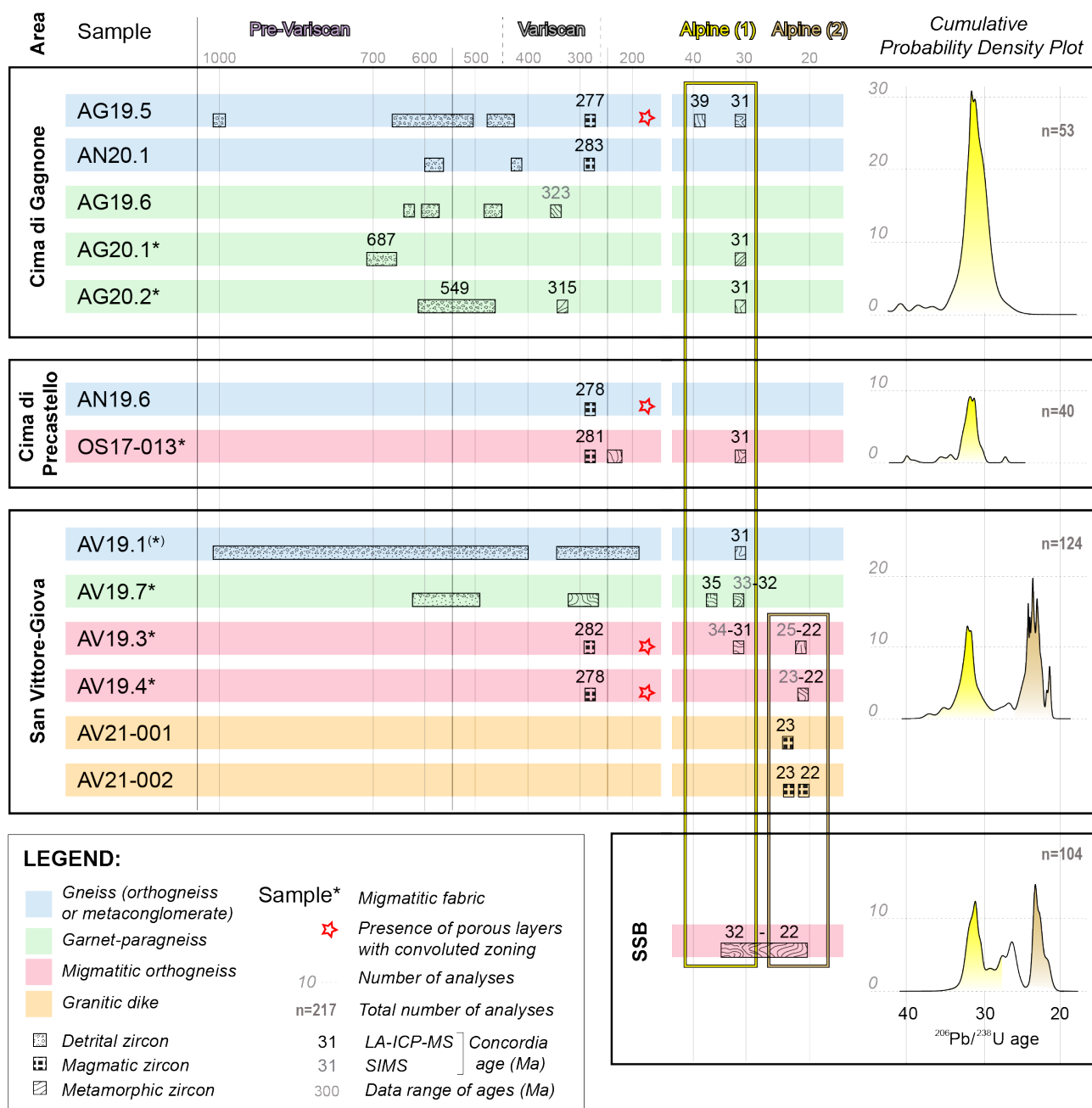


Figure 3.10. Summary of the calculated Concordia ages (both LA-ICP-MS and SIMS ages) and distribution of U-Pb zircon ages. For the distribution of single dates for each sample, see figures F.1 and F.2 in Appendix F.

3.5.3 Combining geological mapping and results on Alpine zircon growth

3.5.3.1 Syn-tectonic migmatites on the sole of the Maggia-Adula nappe

3.5.3.1.1 Migmatites occurrence

The distribution of the syn-tectonic migmatites along the basal shear zone of the Maggia-Adula nappe is not uniform. To the north, in the footwall of the main thrust (*Cima di Gagnone*, [figure 3.3](#)), Alpine leucosomes occur sporadically in the Cima Lunga paragneisses (samples *AG20.1* and *AG20.2*) and are more localized around the ultramafic lenses ([Corvò et al., 2021](#)). Apart from a few domains (see [figure 3.3](#)), most paragneisses do not show any migmatitic texture and Alpine zircon rims are absent (e.g., *AG19.6*). Only a few metamorphic zircon rims could be analyzed in the orthogneisses of the Cima Lunga unit (c.f. *AG19.5* with *AN20.1*).

In the central domain (*Cima di Precastello*, [figure 3.4](#)), widespread metatextitic to diatextitic migmatites were observed in the Maggia orthogneisses at the base of the nappe (*OS17-013*). In the footwall orthogneisses (Simano nappe), only a few migmatites were observed; however, they were not dated. Additionally, the orthogneisses within the base of the Cima Lunga unit (close to the contact with the Simano orthogneisses) do not show any textural evidence for partial melting (*AN19.6*).

To the south (*San Vittore*, [figure 3.5](#)), abundant top-to-NW sheared migmatites occur in the orthogneissic footwall and inside the Mesozoic sequence of the Simano nappe. In the hanging wall, the base of the Adula nappe does not show any direct evidence of partial melting, even though foot- and hanging wall rocks have similar compositions (metagranites and paragneisses) and hanging wall rocks experienced hydrous retrogression during deformation.

In summary, the overall picture shows a migmatitic belt with internal variations in the degree of partial melting in coincidence with local lithological heterogeneities. This migmatitic belt occurs along the main basal shear zones of the current Maggia and Adula nappes, which supports our interpretation of a large-scale Maggia-Adula nappe.

3.5.3.1.2 Migmatization age

In both orthogneissic and paragneissic migmatites, the REE patterns of zircon rims at ca. 31 Ma show equilibrium with melt. In the migmatitic garnet-paragneisses (samples *AG20.1*, *AG20.2* of Cima di Gagnone and *AV19.7* of San Vittore), thick zircon rims developed mostly in the presence of garnet ([Rubatto, 2002](#); [Rubatto & Hermann, 2007](#)), at the beginning of anatectic melt production (absence of Eu anomaly; [figure 3.9](#); [Hoskin & Schaltegger, 2003](#); [Sawyer, 2008](#); [Trail et al., 2012](#)). In the migmatitic orthogneiss *AV19.3* from San Vittore, zircon rims with high HREE contents and Eu-

negative and Ce-positive anomalies (*figure 3.9*) were likely in equilibrium with evolved melts in which plagioclase was already crystallized (Sawyer, 2008) and in the absence of garnet. The absence of garnet in our samples and the extensive migmatization in the orthogneissic migmatites support this geochemical interpretation. In the metaconglomerate *AV19.1* from San Vittore, microtextures typical of incipient partial melting (see *Appendix G*) also suggest zircon crystallization during migmatization. Hence, the zircon rims at ca. 31 Ma of the Cima Lunga orthogneisses (*AG19.5*) and paragneisses (*AG20.1* and *AG20.2*), of the Simano migmatitic orthogneisses (*AV19.3*) and paragneisses (*AV19.7*), of the Maggia migmatitic orthogneisses (*OS17-013*), and in the metaconglomeratic nappe-divider (*AV19.1*) date the event of partial melting (*figures 3.8, 3.10, and 3.11*).

In the Cima di Gagnone region, slightly older ages are reported by Gebauer (1994) on metamorphic zircon domains in kyanite-bearing paragneisses yielding an age of 33.0 ± 0.6 Ma, and by Corvò et al. (2021) on metasediments around ultramafic bodies at 36.0 ± 1.2 Ma (*figure 3.3*). Those ages mark local thermal re-equilibration during decompression and local metasomatism of the units (Corvò et al., 2021). A few older rims at ca. 39 Ma age (orthogneissic sample *AG19.5* in the Cima Lunga unit; *figure 3.8*) are within-error contemporaneous to the ca. 40 Ma old HP garnet-lherzolite (Becker, 1993).

In the San Vittore region, the garnet-paragneiss (sample *AV19.7*) also recorded an initial stage of garnet formation, which was followed (and partially coexisted) with the development of the main metamorphic foliation, associated with partial melting. We suggest that these two phases correspond to the growth of zircon rims at ca. 34.7 Ma and ca. 31.5-32.8 Ma, respectively (*figure 3.8*).

3.5.3.1.3 Post-migmatization ages

Another group of ages, younger than the migmatization stage, is recorded only in the San Vittore area (*figure 3.5*). The migmatitic orthogneiss *AV19.3* is the only migmatite sample that registers both ages (*figures 3.8, 3.10, and 3.11*). The older zircon crystallization stage, at 31-33.7 Ma, developed in the presence of plagioclase (*figure 3.9*) during the syn-tectonic migmatization event. Younger crystallization ages at 21.9-24.8 Ma are recorded in the metamorphic rims of the most external domains of the zircon. Differently, in sample *AV19.4* (migmatitic orthogneiss), the only recorded (metamorphic) imprint is at 22.5-23.4 Ma (*figures 3.8, 3.10, and 3.11*). These rims are characterized by a depletion in REE content (especially MREE), a lower Ce anomaly, and absence of Eu anomaly (*figure 3.9*), confirming that they did not crystallize coeval with plagioclase from a melt, but probably as the result of a metasomatic/hydrothermal process (e.g., Fu et al., 2008; Geisler et al., 2003, 2007; Hoskin, 2005; Hoskin & Black, 2000). The 31 Ma migmatization ages are not recorded in this sample, likely due to a re-equilibration promoted by the close intrusion of two granitic dikes, which could

have reset the zircon system in different portions of the rock (Bindeman & Melnik, 2016). The two granitic dikes (samples AV21-001 and AV21-002) were dated at ca. 22-23 Ma (figures 3.8, 3.10, and 3.11). Their crystallization evolution followed a progressive extreme enrichment in REE (contents 10^6 higher than chondritic; figure 3.9), and garnet formation (Rubatto, 2002; Rubatto & Hermann, 2007). The geochemistry shows this evolution through time, leading to new zircon growth in the evolving dike (figures 3.6 and 3.9). A similar pegmatite, with zircon grains characterized by extremely low Th/U ratios and intensely altered cores, was dated at 25.1 ± 0.6 Ma north of San Vittore by Gebauer (1996).

3.5.3.2 Timing of the regional Barrovian metamorphism: peak T conditions at 31 Ma

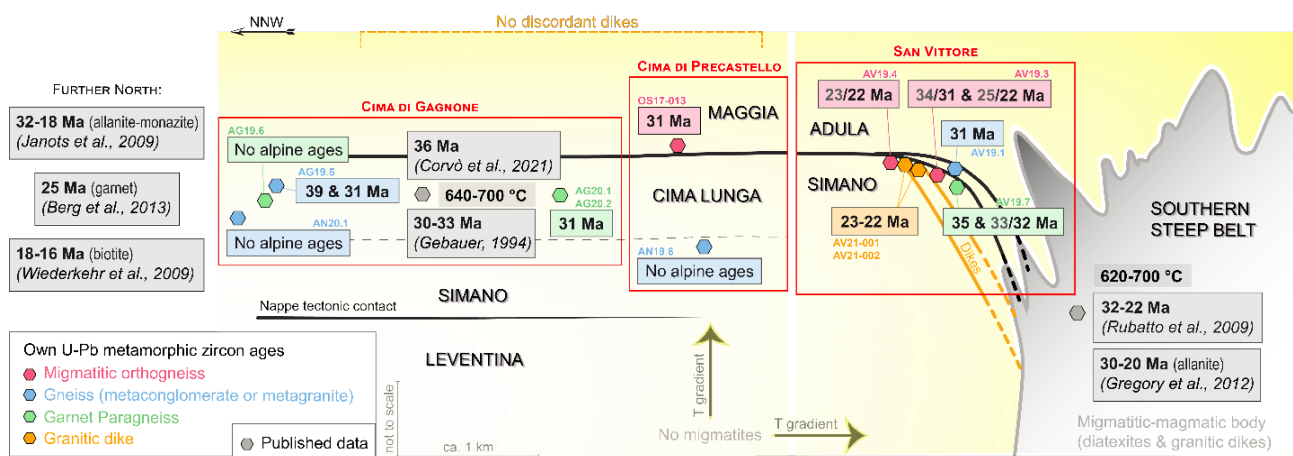


Figure 3.11. Sketched tectonic overview with own data (LA-ICP-MS ages in black/SIMS ages in gray) and some ages from the literature (if not specified, the ages are U-Pb on zircon). T gradients are qualitatively estimated according to the presence of migmatites in gneissic rocks.

The whole Lepontine dome is characterized by a highly penetrative NW-SE lineation (figure 3.1) with an orientation that corresponds to the top-to-NW shear direction of the syn-tectonic migmatites outcropping along the basal Maggia-Adula shear zone (figure 3.5, San Vittore-Giova; figure 3.2F and 3.2G). This observation strongly supports the interpretation that lineation and migmatites formed in the same regional strain regime.

In addition, the lineation is defined by the upper amphibolite mineral assemblage and is always at peak metamorphic conditions. The mineral lineation always marks the peak conditions independently of the T defined by the isograds, which depict concentric shells for the Barrovian metamorphism (figure 3.1). The syn-peak constrictional structures are indeed observed both in the Cima di Gagnone area (figure 3.3) to the north and in the southernmost studied areas (figure 3.4, Cima di Precastello; figure 3.5, San Vittore-Giova), separated by the 650 °C isotherm of Todd & Engi (1997) (figure 3.1B).

Hence, we suggest that lineation, migmatites and isograds developed at the same time at ca. 31 Ma, representing the peak of the regional Barrovian metamorphism in the Lepontine area. In other words, the spatial extent of the regional thermal peak at 31 Ma coincides with the extent of the mineral lineation and can be followed in the field across the Lepontine dome (c.f. [figure 3.1B](#) with [figure 3.12A](#)).

In a metamorphic basement like the Lepontine dome, formed by rocks of similar compositions and within a common metamorphic gradient, the front of incipient melting can be considered as an isograd that corresponds to T of at least 650 °C (e.g., [Spear, 1993](#)). Temperatures above 650 °C at ca. 1 GPa during the local migmatization of the Cima Lunga paragneisses are confirmed by thermo-barometric studies (e.g., [Corvò et al., 2021](#)).

One should consider also that fluid inputs along a tectonic contact may slightly lower the melting temperatures. This mechanism has been proposed for the SSB (e.g., [Berger et al., 2008](#)), where fluid-induced melting produced the reaction: biotite + plagioclase₁ + quartz ± epidote + H₂O = hornblende + plagioclase₂ + melt_(feldspar-rich) ([Berger et al., 2008](#)). The clear recognizable trace left in the field by this reaction would be the presence of amphiboles in the leucosomes or in the restitic fraction. However, in our field areas, most leucosomes and restites do not bear amphiboles.

Consequently, the melting of migmatites seems not to be due to a fluid-induced mechanism, even though fluids were present in the rocks during deformation. Indeed, above and below the migmatitic belt of the Maggia-Adula shear zone, metagranites and paragneisses contain scattered syn-foliation veins, suggesting the presence of fluids during the formation of the main fabric. The host rocks of these veins do not show signs of migmatization despite the bulk-rock compositions being similar to the protoliths of the migmatites (i.e., the Permian granitic protolith of the orthogneisses, c.f. samples *OS17-013* and *AN19.6* in [figure 3.4](#)).

The considerations above strongly suggest that migmatization can be taken as a direct T index and that the border of the migmatitic belt along the Maggia-Adula shear zone can be considered a metamorphic isotherm of at least 650 °C.

From our observations (see [section 3.5.3.1.1](#)), we see that migmatites die out to the north. Consequently, the 650 °C isotherm at 31 Ma forms a lobe that wraps the migmatites of the SSB (which have higher temperatures) and closes to the north, where it cuts the tectonic contact ([figure 3.12D](#)). Considering the shape of the 650 °C isotherm, the local paleo-geotherm at 31 Ma depicts an inverted T gradient across the center of the Lepontine nappe pile. Further north, the lower-grade isotherms (e.g., 600 and 550 °C) corresponding to the same temperature field at 31 Ma also plunge into the Simano nappe cross-cutting the tectonic contact ([figure 3.12D](#)).

In the frontal part of the Lepontine dome, prograde allanite U-Th-Pb ages at ca. 32 Ma (Boston et al., 2017; Janots et al., 2009) document an early stage of thrusting at ca. 550 °C below the Simano nappe attesting northward migration of the thrusts (*figure 3.12D*). The thrust below the Simano nappe started a new prograde metamorphic cycle up to 620 °C registered by Lu-Hf garnet-rutile at 25.4 Ma (Berg et al., 2013) and in the monazite U-Th-Pb ages until ca. 19 Ma (Janots et al., 2009). In some areas of this frontal part, the thermal peak conditions occurred after thrusting (Wiederkehr et al., 2008). We suggest that this T peak is related to the thermal relaxation of the frontal domain of the nappe stack (*figure 3.12E*).

In the proximity of the SSB (*San Vittore, figure 3.5*), new magma intruded at ca. 22-23 Ma. These later intrusion-related ages are recorded in the migmatitic country rock (samples AV19.3 and AV19.4) and in the cross-cutting granitic dikes (samples AV21-001 and AV21-002, *figure 3.5*). In the south, Gebauer (1996) suggests that this magmatic/fluid pulse(s) originated from the SSB within a regional reheating event. However, Rubatto et al. (2009) reported a continuous fluid-induced melting from ca. 32 to 22 Ma in the SSB. Hence, during 10 Ma, the SSB was a continuous migmatitic belt from which magmas were escaping into the surrounding regions and formed a belt of discordant dikes (Burri et al., 2005).

Finally, if we consider the whole Lepontine area, monazite U-Pb ages around 22-23 Ma are spread all over the dome (Köppel & Grünenfelder, 1975). These ages are interpreted as the timing of metamorphism close to peak T conditions at ca. 600 °C (Boston et al., 2017) during a second thermal event (Berger et al., 2011). However, in the central domain of the Lepontine dome, these monazite ages cannot record the peak T condition since U-Pb zircon ages of migmatites record only the 31 Ma event corresponding to peak Barrovian conditions at 650 °C or higher. Hence, the young monazite ages may either reflect cooling below ca. 600 °C after the peak T Barrovian event at 31 Ma or a heating event up to ca. 600 °C at 22-23 Ma.

The latter case of a heating event does not necessarily need an additional heat source. Indeed, we propose that the top-to-bottom heat diffusion consequent to the inverted thermal gradient at 31 Ma may have slowly heated up the rocks below the Maggia-Adula shear zone until ca. 22-23 Ma.

These cooling or heating scenarios remain disputed and may be tested, for example, by the estimation of cooling rates in garnets using diffusion models. This estimation of cooling rates was recently applied to support the importance of shear heating for two crustal-scale shear zones in Rhodope, Greece and Sikkim, Himalaya (Burg & Moulas, 2022).

3.5.4 Geodynamic implications

3.5.4.1 Geodynamic reconstruction

The late Variscan European crust was an old metasedimentary basement intruded in the Permian by magmatic bodies. These magmatic bodies locally formed finger-like intrusions (*figure 3.12B*). A part of this heterogeneous crust was already subducted and exhumed as a sheet-like *mélange* during the Variscan orogeny (Herwartz et al., 2011). In our reconstruction, this *mélange* formed the upper region of the crustal units that today corresponds to the Maggia-Adula and Simano nappes. In the Simano nappe, this *mélange* unit forms now mainly the Cima Lunga unit.

In late Variscan time, the Cima Lunga unit could have been part of the same *mélange* region of the Mergoscia zone. The Mergoscia zone represents the upper part of the late Variscan crustal unit that today forms the Antigorio nappe. A lateral correlation between the Mergoscia zone and the Cima Lunga unit (*figure 3.12A* and *3.12B*) is possible but very speculative since the Mergoscia zone is dominated by orthogneisses and the origin of its eclogitic lenses remains unclear.

The geometry of the late Variscan crust was modified during the Mesozoic extension, but we assume that the first-order paleogeographic relations were not significantly changed. During the Alpine convergence, the thinned late Variscan crust, which was part of the European passive margin, was subducted in the Paleogene. Exhumation started around 38 Ma according to the (U)HP event of Herwartz et al. (2011) and Sandmann et al. (2014), when the thrusting of the Maggia-Adula nappe over the Simano nappe began (*figure 3.12C*). The Alpine eclogitic conditions in the Maggia-Adula nappe were reached in the central part of the nappe, whereas in the northernmost regions only pre-Alpine conditions are recorded (Lu-Hf on garnet in Herwartz et al. (2011); Sandmann et al. (2014)). The exhumation of the Maggia-Adula nappe may have occurred mainly due to buoyancy forces (Candioti et al., 2021; Chemenda et al., 1996; Schmalholz & Schenker, 2016; Vaughan-Hammon et al., 2022), whereby exhumation velocities were likely higher than the horizontal convergence-related velocities (e.g., Dewey et al., 1989; Handy et al., 2015; Schmid et al., 1996).

The shear zone that eventually formed the basal thrust of the Maggia-Adula nappe was initiated in the region of the *mélange* unit that now forms the Cima Lunga unit and the Mergoscia zone (*figure 3.12B* and *3.12C*). Hence, the Cima Lunga unit and the Mergoscia zone were strongly sheared during the overthrusting and exhumation of the Maggia-Adula nappe (*figure 3.12C*). Due to the mechanical heterogeneities as well as the intense and partly strongly localized deformation during overthrusting, the local pressure values likely deviated from the lithostatic pressure estimates (e.g., Moulas et al., 2019; Schmalholz & Podladchikov, 2013). However, the magnitude of such pressure deviations is difficult to constrain and remains disputed (e.g., Pleuger & Podladchikov, 2014; Schenker et al., 2015;

Tajčmanová et al., 2021). For example, in the Cima Lunga unit, the differential stresses (*figure 3.12C*) may have locally caused significant tectonic pressures and shear heating around the rheological anomalies of mafic and ultramafic eclogites (Corvò et al., 2021; Maino et al., 2021; Schmalholz et al., 2014). Indeed, HP, HT and chemical variations within the Cima Lunga unit are concentrated around and within the ultramafic and eclogitic bodies. Corvò et al. (2021) show that these variations reflect a heterogeneous metamorphism which is locally developed rather than locally preserved, invoking local tectonic pressures and shear heating.

The overthrusting and exhumation of the Maggia-Adula nappe continued until 31 Ma and generated the syn-thrusting migmatites along the Maggia-Adula basal shear zone and the intense folding of the Cima Lunga unit. The frontal part of the Maggia-Adula nappe reached upper crustal levels at 31.4 ± 0.9 Ma (Rb-Sr geochronology; Ring & Glodny, 2021), where tangential top-to-E normal faults facilitated the uplift of the nappe. At the same time, thrusting of the Simano nappe was active deeper in the crust, at ca. 550 °C (Boston et al., 2017; Gieré et al., 2011; Janots et al., 2009). More southward, the upwelling of migmatites along the SSB began a long-lasting melting history (Rubatto et al., 2009). This upwelling is likely responsible for the exhumation of other (U)HP lenses at the Alpe Arami and Monte Duria (*figure 3.12D*; e.g., Hermann et al., 2006). These pulses of uprising melt continued until 22 Ma, when new fluid influxes and melting (Gregory et al., 2012; Rubatto et al., 2009) were accompanied by dike intrusions in the portions of the nappes close to the SSB (*figure 3.12E*; this study; Gebauer, 1996). At this stage, the underplating of more internal units (e.g., Leventina and Gotthard nappes) accompanied the uplift and cooling of the whole nappe edifice, reflected in the U-Th-Pb monazite ages until ca. 19 Ma (Boston et al., 2017). Along the NSB, the peak T metamorphism may indeed be related to the underplating of the hot lower units with their sedimentary cover, documented from 25 Ma (Berg et al., 2013) to ca. 20 Ma (e.g., Berger et al., 2011; Janots et al., 2009; Wiederkehr et al., 2008).

3.5.4.2 Heat transfer mechanisms

In our interpretation, a significant amount of heat can be advected due to exhumation and emplacement of the Maggia-Adula nappe (*figure 3.12*). A simple method to estimate the relative importance of advection and diffusion (conduction) during heat transfer is the application of dimensional analysis and the calculation of dimensionless numbers (e.g., Duprat-Oualid et al., 2015; Turcotte & Schubert, 2014).

For example, the Péclet number quantifies, to first order, the relative contribution of advection and diffusion. The Péclet number is calculated as: $Pe = (h \cdot v) / D$, where h is the thickness of the nappe, v is the velocity of emplacement and D is the thermal diffusivity (England & Thompson, 1984; Molnar

& England, 1990). Typical values of D for rocks are approximately 10^{-6} m²/s (e.g., Turcotte & Schubert, 2014). Based on our field studies, we estimate ca. 7 km for the thickness, h , of the Maggia-Adula nappe. To estimate v , we assume that the exhumation of the Maggia-Adula nappe started at ca. 38 Ma (Herwartz et al., 2011; Sandmann et al., 2014; *figure 3.12C*), until ca. 31 Ma (*figure 3.12D*). The Alpine eclogites and ultramafics reached pressures of ca. 1.7-2.2 GPa (Dale & Holland, 2003; Herwartz et al., 2011), which corresponds to ca. 65-80 km depth considering lithostatic pressures and a rock density of 2700 kg·m⁻³, and were exhumed to ca. 20 km depth (0.55 GPa; Herwartz et al., 2011). Since deviations from lithostatic pressure are supported by many authors as a possible mechanism acting in a subduction geodynamic scenario (e.g., Pleuger & Podlachikov, 2014; Schenker et al., 2015), we consider a slightly reduced vertical exhumation (ca. 10 km less than the purely lithostatic depth calculation). Assuming a subduction zone with ca. 45-degree dip (*figure 3.12C*), a vertical exhumation of ca. 60 km corresponds to an oblique exhumation along the subduction zone of ca. 85 km. An exhumation along 85 km within 7 Ma provides a velocity of ca. 1.2 cm/yr. A faster velocity of ca. 2.8 cm/yr is obtained if we assume exhumation within only 3 Ma, as was considered by Piccoli et al. (2021) for the Cima Lunga unit on the basis of U-Pb SHRIMP zircon dating of Hermann et al. (2006) obtained on Monte Duria garnet-peridotite. Velocities of 1.2 and 2.8 cm/yr, a thickness of 7 km and a diffusivity of 10^{-6} m²/s yield values of the Péclet number of 2.7 and 6.2, respectively. Such values of Pe , somewhere between 1 and 10, show that advection is dominating heat transfer over diffusion, but also that diffusion is still significant to heat the underlying Simano nappe during thrusting. Such syn-tectonic diffusion can generate isograds cross-cutting the nappe boundaries (see results of thermo-kinematic numerical models in *figures C.1* and *C.2* of *Appendix C*). For comparison, values of Pe for subducting oceanic slabs, where isotherms are nearly parallel to the slab boundaries because of insignificant diffusion, are typically between 100 and 300, mainly due to larger values of h , representing the thickness of an entire slab, and faster values of v up to 10 cm/yr.

The syn-tectonic partial melting may be supported by a potential localized heat surplus along the main Maggia-Adula basal shear zone and inside the deforming nappes, which could be explained by the heat production related to shear heating (Burg & Gerya, 2005). Many studies suggested that shear heating might produce enough heat to contribute to Barrovian T between 500 and 700 °C (e.g., Burg & Gerya, 2005; Burg & Schmalholz, 2008; Duprat-Oualid et al., 2015; Hartz & Podlachikov, 2008; Maino et al., 2015, 2020; Nabelek et al., 2010; Souche et al., 2013), and shear heating is not negligible along the subduction plate interface (England & Smye, 2022; Smye & England, 2022). However, the contribution of shear heating is still debated (Mako & Caddick, 2018; Platt, 2015; Todd & Engi, 1997). The relative importance of shear heating and diffusion can be estimated with the Brinkman

number, which can be calculated as: $Br = (\eta \cdot v^2)/(k \cdot T)$, where η is the effective rock viscosity, k is the thermal conductivity and T is the representative ambient temperature (Brinkman, 1951; Kiss et al., 2019; Yuen et al., 1978). Values of Br are more difficult to estimate than values of Pe because Br depends on η and its value can vary by several orders of magnitude depending on which flow laws are assumed. Furthermore, values of η can vary significantly within the exhuming and overthrusting nappes due to lithological heterogeneities. For example, recent numerical simulations of Vaughan-Hammon et al. (2022) show variations in η in the exhuming rock units between 10^{19} and 10^{22} Pa·s. Assuming $k = 2.5$ W/m·K, $T = 873$ K and $v = 2$ cm/yr, then $\eta = 10^{19}$ Pa·s yields $Br = 0.002$ and $\eta = 10^{22}$ Pa·s yields $Br = 1.8$. Shear heating should not be completely neglected for heat transfer if $Br > 0.1$, which means that $\eta > 10^{21}$ Pa·s is required for shear heating to be able to contribute to the heat transfer. The applied formulation of Br assumes a constant velocity. However, magnitudes of v can have a temporary significant variation, for example, during episodic aseismic (/seismic) slip events. Furthermore, the applied formulation of Br does not consider the thickness of the deforming zone or the magnitude of the deviatoric stress, τ . An alternative formulation is $Br = (\tau^2 \cdot h^2)/(k \cdot T \cdot \eta)$, which is also referred to as the Gruntfest number (e.g., Kiss et al., 2019), and assumes a constant stress inside a deforming region with a specific thickness. Assuming $h = 7$ km, $k = 2.5$ W/m·K, $T = 873$ K, $\tau = 50$ MPa and $\eta = 10^{20}$ Pa·s, the formulation yields $Br = 0.56$. Larger values of η yield smaller values of Br in this formulation because τ is kept constant. Moreover, another formulation for Br without η is $Br = (\tau \cdot e \cdot h^2)/(k \cdot T)$ where e is the shearing rate (e.g., Kiss et al., 2019). Using the same values as before, $e = 10^{-13}$ s⁻¹ provides $Br = 0.11$. For the assumed values, the magnitude of viscous dissipation, which is the product of stress times shearing rate, $\tau \cdot e = 5 \cdot 10^{-6}$ W/m³. Consequently, if the viscous dissipation inside the nappes during overthrusting is on average larger than approximately $5 \cdot 10^{-6}$ W/m³, then shear heating likely impacts heating and the metamorphism. For comparison, the mean value of radiogenic heat production in granites is $3.7 \cdot 10^{-6}$ W/m³ (e.g., Hasterok & Webb, 2017). Estimating the relative importance of shear heating based on the magnitudes of viscous dissipation likely provides the most robust estimate, because it does not depend on the rock viscosity, which is highly uncertain, as mentioned above, and due to its dependence on mineral composition, fluid content, or grain size. However, due to the many uncertainties and the only first-order estimates from dimensional analysis, more elaborated methods must be applied to quantify the impact of shear heating.

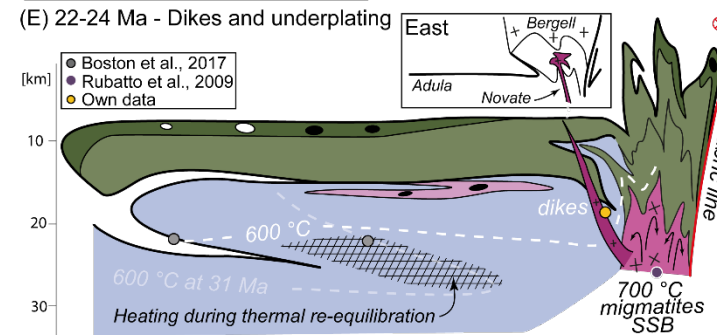
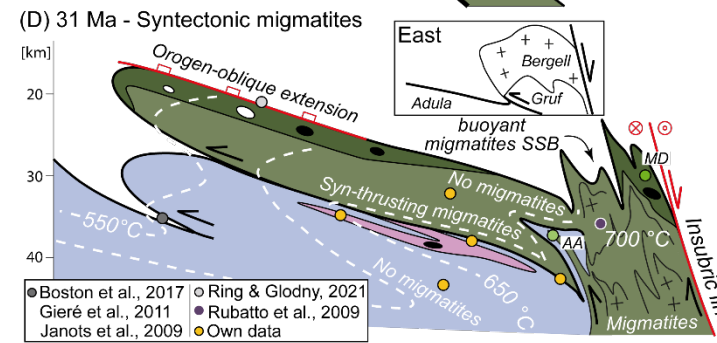
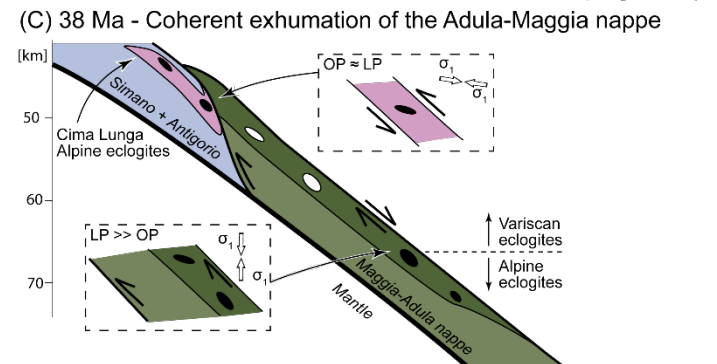
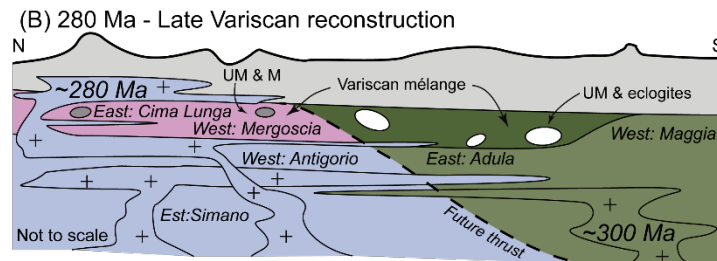
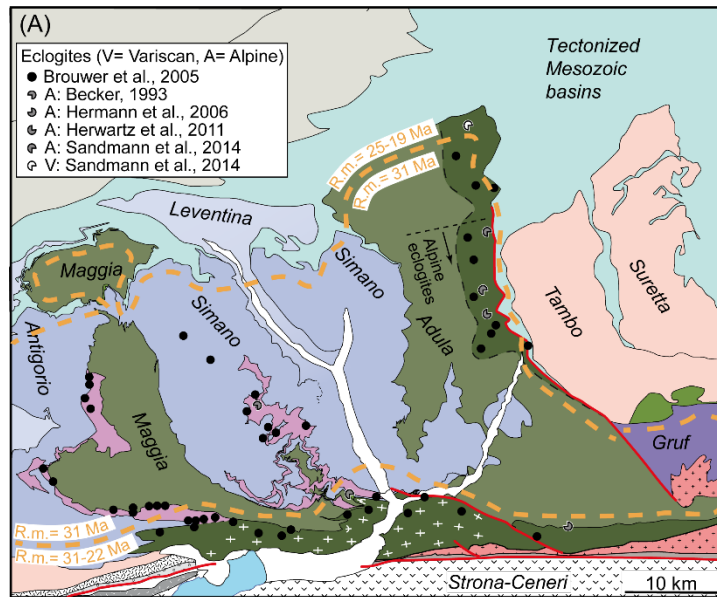


Figure 3.12. *Geodynamic evolution of the Lepontine nappes. References for depth- and T-estimates, and literature ages are mentioned in the main text. (A) Tectonic map of the Lepontine area. The orange dashed lines delimit the areas with common coeval regional metamorphism (R.m.). Note that the area delimited by the 31 Ma peak regional metamorphic event coincides with the area of distribution of the constant NW-SE oriented mineral lineation (c.f. with figure 3.1B). The Cima Lunga unit and the Mergoscia zone are indicated in violet. The dots indicate eclogites (see legend in the figure). (B) Paleogeographic reconstruction in Permian time of the crust prior to the Alpine cycle. This subplot shows the magmatic relations between Permian granitic bodies and the basement. Mafic (M), ultramafic (UM) and eclogitic bodies are indicated with white and gray ellipses. (C) Beginning of overthrusting during the coherent exhumation of the Maggia-Adula nappe over the Simano and Antigorio nappes. The position of the Cima Lunga unit corresponds to the main shear zone. Shear senses and related local stress fields are indicated in the dashed squares (OP: overpressure, LP: lithostatic pressure). Eclogites are indicated with ellipses: black for Alpine eclogites and white for Variscan eclogites. (D) Internal structure of the Lepontine nappe stack at the regional peak Barrovian conditions at 31 Ma. The white dashed lines are the indicative isotherms. In the box: section of the eastern sector, after Galli et al. (2012). AA: Alpe Arami; MD: Monte Duria. (E) Overall thermal re-equilibration of the Lepontine dome. The relaxation of the isotherms (c.f. the white dashed line with the dashed line in transparency) corresponds to local heating. In the box: section of the eastern sector, the age of Novate granite is after Liati et al. (2000).*

3.6 Conclusions

We applied a combined approach including detailed geological mapping, multi-scale structural analysis, U-Pb zircon dating (LA-ICP-MS and SIMS ion probe analyses) and geochemistry to better constrain the tectono-metamorphic processes responsible for the Barrovian metamorphism of the Lepontine dome. Based on our results, we propose the following conclusions:

1. The regional Barrovian metamorphic event in the Lepontine dome occurred at ca. 31 Ma together with the peak T conditions manifested by the regional occurrence of migmatites along the major Maggia-Adula shear zone inside the dome, and a penetrative lineation all over the dome. These migmatites indicate a peak T of at least 650 °C. The younger U-Th-Pb monazite ages until ca. 22 Ma from previous studies throughout the Lepontine dome at lower T of ca. 600 °C result from the thermal re-equilibration of the nappe pile after the thermal peak at ca. 31 Ma. In contrast, only in the southern part of the dome, along the SSB, published migmatite ages indicate continuous Barrovian high temperatures greater than 650 °C between 31 and 22 Ma. These migmatites injected melts at 22-24 Ma into the close surroundings.
2. The Cima Lunga unit is not an Alpine tectonic mélange and does not consist of Mesozoic meta-sedimentary rocks. We suggest that the Cima Lunga unit was a pre-Variscan sedimentary sequence that was intruded by Permian magmas, which are the protoliths of the orthogneisses of the Simano nappe. This hypothesis is based on (i) the absence of Variscan and younger zircon detrital ages (< ca. 400 Ma) within the Cima Lunga unit and the Simano nappe, (ii) the Variscan (ca. 300-320 Ma) metamorphic zircon rims around detrital zircon

grains in the Cima Lunga paragneisses, (iii) the ca. 280 Ma zircon magmatic ages of continuous orthogneissic horizons (likely intruded as sills) within a calc-schist-bearing sequence of the Cima Lunga unit and (iv) the protoliths of the ophiolitic fragments within the Cima Lunga unit which are older than Cambrian, as shown by previous studies. Therefore, we suggest that the rocks forming the Cima Lunga unit and the Simano nappe belonged to the same Permian crustal unit.

3. We suggest a single Alpine Maggia-Adula nappe. This correlation is mainly based on (i) the same structural position of the actual Adula and Maggia nappes in the tectonic pile, (ii) the same U-Pb metamorphic zircon ages in syn-tectonic migmatites along the basal Maggia-Adula shear zone, (iii) the same kinematics, and (iv) lithological affinities, such as similar ages of pre-Alpine intrusions.

We further correlate the Antigorio nappe with the Simano nappe and the Mergoscia zone with the Cima Lunga unit. The Mergoscia zone and Cima Lunga unit were presumably located in the upper regions of the Late Variscan crustal units which form the Antigorio and Simano nappes, respectively. Consequently, we explain the first-order nappe structure of the Lepontine dome with a single exhumation and overthrusting event that ended at ca. 31 Ma. The more deeply subducted Maggia-Adula nappe was thrust over the shallower Simano-Antigorio nappe. During overthrusting, the Mergoscia zone and the Cima Lunga unit were strongly deformed along the basal shear zone of the Maggia-Adula nappe. The subsequent up-arching of the Lepontine dome, the intense deformation along the SSB and erosion caused the present-day geographical separation of the Maggia and Adula nappes.

4. Finally, the heat of the Barrovian metamorphism of the Lepontine dome derives mainly from heat advection associated with exhumation and thrusting of the Maggia-Adula deeper nappe over the shallower Simano-Antigorio nappe. Heat diffusion during nappe emplacement caused isograds cross-cutting the major nappe boundary between the Maggia-Adula and Simano-Antigorio nappes. Shear heating along this basal shear zone and inside the overthrusting nappe may have contributed to Barrovian heating.

Acknowledgements

The authors thank Tarryn Cawood and Michel Ballèvre for their very detailed and constructive reviews, and Whitney Behr for the editorial handling. The authors further thank Benita Putlitz and Michelle Foley for the help in the laboratories of UNIL, Maria Giuditta Fellin for the access to ETH Zurich laboratories, Anne-Sophie Bouvier and Daniela Rubatto for the preparation and treatment of raw SIMS analyses, Daphné Giacomazzi for the help during field work, and swisstopo for the opportunity to work on the production of the new Swiss National Map. This work was supported by the Swiss National Science Foundation Grant n°182041, SUPSI project n°12RAFGOSO and n°12RA1CARTOTIGR.

Chapter 4

FAST AND SPATIALLY HETEROGENEOUS COOLING RATES AT AMPHIBOLITE-FACIES CONDITIONS REVEAL THE SIGNIFICANCE OF LOCAL HEAT SOURCES: A CASE STUDY FROM THE LEPONTINE ALPS (SWITZERLAND)

A. Tagliaferri^{1,2}, E. Moulas³, S. M. Schmalholz² and F. L. Schenker¹

¹*Institute of Earth Sciences, University of Applied Sciences and Arts of Southern Switzerland (SUPSI), CH-6850 Mendrisio, Ticino, Switzerland.*

²*Institute of Earth Sciences, University of Lausanne (UNIL), CH-1015 Lausanne, Vaud, Switzerland.*

³*Institute of Earth Sciences, Johannes Gutenberg-Universität Mainz, D-55128 Mainz, Deutschland.*

This chapter is under review for the American Journal of Science.

Abstract

The Lepontine dome (Central European Alps) is a metamorphic and structural dome formed by the accretion of crystalline-basement nappes during continental collision and characterized by regional Barrovian metamorphism. Peak amphibolite-facies conditions coincide with the final stages of nappe-emplacement at ca. 31 Ma, constrained through U-Pb zircon dating of syn-tectonic migmatites along the major Maggia-Adula shear zone.

Although the age of the temperature peak is well-constrained, the duration of subsequent cooling remains unclear. Here, we examine garnet rim compositional re-adjustment and employ inverse diffusion modelling to estimate the apparent cooling rates from Lepontine dome rocks. We compare our results to cooling rates calculated using simple thermal models. This comparison allows the identification of regional patterns that can be related to orogenic processes.

Six garnet paragneisses were selected at different tectonic levels within the nappe pile. Garnet crystals are pre- to syn-kinematic with respect to the amphibolite-facies metamorphic foliation and display at their rim coupled Mn-increase and Mg-decrease, indicative of retrograde reactions. Using rim compositions, geothermobarometry estimates place the post-peak temperatures of re-equilibration between 577-661 °C at pressures between 0.5-1.3 GPa.

The cooling rates exhibit spatial variability across the study area. The main shear zone shows significantly higher cooling rates, ranging from 100 to 400 °C/Myr, while the footwall exhibits a much lower rate of approximately 2 °C/Myr. Additionally, the migmatitic belt bordering the Lepontine dome to the south displays cooling rates between 20-50 °C/Myr.

Our results suggest that the high cooling rates at approximately 635 °C and 0.8 GPa observed in the main thrust cannot be attributed to regional exhumation processes, even when considering high exhumation velocities. In the middle and lower crust, apparent cooling rates greater than approximately 50 °C/Myr are likely caused by additional local heat sources beyond regional heating, such as percolation of hot fluids or shear heating.

4.1 Introduction

Barrovian metamorphism typically involves rock recrystallization at conditions that are characterized by relatively high temperatures and relatively low pressures. These apparent metamorphic field gradients are 100 to 200 °C hotter than the expected values in the Earth's crust (c.f. [Brown, 2014](#)). Their difference from a normal geothermal gradient can be explained if one considers additional sources of heat during metamorphism (e.g., [Jamieson et al., 1998](#); [Ryan & Dewey, 2019](#); and references therein). During collisional orogeny, metamorphic rocks are placed at larger depths and are eventually heated from the Earth's mantle. Previous studies have also suggested that the deep accretion of crustal rocks, which are rich in radiogenic elements, can contribute to the heat budget of collisional orogens ([Huerta et al., 1999](#); [Engi et al., 2001](#)). However, the conductive thermal timescale requires tens of millions of years to heat the metamorphic rocks at temperatures typical of amphibolite-facies conditions ([Thompson & England, 1984](#); [Huerta et al., 1999](#)). In addition, thermal models that account only for heat conduction, are not always able to explain the spatial distribution of high-grade metamorphic rocks ([Stüwe, 1998](#)). For this reason, researchers have suggested that the heat generated during dissipative deformation (shear or strain heating) may contribute significantly to the heating of collisional orogens ([Burg & Gerya, 2005](#); [Hartz & Podladchikov, 2008](#); [Stüwe, 1998](#)). In contrast to other regional heating mechanisms, local heat sources have thermal histories that are characterized by fast cooling rates at relatively high-grade metamorphic conditions, as shown by thermo-mechanical models ([Stüwe & Ehlers, 1998](#); [Burg & Moulas, 2022](#)). This distinguishing feature can be used to decipher the nature of orogenic heat during collisional orogeny.

Here, we use inverse multicomponent diffusion modelling in garnet crystals from metamorphic rocks to study the thermal evolution of the Lepontine dome in the Central European Alps, Switzerland. Our samples were collected from different structural positions in the deformed metamorphic nappe pile. We performed conventional thermobarometry in combination with inverse diffusion modelling to constrain the apparent cooling rates relevant to the post-peak metamorphic conditions. Considering a spherical garnet crystal with a radius of 0.1 mm, typical diffusivity values for Mg in garnet result in closure temperatures of about 550-600 °C (c.f. [Cygan & Lasaga, 1985](#)). This means that garnet diffusion for Mg is essentially negligible below 500 °C. Therefore, our values for the apparent cooling rates can be used as approximations for the cooling rates of the Lepontine metamorphic rocks when they were experiencing temperatures in the range of 500-660 °C. The information on the degree of cooling in

combination to the pressure and temperature (P-T) conditions of metamorphism can be used to provide us with information regarding the geodynamic environment and the metamorphic processes involved.

In this contribution we present the geological framework and the rationale of the garnet inverse multicomponent-diffusion modelling approach, followed by a brief description of the adopted methodology. Results comprise a multi-scale description of analyzed samples, mineral chemistry evaluation, geothermometry estimates, cooling rates, and thermal model outcomes. A final discussion highlights the implications of our new results on understanding the Lepontine dome's heat budget. Our results suggest that the fast apparent cooling rates obtained in the uppermost structural levels of the nappe pile, within a major shear zone, are likely the result of local heat sources such as viscous shear heating.

4.1.1 Geological overview

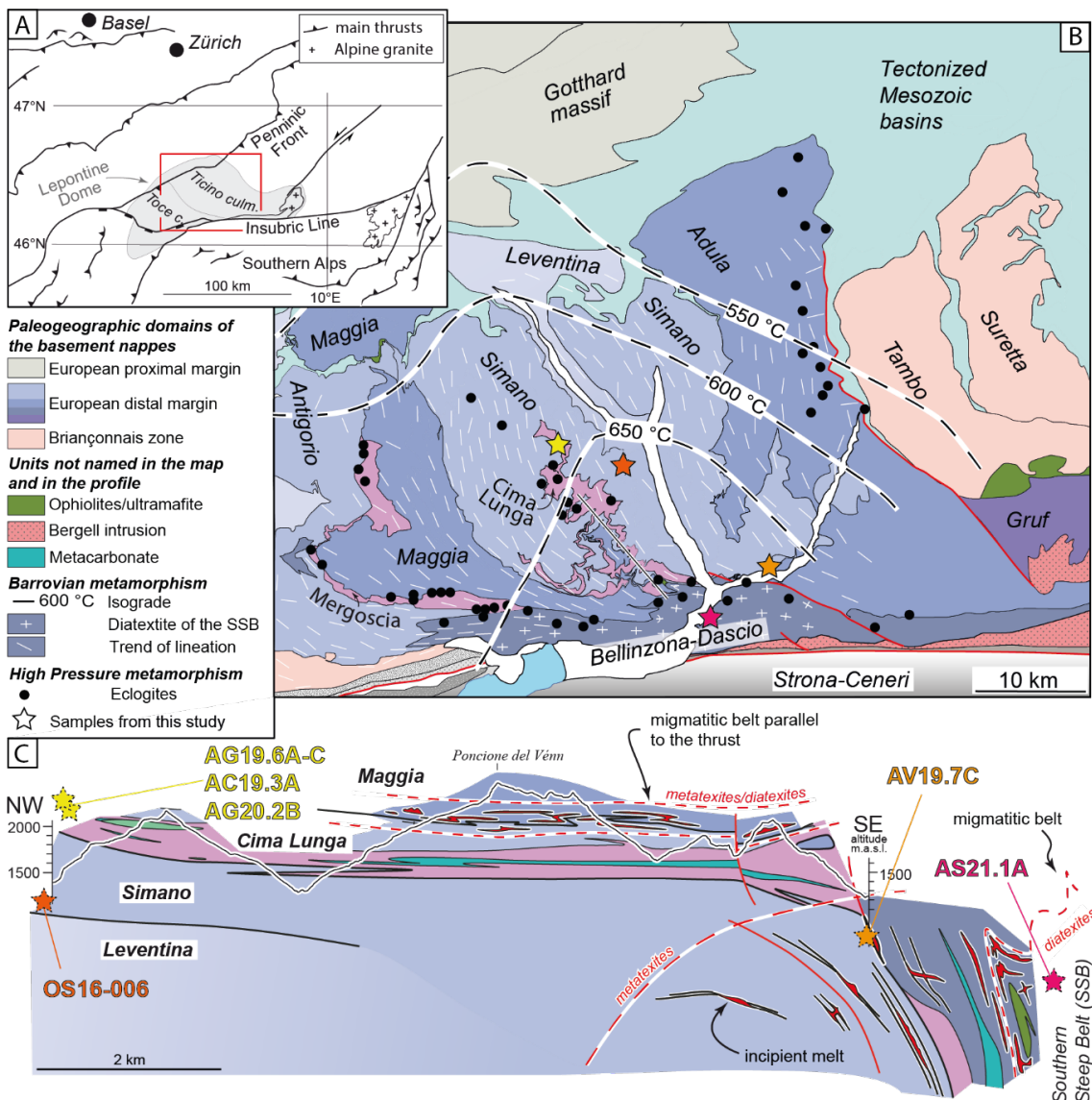


Figure 4.1. Tectonic overview of the Lepontine area and location of samples from this study. (A) Location of the studied area (Ticino culmination of the Lepontine dome) in the Central Alps (modified after Burg & Gerya (2005)). (B) Tectonic map of the Ticino culmination (modified after Brouwer et al. (2005); Cavargna-Sani et al. (2014b); Corvò et al. (2021); Maino et al. (2021); Steck et al. (2013); Tagliaferri et al. (2023); Todd & Engi (1997); Wenk (1955)). (C) Simplified tectonic profile through the central domain of the Ticino culmination.

The Lepontine dome is part of the Penninic domain of the Central European Alps (Switzerland). It is a metamorphic and structural dome characterized by a Barrovian overprint expressed by concentric mineral isograds (e.g., Frey & Ferreiro Mählmann, 1999; Nagel, 2008; Todd & Engi, 1997; Trommsdorff, 1974; Wenk & Keller, 1969; *figure 4.1*). The mineral isograds indicate progressively higher temperature conditions to the south, where the area is bordered by the migmatites of the Southern Steep Belt (SSB; Burri et al., 2005; Gebauer, 1994, 1996; Rubatto et al., 2009). Peak temperatures that have been reported for the metamorphic rocks of the southern margin are ca. 700 ± 50 °C (Burri et al., 2005).

The Lepontine dome is subdivided into two subdomes: to the west the Toce culmination and to the east the Ticino culmination. The internal structure of the Ticino culmination has been described as a tectonic nappe pile (e.g., Dal Vesco, 1953; Maxelon & Mancktelow, 2005; Steck et al., 2013). The nappe stack comprises the Leventina nappe at the bottom, which was overthrust to the north by the Simano nappe. To the west, the Simano nappe is overlaid by the Cima Lunga unit (upper portion of the Simano nappe; Tagliaferri et al., 2023), and to the east by the Adula nappe. To the north, the Simano nappe is in contact with the Maggia nappe. In earlier works, the Adula nappe is referred to as “Adula-Cima Lunga nappe”, putting these two units tectonically together (Dal Vesco, 1953; Trommsdorff et al., 2000). However, the structural relationships of the upper part of the nappe pile have been redefined in the recent study of Tagliaferri et al. (2023). According to Tagliaferri et al. (2023), the tectonic nappes are separated by a major thrust, named Maggia-Adula shear zone. In their interpretation, the Cima Lunga unit lies within the shear zone and belongs to the upper part of the Simano nappe, which was overthrust by the Maggia-Adula nappe.

The tectonic nappe boundaries are locally intersected by metamorphic isograds (*figure 4.1*). This structural relation has been frequently considered as evidence of a heating event that occurred after the end of nappe emplacement (e.g., Frey et al., 1999; Nagel, 2008; Todd & Engi, 1997; Trommsdorff, 1974; Wenk & Keller, 1969; Von Blanckenburg & Davies, 1995). However, using thermo-kinematic models and field relations, Tagliaferri et al. (2023) have re-evaluated the cross-cutting relationship between the isograds and the nappe boundaries. As a

consequence, these authors suggested that such intersections are the result of heat conduction during the emplacement of a relatively hot nappe (Maggia-Adula nappe). In other words, heat conduction occurring simultaneously with tectonic movements is sufficient to create isograds that intersect nappe boundaries. Hence, a separate heating event after nappe emplacement is not necessarily required. Additional local heat sources such as shear heating (i.e., heating due to dissipated mechanical work) may have contributed to the final metamorphic pattern of the Lepontine dome. However, the contribution of such local heat sources remains unclear.

The rocks which constitute the Lepontine basement nappes are mostly gneissic rocks, minor calcschists and marbles, with scarce occurrences of mafic and ultramafic rocks (e.g., [Becker, 1993](#); [Corvò et al., 2021](#); [Evans et al., 1979](#); [Maino et al., 2021](#); [Pfeifer, 1981](#); [Buchmann, 1953](#); [Preiswerk, 1918](#); [Della Torre et al., 2015](#); [Cavargna-Sani et al., 2014a](#); [Jenny, 1923](#); [Nagel, 2008](#)). The metamorphic foliation of these gneissic rocks defines a dome shape, whereas the mineral and stretching lineation in amphibolite-facies has a constant NW-SE direction all over the area. The formation of the lineation has been proposed to be coeval with nappe emplacement and with the generation of syn-tectonic alpine migmatites along the main Maggia-Adula thrust zone ([Tagliaferri et al., 2023](#)).

The late stage of nappe emplacement corresponding to the Barrovian overprint as a main regional event has been dated at 31-33 Ma (e.g., SHRIMP II U-Pb zircon dating in [Galli et al. \(2012\)](#); SHRIMP U-Pb dating in [Gebauer \(1996\)](#); [Herwartz et al. \(2011\)](#); [Nagel \(2008\)](#); SHRIMP U-Pb zircon dating in [Liati et al. \(2009\)](#); LA-ICP-MS and SIMS U-Pb zircon dating in [Tagliaferri et al. \(2023\)](#)). Furthermore, extensive dating has been performed all over the Lepontine area (e.g., [Boston et al., 2017](#)) and in the SSB, where the peak temperature metamorphism is interpreted to have lasted for 10 Ma (from 32 until 22 Ma; allanite U-Th-Pb SHRIMP in [Gregory et al. \(2012\)](#); zircon U-Pb SHRIMP in [Rubatto et al. \(2009\)](#)).

Despite the broad application of different dating techniques, the regional heating scenarios affecting the Lepontine dome are still controversial. The peak temperature is interpreted to have occurred at ca. 31 Ma by using U-Pb zircon dating (see references above). However, monazite U-Pb ages around 22-23 Ma ([Köppel & Grünenfelder, 1975](#)) are considered to record close-to-peak conditions ([Boston et al., 2017](#)). This can be explained with a general regional cooling (and local heating) scenario ([Tagliaferri et al., 2023](#)), or as the effect of a second thermal event within the Lepontine dome ([Berger et al., 2011](#)).

4.1.2 Application of inverse multicomponent-diffusion modelling in garnet

The investigated metamorphic rocks from the Lepontine dome are garnet-bearing metapelites. In these rocks, garnet exhibits evidence of chemical zonation (*figure 4.2B*). The presence of concentration gradients in silicate minerals, such as garnet, has been extensively used in inverse diffusion modelling ([Chakraborty, 2006](#)). Over the last two decades, several applications of major-element diffusion in garnet have been proposed. These applications can be broadly separated into three categories: (i) models that consider the fractionation of mass during garnet growth (e.g., [Caddick et al., 2010](#); [Galli et al., 2011](#); [Gieré et al., 2011](#)), (ii) models that consider the diffusional relaxation of sharp compositional features (e.g., [Ague & Baxter, 2007](#); [Ague & Carlson, 2013](#)) and, (iii) models that consider the near-rim diffusional modification of garnet composition (e.g., [Weyer et al., 1999](#); [Hallett & Spear, 2011](#); [Burg & Moulas, 2022](#)). In the first category, the major-element fractionation during garnet growth, and the multicomponent diffusion in garnet are modelled simultaneously. Thereby, the initial concentration profile is created in a self-consistent way. However, the kinetic factors responsible for garnet crystal growth are commonly poorly constrained (exact shape of pressure-temperature history, degree of metamorphic overstepping, availability of fluids etc.). In addition, the uncertainties of such models can be very large when poly-metamorphic rocks are investigated, which is the case of the Lepontine dome where poly-orogenic garnet crystals have been dated ([Sandmann et al., 2014](#)). In the second approach, an initial chemical zonation is assumed, and forward models of garnet diffusion are evaluated to constrain the thermal history of the metamorphic rocks. This approach seems to have the least assumptions, but it is difficult to distinguish between the diffusion that occurred before, during, or after the peak temperatures. In the third approach, that we follow here, the post-peak thermal evolution of the metamorphic rock is constrained by modelling the last diffusional modification of the rim composition. Thus, this approach can be used to estimate the cooling rate at temperature (T) values that are smaller than the peak temperature but are still larger than the closure temperature. The high closure temperature of major-element diffusion in garnet makes this method complementary to other, low-T thermochronology methods (c.f. [Braun et al., 2006](#)).

In all the three aforementioned model categories, uncertainties in the temperature history have a significant effect on the estimates of diffusional timescales and cooling rates. However, the near-rim compositional modification in garnet is commonly the result of two processes, (i) the retrograde Fe-Mg ion exchange between garnet and an adjacent Fe-Mg bearing phase and, (ii) retrograde consumption of garnet at the advantage of another phase (e.g., [Kohn, 2014](#)). In the

case of high-grade metapelites, it is typical to observe the consumption of garnet at the advantage of biotite during the cooling from peak T conditions (e.g., [Tracy et al., 1976](#); [Florence & Spear, 1995](#)). This process eventually leads to the high concentration of Mn at the garnet outer rims due to the high compatibility of Mn in garnet with respect to biotite (e.g., [Weyer et al., 1999](#); [Kohn & Spear, 2000](#)). The presence of garnet and biotite in combination to chemical zonation in garnet allows to couple multicomponent diffusion in garnet with conventional geothermometry. With such an approach, the uncertainty of the initial temperature used in the cooling rate estimates is minimized. The near-rim compositions of garnet and biotite will result in temperature estimates that will generally be lower than the peak T conditions inferred by other methods (e.g., [Burg & Moulas, 2022](#)). Information about the cooling rates of metamorphic rocks at various temperature conditions provides important constraints on geodynamic models (e.g., [Schlunegger & Willet, 1999](#)). In particular, in the framework of thermal models, the large cooling rates at relatively high temperatures have been used to suggest the presence of local heat sources ([Stüwe & Ehlers, 1998](#); [Burg & Moulas, 2022](#)).

4.2 Methodology

Samples were mostly collected during the fieldwork for the realization of the new large-scale geological maps n°1273 – Biasca, n°1293 – Osogna, and n°1294 – Grono of the Swiss National Map 1:25.000 (mapping at scale 1:10.000), which we produced at the University of Applied Sciences and Arts of Southern Switzerland (SUPSI) for swisstopo.

We selected six amphibolite-facies garnet paragneisses at different tectonic levels of the nappe pile ([figure 4.1C](#), [table 4.1](#)). We collected four samples at the base of the main Maggia-Adula shear zone: *AG19.6A* and *C*, *AC19.3A*, *AG20.2B* within the Cima Lunga unit; *AV19.7C* at the contact between Adula and Simano nappes, closer to the SSB. These two regions have been the object of study in the previous work of [Tagliaferri et al. \(2023\)](#). Furthermore, we collected sample *OS16-006* at the base of Simano nappe, at lower tectonic levels, approximately 800-1000 m beneath the Cima Lunga unit, and sample *AS21.1A* within the SSB.

Sample – Profile <i>Locality</i>	Tectonic location	Swiss grid coordinates (CH1903+/LV95)		Mineral assemblage	Geothermobarometers				GDIFF	
		E	N		“outer rims”		“inner rims”		outputs	
					T (°C)	P (GPa)	T (°C)	P (GPa)	Δt (Myr)	CR (°C/Myr)
★ AG19.6A – L1-rim <i>Guglia</i>	Upper Simano (Cima Lunga) (Maggia-Adula shear zone)	2708804	1132391	grt, qtz, feld, bt, wm, chl, ky, st, zr, ep, rt, ap, ox	619	0.71	664	0.81	0.25	100
★ AG19.6C – L2 <i>Guglia</i>				642	0.65	670	0.78	0.08	220	
★ AC19.3A – CL1 <i>Pizzo Cramosino</i>		2708057	1134983	qtz, feld, grt, bt, wm, ky, zirc, rt, cord, ep, ox	641	1.3	676	1.5	0.05	400
★ AG20.2B – D10 <i>Cima di Gagnone</i>		2708337	1131193	qtz, feld, grt, bt, chl, zr, rt, cld, ox	623	0.84	673	1.12	0.2	110
★ AG20.2B – D14 <i>Cima di Gagnone</i>				623	0.84	673	1.12	0.12	200	
★ AV19.7C – L1 <i>San Vittore</i>	Upper Simano (Simano-Adula contact)	2728838	1122423	qtz, feld, grt, bt, wm, chl, ky, st, zr, ep, rt, ap, amph, cld, ox	661	0.84	685	0.97	0.25	100
★ OS16-006 – L-rim <i>Iragna</i>	Lower Simano (Simano-Leventina contact)	2716045	1130959	qtz, feld, grt, bt, chl, zirc, ox, Fe- ox	577	0.72	614	0.67	10	2
★ AS21.1A – AL4 <i>Sasso Corbaro castle</i> <i>(Bellinzona)</i>	SSB	2723005	1116465	grt, bt, sill, qtz, ky, pl, wm, rt, ilm, zirc, ox, Fe- ox, cord?	600	0.47	657	0.67	1.1	20
★ AS21.1A – BL2 <i>Sasso Corbaro castle</i> <i>(Bellinzona)</i>				605	0.54	673	0.71	0.5	50	

Table 4.1. Samples’ tectonic and geographic location, mineral assemblage, geothermobarometric estimates and outputs of “GDIFF” diffusion models. T (°C) is calculated with the garnet-biotite geothermometer of [Holdaway \(2000\)](#), P (GPa) is calculated with the GASP geobarometer of [Caddick & Thompson \(2008\)](#) for all samples. The T and P conditions of sample AC19.3A are computed with garnet-phengite thermometer and phengite barometer ([Caddick & Thompson, 2008](#)). “outer rims” refers to the part of the garnet rim closer to the mineral edge and indicates post-peak T conditions. “inner rims” refers to peak T conditions and were calculated using the inner part of the garnet (just before the Mn content increase or garnet core) and matrix phases. “GDIFF” model inputs are the T and P conditions calculated for “outer rims”. The time necessary to diffuse the initial step-function profile to fit the measured profile is Δt in the case of constant- T models.

Thin and thick sections were realized and observed under the optical microscope. We describe in detail their petrography in *Appendix G*. We performed major element analyses with an electron microprobe analyser (EMPA) at the University of Lausanne with a JEOL JXA-8530F HyperProbe, and at the Johannes-Gutenberg University Mainz with a Jeol JXA 8900RL Probe. Mineral analyses used an accelerating voltage of 15 kV and a beam current of 20 nA. All the microprobe analyses are in *Appendix H – folder Microprobe analyses online*.

We also produced X-ray maps which permitted to detect the domains of interest within garnet crystals to set line analyses (*figure 4.2; Appendix I*). The location of profiles was set orthogonal to the garnet rim, coinciding with an observed increase in spessartine component (see *figures 4.2B and 4.2D*). The microprobe profiles shown in *Appendix I* are entirely measured within the garnet rims.

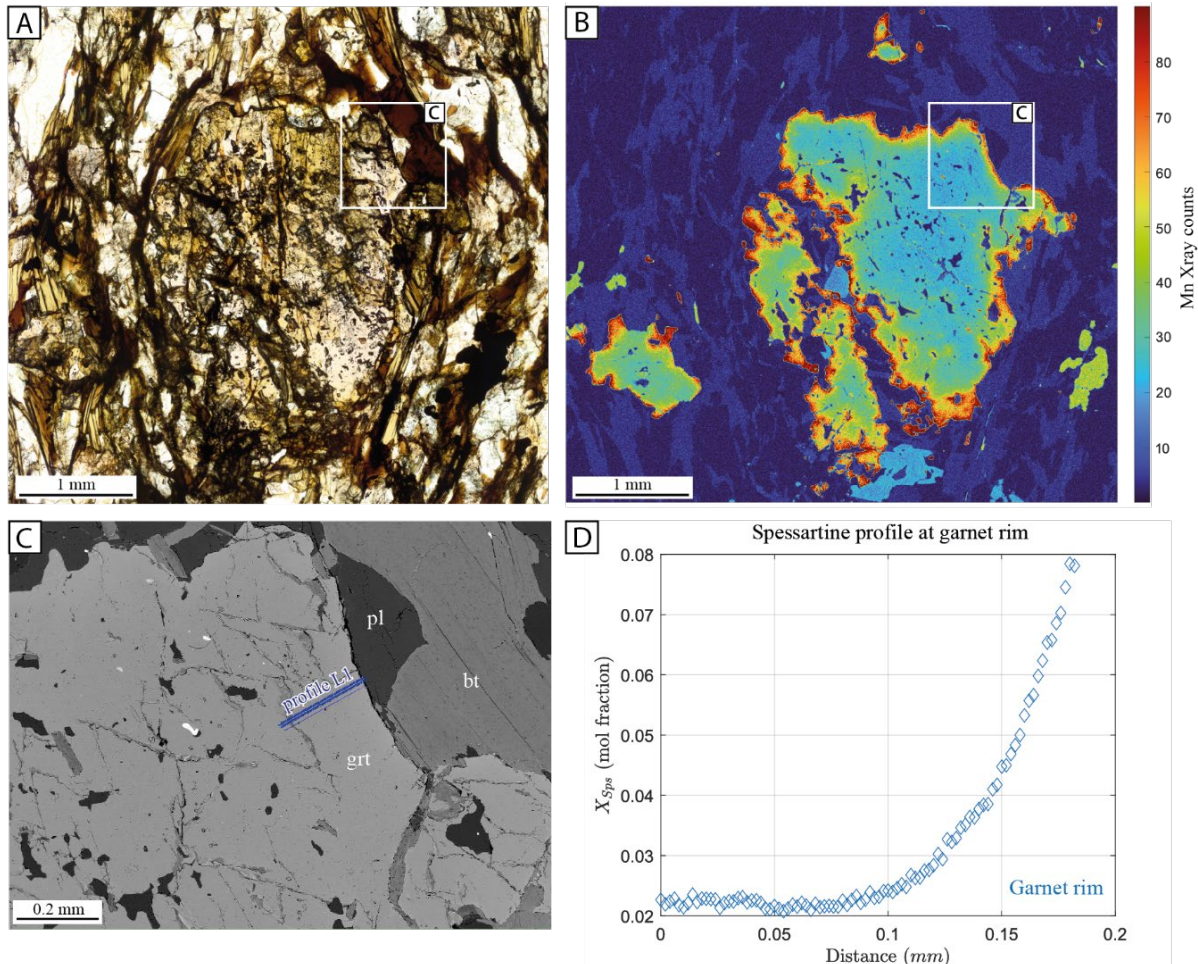


Figure 4.2. Photomicrographs and microprobe data for sample AV19.7C. The photomicrographs and microprobe data for all the analyzed samples are in Appendix I. (A) Photomicrograph of the analyzed garnet. (B) Mn X-ray microprobe map of the analyzed garnet. (C) Microprobe BSE image with location of the analyzed profile L1. Mineral abbreviations are after *Siivola & Schmid (2007)*. (D) Spessartine component on the analyzed garnet profile L1.

We applied thermobarometric calculations (see *Appendix H – GeoTB.xlsx online*) to constrain the peak- and post-peak temperature conditions of the studied metamorphic rocks. The geothermometers and geobarometers applied are the garnet-biotite thermometer of *Holdaway (2000)* and garnet-aluminosilicate-quartz-plagioclase barometer (GASP) of *Caddick & Thompson (2008)* for all samples (*table 4.1*). Garnet-phengite thermometer and phengite barometer of *Caddick & Thompson (2008)* were adopted for sample AC19.3A (*table 4.1*).

Prior to these calculations, we evaluated the abundance of biotite in each sample. The amount of biotite was considered to be significant when the composition of matrix biotite and biotite close to garnet was the same despite the retrograde exchange. This inference is based on the fact that the diffusional modification of biotite due to retrogression was minor and did not change its Mg# ($\frac{Mg}{Mg+Fe}$) significantly (e.g., Spear & Florence, 1992). Therefore, we could use for the calculations of *inner rim* and *outer rim* temperatures (see [table 4.1](#)) one biotite coupled with two different garnet compositions (e.g., respectively in the center and at its rim). In the results ([section 4.3.1](#)) we present chemical compositions used for thermobarometric estimates. The *outer rim* P-T estimates ([table 4.1](#)) are used as initial conditions for our diffusion models.

We set step-like initial conditions (dashed lines in [figure 4.3](#)) that fit the measured microprobe profiles. Since we focus on the post-T-peak metamorphic conditions that resulted in the modification of the outer garnet rims, we considered only the most external diffusion profile of our garnet rims. The step-functions of spessartine, grossular and pyrope were set to mimic the plateau of the measured profiles (c.f. [Ague & Carlson, 2013](#); see [Appendix I](#)), and almandine step-function profile was dependent on the other three components. Since garnet components depend on each other, the uncertainties in setting all the initial steps simultaneously are small. We focused on the spessartine profile (see [figures 4.2D](#) and [4.3](#)), since Mn is the fastest diffusing element in garnet. Thus, we set homogeneous Mn initial conditions and we considered the measured boundary values as boundary conditions in each sample ([figure 4.3](#)).

We computed the diffusional relaxation of the concentration profiles from the initial step-like configuration at the *outer rim* initial conditions and we estimated the apparent cooling rates based on garnet multicomponent diffusion modelling. The garnet diffusion modelling has been performed with the algorithm “GDIFF” of [Moulas \(2023\)](#). This algorithm allows to model diffusion during cooling for all elements and to infer two different quantities depending on the input assumptions. On one hand, if temperature is assumed constant, GDIFF can be used to invert for the duration of diffusion (Δt in [table 4.1](#)). On the other hand, if the initial temperature and a cooling rate are specified, GDIFF can be used to infer a cooling rate (assumed constant; *CR* in [table 4.1](#)). The results for both GDIFF models are reported in [table 4.1](#) and in [Appendix I](#). The results of the T-cooling model are shown in [figure 4.3](#). Since diffusion processes are thermally activated, it is expected that inverse diffusion models that require short apparent durations will also require relative high cooling rates. For the estimation of apparent cooling rates we follow the procedure presented in [Burg & Moulas \(2022\)](#).

4.3 Results

4.3.1 Sample description and mineral chemistry

Sample AG19.6

Sample *AG19.6* is a garnet-paragneiss from the Cima Lunga unit, which has been already described in the work of [Tagliaferri et al. \(2023\)](#). It has no mesoscopic evidence of partial melting, its mineral assemblage is formed by garnet, quartz, feldspar, biotite, white mica, chlorite, kyanite, staurolite, zircon, epidote, rutile, apatite, oxides. Cm-scale pre- to syn-tectonic snowball garnet crystals have multiple growth stages (see thin section *AG19.6A* in *Appendix G* and *I*).

In thin section *AG19.6A*, the largest garnet porphyroblast shows a chemical zonation with core composition: pyrope 6%, grossular 19%, almandine 69%, spessartine 6% (Prp₆Grs₁₉Alm₆₉Sps₆). Ca content is higher in the core (CaO content around 8 wt%), however locally increases at the garnet rim (CaO below 2 wt%, but locally as high as ca. 7.5 wt%). Mg increases towards the rim but drops in a narrow zone at the garnet border (MgO ca. 2.5 wt%), where Mn increases (MnO up to ca. 3.5 wt%). On the analyzed profile L1, the composition of the inner part of the rim (*inner rim*) is Prp₁₆Grs₇Alm₇₆Sps₁, whereas at its rim (*outer rim*) the composition is Prp₁₂Grs₇Alm₇₈Sps₃ (mineral compositions are in *Appendix H*). Average Mg# of biotite next to garnet rim is 0.45, and 0.42 for matrix biotite. XCa of matrix plagioclase varies between 0.18 and 0.26.

In thick section *AG19.6C*, garnet crystals have varying Ca content, while Mg-decrease is associated with Mn-increase at the garnet rim. On the analyzed profile L2, garnet has *inner rim* composition Prp₁₆Grs₇Alm₇₆Sps₁, and *outer rim* Prp₁₄Grs₅Alm₇₈Sps₃. Mg# is 0.44 for biotite next to garnet, whereas 0.41 for matrix biotite. Plagioclase XCa is 0.26.

Sample AC19.3A

Sample *AC19.3A* is a garnet paragneiss belonging to the uppermost tectonic levels of the Cima Lunga unit. At the meso-scale, the foliation is marked by biotite, white mica, kyanite and variable-sized garnet. Garnet-content increments tectonically up-section in the field where micaschists with abundant white mica have garnet crystals up to 2.5 cm in diameter.

The sample contains pre- to syn-kinematic garnet, quartz, feldspar, white mica, biotite, kyanite, staurolite, rutile, zircon, epidote, chlorite, oxides. Garnet rims are chemically zoned. Mg

decreases in the narrow zone at the garnet rim where Mn increases. The composition along the analyzed garnet profile CL1 is Prp₉Grs₁₁Alm₇₄Sps₆ for the *outer rim* and Prp₁₅Grs₁₄Alm₆₉Sps₂ for the *inner rim*. The average Si content in white mica is 3.1 apfu (atoms per formula unit).

Sample AG20.2B

Sample *AG20.2B* is a garnet-paragneiss which also belongs to the Cima Lunga unit. It has been already described in detail in the work of [Tagliaferri et al. \(2023\)](#). U-Pb dating of zircon rims gave a concordant age of 31 Ma. HREE distribution in these zircon rims indicates that they grew coeval with garnet. Garnet crystals are pre- to syn-kinematic with respect to the main metamorphic foliation.

We analyzed two profiles on the same garnet, in contact with plagioclase (profile *D10*) and biotite (profile *D14*). The garnet shows Mg-decrease and Mn-increase at its rims. The representative composition of the garnet core is Prp₂₀Grs₂₁Alm₅₇Sps₂ and the average *outer rims* composition is Prp₁₅Grs₁₆Alm₆₃Sps₆. Biotite Mg# is approximately constant at 0.55, and XCa is lower for matrix plagioclase (0.29) with respect to plagioclase next to garnet (0.34).

Sample AV19.7C

Sample *AV19.7C* is a mylonitic-migmatitic garnet paragneiss, collected at the tectonic contact between the lower Simano nappe and the Adula nappe on top. It is described and dated in the paper of [Tagliaferri et al. \(2023\)](#). Also in this sample, the main zircon rims ages are ca. 31 Ma. Zircon metamorphic rims grew in the presence of garnet, as testified by their HREE distribution. The mineral assemblage of this sample is garnet, quartz, feldspar, biotite, white mica, chlorite, kyanite, staurolite, zircon, rutile, apatite, oxides, chloritoid. Poikiloblastic garnet grains are pre- to syn-tectonic.

Grossular content in garnet cores is approximately constant (ca. 5.5-6 wt%), however a decrease at the rim can be observed (as low as ca. 3.5 wt%). We analyzed profile L1 ([figure 4.2](#)) on a garnet with decreasing Mg and increasing Mn content at its rims. *Inner rim* composition is Prp₂₁Grs₁₃Alm₆₄Sps₂ whereas *outer rim* composition is Prp₁₆Grs₁₂Alm₆₆Sps₆. Biotite at garnet rim has lower Mg# (0.49) with respect to the matrix biotite (0.52), whereas plagioclase XCa is higher when close to garnet rim (0.34) and lower when in matrix (0.29).

Sample OS16-006

Sample *OS16-006* is the structurally lowest and was collected at the base of the Simano nappe, close to the tectonic contact with the lower Leventina nappe. It is a garnet-paragneiss which

contains quartz, feldspar, biotite, chlorite, zircon, rutile, ilmenite, epidote, oxides. Garnet crystals are pre- to syn-kinematic.

The analyzed garnet shows an increased Mn content at the rim, which is coupled with Mg-decrease. On the profile L, *inner rim* composition is Prp₁₈Grs₂Alm₇₁Sps₉, and *outer rim* is Prp₁₇Grs₂Alm₇₁Sps₁₀. Biotite Mg# at garnet border is 0.64, in matrix biotite it is 0.57. Plagioclase XCa is 0.04 next to garnet, and 0.06 in matrix plagioclase.

Sample AS21.1A

We collected sample *AS21.1A* within the SSB. It is a migmatitic garnet paragneiss with the mineral assemblage: quartz, feldspar, garnet, biotite, sillimanite, kyanite, white mica, rutile, ilmenite, zircon, oxides. Garnet crystals are pre- to syn-kinematic.

Garnet porphyroblasts are homogeneous in Ca content. The average composition of garnet cores is Prp₁₆Grs₄Alm₇₇Sps₃. Only where garnet rim is in contact with biotite, its Mg decreases and its Mn increases. We analyzed two profiles, *AL4* at the contact of garnet with a biotite inclusion and *BL2* on a garnet-biotite contact in the matrix (see *Appendix I*). The composition of garnet next to the inclusion is Prp₁₀Grs₄Alm₈₀Sps₆, Mg# of the biotite inclusion is 0.4, and XCa of plagioclase inclusion is 0.23. The garnet rim next to matrix biotite has composition Prp₁₁Grs₄Alm₈₀Sps₅, and the biotite has Mg# of 0.42. Matrix biotite Mg# varies between 0.38 and 0.41 whereas matrix plagioclase has a XCa value of 0.2.

4.3.2 Geothermometry and cooling rate estimates

The garnet rims of all the analyzed profiles show both Mg-decrease and Mn-increase (see *figures 4.2B* and *4.2D* and profiles in *Appendix I*). This pattern is indicative of retrograde diffusional modification; therefore, the calculation of garnet *outer rim* temperature is relative to the post-peak thermal history. A quantitative control of biotite abundance was made on each sample. The abundance of biotite ensures that its Mg# remains effectively unaffected during retrograde reactions and thus, it allows the usage of *inner rim* mineral compositions for the inference of near-peak T conditions. We checked the composition of biotite next to the garnet and in the matrix and obtained comparable compositions. The calculated peak temperature (from *inner rim* compositions) is always higher (from 24 to 60 °C higher than *outer rim* temperature; see *table 4.1*). In the uppermost structural levels, in the Cima Lunga unit, temperatures computed from the *outer rim* compositions vary from 619 °C to 641 °C at pressures from 0.65 and 1.3 GPa (samples *AG19.6A* and *C*, *AC19.3A*, *AG20.2B*). Closer to the

SSB, the computed temperature on the thrust is 661 °C at 0.84 GPa (sample *AV19.7C*). In the footwall of the Maggia-Adula thrust, at the bottom of the Simano nappe, the calculated temperature is 577 °C at 0.72 GPa (sample *OS16-006*). Finally, within the SSB, calculated temperatures are ca. 600 °C at 0.5 GPa (sample *AS21.1A*).

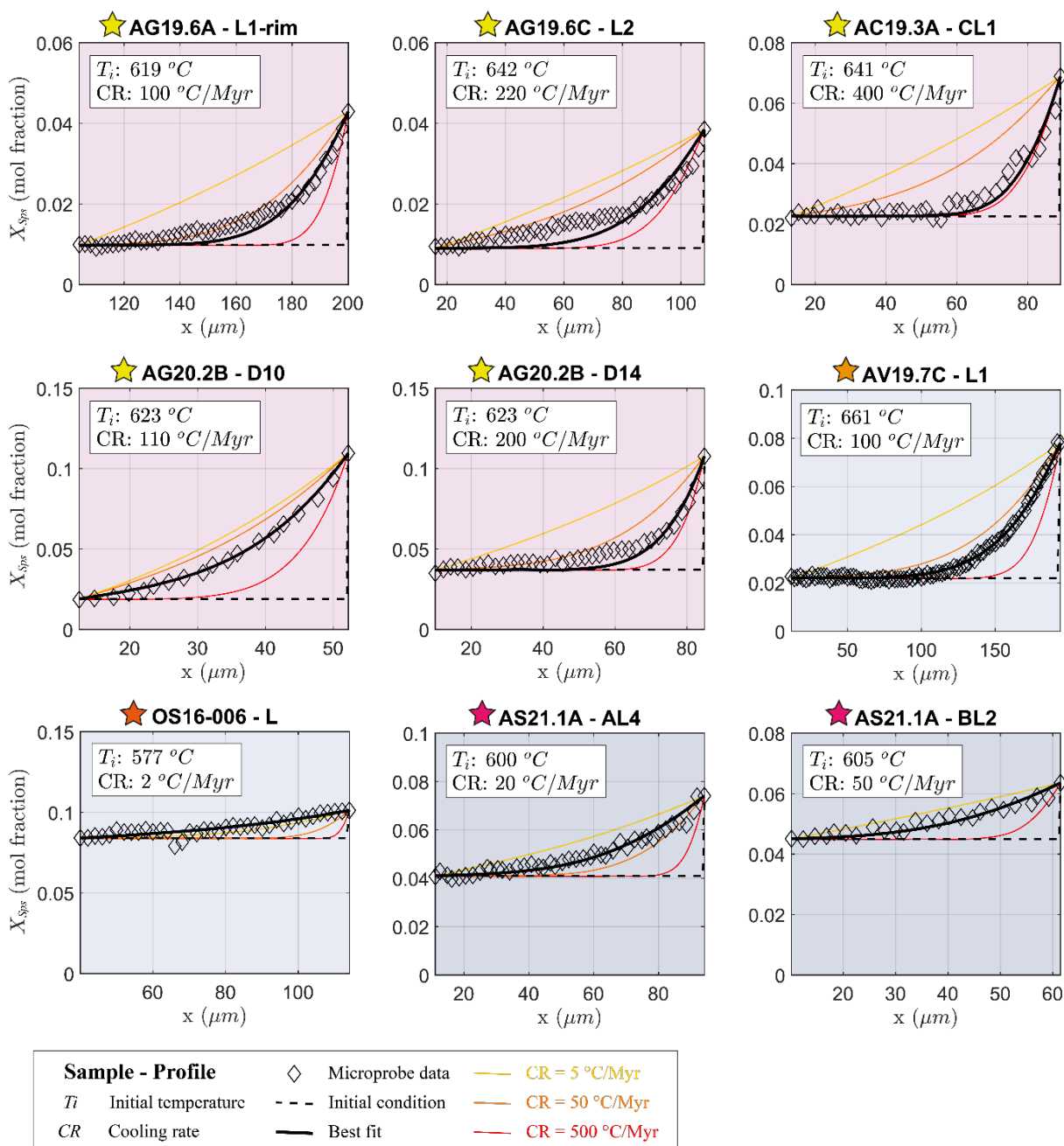


Figure 4.3. *T*-cooling model results for all samples, shown on spessartine (*Sps*) profiles. Diamonds are the point analyses measured at the microprobe (spacing: 2 μm), dashed lines are the initial profiles, thick lines are the model results after diffusion. T_i = input initial temperature; x = distance on the profile; X_{Sps} = spessartine mole fraction ($\frac{Mn}{Mg+Fe+Ca+Mn}$). Yellow, orange, red lines are the model results obtained using CR of 5, 50, 500 °C/Myr respectively. The background colors of each plot correspond to the colors of the relevant nappe and colored stars are the same as the symbols used to indicate samples in figure 4.1.

The concentration profiles we modelled using GDIFF fit the measured profiles, with a maximum deviation of ca. 5% in spessartine mole fraction (X_{SpS}) between the two curves ([figure 4.3](#)). Once put into a more regional context, the model results show a clear pattern in the CR distribution through the nappe pile. Six profiles measured on rocks within or close to the Maggia-Adula tectonic contact have apparent cooling rates of hundreds of °C/Myr. Within the Cima Lunga unit, CR can reach a peak of 400 °C/Myr (sample *AC19.3A*, [figure 4.3](#)). The tectonically lowermost sample *OS16-006* has instead a CR of 2 °C/Myr, two orders of magnitude lower than the rocks tectonically above. Finally, the sample *AS21.1A* within the SSB has an intermediate CR of 20-50 °C/Myr, obtained at the contact with a biotite inclusion (profile *AL4*) and a matrix biotite (profile *BL2*) respectively (see [section 4.3.1 – Sample AS21.1A](#) and [Appendix I](#)).

For comparison, we run also models with a fixed CR value of 5, 50, 500 °C/Myr for all samples. The results show how much the modelled profiles deviate from the best fit solution ([figure 4.3](#)). The relations between these extreme cases display the dependence of the final solution on the chosen cooling rate. The results show, as expected, that when the CR is lower, the profile is more diffused.

4.3.3 Thermal models

To get more insights into the cooling rate estimates, we performed simple 1D thermal models of exhumation. These models are useful for the understanding of the CR versus T relationships during exhumation (e.g., [Stüwe & Ehlers, 1998](#)). Our model setup follows the approach of [Braun et al. \(2006\)](#) and the 1D model with constant exhumation velocity presented in [Burg & Moulas \(2022\)](#) in the case of a regional cooling scenario. We consider a region where isotherms do not have lateral perturbations and we assume an initial T profile that corresponds to the steady state geotherm expressed by the following equation (e.g. [Turcotte & Schubert, 2002](#)):

$$T(y) = T_s + \frac{Q_s}{k} \cdot y - \frac{H_r}{2k} \cdot y^2 \quad (1)$$

T_s is the surface temperature (in °C), which is set to zero; y indicates depth (in m); surface heat flux (Q_s) is $60 \cdot 10^{-3}$ W/m²; thermal conductivity (k) is 3 W/(m·K); radiogenic heat production (H_r) is $0.5 \cdot 10^{-6}$ W/m³.

The model calculates the distribution of temperature with time by solving the transient solution of the heat transfer equation (e.g., [Braun et al., 2006](#); for an Eulerian reference frame):

$$\frac{\partial T}{\partial t} = \frac{k}{\rho C_p} \cdot \frac{\partial^2 T}{\partial y^2} + \frac{H_r}{\rho C_p} + \dot{\epsilon} \cdot \frac{\partial T}{\partial y} \quad (2)$$

Rock density (ρ) is 3000 kg/m³; heat capacity (C_p) is 1000 J/kg·K; exhumation velocity ($\dot{\epsilon}$ [m/s], expressed here in [mm/yr]) is set constant. In each calculation, we monitor the resulting surface heat flux (Q_s [mW/m²]) of the thermal model. This serves as a constraint in our geodynamic interpretation.

Exhumation velocity refers to the movement of rocks with respect to the surface. We run three models with different exhumation velocities of 1 mm/yr ($\dot{\epsilon}1$), 5 mm/yr ($\dot{\epsilon}5$) and 20 mm/yr ($\dot{\epsilon}20$). Exhumation velocities lower or close to 1 mm/yr are typical for a regional exhumation scenario (c.f. exhumation velocities in the Alps in [Fox et al., 2015](#); [Schlunegger & Willett, 1999](#); [Wölfler et al., 2023](#)), the model with a 5 mm/yr exhumation velocity shows the effect of higher exhumation velocities on CR behavior, and 20 mm/yr corresponds to the rapid exhumation proposed for the rocks of the Cima Lunga unit in a recent study of [Piccoli et al. \(2021\)](#).

The results show the change in P, T, and CR of rocks when following their exhumation trajectories from depth to the surface (model $\dot{\epsilon}1$ for 1 mm/yr in [figure 4.4](#) and models $\dot{\epsilon}5$ and $\dot{\epsilon}20$ for 5 and 20 mm/yr in [figures J.1](#) and [J.2](#) of [Appendix J](#)). For exhumation velocities of 1 mm/yr, the initial exhumation phase of individual rock markers is almost adiabatic for the deepest rocks at $P > \text{ca. } 0.8 \text{ GPa}$ ([figures 4.4A](#) and [4.4B](#)), and then the temperature decreases almost exponentially until the rock reaches the surface. For exhumation velocities of 5 mm/yr and 20 mm/yr the adiabatic exhumation lasts until P of ca. 0.5 GPa and ca. 0.2 GPa, respectively (see [figures J.1](#) and [J.2](#) of [Appendix J](#)). In all these models most of the cooling occurs close to the surface.

In the model $\dot{\epsilon}1$, computed with an exhumation velocity of 1 mm/yr, the highest cooling rates are obtained only at low T ($T < 200 \text{ }^\circ\text{C}$) and P ($P < 0.2 \text{ GPa}$). For example, at T of 600 °C and $P > 0.5 \text{ GPa}$, cooling rates are lower than 20 °C/Myr ([figures 4.4C](#) and [4.4D](#)). During exhumation, the geotherm moves up and the surface heat flux increases reaching a value of 147 mW/m² (Q_s in [figure 4.4A](#)).

We display the trajectories of the deepest rock markers (initial condition at ca. 600 ± 50 °C and 1.2 GPa) of this model $\dot{\epsilon}1$ in CR vs. P and CR vs. T plots in [figure 4.5](#) where we compare them with the trajectories obtained for rocks starting their exhumation at similar conditions for models $\dot{\epsilon}5$ and $\dot{\epsilon}20$. The comparison of CR vs. P trajectories for the different exhumation velocities ([figure 4.5A](#)) confirms the trend of higher CR at low P for all the tested models. Moreover, to identify the possible thermal history of our analyzed samples, we further compared their post-peak P-T conditions and their CR (samples are indicated by stars in [figure 4.5](#)) with the rock trajectories computed for the three different exhumation rates. The P-T-CR range described by the standard exhumation model $\dot{\epsilon}1$ is compatible only with few samples (*OS16-006* and *AS21.1A-AL4*; [figure 4.5](#)).

When increasing the exhumation velocity, the CR increases and eventually reaches high values when the temperature is still high (300-400 °C/Myr at 600 °C for model $\dot{\epsilon}20$; see [figure 4.5B](#)). However, these CR values are reached only at very low pressures ($P < 0.2$ GPa) which does not reflect any of the observed sample conditions ([figure 4.5A](#)). P-T-CR conditions of the sample from the SSB (sample *AS21.1A*) may fit the trajectories of the 5 mm/yr exhumation velocity, however, the CR obtained for profile *AS21.1A-BL2* is too high at the corresponding post-peak pressure of 0.5 GPa ([figure 4.5A](#)). The P-T-CR conditions of the samples collected within the shear zone (samples *AG19.6A* and *C*, *AC19.3A*, *AG20.2B*) do not fit any possible regional exhumation trajectory, because the cooling rates are too high at their post-peak pressures that are between 0.65 and 1.3 GPa ([figure 4.5A](#)).

Furthermore, the final heat flux predicted by the high-velocity exhumation models is unrealistically high and it results in 412 mW/m^2 and 1310 mW/m^2 for model $\dot{\epsilon}5$ and model $\dot{\epsilon}20$ respectively (see [figure 4.5](#) and [Appendix J](#)).

Exhumation velocity: 1 mm/yr

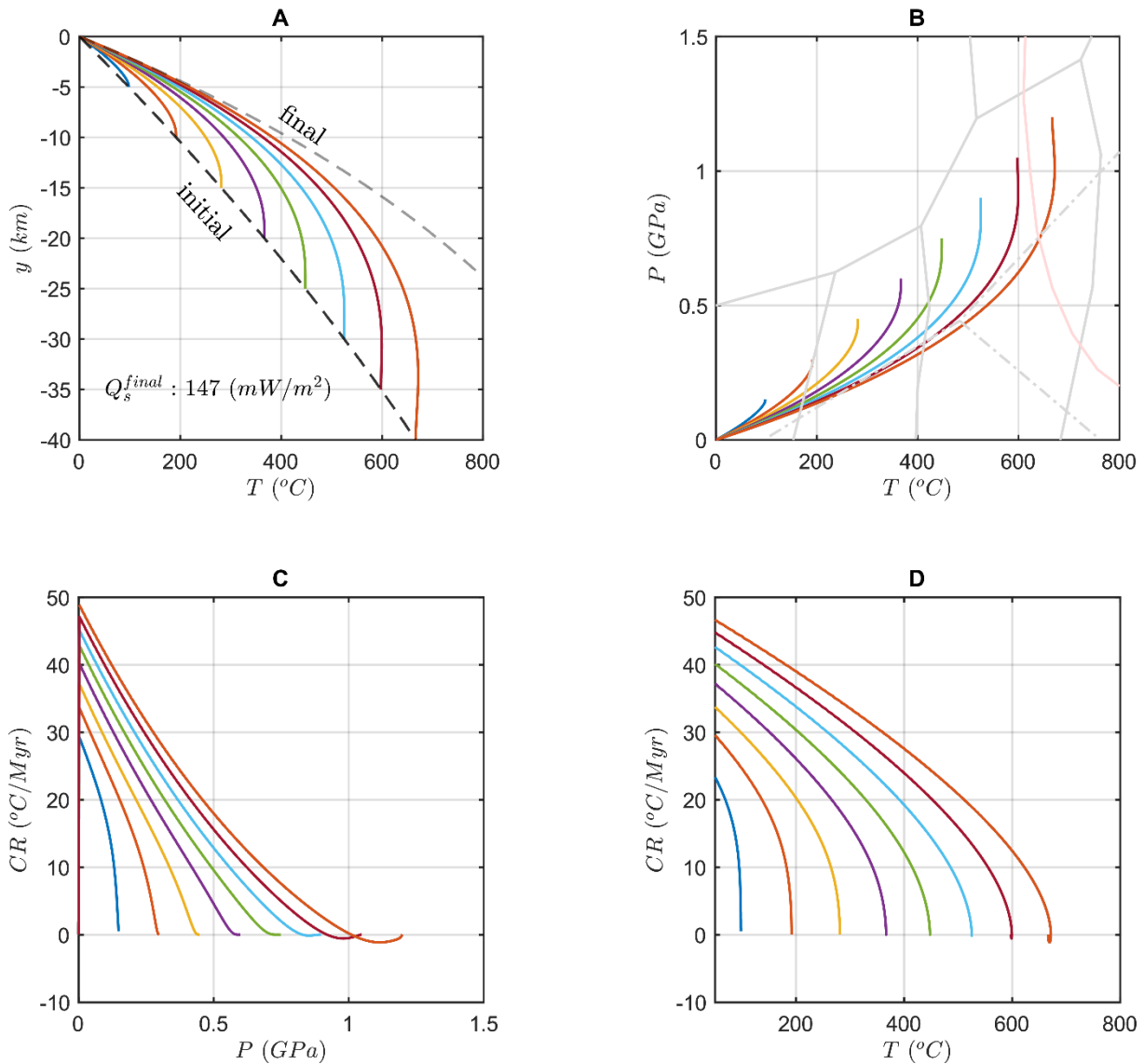


Figure 4.4. 1D thermal model results for an exhumation velocity of 1 mm/yr. Rock trajectories are indicated with lines of different colors. **(A)** Rock trajectories in the depth-T plot. The initial and final geotherms are in dashed lines. Q_s^{final} is the final surface heat flux. **(B)** Rock trajectories in the P-T plot, pressures are calculated from depth (y) assuming lithostatic pressure. Gray-transparent lines divide metamorphic facies fields (from *Stüwe (2002)*), the dot-dashed line divides the aluminosilicate stability fields, and the red-transparent line is the solidus. **(C)** CR-P plot showing the variation of P and CR over time for each rock. **(D)** CR-T plot showing the variation of T and CR for the same rock markers.

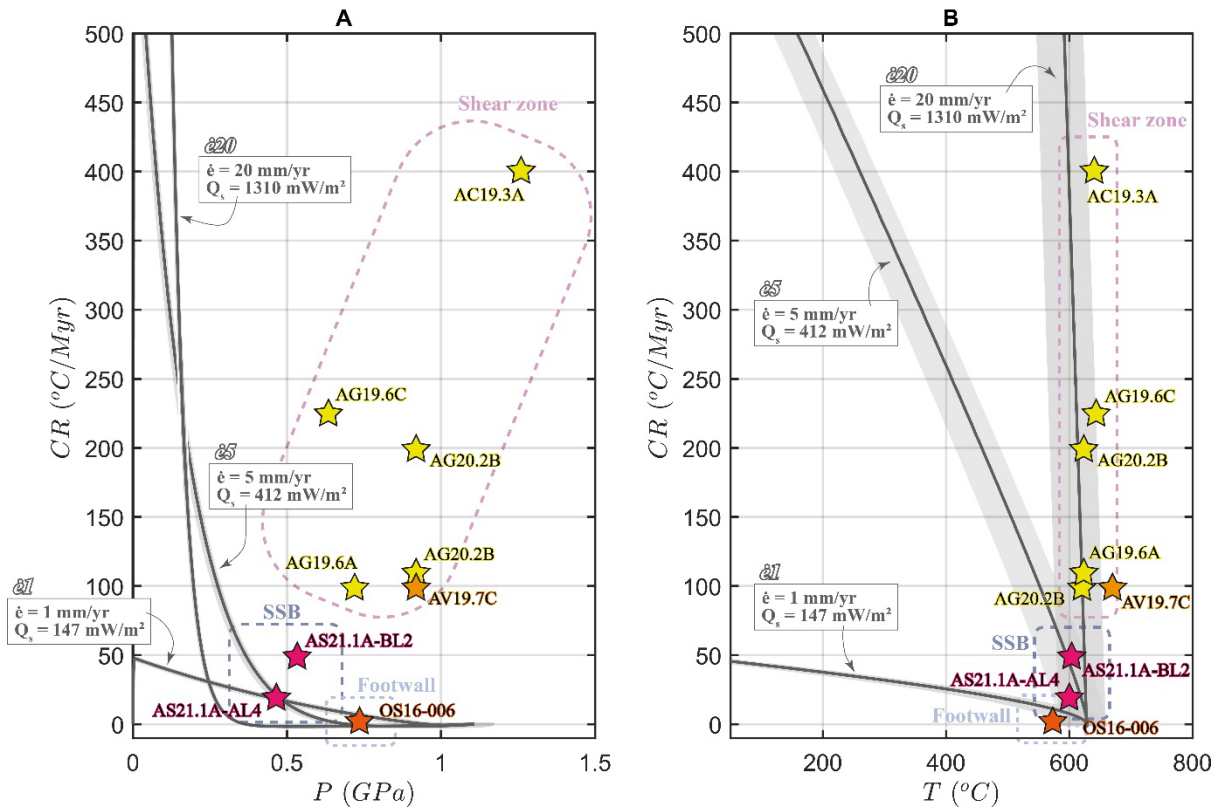


Figure 4.5. Results of 1D thermal models with constant exhumation velocities of 1 mm/yr ($\dot{\epsilon}1$), 5 mm/yr ($\dot{\epsilon}5$) and 20 mm/yr ($\dot{\epsilon}20$) for rocks that exhume close to Barrovian conditions. $\dot{\epsilon}$ is the exhumation velocity in mm/yr, Q_s is the final heat flux computed by the exhumation model in mW/m². Samples are plotted as stars with their relevant names. Samples' P-T conditions are the post-peak T and P calculated using geothermobarometry. The dashed boxes group samples in the same tectonic locations. Notice that the P-T conditions predicted by the exhumation models never succeed in fitting the post-peak conditions recorded by samples with the highest CR.

4.4 Discussion

4.4.1 The T and CR pattern through the nappe pile

In the studied area of the Lepontine dome, geothermometric estimates show higher temperatures (664–685 °C for *inner rims* and 619–642 °C for *outer rims*) in the tectonically uppermost levels of the nappe pile ([table 4.1](#) and [figure 4.6](#)). Lower temperature values are recorded instead in the lowermost structural levels (614 °C for *inner rims* and 577 °C for *outer rims*). The possible error overlaps of ± 20 °C and 0.1 GPa on thermobarometric estimates do not affect the robustness of the regional trend of both T and P since we consistently adopted the same geothermometer and geobarometer for almost all samples. This temperature distribution is inverted with respect to the classical gneiss dome structures, where higher temperatures occur in the core of the dome ([Burg et al., 2004](#)). Peak temperatures of 657–673 °C (*inner rims*) in the

SSB agree within-error with values reported by previous authors (e.g., Berger et al., 2008; Burri et al., 2005; Rubatto et al., 2009) and post-peak temperatures of 600 °C fall in the range 550–650 °C indicated by the recrystallization of zircon rims (Vonlanthen et al., 2012). Also, on the main Maggia-Adula thrust the cooling rates are higher (hundreds of °C/Myr) than the standard regional cooling rate (Schlunegger & Willett, 1999), and in the footwall of the thrust the CR is lower (< 10 °C/Myr) (figures 4.5 and 4.6).

The overall T-P-CR pattern in the Lepontine dome during the post-peak stage shows a shear zone which cooled down from ca. 640 °C and 0.9 GPa at CR between 100–400 °C/Myr (samples AG19.6A and C, AC19.3A, AG20.2B, AV19.7C), with the fastest CR computed for the structurally uppermost sample AC19.3A. Whereas, the footwall of this shear zone cooled down from ca. 580 °C and 0.7 GPa with a rate of 2 °C/Myr (sample OS16-006). To the south, within the SSB, rocks at 600 °C and 0.5 GPa cooled with intermediate rates of 20–50 °C/Myr (sample AS21.1A; figures 4.5 and 4.6), in accordance with the results of Hurford (1986) and Hansmann (1996).

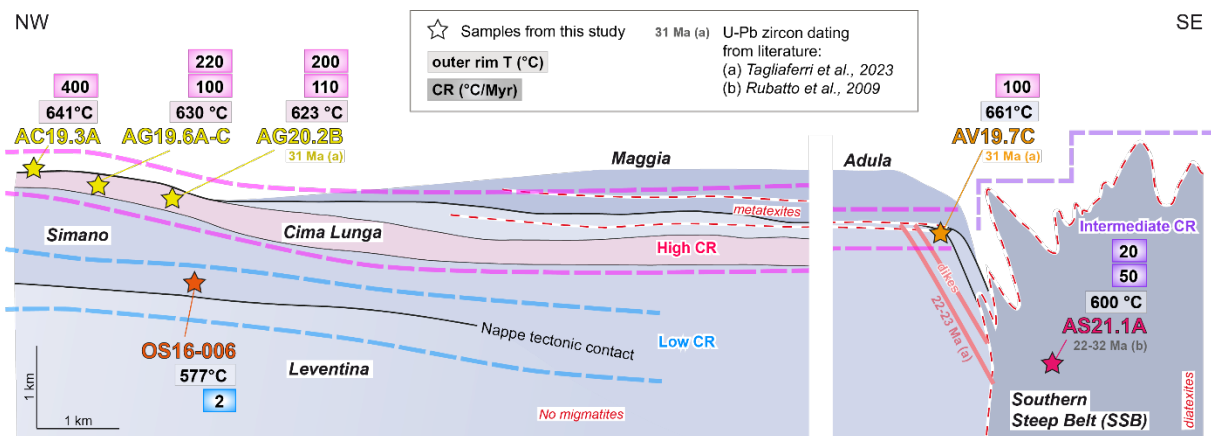


Figure 4.6. Schematic section of the Lepontine nappe pile with T, CR and U-Pb zircon ages distribution. Pink, blue, violet dashed lines identify the tectonic locations characterized by high, low, intermediate CR. Cooling rate estimates are reported in boxes with the same colors.

4.4.2 CR and 1D thermal model results

We analyzed the CR distribution within the Lepontine dome through 1D thermal models. These models predict an expected regional exhumation scenario and highlight how much our calculated CR deviate from such a scenario (see both in figure 4.5). We proceed by discussing the results based on the tectonic location of samples within the nappe pile.

4.4.2.1 Higher tectonic levels: the Maggia-Adula shear zone

In our thermal models, the fast CR close to peak conditions within the shear zone cannot be explained with standard exhumation velocities. Only when we considerably increase the exhumation velocity (see in *figure 4.5 model è20*) we obtain CR values of hundreds °C/Myr for the Barrovian T conditions of interest (around 600 °C). However, even when the exhumation velocity increases, the CR never becomes high at peak P conditions typical of the Barrovian metamorphism in the Lepontine dome (> 0.5 GPa, as in our samples). This is because fast exhumation velocities lead to quasi-isothermal P-T paths that experience most of the cooling when they are near the surface (see *Appendix J*). Furthermore, a higher exhumation velocity generates an unrealistically high (> 150 mW/m²) surface heat flux (Schlunegger & Willett, 1999). Such heat fluxes are not observed in nature and therefore, a regional cooling scenario cannot explain the T-P-CR relation calculated for rocks on the Maggia-Adula thrust.

A limitation in the use of 1D models may reside in the assumption of considering a region with negligible lateral thermal gradients. However, the general trend described by our models (high CR close to the surface) is still maintained in 2D models, either in the case of exhumation through a compressional thrust sheet (Thigpen et al., 2021) or within an extensional detachment (Schenker et al., 2012).

Fast cooling rates can be produced by a transient local heat source on the thrust followed by rapid thermal quenching (Burg & Moulas, 2022; Schmalholz & Duretz, 2015; Stüwe & Ehlers, 1998). Possible solutions can include localized hot fluid pulses, magma injection (e.g., Chu et al., 2018), or mechanical work dissipation acting during nappe emplacement (Burg & Moulas, 2022; Schmalholz & Duretz, 2015). In our field areas far from the SSB, no evidence of magma intrusion synchronous to thrusting has been observed. Whereas local syn- to post-tectonic veins in the core of the Lepontine dome indicate the presence of fluids during metamorphism (Allaz et al., 2005). The estimation of these fluids' contribution to the overall heat budget is difficult to quantify. Qualitatively, we suggest that the impact of fluids in raising the regional T is minor since the volume of the veins within the nappe pile is relatively small. In addition, the presence of a large amount of fluids would have likely produced a wider migmatitic belt and partial melting evidence in all the analyzed samples (see arguments in Tagliaferri et al., 2023). On the other hand, many authors suggested the importance of shear heating in producing Barrovian T conditions (e.g., Burg & Gerya, 2005; Burg & Schmalholz, 2008; Duprat-Oualid et al., 2015; Hartz & Podladchikov, 2008; Maino et al., 2015, 2020; Nabelek et al., 2010; Souche et al.,

2013). Shear heating can indeed be responsible for high temperatures localized on a thrust surface or in its immediate vicinity (e.g., Kiss et al., 2019), which would produce a transient temperature field in a limited area. Recently, Burg & Moulas (2022) showed with 1D thermal models including viscous heating that in the immediate vicinity of a thrust zone (i.e., within 2 km from its center) cooling rates larger than 100 °C/Myr at 650 °C temperature are feasible. In the Lepontine dome, the local presence of Alpine migmatites on the Maggia-Adula shear zone (Tagliaferri et al., 2023) corroborates such a local transient heat pulse hypothesis.

4.4.2.2 Footwall of the Maggia-Adula thrust

The sample *OS16-006* is tectonically located low in the nappe pile, at the base of the Simano nappe which is the footwall of the main Maggia-Adula thrust. Despite this sample was collected above the diffuse tectonic boundary of the Simano and Leventina nappes, the obtained CR is much lower (2 °C/Myr). This low CR can fit within-error the thermal history of model *è1* (figure 4.5) and the exhumation velocities computed for the Lepontine dome (1.3-2.0 mm/yr in Malusà et al. (2011); ca. 0.3 mm/yr in Schlunegger & Willet (1999)) without invoking additional local heat sources. The close-to-peak conditions (“inner rim” at $T = 614$ °C and $P = 0.67$ GPa) recorded in this sample would correspond to the beginning of the regional exhumation history in the core of the Lepontine dome, after the emplacement of the Maggia-Adula nappe.

Following the outcomes of Tagliaferri et al. (2023), we hypothesize that the regional Barrovian thermal anomaly of the Lepontine dome primarily results from the advection of heat. This heat was advected during the exhumation of the deeper Maggia-Adula nappe over the relatively shallower Simano nappe. Heat diffused down-section during deformation and produced metamorphic isograds which crosscut the tectonic contacts. Besides, shear heating significantly contributed to the rise of the thermal conditions within the main Maggia-Adula shear zone. In the footwall, we obtain high CR only in the highest-strain domains just below the shear zone. Approximately 1 km beneath (where sample *OS16-006* is collected), the shear heating contribution seems to be negligible.

It may be argued that the final garnet diffusion profile of sample *OS16-006* was generated by several heat pulses affecting the rock. The resetting of the garnet profiles would have obliterated the intermediate profile variations. In this case, the apparent low CR would be the result of two (or more) fast heat pulses. If a spasmodic history is invoked, the close-to-peak conditions of these different events would not have overcome the peak T of ca. 614 °C (“inner rim” T

condition). We deduce that also in a thermal history characterized by more than one heat pulse, the base of the Simano footwall nappe remained colder than the peak T recorded at the Maggia-Adula thrust, supporting the shear heating hypothesis within the main shear zone.

4.4.2.3 The Southern Steep Belt

Intermediate CR values of tens °C/Myr up to 20-30 °C/Myr agree within-error with an exhumation between 1-5 mm/yr (see thermal models $\dot{\epsilon}5$ and $\dot{\epsilon}1$ in [figure 4.5](#)). However, the CR of 50 °C/Myr of sample *AS21.1A* (profile *BL2*) at ca. 600 °C and 0.5 GPa is excessive to be explained solely by regional exhumation.

It cannot be excluded that this medium-high CR might be linked to some process capable of keeping the temperature high before the final cooling. Such processes include (i) the release of latent heat during melt crystallization or during regional retrograde metamorphism (e.g., [Schorn et al., 2018](#)), (ii) diapirism causing the uprise of hotter material, or (iii) local percolation of hot fluids at different times of the melting history of the SSB migmatites.

Diapiric uprise of migmatites has been shown also in other migmatitic belts (e.g., [Schenker et al., 2012](#)), where convection cells within the migmatitic core may have contributed to keep hot conditions over 10-20 Ma. Indeed, zircon U-Pb dating of rocks from the SSB testifies that this migmatitic belt was affected by continuous melting over 10 Myr ([Rubatto et al., 2009](#)). A combination of both local fluid advection and diapirism seems to be confirmed by field relationships within the SSB diatexites.

4.4.3 Relation between U-Pb zircon dating and obtained CR

As already mentioned in the results section, samples *AG20.2B* and *AV19.7C* have been dated in the recent paper of [Tagliaferri et al. \(2023\)](#). U-Pb ages of zircon rims in equilibrium with garnet are ca. 31 Ma, which has been interpreted to pinpoint the final stage of nappe emplacement. Therefore, we assume that the garnet diffusion modelled in this work starts at 31 Ma, after the T peak. From our cooling rates, in the rocks within the Maggia-Adula tectonic contact, the time to reach garnet closing temperature at 480 °C varies between 0.4-1.8 Ma. This rapid cooling agrees with field relationships which show 31 Ma old migmatites crosscut by 22-23 Ma old dikes ([Tagliaferri et al., 2023](#)).

To the south, in the SSB the continuous melt production resulted in a distribution of U-Pb zircon ages between 22 and 32 Ma ([Rubatto et al., 2009](#)). For sample *AS21.1A*, the cooling time to reach 480 °C is 2.5 and 6 Ma for the two measured profiles. Therefore, while the post-peak

stage on the main thrust lasted until ca. 29 Ma, in the south it could have lasted until 16-19 Ma. Low-T geochronometers testify indeed that the regional cooling of the Lepontine dome below ca. 350-500 °C started after 19 Ma (Rb-Sr and K-Ar in muscovite in [Hurford \(1986\)](#); monazite in [Janots et al. \(2009\)](#)).

Within the central Lepontine dome, literature data indicate that the thrusting of the Simano nappe over Leventina and Gotthard nappes was active at ca. 31 Ma but at lower temperatures of ca. 550 °C ([Boston et al., 2017](#); [Gieré et al., 2011](#); [Janots et al., 2009](#)). At different tectonic levels of the Simano nappe, [Köppel & Grünenfelder \(1975\)](#) found monazite U-Pb ages around 22-23 Ma which are considered by [Boston et al. \(2017\)](#) to record close-to-peak conditions. Hence, the low CR (2 °C/Myr) of sample *OS16-006* at the base of the Simano nappe suggests that the peak conditions recorded by monazite can still be part of the same regional exhumation event related to lower nappes emplacement at 31 Ma, coeval with the last phases of Maggia-Adula thrusting.

Finally, the described pattern indicates that the Lepontine dome cooled down from peak conditions in a non-homogeneous manner. This cooling implies that the direction of the heat flux within the dome changed over time.

4.5 Conclusion

We presented cooling rate (CR) constraints, based on garnet diffusion modelling, for rocks at different tectonic locations within the Barrovian sequence of the Lepontine dome. An inverted metamorphic field gradient and an inverted, spatially heterogeneous distribution of CR values characterize the area.

High apparent cooling rates (100-400 °C/Myr) are computed only for rocks that are from the main Maggia-Adula shear zone. Such high CR cannot be obtained with a regional exhumation thermal model. The high cooling rates are likely the result of local, transient heat sources such as shear heating within the shear zone. Indeed, one-dimensional thermal models highlight that high exhumation velocities never lead to fast CR at Barrovian conditions above 0.5 GPa, if local heat sources are not considered. The record of peak P-T conditions produced during the initial stages of regional exhumation of the Lepontine nappe pile is registered only in the lowest structural levels of the footwall of the main thrust, as indicated by the low CR of 2 °C/Myr.

Intermediate CR in the Southern Steep Belt may indicate regional exhumation combined with possible local transient input of hot fluids or diapirism in the migmatitic system.

The observed CR pattern shows that the overall heat budget in the Lepontine dome cannot be described by a simple regional heating/cooling scenario. Local and transient heat sources due to shear heating and/or hot fluids play a crucial role in the generation of T-P conditions recorded by rocks, especially within major shear zones. In general, the relationships between thermal and mechanical histories should always be considered for the analysis of the transient character of high-grade metamorphic processes.

Acknowledgements

The authors thank Martin Robyr and Stephan Buhre for the setting of the microprobe, and swisstopo for the opportunity to work on the production of the new Swiss National Map. This work was supported by the Swiss National Science Foundation Grant n°182041, SUPSI project n°12RAFGOSO and n°12RA1CARTOTIGR. EM would like to acknowledge the German Research Foundation (DFG; grant n°512790090) for financial support in relation to the code and methodology development.

Chapter 5

DISCUSSION AND CONCLUSIONS

The aim of this thesis was to disclose the thermal history of the Lepontine dome. We performed a combined study of multiple disciplines to dive into the origin of Barrovian metamorphism in this region of the Central Alps. Our work was strongly field-based. We performed extensive geological mapping in the mountains of Ticino and Grisons (Switzerland) and we collected samples for lab analyses. Lab work comprised major and minor elements, trace elements and isotopes (U-Pb zircon dating) analyses. The last discipline involved in this thesis was numerical modelling, which we used to simulate simple crustal-scale scenarios and to perform crystal-scale modelling. The combination of these methodologies was a necessity in such a multifaceted case study like the Lepontine dome.

As main outcomes of our research, we propose that the Barrovian metamorphism in the Lepontine dome:

- Is regional and locally inverted.
- Is coeval to nappe emplacement, and peaked at 31 Ma.
- Is linked to the activity of a major shear zone at the base of the Maggia-Adula nappe (Maggia-Adula shear zone), which we defined based on structural relationships in the field and new U-Pb zircon ages.
- Is the result of heat advected during the exhumation of the Maggia-Adula nappe emplacement and local transient heat sources (shear heating).
- Is the record of peak temperature conditions which were followed by close-to-peak temperature heterogeneous cooling.

In this chapter we will briefly retrace our research and summarize these results. We will highlight the implications of our work, and relate them to the feasible geodynamic scenarios that we presented in the introduction of this thesis (see *section 1.4.3* in *Chapter 1*). For these purposes, we refer to *figure 5.1*, which is a modified reproduction of *figure 1.6*, and to *figure 5.2*, where the main results are summarized. Lastly, we will also address the still open questions and limitations of the techniques we applied.

Figure 5.1. Possible *T* evolution with depth in the nappes of the Lepontine dome according to different geodynamic scenarios, modified after *figure 1.6* in *Chapter 1*. In transparency are the hypotheses which have been discarded based on the results of this work. Comments in red justify why these hypotheses are not suitable for explaining the origin of Barrovian metamorphism in the Lepontine dome. In pink are the observations from the field. See detailed description in the main text.

5.1 Redefinition of nappe boundaries in the Lepontine dome

The comprehensive geological study presented in this thesis permitted to re-define the nappe structure of the Lepontine dome.

In *Chapter 3*, we analyzed in the field the relative structural positions of Simano, Cima Lunga, Adula and Maggia, and we considered their lithological affinities. Moreover, we connected these field observations with results from U-Pb zircon dating at the top of the Simano, within the Cima Lunga and at the base of the Maggia nappe.

We discovered new syn-tectonic Alpine migmatites at 31 Ma at the top of the Simano nappe that define an important tectonic contact, which we named “Maggia-Adula shear zone”. This contact is a shear zone that divides the Simano nappe to the bottom and the Adula-Maggia nappe in the hanging wall. In our view, Maggia and Adula are considered as a big major nappe (as already proposed by [Jenny \(1923\)](#)) whose emplacement contributed to heat advected with it, diffused from it, and produced at its base (see *section 5.3*).

As a consequence, we do not share the common view where Cima Lunga and Adula are part of the same nappe (e.g., [Dal Vesco, 1953](#); [Trommsdorff et al., 2000](#)). Rather, Cima Lunga would represent the upper portion of the Simano nappe and would be part of the Maggia-Adula major shear zone, as testified by its high deformation. Zircon U-Pb ages reveal detrital zircon cores and metamorphic Variscan rims (ca. 300-320 Ma) within the paragneisses of the Cima Lunga unit. These new ages suggest that the Cima Lunga unit is a pre-Variscan sedimentary sequence and not, as previously stated ([Engi et al., 2001](#); [Trommsdorff, 1990](#); [Trommsdorff et al., 2000](#)), an Alpine tectonic mélange. Besides, the continuous gneissic and metacarbonate horizons argue against a mixing-like origin.

The re-definition of the Cima Lunga unit and its position with respect to the Maggia-Adula nappe puts in discussion the Cima Lunga nappe intrusion model as a feasible geodynamic scenario (*figure 5.1B-vi* and *C-vi*). In our view, the big Maggia-Adula nappe thrusts on top of the Simano nappe, and the Cima Lunga unit was pinched and stretched within this shear zone. If the Cima Lunga unit would have tectonically intruded within the Simano nappe, (i) the shear sense identified in the migmatites would have been the opposite of what we observed in the field, and (ii) we would have observed syn-kinematic migmatites both at its top and bottom in its central and frontal domains.

5.2 Peak conditions in the field

The Barrovian metamorphism of the Lepontine dome is described by concentric, asymmetric isograds defining higher metamorphic conditions to the south (Todd & Engi, 1997; Wenk & Keller, 1969; *figures 1.3, 3.1, 4.1*), where the migmatitic Southern Steep Belt (SSB) outcrops. Isograds indicate the peak temperature (T) (and pressure (P) at peak T) conditions to which the dome has been subjected during the Alpine history, identified by marker mineral associations.

Another feature related to the Lepontine Barrovian metamorphism is the mineral and stretching lineation which originates at peak amphibolite conditions. This lineation is defined by the preferential growth of micas, kyanite, hornblende, and by elongated quartz and feldspar aggregates. The lineation is constantly found on the foliation plane of the basement crystalline rocks all over the Lepontine dome. Its orientation is NNW-SSE in the core of the dome whereas it turns toward E to the north (NE of Adula nappe) (Wenk, 1955; see *figures 3.1* and *4.1*). This rotation is likely due to the activity of orogen-oblique extensional motion during nappe stacking (Ring & Glodny, 2021). The lineation in the core of the dome has pervasively the same orientation independent of the attitude of the foliation planes on which it develops. This constant orientation points to a single deformation event in which the attitude of geological structures such as foliation planes rotated, while the lineation trend remained parallel to the kinematic NNW-SSE direction. Indeed, if we assume that different strain regimes would have affected the Lepontine area, the resulting lineation would have been either overprinted by a later lineation with variable directions corresponding to the change in strain over time, or rotated around the fold axis of a later folding event. We identify the NNW-SSE oriented constrictional deformation that caused the development of the pervasive lineation as the main nappe emplacement event. Indeed, tectonic models of the Central Alps highlight the dominance of top-to-N/NW foreland-directed movements due to nappe stacking (e.g., Coward & Dietrich, 1989; Schmid et al., 1996; Rosenberg et al., 2021; Rosenberg & Kissling, 2013).

A third evidence of peak T conditions is represented by localized migmatites that we mapped for the first time within the Lepontine dome. We describe some of these rocks in *Chapter 3* as syn-kinematic migmatites with a top-to-NW shear sense. These migmatites (metatexites and diatexites) are localized at the tectonic contact between Maggia-Cima Lunga-Simano to the west, and between Adula-Simano to the east. Their structural position at the top of the Simano nappe defines a major shear zone, which we newly defined as the Maggia-Adula shear zone (see *Chapter 3* and *section 5.1*). These observations attest that the formation and shear sense orientation of these migmatites are coherent with nappe emplacement. Therefore, to prove their Alpine origin, we performed U-Pb zircon

dating (*Chapter 3*) and we obtained an age of ca. 31 Ma. This age is compatible to the timing of peak Barrovian metamorphism as suggested by previous authors (e.g., [Liati et al., 2009](#); [Nagel, 2008](#)).

Summarizing, in the field we identify three pieces of evidence which are the result of coeval peak T Barrovian conditions: isograds, lineation and migmatites. Both lineation and migmatites are syn-tectonic and formed during the late stage of the nappe emplacement phase, at 31 Ma. Therefore, we suggest that the peak Barrovian T conditions are coeval with nappe emplacement at 31 Ma, and they are not the result of a post-nappe emplacement heating as previously stated (see *Chapter 1* and references therein). This first outcome excludes that the geodynamic scenario of a second thermal pulse from the asthenosphere is responsible for the Lepontine Barrovian metamorphism (*figure 5.1D*). Also, the downward-increasing high T predicted by this scenario is not recorded within the Leventina nappe (e.g., [Rütti et al., 2008](#)).

5.3 The “problem” of cross-cutting isotherms and the numerical model solution

The argument which has been used by previous authors to support the hypothesis of a heat event occurred after the formation of the Lepontine nappe stack is the observation of intersection relationships between the main tectonic contacts and isograds (e.g., [Berger et al., 2011](#); [Frey et al., 1999](#); [Nagel, 2008](#); [Todd & Engi, 1997](#); [Trommsdorff, 1974](#); [Wenk & Keller, 1969](#); [Wiederkehr, 2009](#)). The discovery of a belt of syn-tectonic migmatites along the Maggia-Adula shear zone represents a first obstacle to this theory. Indeed, these migmatites can be considered as well as an isograd parallel to the contact (if we do not consider possible fluids percolation promoting melt production; see *section 5.4.1*). Furthermore, in a section dissecting the nappes from top to bottom, the position of these migmatites with respect to the surrounding amphibolite rocks defines an inverted metamorphism. On the base of these observations, we exclude that isograds are the result of a configuration where isotherms are constructed, i.e., pre-nappe emplacement and passively dislocated due to thrusting (*figure 5.1B-v* and *C-v*).

To explain both intersection relationships and overturned isotherms, we developed 2D thermo-kinematic numerical models simulating a simple nappe emplacement scenario (*Chapter 2*). These models quantify the interaction between advection, conduction and production of heat, where with production we address to shear heating on the thrust surface. The heat of the Barrovian metamorphism derived mainly from advection associated with the emplacement of the Maggia-Adula nappe. Conduction had the effect of smoothing the temperature profiles during thrusting, thus it enhanced the development of the intersection relationships between isograds and tectonic contacts. At the same

time, production acted during shearing and, together with advection, may have produced the inverted isotherm configuration around the Maggia-Adula shear zone. Shear heating determined a heat surplus on the Maggia-Adula thrust (*Chapter 4*).

All these three mechanisms operated together during overthrusting and their contribution may have changed over time in the Barrovian history of the Lepontine dome due to changes in the emplacement velocity or rocks viscosity. The final result of their interaction is the current distribution of isograds. Therefore, it is not possible to explain nappe emplacement with only one end-member, and both only-advection or only-shear heating dominated geodynamic scenarios are incomplete (*figure 5.1B-ii* and *B-iii*, *C-ii* and *C-iii*).

A limitation of our thermo-kinematic model approach is that we modelled only the T evolution during thrusting, whereas isograds are indicative of both T and P conditions (peak T and P at peak T). The choice of referring to isotherms' distribution is justified by the focus of this thesis, which was to study the heat budget of the Lepontine dome, quantified through the peak T record. We chose to investigate T evolution through thermo-kinematic numerical models because they are able to display in a simple way the main controlling factors of this geological problem. For more insights we refer to thermo-mechanical numerical models which can predict more variables, such as the peak P conditions (e.g., [Candioti et al., 2021](#); [Vaughan-Hammon et al., 2022](#)). Anyway, the overall behavior described in our thermo-kinematic models matches what is observed in these more complex numerical models.

5.4 The importance of local heat sources

Shortly after the peak of Barrovian conditions in the Lepontine dome, the area cooled non-homogeneously. We studied this cooling at close-to-peak T conditions through multicomponent-diffusion modelling in garnet. The compositional re-equilibration of garnet rims happened in the post-peak T phase, around 31 Ma, before garnet closure T (see details in *Chapter 3 – section 3.5.3.1.2*). The cooling was fast (100-400 °C/Myr) for rocks on the Maggia-Adula tectonic contact, slow (2 °C/Myr) for footwall rocks (base of Simano nappe), and medium (20-50 °C/Myr) for the rocks of the SSB. Low cooling rates below 10 °C/Myr in the lowermost tectonic levels of the nappe stack are coherent with the regional exhumation of the Lepontine area between 25-30 Ma (< 20 °C/Myr in [Schlunegger & Willett \(1999\)](#)). An additional, local, heat source identified as shear heating acted within the shear zone and determined high cooling rates above 100 °C/Myr. Thus, shear heating effectively contributed to the Barrovian imprint of the Lepontine dome within the Maggia-Adula shear zone.

5.4.1 Shear heating vs. Fluids

Some authors may argue that the percolation of hot fluids or melts could have caused the local, transient heating shown by high cooling rates and the genesis of migmatites on the Maggia-Adula thrust. In *Chapter 3* and *Chapter 4* we discussed this critical issue and we discarded this hypothesis based on field observations (absence of amphiboles in the main mineral assemblage of migmatites and too small volumes of veins during metamorphism). Furthermore, since syn-foliation veins are present also in the core of the dome, such a scenario of fluid-induced melting would have caused a geological asset similar to the SSB, where medium cooling rates are recorded.

The absence of extensive migmatization in the core of the Lepontine dome goes against a geodynamic scenario where multiple hot-fluids injections happened at different levels of the nappe pile (*figure 5.1B-i* and *C-i*). Also, there is no record of magmatic intrusions which would have caused a local T increase and local inverted-metamorphism at various levels of the nappe stack.

5.4.2 Timing of shear heating

In *Chapter 2* we deduced that shear heating can happen in the very first stage of overthrusting before an early viscosity drop, but also in a second stage due to strain or velocity increase.

We propose that the first phase when shear heating acted, corresponded to the onset of thrusting at 38-40 Ma (e.g., [Herwartz et al., 2011](#); [Sandmann et al., 2014](#)). The record of this early phase is found in the migmatitic aureoles around the mafic and ultramafic rocks of the Cima Lunga unit, where monazite and zircon U–(Th)–Pb dating reveals Alpine ages around 35-38 Ma ([Corvò et al., in review](#)).

The second stage when the heat transfer equilibrium moved toward the shear heating term could have taken place simultaneously with two possible processes. One process was likely enhanced by the strongly non-homogeneous geological asset of the Maggia-Adula shear zone and it is represented by strain and strain rate concentration around the Cima Lunga heterogeneities (mafic and ultramafic rocks) and on the Maggia-Adula thrust. The partial melting associated to this feasible local strain accumulation was dated at 30-33 Ma around Cima Lunga heterogeneities (monazite and zircon U–(Th)–Pb dating in [Corvò et al. \(in review\)](#)), and at 31 Ma (this thesis) in syn-kinematic migmatites on the Maggia-Adula thrust. The other possible process could have been a conspicuous increment in the emplacement velocity of the Maggia-Adula shear zone (above 10-20 cm/yr). For this latter case, the required velocities are too high with respect to the exhumation velocities proposed for the Lepontine dome (e.g., ca. 3 cm/yr for Cima Lunga in [Piccoli et al. \(2021\)](#)). Even though, we can imagine that a short-term velocity phase might have happened at some point (likely around 31 Ma) in the exhumation history.

Figure 5.2. Overview on the results of this thesis. All the abbreviations correspond to figures in the precedent chapters of this thesis (panel A: figure 1.6; panel B: figure 2.4 and 2.6; panel C: figure 3.2, 3.6, 3.11, 4.6). In panel (A): the initial working hypothesis which resulted to be feasible for the explanation of the origin of the Lepontine Barrovian metamorphism. (A') reproduces these results in the same scale of the tectonic profile (the location is indicated in yellow in panel C). Panel (B): results of the 2D thermo-kinematic numerical model with shear heating and T -dependent viscosity, v indicates the velocity. On the right are displayed the two possible explanations for the dominance of the shear heating term in the scenarios of shear zone with a thickness d (less than 1 km for the Maggia-Adula shear zone, see panel C) and buoyancy-driven exhumation. Panel (C): schematic tectonic section of the Lepontine dome with position of all samples and relevant zircon U-Pb Alpine ages (Chapter 3), post-peak T and P , and cooling rates (CR) (Chapter 4). To the right, cathodoluminescence of a zircon from sample AV19.7 with LA-ICP-MS points analyses and ages, and photos of migmatites in the field. An online version of this figure is available at: <https://zenodo.org/record/8399771>.

5.5 Possible outlooks

Our work permitted us to better understand the heat associated to the formation of the Lepontine dome of the Central Alps as an example of collisional Barrovian metamorphism. In this thesis we addressed the main questions concerning the relationships between Barrovian metamorphism and shear zones activity. All the results are summarized in [figure 5.2](#), divided into panels corresponding to the topics investigated in our research.

In addition to what has already been discussed, here we propose more possible target studies specific to the Lepontine area.

5.5.1 Geodynamic scenarios and numerical models

In the previous sections we mentioned which geodynamic scenarios should be discarded for the interpretation of the origin of the Lepontine Barrovian metamorphism. In *panel A* of [figure 5.2](#) we show that the scenario which combines advection, diffusion and shear heating suits our results best (case corresponding to [figure 5.1B-iv](#) and [C-iv](#)). Our 2D thermo-kinematic numerical models, shown in *panel B* of [figure 5.2](#), calculate indeed the contribution of all these three terms. However, in these models (i) the thrust has no thickness and (ii) the velocity is kept constant. We demonstrated that in natural scenarios these two aspects must be considered.

Thermo-mechanical numerical models can be employed to address this gap. Numerical models applied to the Lepontine dome could be adopted to monitor the change in viscosity, peak temperature-pressure conditions and localization of migmatization over time, together with velocity fluctuations of markers at different crustal-depths. Such study could be applied to the heating phase during the prograde path from the beginning of nappe emplacement at 38 Ma to the last phases at 31 Ma. A possible application could put together these numerical simulations with analyses of samples

collected in the field. Prograde P-T paths predicted by thermo-mechanical numerical models can be used as prescribed heating path for the calculation of garnet compositions, following for example what has been done by [Caddick et al. \(2010\)](#). The model results could then be compared with natural samples from the Lepontine dome.

5.5.2 The geochronology of the Cima Lunga unit

Panel C of [figure 5.2](#) displays the extensive sampling and dating that we performed to characterize the Maggia-Adula shear zone. In this figure are not shown the older non-Alpine ages which, for instance, permitted us to define the Cima Lunga unit as a pre-Variscan sedimentary basin.

Some of the samples we collected within the Cima Lunga unit contain garnets with pre-Alpine cores (see *Appendix G* and *D*). Dating these garnets (e.g., Lu-Hf dating) would permit us to tackle the age of their cores (Variscan or pre-Variscan) and of the recorded Alpine history at their rim.

We should mention that so far, the interpretation of garnet ages from high-grade rocks is subjected to uncertainties (e.g., crystallization vs. cooling ages; e.g., [Dutch & Hand, 2010](#); [Smit et al., 2013](#)). We believe that the application of garnet geochronology in such a well-studied area as the Cima Lunga unit, where field data and U-(Th)-Pb zircon and monazite ages are already available, would be a perfect case study to contribute towards a deeper understanding of the garnet-dating technique.

Appendix A

ANALYTICAL METHODS AND EVALUATION OF UNCERTAINTY IN LA-ICP-MS

Our case study required an interdisciplinary geological, petrological, thermodynamic, geochronological and numerical approach. Extensive geological mapping and rock sampling across multiple sections along the nappe pile were the basis of our work. Detailed description of the rock types, their field relationships and structures are necessary to constrain the relationships between and within the Lepontine nappes.

Geological survey at scale 1:10.000 was performed at the University of Applied Sciences and Arts of Southern Switzerland (SUPSI) and covered multiple locations in Ticino and Grisons at variable altitudes (mostly above 1500-2000 msl, up to ca. 2720 msl). This work has been carried out in parallel with the geological mapping for swisstopo for the production of the new Swiss National geological maps 1:25.000 n°1293 Osogna, 1273 Biasca, 1294 Grono, 1274 Mesocco, 1254 Hinterrhein.

The collected samples were analyzed at the University of Lausanne (UNIL) and Johannes-Gutenberg University Mainz (JGU). In this appendix we briefly review the applied analytical methods. These techniques and the conditions of work for each instrument are described in detail in *Chapter 3* and *Chapter 4* and in the relevant supplementary material (*Appendix D*). Also, a detailed discussion on the evaluation of uncertainty in geochronological analyses is described, with a focus on LA-ICP-MS technique.

X-ray Micro-Computed Tomography (CT)

We adopted the X-ray Computed Tomography to visualize the internal 3D geometries of a garnet-bearing rock sample which was cut for the realization of thin (30 μm thickness) and thick (80 μm) sections.

The CT is a non-destructive technique which permits to obtain digital information of solid objects. The instrument is equipped with an X-ray source, a series of detectors measuring X-ray intensities along multiple beam paths (CCD camera), and a rotational stage on which the sample is placed. We used a SKYSCAN 1273 equipped with an X-ray tube source (Hamamatsu L9181-02) which worked at 100 kV source voltage and 150 μA source current, and a CCD camera (DEXELA-2315[v2], S/N 55043) with 74.8 μm pixel size which produced 13.0 μm pixel size images. The rotation step was 0.25 degrees.

Raman Spectroscopy

We adopted Raman spectroscopy to identify the nature of crystal inclusions in a garnet from the Cima Lunga paragneisses. Raman is a non-destructive chemical analysis technique which provides information about the chemical structure and crystallinity of mineral samples. The instrument consists in a spectrometer and is equipped with an optical microscope and a source of monochromatic light (laser) which is focused on the sample surface.

We used the confocal high-resolution Raman spectrometer LabRam HR800 (HORIBA Scientific, Jobin-Yvon). The microscope is an Olympus BX1, which is coupled confocally to an 800 mm focal length spectrograph. The spectrograph is equipped with two switchable gratings (600 l/mm and 1200 l/mm or 2400 l/mm), an external (Diode laser 532 nm) and internal (He-Ne 633 nm) laser, and a 1024 x 256 pixels CCD detector.

Raman permits to obtain a spectrum with specific features such as number, height and width of peaks, which represent a distinct chemical fingerprint and hence is used for the identification of specific materials.

Electron Probe Microanalyzer (EPMA)

The Electron Probe Microanalyzer is an instrument used for the in situ non-destructive chemical analysis of solid samples. We used the EPMA to get quantitative chemical analyses of point, lines and to get X-ray maps of specific domains in thin and thick sections (see *Chapter 4*).

The instrument works in vacuum conditions and is equipped with an electron gun and a series of lenses which produce a focused electron beam interacting with the sample to generate back-scattered electrons (BSE), secondary electrons (SE) and characteristic X-rays. These X-rays are used to obtain a quantitative chemical analysis. The sample surface must be perfectly polished and carbon-coated prior to the analysis. The detection limit of EPMA is ca. 100 ppm.

Scanning Electron Microscopy (SEM)

The Scanning Electron Microscope is an electron microscope capable of producing images of the surface of solid specimens. This instrument uses a focused high-energy electron beam which interacts with the sample in a low-vacuum chamber. Similarly to what happens in the EPMA, the interaction between electron beam and sample generates a series of signals. These signals include also visible light (cathodoluminescence, CL) which we used for the characterization of the internal structure of zircon crystals and to distinguish zircon growth domains (see *Chapter 3*).

Laser Ablation Inductively-Coupled Plasma Mass Spectrometry (LA-ICP-MS)

ICP-MS is a technique which permits the determination of elemental composition and isotope ratios of both solid and liquid samples.

The sample to analyze is introduced in an Ar plasma torch running at atmospheric pressure. The material in the torch is ionized and ions are directed into the vacuum part of the spectrometer. This material is focused into an ion beam through a collimator system. Then the ion beam is separated according to the mass or charge ratio in a mass discriminator and counted by an ion detector.

In the Laser Ablation technique, the analysis is done in situ and the sample is introduced in the torch through an ablation. In this procedure, a laser beam is focused on the specimen inside an ablation cell through which He flows. The laser leaves an ablation crater on the sample surface.

The detection limit for LA-ICP-MS is 0.01 ppm.

The LA-ICP-MS is the technique we used for zircon U-Pb dating and trace element analyses (see *Chapter 3*).

Secondary Ion Mass Spectrometry (SwissSIMS ion probe)

Similarly to LA-ICP-MS, SIMS is an in situ technique which adopts a mass spectrometer for the determination of compositions and isotope ratios, but only for solid samples which must be stable under vacuum.

The instrument consists of a primary beam ion source (O^- , O^{2-} , Cs^+) connected to a mass spectrometer equipped with energy and mass filters. The primary ion beam is used to bombard the specimen which ejects secondary ions. The secondary ions are then accelerated through the instrument and the resulting secondary ion beam is magnified prior to entering in a double-focusing mass spectrometer. Finally, the ions are collected by a detection system to record the magnitude of the secondary ion signal (i.e., Faraday cup or electron multiplier). The ions of interest can be detected either in mono-collection or multi-collection mode.

The detection limit of SIMS is below 1 ppm (between 0.01-1 ppm), although it depends on the element ionization yield.

We employed the SwissSIMS ion probe in one session for U-Pb zircon dating (see *Chapter 3*).

Uncertainty in U-Pb LA-ICP-MS analyses

Uncertainty in LA-ICP-MS measurements was considered by many only as a problem of short-term precision, where the dispersion of measurement data around a mean age is related to the uncertainty of the intensity ratio and of the relative sensitivity factor derived from calibration(s) performed on the day of measure. This approach has many advantages: conceptual simplicity, rigorous propagation of uncertainties (confidence intervals) of the input parameters, negligible role of empirical assumptions. Also, this approach permits to have small uncertainty values. However, it does not consider the role of inaccuracies.

Within their small short-term (or measured) uncertainties, U-Pb dates obtained by LA-ICP-MS are not always matched with the ‘reference’ age that can, for example, be obtained for the same sample by ID-TIMS. Moreover, the above mismatch cannot be fully eliminated by known technical means (e.g., sample annealing, ‘soft’ ablation settings, robust spectrometer optimization, a ‘better’ intensity ratio definition), but it can only be reduced. One solution to fix inaccuracy problems is to consider inaccuracy as a sort of imprecision, applying a method where the uncertainty value for the studied sample is increased in order to include such inaccuracy in the uncertainty value. The following paragraphs aim to systematically describe the mathematical and technical implementation of this solution.

When series of analyses of the same sample (e.g., a large homogeneous zircon) are performed in different days, the mean age for a particular day can be different from the reference age of the sample within its short-term uncertainty. Also, the mean ages of the different days might not match and can deviate one from the other as much as 1.5-2% (*figure A.1*). In the extreme case, the *grand* mean computed over many days can be biased relative to the reference age (not the case observed in the ICP-MS laboratory of the University of Lausanne involved in obtaining data for this thesis).

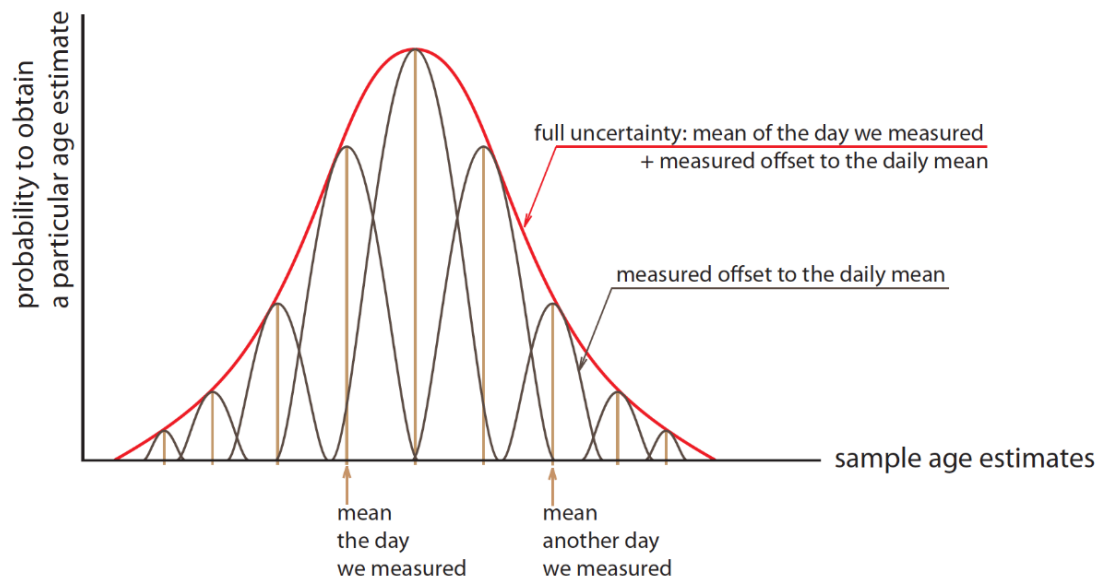


Figure A.1. Visualization of the short-term and full-term uncertainties relevant to sample age estimates. The probability to obtain a specific age estimate depends on the measured mean ages of single days of analyses with their offsets, and on the variation between different days of analysis.

The described process is non-stationary, i.e., a statistical process in which the mean value is a random parameter. Any sample age can be represented as:

$$\text{sample age} = \text{mean of the day of measure} + \text{offset to that mean}$$

Where the *sample age* can represent either the sample age from an individual ablation spot or the mean of several individual sample spots with a reduced uncertainty. Consequently, the variance of the sample age is defined as:

$$\text{Var}(\text{sample age}) = \text{Var}(\text{mean of the day of measure}) + \text{Var}(\text{offset to that mean})$$

Here, $\text{Var}(\text{mean of the day of measure})$ is called long-term, or systematic uncertainty. It can also be designated as $\text{Var}(\text{mean day-to-day})$. Whereas, $\text{Var}(\text{offset to that mean})$ is called short-term, or measured uncertainty characterizing the scatter between the replicate age estimates obtained during a single day or estimated from intensity and calibration statistics for a particular spot analysis. The short-term uncertainty is reported by default in a data reduction software (e.g., Lamtrace). The evaluation of the systematic uncertainty is not trivial, since the replicated analysis of the same sample for many days is not sustainable. Hence, two methods can be applied for the evaluation of the systematic uncertainty: analytical and empirical. Both of them contain empirical assumptions, and both do not provide a deterministic estimate of $\text{Var}(\text{mean of the day of measure})$. Indeed, they establish a maximum value for this variance that corresponds to the upper limit confining the full sample age uncertainty between the short-term (measured) and maximum full uncertainty values.

The analytical method

The conventional data reduction scheme of LA-ICP-MS is based on the single-standard calibration of the relative sensitivity factor (Longerich et al., 1996). This method consists in the analysis of a primary standard, often in replicates, to obtain the relative sensitivity as intensity ratio divided by mass abundance ratio.

For a primary standard, in the case of ^{206}Pb and ^{238}U isotopes, the following equation applies:

$$\frac{I^{206}}{I^{238}} = \beta \frac{C^{206}}{C^{238}} \quad (1)$$

The left side of the equation is the net intensity ratio defined by the analysis of the standard by LA-ICP-MS. On the right side, the relative sensitivity factor β is multiplied by the mass abundance ratio of the measured isotopes. The relative sensitivity factor is the only unknown of this equation and represents the main outcome of the standardization process, computed as:

$$\beta = \frac{I^{206}/I^{238}}{C^{206}/C^{238}} \quad (2)$$

The equation 1 is then applied to a sample. The relative sensitivity factor is assumed to be the same as obtained from the primary standard, and mass abundance ratio can thus be computed:

$$\frac{C^{206}}{C^{238}} = \frac{I^{206}/I^{238}}{\beta} \quad (3)$$

The uncertainty is defined accordingly:

$$\text{Var}\left(\frac{C^{206}}{C^{238}}\right) = \text{Var}\left(\frac{I^{206}/I^{238}}{\beta}\right) \quad (4)$$

This uncertainty equation depends on the knowledge of three terms: $\text{Var}(\beta)$; $\text{Var}\left(\frac{I^{206}}{I^{238}}\right)$; $\text{Covar}\left(\frac{I^{206}}{I^{238}}, \beta\right)$. The variance of the relative sensitivity factor can be computed from the day-to-day statistics of β obtained using the same instrument and measurement protocol. The intensity ratio uncertainty can be assessed using the statistics of the intensity ratio from the standard. Differently, the covariant term cannot be estimated.

Therefore, the deterministic solution is substituted by a limiting solution that yields a maximum

$$\text{limit for } Var \left(\frac{I^{206}}{I^{238}} / \beta \right)_{sample} .$$

An empirical postulate is the base of the evaluation of this limiting solution: the scatter of

$$\left(\frac{I^{206}}{I^{238}} / \beta \right)_{sample} \quad \text{when both intensity ratio and } \beta \text{ are random and co-vary is smaller than the scatter}$$

where intensity ratio is fixed and only β is random. This postulate is supported by data from the

LA-ICP-MS laboratory of the University of Lausanne, but also comes naturally from the equation:

$$\frac{\left(\frac{I^{206}}{I^{238}} \right)_{sample}}{\beta} = \frac{\left(\frac{I^{206}}{I^{238}} \right)_{sample}}{\left(\frac{I^{206}}{I^{238}} \right)_{std} / \left(\frac{C^{206}}{C^{238}} \right)_{std}} \quad (5)$$

If the mean intensity ratio for the standard increases (β increases), also the mean intensity ratio for the sample will likely increase on the same day of measure.

Consequently, the maximum estimate for the long-term sample uncertainty in the $^{206}\text{Pb}/^{238}\text{U}$ system is:

$$Var \left(\frac{C^{206}}{C^{238}} \right)_{sample} = Var \left(\frac{\left(\frac{I^{206}}{I^{238}} \right)_{sample}}{\beta} \right) = \left(\left(\frac{I^{206}}{I^{238}} \right)_{sample} \right)^2 Var \left(\frac{1}{\beta} \right) = \frac{\left(\left(\frac{I^{206}}{I^{238}} \right)_{sample} \right)^2}{\beta^4} Var(\beta) \quad (6)$$

Or, in alternative notation:

$$Var \left(\frac{C^{206}}{C^{238}} \right)_{sample} = \frac{\left(\left(\frac{C^{206}}{C^{238}} \right)_{sample} \right)^2}{\beta^2 \left(\left(\frac{C^{206}}{C^{238}} \right)_{std} \right)^2} Var \left(\frac{I^{206}}{I^{238}} \right)_{std} \quad (7)$$

$$s \left(\frac{C^{206}}{C^{238}} \right)_{sample} = \frac{\left(\left(\frac{C^{206}}{C^{238}} \right)_{sample} \right) s \left(\frac{I^{206}}{I^{238}} \right)_{std}}{\beta \left(\left(\frac{C^{206}}{C^{238}} \right)_{std} \right)} \quad (8)$$

The minimum estimate for the long-term uncertainty is zero, implying a full correlation between the sample intensity ratio and β means per day. This is the case when the sample is equal to the primary standard.

Summarizing, the full uncertainty for an individual sample is thus given as a range. The minimum limit corresponds to the measured uncertainty of the day of the analysis (of a particular spot or sample). The maximum limit is the sum of the maximum value of the long-term uncertainty and the measured uncertainty.

In conclusion, the analytical method is theoretically valuable, because it illustrates statistical ideas and limitations behind the concept of long-term uncertainty. But it is not entirely analytical since it contains an empirical postulate as a key part, whose implementation shows that this method may be too conservative.

For example, the most commonly used primary standard of the LA-ICP-MS laboratory of the University of Lausanne is a GJ-1, of which the scatter of the mean intensity ratio of each single day of analysis amounts to 0.003 (1s). The most commonly used secondary standard is Plesovice. On a particular day, the Plesovice yielded the following individual spot data:

$$\left(\frac{C^{206}}{C^{238}}\right)_{Plesovice} = 0.0541 \quad RSD\left(\frac{C^{206}}{C^{238}}\right)_{Plesovice} = 0.38\% = 0.0038 (1s)$$

$$s\left(\frac{C^{206}}{C^{238}}\right)_{Plesovice} = 0.0541 \cdot 0.0038 = 0.00021$$

Where *RSD* indicates the relative standard deviation, and *s* the uncertainty.

The maximum long-term uncertainty is estimated from *equation 8* as:

$$s\left(\frac{C^{206}}{C^{238}}\right)_{sample} = \frac{\left(\left(\frac{C^{206}}{C^{238}}\right)_{sample}\right) s\left(\frac{I^{206}}{I^{238}}\right)_{std}}{\beta\left(\left(\frac{C^{206}}{C^{238}}\right)_{std}\right)} = \frac{0.054 \cdot 0.003}{0.867 \cdot 0.098} = 0.00190$$

It follows that the maximum long-term uncertainty is 9-10 times higher than the measured uncertainty for an individual spot analysis. Such conservative behavior derives from the exclusion of the covariance term by means of the postulate described above, combined with significant day-to-day variations of the state of the spectrometer. It would be important to have a less conservative method providing a narrower uncertainty interval.

The empirical method

It is possible to approach the problem of the long-term (systematic) uncertainty with an empirical method. This methodology uses representative sets of zircon crystals with known reference ages (ID-TIMS) to establish a confidence interval. This confidence interval is usually in percentage points of the age obtained by replicate LA-ICP-MS measurements of the same sample zircon, into which its ID-TIMS age is expected to fall with some pre-defined, high probability.

The commonest implementation of this method implies that a set of 3-5 well known standard zircon crystals (e.g., Harvard 91500, Plesovice, Temora) is analysed by many replicate LA-ICP-MS measurements against a primary standard (e.g., GJ-1), allowing to compute a precise mean age for each of the above standard zircon crystals. Each of these mean ages is then compared to the respective reference age. The resulting differences would typically range from zero to $\pm 2\text{-}3\%$ of the reference age (Klötzli et al., 2009). This implementation is laboratory-specific and it is influenced by the hardware settings, choice of the standards (including the primary standard), timing (over how many days/years have been analyzed), and also by the possibility to enhance the statistics using sample zircon crystals with a well-defined ID-TIMS ages. In the ICP-MS laboratory of the University of Lausanne, at this time, the reference (ID-TIMS) age is confined within $\pm 1.6\%$ of inaccuracy on the LA-ICP-MS age, as shown by repeated analyses of reference zircon crystals and zircon samples with well interpretable ID-TIMS ages for several years using the same protocol. The relevant mathematical formalism can be described by the following example:

- Mean sample age, as measured by LA-ICP-MS = 22 ± 0.30 Ma (95% conf.)
- Maximum difference to the ID-TIMS age, assuming a worst inaccuracy of $1.6\% = 22 \cdot 0.016 = \pm 0.35$ Ma, which defines an interval from $22-0.35$ till $22+0.35$ Ma (from 21.65 to 22.35 Ma).
- The length of the confidence interval from 21.65 till 22.35 is assumed to be equivalent to $3s$.
- $1s = (22.35-21.65)/3 = 0.23$ Ma, $1.96s = 0.45$ Ma (95% conf.), respectively.

Combining the long-term and the measured uncertainty:

$$\text{Var}(\text{sample age}) = \text{Var}(\text{mean of the day of measure}) + \text{Var}(\text{offset to that mean})$$

$$\text{Var}(\text{sample age}) = 0.45^2 + 0.30^2 = 0.2925; \text{Uncertainty}(\text{sample age}) = 0.54 \text{ Ma (95\% conf.)}$$

Similar to the analytical method, the above calculations yield maximum estimates of the long-term and of the full uncertainty. The sample uncertainty thus remains unknown but it is confined by the measured uncertainty as the lower, and the maximum full uncertainty as the maximum limit. In the example above, this interval extends from 0.30 to 0.54 Ma (95% conf.).

It is worth emphasizing the limiting nature of the so-obtained estimates. The worst inaccuracy ever observed using a given set of hardware conditions and analytical protocol equally applies to any sample. On the other hand, if the unknown sample is the same as the primary standard, the long-term uncertainty is zero. Thus, depending on how well the primary standard and the sample are matched, the long-term uncertainty can be less than the worst inaccuracy computed above.

Also, this solution is highly empirical. The ‘representative set of reference zircon crystals may cover or not the long-term age variations of the unknown sample. Therefore, in this context, it is important to understand how well the primary standard and the other reference zircon crystals are matched, i.e., considering the long-term covariance parameter $Cov\left(\frac{I^{206}}{I^{238}}, \beta\right)$. The larger is the pool of reference zircon crystals and the longer is the period of observation, the better. Otherwise, there is a risk to be bound to a set of reference zircon crystals that are well matched with the primary standard used to calibrate the relative sensitivity factor. A representative implementation of the empirical method is given in the *figure A.2* below.

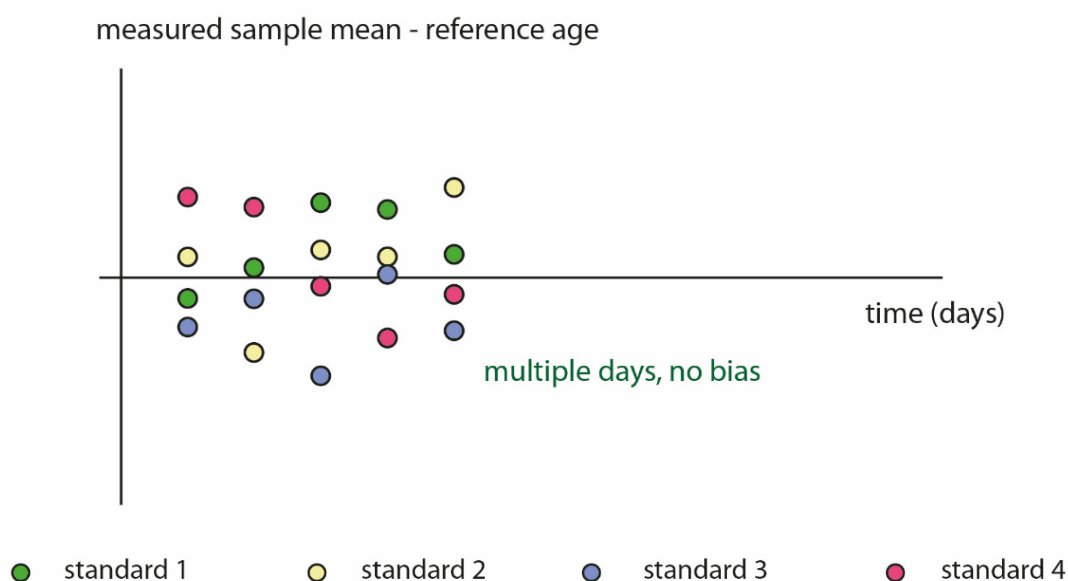


Figure A.2. Visualization of the implementation of the empirical method. The figure shows the variation in measured ages for four standards in different days, plotted with respect to the measured sample mean age/reference age. The bias related to the coupling between different standards is often reduced using a bigger number of standards or analyzing them for multiple days.

Secondly, it is not given that the differences between the mean age measured by LA-ICP-MS and the reference age are symmetrically distributed around zero, allowing to use a simple notation (e.g., $\pm 1.6\%$). As such measurements are bound to a single standard, a unidirectional bias is possible.

Thirdly, assigning a confidence level to a variation interval obtained for the reference zircon crystals (e.g., 0.45 Ma at 95% conf. in the above example) is an arbitrary step. In the example above, it may also be possible to assign the confidence interval from 21.65 till 22.35 to 2s, or 4s.

In conclusion, the empirical method has two clear advantages: it is simple and not excessively conservative. Currently, it is used by some SIMS laboratories (where data reduction schemes share some common aspects with LA-ICP-MS) and it also begins to be employed in the field of U/Pb LA-ICP-MS (Foley et al., 2023; Ruiz et al., 2022).

‘Trash generators’

One can notice that the analytical approach to the full uncertainty evaluation already contains an empirical term (the postulate at its base), on the other hand, the probabilistic meaning of standard deviation in the empirical approach vanishes to a variable extent depending how rigorously this approach is being implemented. As an alternative solution, some authors suggested to implement ‘trash generators’, i.e., adding an unexplained value or altering (increasing) the measured uncertainty in order to reduce or eliminate the potential inaccuracy.

The most frequently employed trash generator was introduced by Horstwood et al. (2016). According to them:

$$\begin{aligned} \text{Var}(\text{sample age, mean day-to-day} + \text{measured that day}) = \\ \text{Var}(\text{mean day-to-day from a secondary standard}) + \text{Var}(\text{measured that day}) \end{aligned}$$

The consequences of this solution are:

- When the secondary standard equals the primary standard, there is no long-term uncertainty.
- When the secondary and primary standards are coupled, there is a long-term uncertainty that depends on how well the two standards are matched. More precisely, it depends on the unknown covariance between sample intensity ratio and relative sensitivity factor β day-to-day.
- To use this approach, the sample must be equal to the secondary standard, which is unreal.

Other trash generators exist. All trash generators aim to provide a deterministic value to the full uncertainty, and not a min-to-max range.

Advice and outlook

What exposed above can be summarized in the following points:

- If one single primary standard is used, the long-term (systematic) uncertainty may be the dominant term of the total uncertainty. Hence, its role must be considered.
- The systematic uncertainty can be propagated through either an analytical or empirical approach. Currently, this latter is recommended, since the analytical approach seems to be more conservative.
- The empirical approach can be implemented at a variable level of rigor.
- Both measured and maximum full uncertainties (including the long-term) need to be reported with the measured data. However, caution needs to be exercised when introducing the long-term uncertainty in an age. Individual spot measurements should be reported with their measured uncertainties only, indeed introducing the long-term uncertainty in a particular spot analysis requires a randomizer. It is better to report the long-term uncertainties only for mean ages.
- In general, a multi-standard calibration can be applied. The multiple standard calibration of the relative sensitivity factor is a solution whose consequence is an increase of the measured uncertainty, and a decrease of the long-term uncertainty.

Selected references

In addition to the articles mentioned above, the following publications can be used as references:

[Ulianov et al., 2015](#); [Schaltegger et al., 2014](#).

Appendix B

CODE FOR DIMENSIONAL ANALYSIS (CHAPTER 2)

This appendix is available online at: <https://zenodo.org/record/8399771>.

The codes for dimensional analysis calculations described in *Chapter 2* have been uploaded onto the general-purpose open-access repository Zenodo in the folder *Dimensional analysis*: <https://zenodo.org/record/8399771>. Here follows the main code *Dimensional_Analysis.m*.

Matlab code for dimensional analysis

```
clear variables; close all; clc
figure(1)
% ~~~~~
%           DIMENSIONAL ANALYSIS : calculation of
%                               Pécelet and Brinkman numbers
% ~~~~~

%           VALUES
h           = 5e3; % thickness of nappe [m]
ramp        = 15; % ramp angle of the thrust [°]

T_0         = 500 + 273.15; % initial temp at the depth zf [K]
rho_c       = 2700*1e3;      % Density * Heat Capacity [J/m^3*K]
k           = 2.5;          % Thermal Conductivity [W/m*K]
k_diff      = k/rho_c;      % Thermal Diffusivity [m^2/s]

eta         = [5e19 5e20 5e21 5e22];          % Viscosity [Pa*s]
vx_bg_v     = [0:0.1:200];                    % Velocity [cm/yr]
% horizontal, prescribed, background velocity [m/s]:
vx_bg       = vx_bg_v *1e-2 / (3600*24*365.25);

% representative velocities for triplot [cm/yr]:
velocity = [0 0.5 1 2 3 5 10 20 50 100 200];

%=====

col = {'-g', '-b', '-r', '-m'}; % set colours for different viscosities

%           CALCULATIONS

A = ones(length(velocity),4,length(eta));

for ie = 1:length(eta)

    Pe(ie,:) = h*vx_bg*sind(ramp)/k_diff;% Peclet Number (Adv vs Diff)
    Br(ie,:) = eta(ie).*vx_bg.^2/(k*T_0);% Brinkman Number(Prod_sh vs Diff)

    hold on
    plot(Pe(ie,:),Br(ie,:),col{ie},'linewidth',1.5) % 2D Pe-Br plot

    % plot points with same background velocity and store Pe, Br values:

    VALUES = ones(length(velocity),4);

    for iv=1:length(velocity)

        % find index of matrix vx_bg_v with value = matrix velocity:
        item(iv) = find(abs(vx_bg_v)==velocity(iv));
        % plot the corresponding point in Pe-Br plot:
```

```

plot(Pe(ie,item(iv)),Br(ie,item(iv)),'ok','linewidth',1,...
     'HandleVisibility','off')

% plot isovelocity lines
% Pe corresponding to vx_bg_v = velocity(iv):
v_value_line = Pe(ie,item(iv));
plot((v_value_line*(ones(1,length(vx_bg_v))))),Br(ie,:),'k',...
     'linewidth',1,'HandleVisibility','off')
t = text(Pe(ie,item(iv)),1.65,['\leftarrow' ...
     num2str(vx_bg_v(item(iv))) ' cm/yr'])
t.Rotation = 60;
hold on

% calculate new dimensionless parameters for ternary plot
% (Duprat-Oualid et al., 2015)
R_adv(ie,:) = Pe(ie,item(iv)) /... % Advection contribution
             (Pe(ie,item(iv))+1+Br(ie,item(iv)));
R_diff(ie,:) = 1 /... % Diffusion contribution
             (Pe(ie,item(iv))+1+Br(ie,item(iv)));
R_pro(ie,:) = Br(ie,item(iv)) /... % Production contribution
             (Pe(ie,item(iv))+1+Br(ie,item(iv)));
values(ie,:) = [R_diff(ie,:) R_adv(ie,:) ...
               R_pro(ie,:) vx_bg_v(item(iv))];

VALUES(iv,:) = values(ie,:);

end

VALUES_eta(:, :, ie) = VALUES(:, :);

end

%=====

% 2D plot
plot([0 1 1],[1 1 0],'k','linewidth',2,'HandleVisibility','off')
plot([1 2],[1 2],'k','linewidth',2,'HandleVisibility','off')
axis equal
title({'Dimensional Analysis'})
le=legend('5*10^{19} Pas','5*10^{20} Pas','5*10^{21} Pas','5*10^{22} Pas');
set(le,'position',[0.6192 0.3891 0.1782 0.1883])
xlabel('Péclet Number'),ylabel('Brinkman Number')
axis([0 2 0 2])
hold off

set(gcf, 'Position', [[1032 409 664 541]])
stringg = ['print -dpng Dimensional_analysis','.png -r300'];eval(stringg);

%=====

% Ternary plot (modified after Theune, U. (2002-2005):
% https://www.mathworks.com/matlabcentral/fileexchange/7210-ternary-plots
% MATLAB Central File Exchange)

figure(2)
warning off MATLAB:griddata:DuplicateDataPoints

[h,hg,htick]=terplot; % Plot the ternary axis system
colormap(colorcube)
set(gca, 'ColorScale', 'log')

```

```
for ie = 1:length(eta)
    A = VALUES_eta(:,:,ie); % diff - adv - pro - v(cm/yr)
    eta_new = eta(:,ie);
    [hd,hcb]=ternaryc(A(:,1),A(:,2),A(:,3),A(:,4),'o',eta_new); % Plot data
end

    hlabels=terlabel('R diff','R adv','R pro');
    hold on

set(gcf, 'Position', [[1032 409 664 541]])
stringg = ['print -dpng Dimensional_analysis_triplet','.png -r300'];...
    eval(stringg);
```

Appendix C

CODE FOR 2D THERMO-KINEMATIC MODELS AND NUMERICAL MODEL RESULTS (CHAPTER 2 AND CHAPTER 3)

This appendix is available online at: <https://zenodo.org/record/8399771>.

The codes for the 2D thermo-kinematic numerical models described in *Chapter 2* have been uploaded onto the general-purpose open-access repository Zenodo in the folder *Thermokin_model*: <https://zenodo.org/record/8399771>. Here follows the main code *TK_code.m*. A movie resulting from the numerical simulation with shear heating and temperature-dependent viscosity has also been uploaded (*Movie_overthrust.avi*).

Matlab main code for 2D thermo-kinematic model

```
clear variables; close all; clc

% ~~~~~
%                               INPUT
% ~~~~~

movie           = 0;
% PLOTTING
grids           = 0; % plots the Lagrangian and Eulerian grids
plot           = 1; % main nappe emplacement plot
zoom           = 0; % nappe emplacement plot: zoom on the thrust ramp
values         = 0; % plots the variation of viscosity,
                % radiogenic heating, shear heating term

% MODEL CONDITIONS
Tdep_eta       = 1; % T-dependent viscosity?
SH             = 1; % Shear heating?
H_depth       = 0; % Depth-dependent radiogenic heating (exp decay)?

% STORE VALUES
% save temperature and viscosity values for each timestep?
T_and_eta     = 0;
% save viscosity values on the reference point stored for each timestep ?
T_and_eta_ref = 0;
% calculate and save Pe, Br values?
dimless_num   = 0;

% TIME
tt            = 300; % [s]
time_tot      = 5.1 * (3600*24*365.25*1e6);
% GEOMETRY
v_angle       = 15*pi/180; % rotation angle
                % (for Lagrangian Velocity-grid) [rad]
ramp          = 15*pi/180; % theta angle [rad] == ramp angle
height        = 5*1e3;    % height of the ramp [m]

% PHYSICS
grad          = 0.01;    % Geothermal Gradient [K/m]
k             = 2.5;    % Thermal Conductivity [W/m*K]
rho_c        = 2700*1e3; % Density * Heat Capacity [J/m^3*K]
DcT          = k/rho_c; % constant Thermal Diffusivity [m^2/s]
eta0         = 1e21;    % Viscosity [Pa*s]
Q            = 2e5;    % Activation Energy [J/mol]
R_gas        = 8.314;   % Gas constant [J/K*mol]
H_rad_surf   = 5e-7;   % Rad Heat Prod at the surface [W*m^-3]
% length scale for rad heat prod decrease with depth [m]:
hr           = 1e4;
```

```

% horizontal, prescribed, background velocity [m/s] (to obtain Pe=1):
% vx_bg = 0.60649*1e-2 / (3600*24*365);

% horizontal, prescribed, background velocity [m/s]:
vx_bg = 2 * 1e-2 / (3600*24*365);

T_0_viscosity = 500 + 273.15; % reference temperature [K]

% NUMERICS
dt = 0.05;
nt = ceil(tt/dt);
nout = 50;

% INITIAL
time = 0;

% ~~~~~
% TEMPERATURE
% ~~~~~

Lx_T = 130*1e3; % [m]
y_lowernappe_T = 20*1e3; % [m]
Ly_T = 30*1e3 + y_lowernappe_T; % [m]
nx_T = 100;
ny_T = 50;
dx_T = Lx_T / (nx_T - 1);
dy_T = Ly_T / (ny_T - 1);
x_T = 0:dx_T:Lx_T;
y_T = 0:dy_T:Ly_T;
% 2D coordinate grid for Temperature (Eulerian > fixed):
[X_T Y_T] = ndgrid(x_T, y_T);

x_vx_T = -dx_T/2:dx_T:Lx_T+dx_T/2;
% 2D coordinate grid for Vx (Eulerian):
[X_Vx_T Y_Vx_T] = ndgrid(x_vx_T, y_T);
y_vy_T = -dy_T/2:dy_T:Ly_T+dy_T/2;
% 2D coordinate grid for Vy (Eulerian):
[X_Vy_T Y_Vy_T] = ndgrid(x_T, y_vy_T);
% 2D coordinate grid for Velocity differentials:
[X_diffV Y_diffV] = ndgrid(x_vx_T, y_vy_T);

VX_T = zeros(size(X_Vx_T));
VY_T = zeros(size(X_Vy_T));

% fault
xramp_T = Lx_T/5; % starting point (in x coordinate) [m]

% reference point
x_ref_T = xramp_T + height*cot(ramp);
y_ref_T = height + y_lowernappe_T;

% NUMERICS
dt_diff_T = 1/4.1*min(dx_T, dy_T)^2/DcT;

% Initial Temperature profile
% set initial temperature on the reference point:
T(ceil(x_ref_T/dx_T), ceil(y_ref_T/dy_T)) = T_0_viscosity;
% temperature at the bottom of the Tgrid:

```

```

T_bottom_T      = T_0_viscosity + grad*(height+y_lowernappe_T);

% initial temperature (set on the Tgrid):
T_0             = T_bottom_T*ones(size(Y_T)) + grad.*(-Y_T);

if H_depth == 1
    % depth-dependent heat production (exponential decay)
    [T, H_rad] = radiogenic_heat_production(H_rad_surf,hr,T_0,Y_T,nt,...
        dt_diff_T,time,DcT,rho_c,dx_T,dy_T);
elseif H_depth == 0
    % constant radiogenic heat production
    [T, H_rad] = radiogenic_heat_production_constant(H_rad_surf,hr,T_0,...
        Y_T,nt,dt_diff_T,time,DcT,rho_c,dx_T,dy_T);
end
T_INI          = T;

% ~~~~~
%                               KINEMATICS
% ~~~~~

Lx_V           = 190*1e3;                % [m]
y_lowernappe_V = 60*1e3;                % [m]
Ly_V           = 70*1e3 + y_lowernappe_V; % [m]
nx_V           = 150;
ny_V           = 75;
dx_V           = Lx_V/(nx_V-1);
dy_V           = Ly_V/(ny_V-1);
x_V            = 0:dx_V:Lx_V;
y_V            = 0:dy_V:Ly_V;
% 2D coordinate grid for Velocity (Lagrangian > moving):
[X_V Y_V]      = ndgrid(x_V,y_V);

VX_V           = zeros(size(X_V));
VY_V           = zeros(size(Y_V));

% fault
xramp_V        = Lx_V/5;                % starting point (in x coordinate) [m]

% reference point
x_ref_V        = xramp_V + height*cot(ramp);
y_ref_V        = height + y_lowernappe_V;

% Minimize Eq. 11.8 to obtain gamma from the input ramp angle (theta)
% (Allmendinger et al., 2011)
options        = optimset('display','off');
gamma          = fzero('SuppeEquation',1.5,options,ramp);
% Compute slip ratio R (Eq. 11.8)
R              = sin(gamma - ramp)/sin(gamma);

% Geometry
% define fault geometry:
yf_V = faultgeometry(X_V,nx_V,x_V,xramp_V,height,ramp,y_lowernappe_V);
% define line 1 (between domains 1-2):
y1_V = -tan((pi-ramp)/2)*x_V + xramp_V*tan((pi-ramp)/2) + y_lowernappe_V;
% define line 2 (between domains 2-3):
y2a_V = (sin(ramp)/(cos(ramp)-R)) * x_V ...
        - (sin(ramp)/(cos(ramp)-R)) * (xramp_V+height*cot(ramp)) + height ...
        + y_lowernappe_V; % from eq. 11.12 (used for stage a)
y2b_V = -tan((pi-ramp)/2)*x_V ...
        + (xramp_V+height*cot(ramp))*tan((pi-ramp)/2) + height ...
        + y_lowernappe_V; % (used for stage b)

```

```

% ~~~~~
% ACTION
% ~~~~~

it = 0;
while time < time_tot
    it      = it+1;
    time    = time + dt;

    % VELOCITY FIELD
    for ix = 1:nx_V
        for iy = 1:ny_V
            [VX_V VY_V] = velocityfield(it,ix,iy,Y_V,X_V,VX_V,VY_V,...
                yf_V,xramp_V,ramp,height,vx_bg,R,dt);
        end
    end

    % ROTATION of the kinematic grid (Vgrid)
    % velocity field
    VX_V_rot = VX_V*cos(v_angle) - VY_V*sin(v_angle);
    VY_V_rot = VY_V*cos(v_angle) + VX_V*sin(v_angle);
    % grid
    X_V_rot  = X_V*cos(v_angle) - Y_V*sin(v_angle);
    Y_V_rot  = Y_V*cos(v_angle) + X_V*sin(v_angle);
    % reference point (reference point on the Vgrid)
    x_ref_V_rot = x_ref_V*cos(v_angle) - y_ref_V*sin(v_angle);
    y_ref_V_rot = y_ref_V*cos(v_angle) + x_ref_V*sin(v_angle);
    %Fault
    xf_V_rot    = x_V*cos(v_angle) - yf_V*sin(v_angle);
    yf_V_rot    = yf_V*cos(v_angle) + x_V*sin(v_angle);

    % difference between the coordinates of the reference points
    dX_ref_rot = x_ref_V_rot - x_ref_T;
    dY_ref_rot = y_ref_V_rot - y_ref_T;
    % grid
    X_V_rot    = X_V_rot - dX_ref_rot;
    Y_V_rot    = Y_V_rot - dY_ref_rot;
    % reference point
    x_ref_V_rot = x_ref_V_rot - dX_ref_rot;
    y_ref_V_rot = y_ref_V_rot - dY_ref_rot;
    % fault
    xf_V_rot    = xf_V_rot - dX_ref_rot;
    yf_V_rot    = yf_V_rot - dY_ref_rot;

    % INTERPOLATION of the velocity field on the Temp grid (Eulerian)
    [VX_T] = griddata(X_V_rot,Y_V_rot,VX_V_rot,X_Vx_T,Y_Vx_T,'nearest');
    [VY_T] = griddata(X_V_rot,Y_V_rot,VY_V_rot,X_Vy_T,Y_Vy_T,'nearest');

    %=====
    % PLOT grids & velocity arrows
    if grids == 1
        new_gridplot(x_ref_T,y_ref_T,X_V_rot,Y_V_rot,X_T,Y_T,...
            x_ref_V_rot,y_ref_V_rot,VX_V_rot,VY_V_rot,xf_V_rot,...
            yf_V_rot,X_Vx_T,Y_Vy_T,VX_T,VY_T,T);
    end
    %=====

    % time-steps
    dt_adv_T = min(dx_T/max(abs(VX_T(:))),...
        dy_T/max(abs(VY_T(:))))/10.1; % time-step for advection

```

```

dt          = min(dt_diff_T,dt_adv_T);

% CALCULATIONS
% Strainrates
dVX_dx      = diff(VX_T,1,1)/dx_T;
dVY_dy      = diff(VY_T,1,2)/dy_T;

dVX_dy      = diff(VX_T,1,2)/dy_T;
dVX_dy_c    = (dVX_dy(1:end-1,:) + dVX_dy(2:end,:))/2;
dVX_dy_c    = (dVX_dy_c(:,1:end-1) + dVX_dy_c(:,2:end))/2;

dVY_dx      = diff(VY_T,1,1)/dx_T;
dVY_dx_c    = (dVY_dx(1:end-1,:) + dVY_dx(2:end,:))/2;
dVY_dx_c    = (dVY_dx_c(:,1:end-1) + dVY_dx_c(:,2:end))/2;

if Tdep_eta == 0
    % Viscosity constant
    eta = eta0*ones(size(T));
elseif Tdep_eta == 1
    % Viscosity T-dep
    ex_fun      = (Q/R) .* (1./T-1./T_INI);
    ex_fun(ex_fun>0) = 0;
    ex_fun(ex_fun<-3) = -3; % lower cutoff

    eta = eta0 * exp( ex_fun );

    eta(eta>1e21) = 1e21;
    eta(eta<1e18) = 1e18;
end

% store_viscosity values at the reference point:
eta_ref(it) = eta(ceil(x_ref_T/dx_T),ceil(y_ref_T/dy_T));

if SH == 0
    H_shearheat = zeros(size(dVX_dx(2:end-1,2:end-1)));
elseif SH == 1
    % Shear Heating
    D_XY      = (dVX_dy_c(2:end-1,:) + dVY_dx_c(:,2:end-1))/2; % def
    D_YX      = D_XY;
    Tau_XX    = 2*eta(2:end-1,2:end-1).*dVX_dx(2:end-1,2:end-1);
    Tau_YY    = 2*eta(2:end-1,2:end-1).*dVY_dy(2:end-1,2:end-1);
    Tau_XY    = 2*eta(2:end-1,2:end-1).*D_XY;
    Tau_YX    = Tau_XY;

    H_shearheat = Tau_XX .* dVX_dx(2:end-1,2:end-1) + ...
        Tau_YY .* dVY_dy(2:end-1,2:end-1) + ...
        Tau_XY .* D_XY + Tau_YX .* D_YX; % [Pa/s] = [W/m^3]
end

% DIFFUSION-ADVECTION of Temp
qx      = - DcT*diff(T(:,2:end-1),1,1)/dx_T;
qy      = - DcT*diff(T(2:end-1,:),1,2)/dy_T;
dTdt    = (diff(-qx,1,1)/dx_T + diff(-qy,1,2)/dy_T) ...
    - VX_T(2:end-2,2:end-1).*diff(T(1:end-1,2:end-1),1,1)/dx_T ...
    - VY_T(2:end-1,2:end-2).*diff(T(2:end-1,1:end-1),1,2)/dy_T ...
    + H_shearheat/rho_c + H_rad(2:end-1,2:end-1)/rho_c;

dTdt_ad = - VX_T(2:end-2,2:end-1).*diff(T_INI(1:end-1,2:end-1),1,1)/...
    dx_T - VY_T(2:end-1,2:end-2).*diff(T_INI(2:end-1,1:end-1),1,2)/dy_T;

```

```

T(2:end-1,2:end-1) = T(2:end-1,2:end-1) + dTdt*dt;
T(1,:)             = T(2,:);
T(end,:)           = T(end-1,:);
T_INI(2:end-1,2:end-1) = T_INI(2:end-1,2:end-1) + dTdt_ad*dt;
T_INI(1,:)         = T_INI(2,:);
T_INI(end,:)       = T_INI(end-1,:);

% Calculate the coordinates of the points in the Lagrangian grid
% (ADVECTION GRID)
X_V(2:end,:) = X_V(2:end,:) + VX_V(2:end,:) * dt;
Y_V          = Y_V          + VY_V          * dt;

% REFINEMENT of Lagrangian mesh
horizontal_distance_V = X_V(2,(ceil(y_lowernappe_V/dy_V)+1)) - ...
    X_V(1,(ceil(y_lowernappe_V/dy_V)+1));
if horizontal_distance_V > 2*dx_V
    X_V_c = (X_V(1,:) + X_V(2:,:))/2;
    X_V   = [X_V(1,:); X_V_c; X_V(2:end,:)];
    Y_V   = [Y_V(1,:); Y_V(1,:); Y_V(2:end,:)];
    VX_V  = [VX_V(1,:); VX_V(1,:); VX_V(2:end,:)];
    VY_V  = [VY_V(1,:); VY_V(1,:); VY_V(2:end,:)];
end

%=====
% PLOT
if mod(it,nout)==0

    if plot ==1
        new_plot(T_INI,X_T,Y_T,T,X_Vx_T,Y_Vx_T,VX_T,VY_T,X_V_rot,...
            Y_V_rot,VX_V_rot,VY_V_rot,xf_V_rot,yf_V_rot,...
            H_shearheat,eta,Lx_T,Ly_T,y_T,time,dX_ref_rot,...
            dY_ref_rot,x_ref_T,y_ref_T,x_ref_V_rot,y_ref_V_rot);
    end
    % ZOOM ON THE RAMP
    if zoom == 1
        new_plot_zoom(X_T,Y_T,T,X_Vx_T,Y_Vx_T,VX_T,VY_T,X_V_rot,...
            Y_V_rot,VX_V_rot,VY_V_rot,xf_V_rot,yf_V_rot,...
            H_shearheat,Lx_T,Ly_T,y_T,time)
    end
    % PLOT values
    if values ==1
        plot_values(Y_T,T,eta,H_rad,rho_c,H_shearheat);
    end

%=====
% Create IMAGES for the movie
if movie == 1
    print(['./faultbendfold_' num2str(it,'%05d')],'-dpng','-r300')
end
%=====

end

%=====
% SAVE values
if T_and_eta == 1
    mkdir Temp_Visc
    [a, MSGID] = lastwarn();
    warning('off', MSGID)
    save(['./Temp_Visc/Temp_Visc' num2str(time./(3600*24*365*1e6),2)...
        '.mat'],'T','eta')
end

```

```

end
%=====

if dimless_num == 1
% ~~~~~~
% CALCULATION OF DIMENSIONLESS NUMBERS (Duprat-Oualid et al., 2015)
% ~~~~~~

Pe(it) = height*vx_bg/DcT;           % Peclet Number (Adv vs Diff)
Br(it) = (eta_ref(it)*(vx_bg^2))/...% Brinkman Number(Prod_sh vs Diff)
        (k*T(ceil(x_ref_T/dx_T),ceil(y_ref_T/dy_T)));

R_adv(it) = Pe(it) / (Pe(it)+1+Br(it)); % Advection contribution
R_diff(it) = 1 / (Pe(it)+1+Br(it));    % Diffusion contribution
R_pro(it) = Br(it) / (Pe(it)+1+Br(it)); % Production contribution

% Store Pe, Br, R dimensionless numbers
PeBr(it,:) = [Pe(it) Br(it) time./(3600*24*365*1e6)];
R_numbers(it,:) = [R_adv(it) R_diff(it) R_pro(it) ...
                  time./(3600*24*365*1e6)]; % time in Myr
end

end

%=====
% SAVE values

if dimless_num == 1
    writematrix(R_numbers, 'R_numbers.csv')
    writematrix(PeBr, 'PeBr.csv')
end

if T_and_eta_ref == 1
    mkdir Temp_Visc_ref
    save(['./Temp_Visc_ref/Temp_Visc_ref' num2str(it) '.mat'], 'eta_ref')
end
%=====

```

Results of 2D thermo-kinematic numerical models of nappe overthrusting

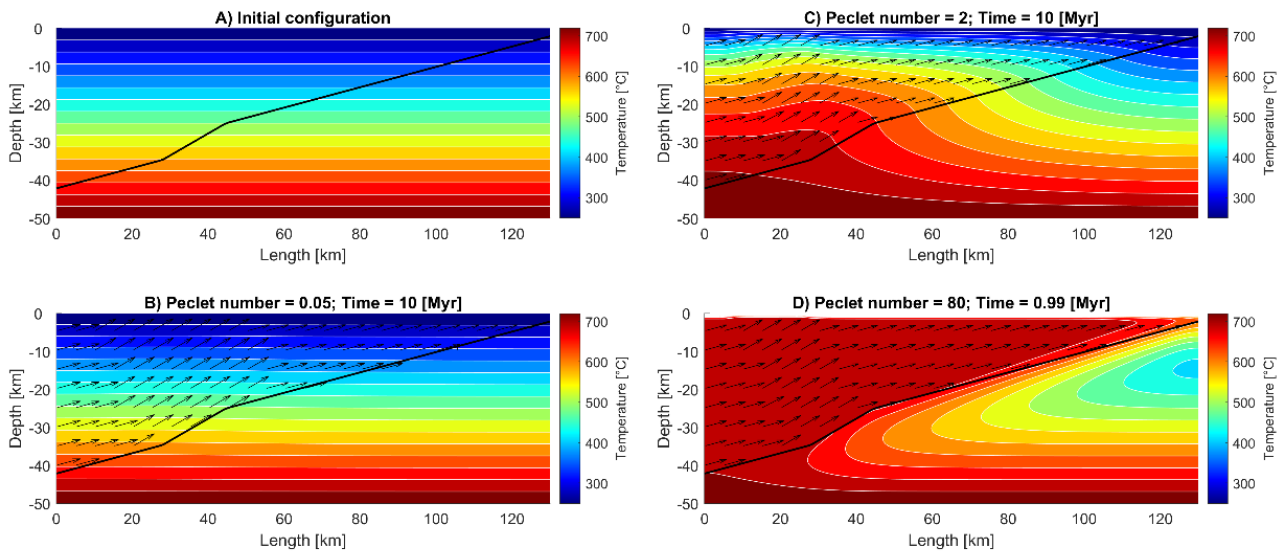


Figure C.1. Results of 2D thermo-kinematic numerical simulations of nappe overthrusting, realized with Matlab. Final thermal configuration of the system is shown in B, C, D panels for different Peclet numbers.

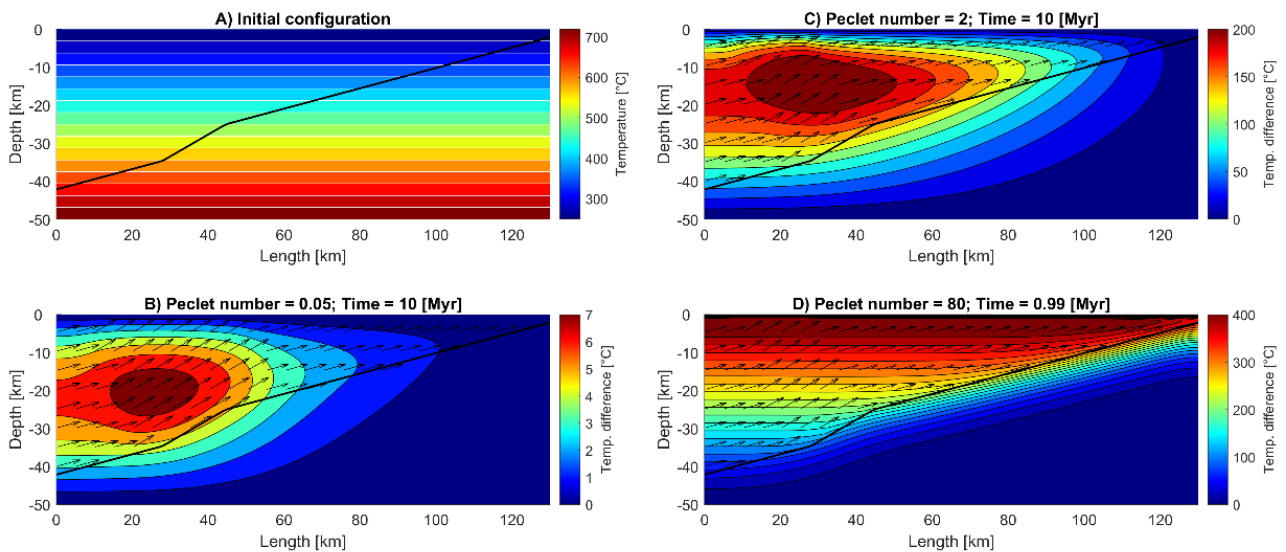


Figure C.2. Results of 2D thermo-kinematic numerical simulations of nappe overthrusting, realized with Matlab. Final thermal configuration of the system is shown in B, C, D panels for different Peclet numbers, expressed as temperature difference from the initial configuration (panel A).

An online version of [figures C.1](#) and [C.2](#) is available in Zenodo repository ([Peclet.png](#) and [Peclet_TDiff.png](#)).

Appendix D

METHODOLOGY (CHAPTER 3)

Fieldwork and sampling strategy

Geological mapping, coupled with structural analysis, was performed in different localities covering the valleys of Ticino (Switzerland). Lithologically different samples were collected during the mapping considering their tectonic position in the nappe structure, both within the nappes and at the main tectonic contact.

Already at the outcrop scale, only the part of interest of the rock has been collected to be subsequently treated in laboratory: e.g. in the migmatitic gneisses we sampled the leucocratic pots to date the melting event. Foliation and lineation were measured before removing the sample from the rock, and a GPS point has been associated to each sampled site (see *table 3.1* in *Chapter 3*). A thin section has also been realized for each sample (see the complete description in *Appendix G*).

Zircon extraction

Zircon grains were extracted from the collected samples following a specific procedure, performed at the University of Lausanne, which takes advantage of zircon mineral properties. Each sample was crushed with a mechanic press to reduce the rock size, and the smaller pieces obtained have been subsequently put in an agate ball mill machine. Four fractions were divided using a sieves column (fr. >250 μm , fr. 250-125 μm , fr. 125-90 μm , fr. <90 μm). The two fractions 250-125 μm and 125-90 μm were taken for the following separation steps. Hand panning permitted to separate the light fraction (floating white micas and lighter minerals) from the heavier fraction (quartz, feldspar, \pm biotite, garnet, zircon, and heavier minerals). The procedure was carefully followed by a continuous check at the stereoscope. The heavy fraction was taken to a Frantz machine for the magnetic separation, this permitted to divide the huge amount of biotite and, for some samples (paragneisses) also garnet. Finally, the non-magnetic fraction was subjected to heavy liquid separation. Methylene was used to separate zircon crystals (specific gravity of 4.6-4.7; [Klein et al., 1993](#)) from lighter minerals. The whole procedure was performed with a clean lab preparation to avoid contamination during the process.

Some samples (*Sample OS17-013; AV21-001; AV21-002; AN20.1; AG20.1; AG20.2*) were treated at ETH Zürich with a different extraction procedure: after the standard grinding, a Wilfley table was used for zircon separation before picking and mounting procedures.

Mounting and cathodoluminescence

Zircon grains were picked from the obtained fraction and mounted in epoxy resin. The mounts were polished down to expose grain centers. Cathodoluminescence (CL) imaging was carried out at the Scanning Electron Microscope at the University of Lausanne with a CamScan MV2300, consisting in a SEM (Scanning Electron Microscope) equipped with a standard thermionic source (tungsten filament), working with a Probe Current between 6 kV and 10 kV, and 15-19 mm working distance.

CL-images were used to set point analyses on the target zircon domains.

Laser Ablation Inductively Coupled Plasma Mass Spectrometry

Analyses were performed using Laser Ablation Inductively Coupled Plasma Mass Spectrometry (LA-ICP-MS) facility at the University of Lausanne, equipped with a sector-field spectrometer Element XR (Thermo Fisher Scientific) interfaced to a RESOLUTION SE 193 nm ArF excimer ablation system with an S155 2-volume ablation cell (Australian Scientific Instruments).

The laser spot diameter for the U-Pb dating was set to 20 μm , with a pre-ablation at 30 μm . Only for one session, the beam size was set to 30 μm to increase the precision of the analyses and cross-check the results. The GJ-1 reference zircon ([Boekhout et al., 2012](#); [Ulianov et al., 2012](#)) was used for the standardization of relative sensitivity factors, and the Plešovice reference zircon ([Sláma et al., 2008](#)) as a secondary standard for accuracy control. Trace elements were also analyzed for selected samples by LA-ICP-MS, setting spot diameters depending on the size of the target zircon domain (50, 38, or 30 μm), and using the NIST SMR612 glass ([Jochum et al., 2011](#)) as the primary standard, and the BCR-2G basaltic glass for quality control.

The raw data were treated using Lamtrace data reduction software ([Jackson, 2008](#)). No common lead correction was applied due to the presence of mercury in the system. The net signals for Hg^{201} and $(\text{Hg}+\text{Pb})^{204}$ were monitored during the data treatment, and analyses with detectable Pb^{204} were rejected. Age estimates influenced by the presence of common lead and mixed ages were discarded. Selected analyses representing the output of this first check are reported in *Appendix F*. Analytical results and Concordia diagrams of reference materials are also in *Appendix F*.

The last step performed to evaluate the significance of each spot analysis was a second cathodoluminescence imaging check to verify if the laser spot was set on the right target zircon

domain. Analyses obtained on densely fractured spots or with inclusions were not further considered.

Finally, the results were plotted on a Concordia diagram using IsoplotR (Vermeesch, 2018). All graphically discordant analyses were avoided from the Concordia age calculation. We adopted this approach due to the large variety of zircon textures and number of data trend analyzed, for which the calculation of a Concordia age on the base of concordant data only was the best choice to obtain meaningful results.

Zircon ages are indicated in the main text as Concordia ages with a 2σ confidence interval.

Secondary Ion Mass Spectrometry

In order to improve spatial resolution, one session of analyses was performed via SwissSIMS ion probe (Secondary Ion Mass Spectrometry) at the University of Lausanne (*SwissSIMS Ion probe national facility in Switzerland*), using a Cameca IMS 1280-HR large radius secondary ion microprobe, which is equipped with an high-brightness Hyperion H201 RF plasma oxygen ion source.

The procedure for zircon extraction and mount preparation was identical to the one adopted for the other mounts. Three standards were mounted together with the zircon grains: Temora (Black et al., 2004), Plešovice (Sláma et al., 2008), and Plenglai (Li et al., 2010).

To completely avoid any topographic effect, the epoxy mount was cut with a precision diamond saw and mounted in Indium.

Zircon crystals were analyzed for U-Pb dating using a O^{2-} primary beam intensity of 3 nA, resulting in a spot of $10 \times 8 \mu\text{m}$ on the sample surface. Oxygen flooding was used to enhance the Pb yield. The mass resolving power ($M/\Delta M$) was set to ~ 5000 . After 120 s of presputtering, the following masses were measured in monocollection on the axial electron multiplier (counting time in sec): $^{90}\text{Zr}_2 \text{ }^{16}\text{O}$ (2sec), $^{94}\text{Zr}_2 \text{ }^{16}\text{O}$ (2sec), ^{204}Pb (8sec), $^{204.3}$ (8sec), ^{206}Pb (25sec), ^{207}Pb (21sec), ^{208}Pb (8sec), ^{238}U (10sec), $^{232}\text{Th} \text{ }^{16}\text{O}$ (2sec), $^{238}\text{U} \text{ }^{16}\text{O}$ (2sec) and $^{238}\text{U} \text{ }^{16}\text{O}_2$ (2sec). Each sequence was repeated 6 times during a single analysis. One analysis thus took ~ 15 min. The results are reported in *Appendix F*.

No common lead correction was applied. The typically adopted approach to obtain a common lead corrected data from SIMS analyses is to plot the regression of $\text{Pb}^{207}/\text{Pb}^{206}$ versus $\text{U}^{238}/\text{Pb}^{206}$ mass ratios in the Tera-Wasserburg diagram and calculate a lower intercept. This method is

particularly useful if data demonstrate a large spread along a line of regression, which implies the presence of common lead rich zircon grains in the dataset, which was not seen in our datasets. For the sake of consistency and in order to perform an equal comparison between LA-ICP-MS and SIMS datasets, in the main text we present all data calculated with the same methodology (Calculation of a Concordia age on a Wetherill Concordia plot, discarding discordant data).

For comparison, the results from the Discordia Model-1 of IsoplotR ([Vermeesch, 2018](#)) in Tera-Wasserburg diagram are reported in *Appendix F*.

Appendix E

GEOLOGICAL MAPS (CHAPTER 3)

This appendix is available online at: <https://zenodo.org/record/8399771>.

In this appendix we provide an extended version of the geological maps in *figures 3.3, 3.4 and 3.5* of *Chapter 3*.

The extended version of these figures contain structural data, geological maps and U-Pb zircon dates for Alpine zircons for the three areas analyzed in *Chapter 3*: Cima di Gagnone (*figure E.1*), Cima di Precastello (*figure E.2*) and San Vittore-Giova (*figure E.3*).

An online version (*Maps_extended.pdf*) is available in the open-access Zenodo repository: <https://zenodo.org/record/8399771>.

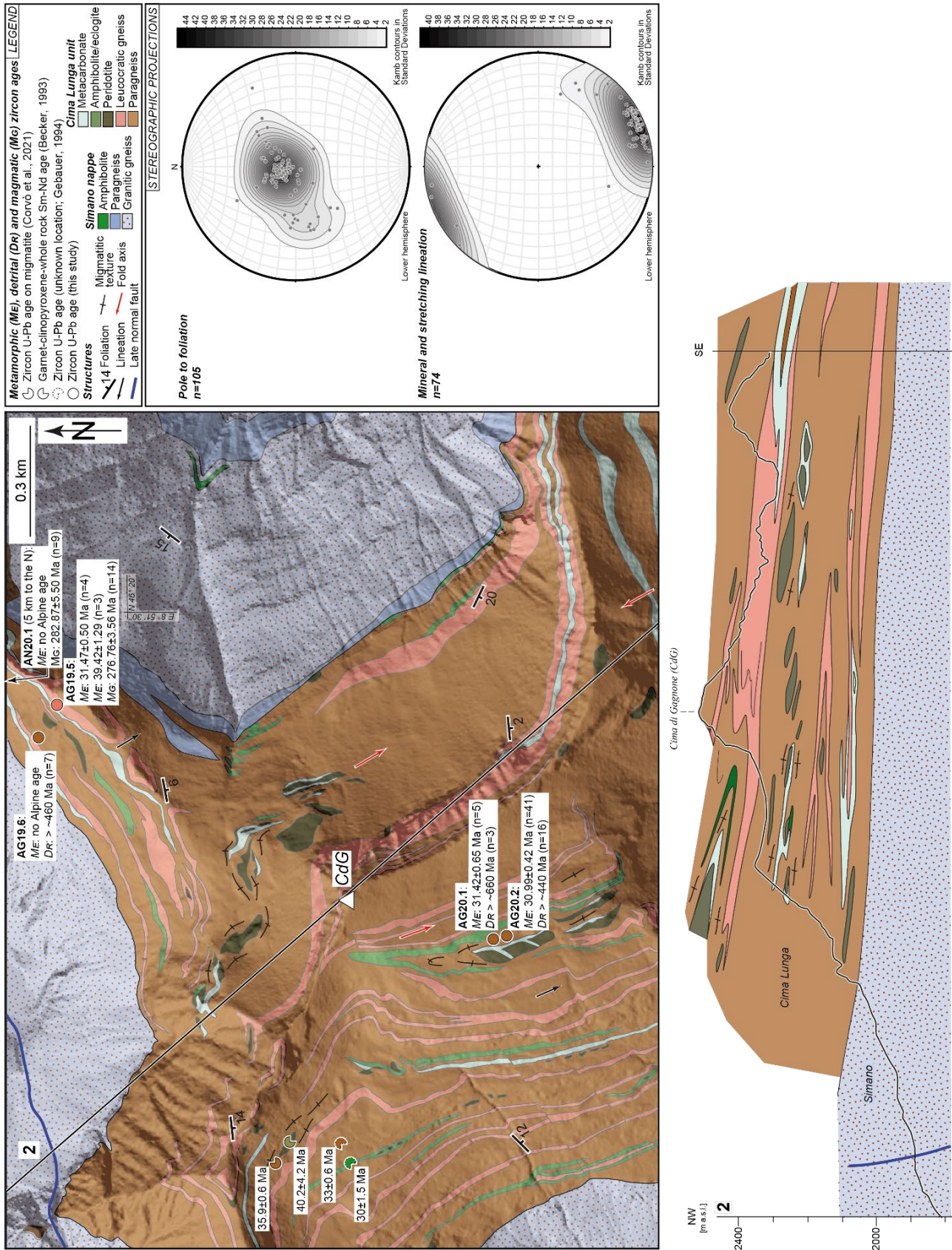


Figure E.1. Extended version of figure 3.3 in Chapter 3. Geological-structural map of the Cima di Gagnone area (with minor modifications after Corvò et al. (2021); Pffner & Trommsdorff (1997)), with the relevant geological section at the same scale (Profile 2), and stereographic projections. The ages of samples studied in this thesis and literature data are indicated in the map. Zircon U-Pb ages from this study indicated in this map are LA-ICP-MS ages. See Chapter 3 for further details.

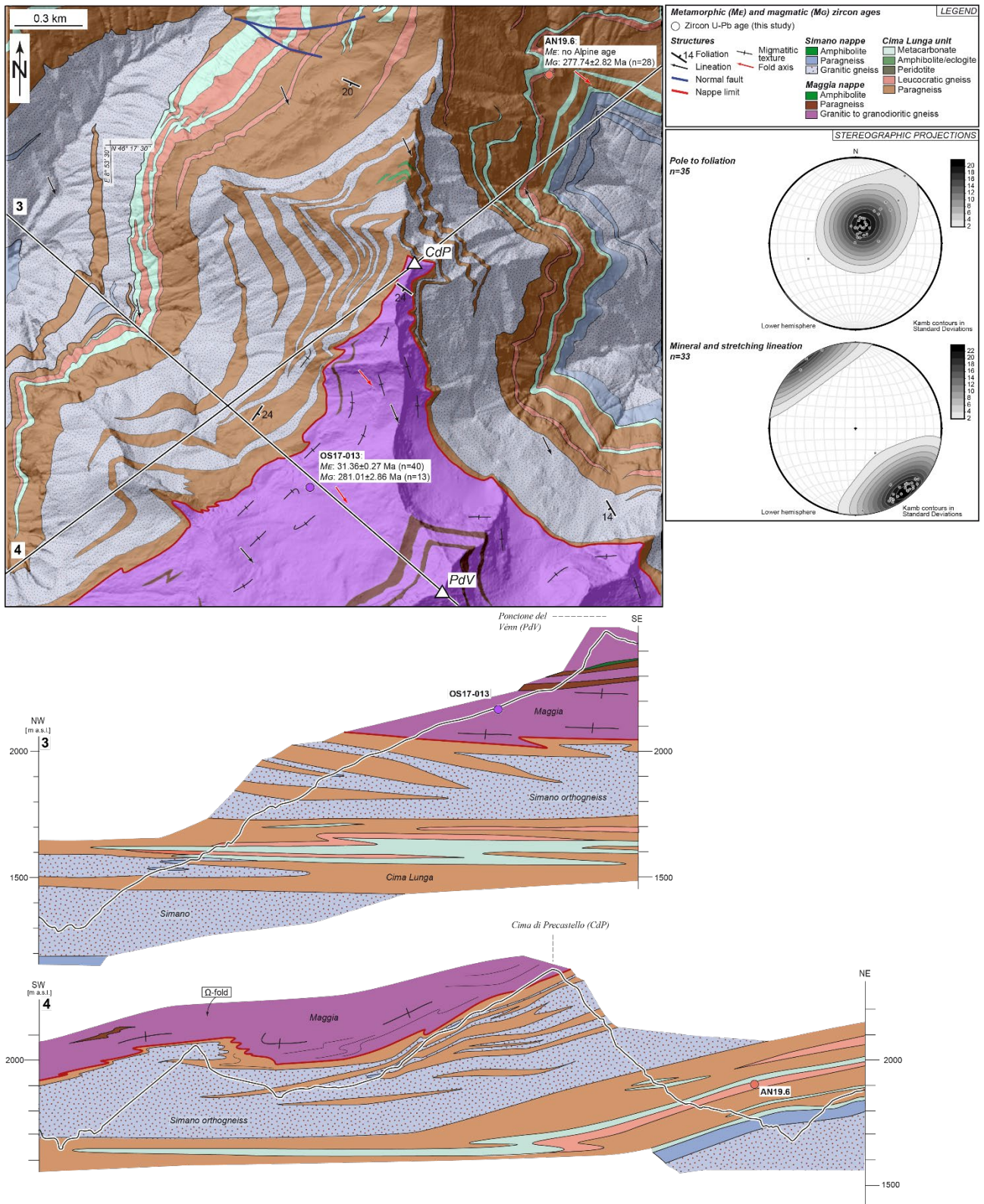


Figure E.2. Extended version of figure 3.4 in Chapter 3. Geological-structural map of the Cima di Precastello area, with the relevant geological sections at the same scale (Profiles 3 and 4) and stereographic projections. Own samples and LA-ICP-MS U-Pb zircon ages are indicated in the map. See Chapter 3 for further details.

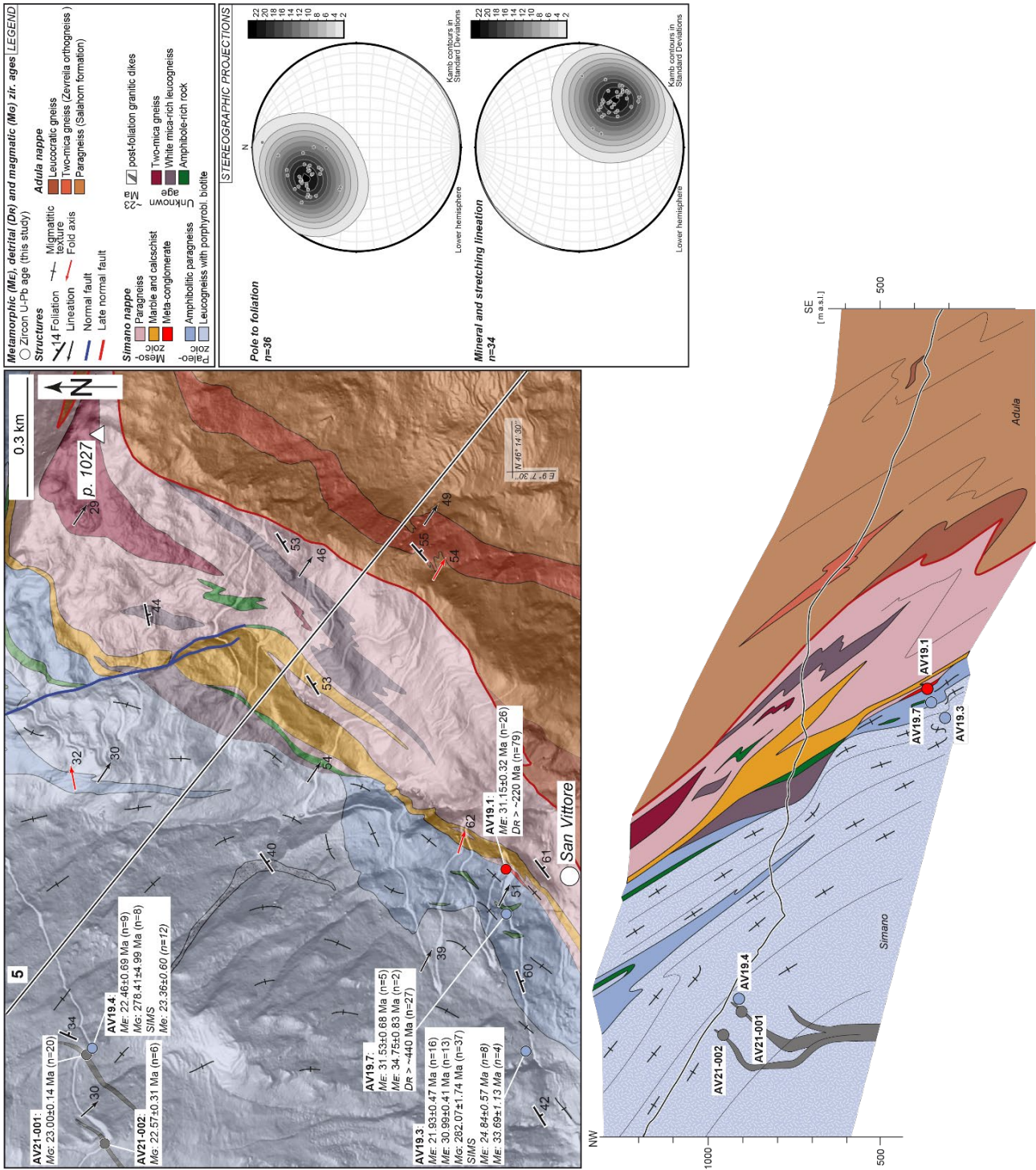


Figure E.3. Extended version of figure 3.5 in Chapter 3. Geological-structural map of the San Vittore-Giova area, with the relevant geological section at the same scale (Profile 5), and stereographic projections. Own samples and U-Pb zircon ages are indicated in the map. If not specified, zircon U-Pb ages are LA-ICP-MS ages. See Chapter 3 for further details.

Appendix F

LA-ICP-MS AND SIMS ANALYSES (CHAPTER 3)

This appendix is available online at: <https://zenodo.org/record/8399771>.

All data related to LA-ICP-MS and SIMS analyses presented in *Chapter 3* have been uploaded onto the general-purpose open-access repository Zenodo: <https://zenodo.org/record/8399771>. In this page we briefly describe the contents of each file.

LA-ICP-MS trace element analyses

The file *Trace_LAICPMS.xls* contains the results of LA-ICP-MS trace element analyses for the selected samples. Both sample names and analyzed zircon domains are indicated for each data entry. Chondrite values for normalization are from [McDonough & Sun \(1995\)](#).

LA-ICP-MS analyses for U-Pb zircon dating

The folder *UPb_LAICPMS* contains Excel tables with the results of all the analyses performed using LA-ICP-MS for U-Pb dating on zircon crystals. Each Excel file corresponds to a specific sample. Within each Excel file, the first sheet is compiled with information concerning for example the day of analysis and a legend for the description of the internal zircon stratigraphy, while in the second working sheet are reported all the analyses on the sample. We show all the analyses which have not been discarded after the first check performed with the help of Lamtrace data reduction software ([Jackson, 2008](#)). This first control consisted in common-Pb check, possible double-zircon measure, modification of the selected acquisition window and presence of spikes in the signal. These data have been further selected for age calculations. The discarded data are indicated with an “x” in the second working sheet of the excel files.

The file *Stds_LAICPMS.xls* contains LA-ICP-MS measures on the standards used for calibration (GJ-1, Plesovice, SRM612) for the U-Pb dating, with the relevant Concordia plots. Data entries are divided in different Excel sheets, each corresponding to a specific day of analysis.

SIMS analyses for U-Pb zircon dating

The file *UPb_SIMS.xlsx* is an Excel table containing the results of analyses for U-Pb dating on zircon crystals with SIMS probe. The Excel file contains multiple sheets comprising the calibration data summary, calculations of Concordia ages for the standards used for calibration, table with results of the analyses and a table for each of the samples analyzed with the relevant results.

We uploaded onto the Zenodo repository also the electronic version of two figures showing the distribution of LA-ICP-MS dates for all samples analyzed in *Chapter 3* (*figures F.1* and *F.2*; *KDE_LAICPMS.pdf* in the repository) and one figure containing Tera-Wasserburg plots for selected SIMS U-Pb analyses (*figure F.3*; *Tera-Wasserburg_SIMS.pdf* in the repository).

Distribution of LA-ICP-MS dates for all samples analyzed in *Chapter 3*

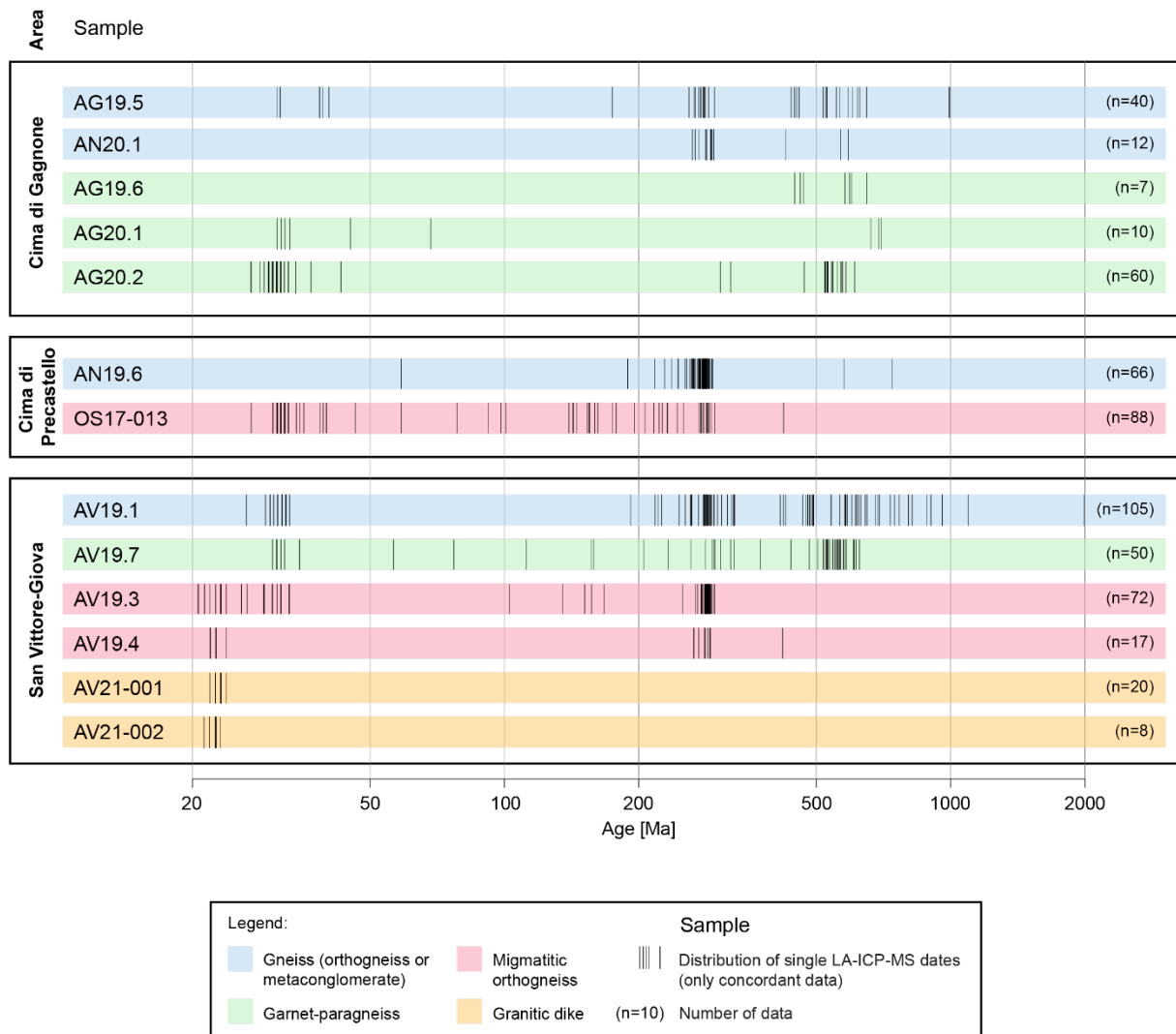


Figure F.1. The distributions of single data (reported as Concordia ages) have been created with *IsoplotR* (computation of KDE function; [Vermeesch, 2018](#)). Note: this diagram shows the distribution of all concordant dates, to correctly identify the corresponding (geologically meaningful) ages see the main text.

Kernel Density Estimates of LA-ICP-MS dates for all samples analyzed in Chapter 3

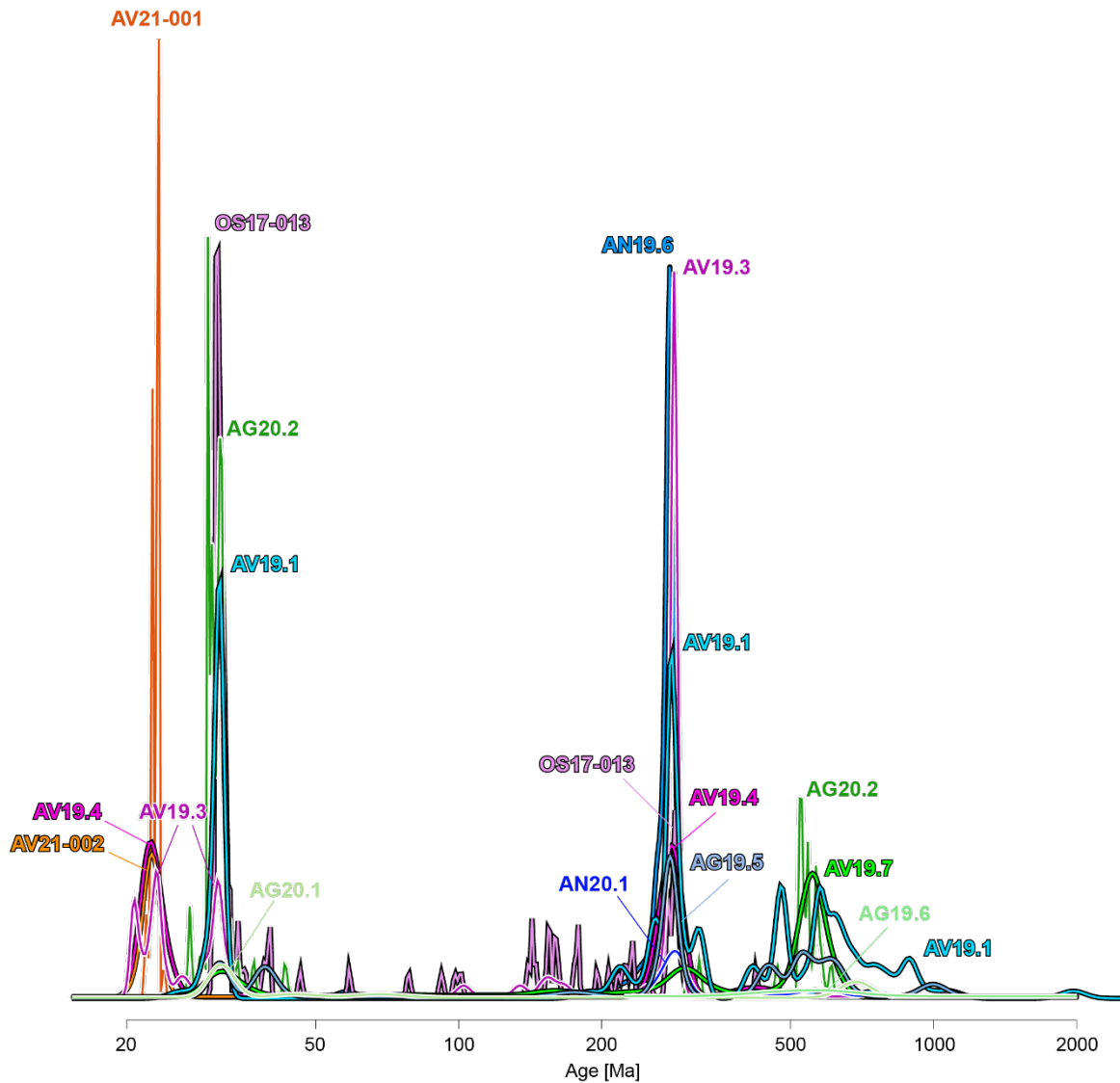


Figure F.2. Kernel Density Estimates (KDE) have been computed with IsoplotR (Vermeesch, 2018) with an automatic Kernel bandwidth (ca. 0.01). The diagram is particularly useful in identifying data clusters for each sample. No vertical scale is indicated because histograms of the single counts have been removed from this figure. Note: this diagram shows the distribution of all concordant dates (reported in the plot as Concordia ages), to correctly identify the corresponding (geologically meaningful) ages see the main text.

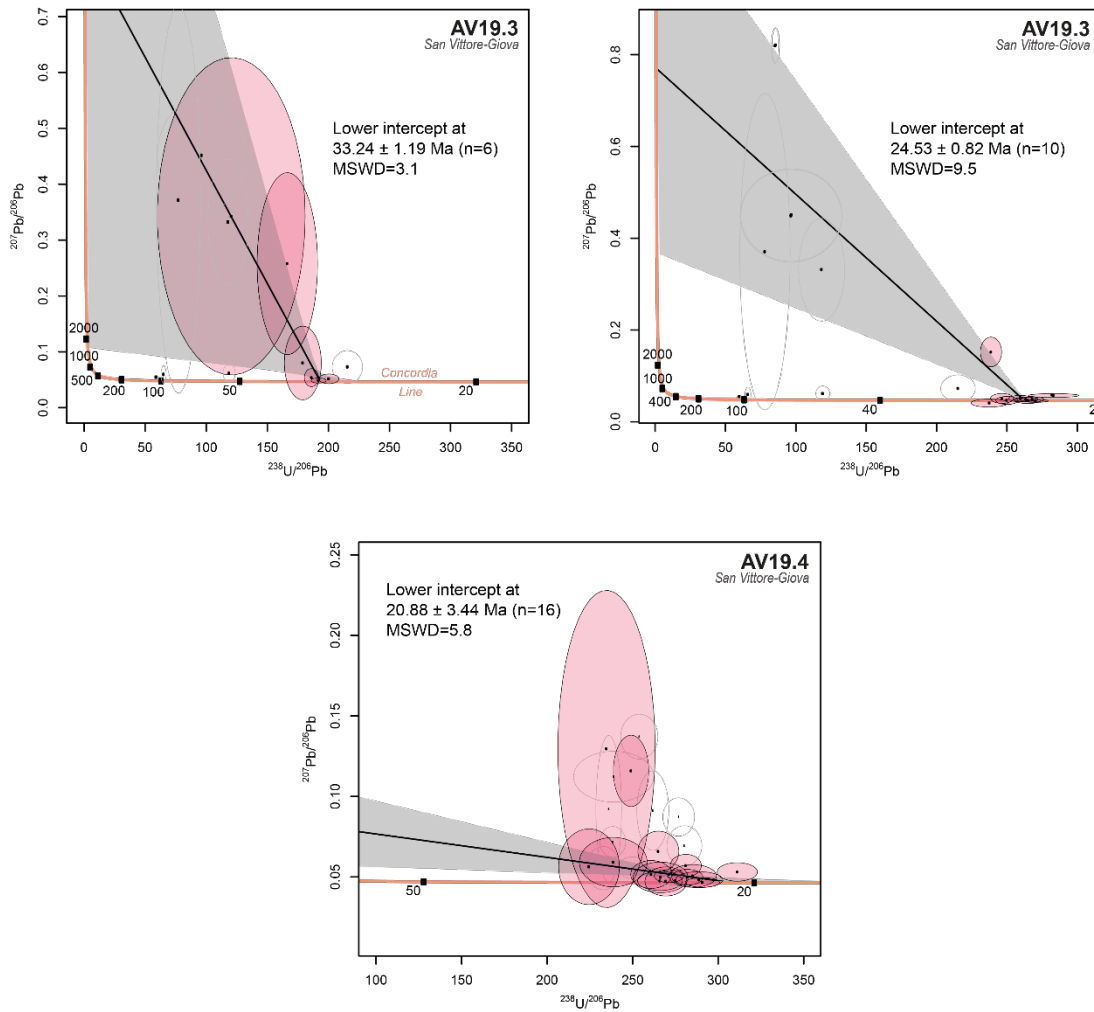
Tera-Wasserburg plots for selected SIMS U-Pb analyses (*Chapter 3*)

Figure F.3. Tera-Wasserburg plots for selected SIMS U-Pb analyses (metamorphic zircon rims in migmatitic orthogneisses samples AV19.3 and AV19.4), computed with IsoplotR (Vermeesch, 2018). Errors are expressed as 2σ . Both concordant and discordant data have been considered for lower intercept calculation. Gray ellipses represent data discarded on the base of analytical/CL-checks (see Appendix D).

Appendix G

DESCRIPTION OF THIN SECTIONS
(CHAPTER 3 AND CHAPTER 4)

We analyzed a total of sixteen samples which we described in *Chapter 3* and *Chapter 4* of this thesis. In this appendix, we describe in detail the petrography of the thin sections which have been realized for each sample. Samples are ordered on a lithological base.

For some samples, more than one thin section was described. The orientation of each section is displayed in the white box on top of the relevant photos by two red arrows: one indicates the top of the sample (pointing up or down) and the other the dip direction of the lineation (horizontal arrow). Most of the samples were cut parallel to the mineral lineation.

Abbreviations:

SPO = shape preferred orientation

LPO = lattice preferred orientation

GBM = grain boundary migration

SR = subgrain rotation

Gneiss

Sample AN19.6

Section AN19.6A

Panoramics:



Mineral assemblage:

Quartz, feldspar, biotite, white mica, chlorite, zircon, rutile, apatite, oxides.

Mineral distribution:

Heterogeneous distribution of minerals.

- Small to large size ipidiomorphic quartz and feldspar, inequigranular, interlobate. Elongated quartz ribbons made of aggregates.
- Fine biotite with SPO coinciding with LPO has ipidiomorphic to anhedral shape.
- White mica is in medium size grains with SPO and LPO.
- Fine chlorite is present only locally in some places (anhedral) or as substitution of small biotite grains (pseudomorphic substitution).

Fabric:

Tectonic fabric.

Foliation:

The rock is foliated. The foliation is continuous and it is defined by the preferred orientation of mica grains, elongated quartz and feldspar grains and their aggregates.

A crenulation cleavage formed on the main foliation. White mica and biotite have the same SPO defining the main foliation, however the biotite has sometimes a different orientation which “cuts” the white mica forming mica fish. This defines a sort of crenulation that can be seen only in the thin section.

Deformation mechanisms:

- Undulose extinction of quartz and SR, GBM, window structures, pinning, recrystallization in small aggregates.
- Locally, old plagioclase grains can show ipidiomorphic shape, partly substituted by small quartz drops, and saussurite alteration on top of pre-existing lamellae. Undulose extinction and deformation lamellae can be seen in feldspar, together with SR. In a very few cases GBM in plagioclase (e.g. dragging). Flame perthites.
- Myrmekites.
- Locally, biotite is substituted by chlorite. Biotite is usually resorbed at the edges.
- Boudinage of white mica and loss of elements at the borders.
- Mica fish of white mica.

Notes:

- Zircon as inclusion in other mineral phases (e.g. quartz, white mica).
- Rutile is parallel to the main foliation.

Relative age diagram (blastesis-deformation tab):

Quartz

Feldspar

White mica

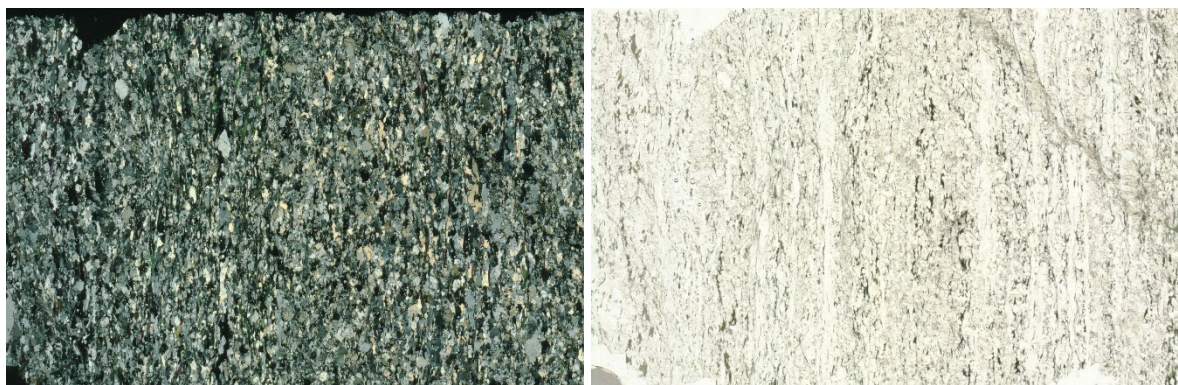
Biotite

Chlorite



Section AN19.6B

Panoramics:



Mineral assemblage:

Quartz, feldspar, biotite, white mica, chlorite, apatite, zircon, rutile, oxides.

Mineral distribution:

Heterogeneous distribution of minerals.

- Medium-fine quartz and feldspar grains with SPO or in elongated aggregates. They are interlobate, with ipidiomorphic (feldspar) to anhedral shapes.
- Biotite is mostly anhedral to subhedral, with SPO usually coinciding with LPO, in medium-fine size grains.
- Medium size white mica grains with SPO.
- Local fine grain chlorite has anhedral to subhedral shape.

Fabric:

Tectonic fabric.

Foliation:

The rock is foliated. The foliation is continuous and it is defined by the preferred orientation of mica grains and elongated quartz and feldspar aggregates.

The main foliation is defined by biotite and white mica. Like in the previous thin section described, a crenulation cleavage developed on this foliation, forming white mica fish. The cleavage is defined by biotite, locally very fine, which can be substituted by fine white mica and chlorite.

Deformation mechanisms:

- SR, GBM, recrystallization, accompanied by pinning in quartz.
- Deformation lamellae and saussuritic alteration in plagioclase. Flame perthites.
- Chlorite substitution of biotite.
- Loss of elements at the borders of white mica grains, and local boudinage.
- Mica fish of white mica.

Notes:

- Zircon as inclusion in other mineral phases (e.g. plagioclase).
- Rutile grains are parallel to the foliation.

Relative age diagram (blastesis-deformation tab):

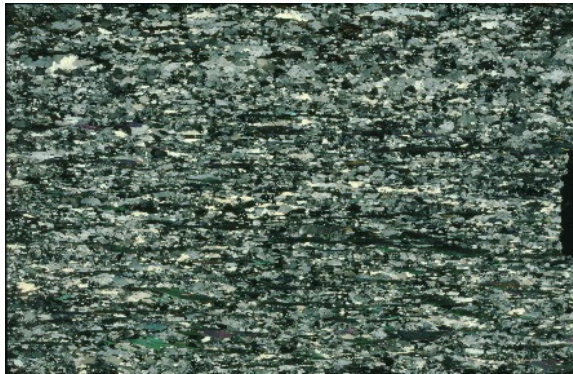
Quartz

Feldspar

White mica

Biotite

Chlorite

*Sample AG19.5**Panoramics:**Mineral assemblage:*

quartz, feldspar, plagioclase, white mica, biotite, chlorite, staurolite, epidote, zircon, rutile, chloritoid.

Mineral distribution:

Heterogeneous distribution of minerals.

- Quartz and feldspar grains are elongated with SPO coinciding with the direction of the foliation. They are in inequigranular aggregates with medium to medium-small size grains, interlobate, ipidiomorphic.
- Medium size, elongated white mica crystals with SPO \equiv LPO.
- Dark greenish biotite grains (rich in Fe and Al), fine to medium-fine in size, have SPO \equiv LPO.
- Medium-fine size staurolite with idiomorphic shape, fractured, with SPO coinciding with the direction of the foliation.

Fabric:

Tectonic.

Foliation:

The foliation is continuous, defined by SPO of mica and quartz/feldspar grains (and locally also chloritoid SPO).

Deformation mechanisms:

- Tartan pattern in feldspar.
- Fractures in feldspar.
- GBM of quartz and feldspar with evidence of: pinning and window microstructures; sub-grain rotation indicative of dynamic recrystallization in quartz.
- Locally, deformation lamellae in plagioclase.

- Locally, chlorite substitutes biotite grains (pseudomorphic growth).
- Static recrystallization, locally suggested by triple points.
- Local myrmekites.

Notes:

- Locally, polysynthetic twinning in plagioclase.

Relative age diagram (blastesis-deformation tab):

Quartz
Feldspar
White mica
Biotite
Chlorite



Sample AV19.1

Panoramics:



Mineral assemblage:

Quartz, feldspar, biotite, white mica, chlorite, zircon, epidote, apatite, rutile, oxides.

Mineral distribution:

Heterogeneous distribution of minerals.

- Fine to medium-size quartz and feldspar grains with SPO. Feldspar grains usually have lobate shapes, but locally sharp-straight boundaries can be seen. Polysynthetic twinning is common in plagioclase. Feldspar grains can have zircon and/or mica inclusions. Quartz grains have a lobate shape and are elongated in the foliation.
- Medium to fine-size, brownish biotite grains have SPO usually coinciding with LPO. Biotite crystals locally have zircon inclusions.
- Fine-size, idiomorphic to ipidiomorphic grains of white mica are included in feldspar.

Fabric:

Tectonitic fabric.

Foliation:

The rock is foliated. The foliation is continuous and defined by the SPO of biotite and chlorite, and by the preferred orientation of quartz and feldspar grains.

Deformation mechanisms:

- Undulose extinction in quartz and newly formed grains indicative of dynamic recrystallization.
- Deformation lamellae in plagioclase.
- Small portions of feldspar grains are substituted by sericite.
- Triple points between feldspar grains indicative of static recrystallization.

- GBM, pinning, and local window structures.
- Resorption of biotite's edges and local chloritization.
- Perthites in feldspar.

Notes:

- Evidence of partial melting: polysynthetic twinning in plagioclase, rounded melt drops on top of mineral grains (quartz “drops” on feldspar), cusped quartz grains. Locally, on top of medium-small size plagioclase with polysynthetic twinning, rounded fine-size quartz crystals with a lobate shape convex from the plagioclase border grow towards the inner part of the plagioclase grain.

Relative age diagram (blastesis-deformation tab):*Sample AN20.1**Panoramics:**Mineral assemblage:*

Feldspar, quartz, biotite, white mica, chlorite, oxides, epidote, zircon.

Mineral distribution:

Heterogeneous distribution of minerals.

- Big K-feldspar porphyroclasts are idiomorphic, elongated parallel to the foliation, with local myrmekite growth along their boundaries.
- Idiomorphic medium-size, plagioclase grains with SPO can be locally seen. In the matrix, also idiomorphic plagioclase medium-size blasts without SPO are present. They show polysynthetic twinning.
- Big to medium-size quartz grains in the foliation are elongated, with interlobate borders.
- Biotite is medium-fine grainsize, often with SPO.
- White mica is in medium-size grains, with SPO coinciding with LPO, defining the foliation.

Fabric:

Tectonic fabric. Lepidoblastic fabric of white mica grains.

Foliation:

The rock is foliated. The foliation is continuous and defined by the preferred orientation of biotite and lepidoblastic fabric of white mica.

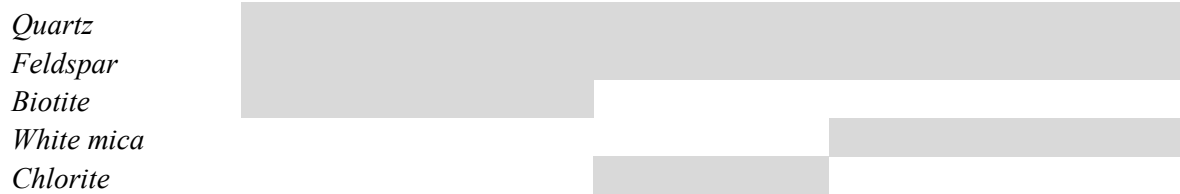
Deformation mechanisms:

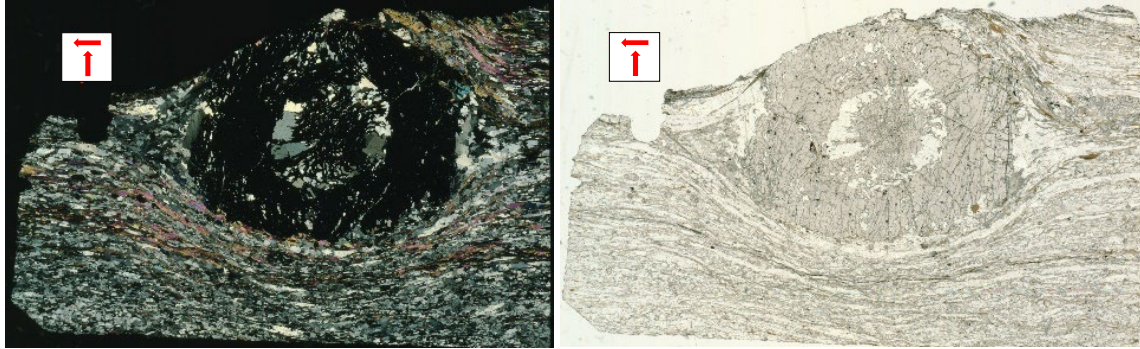
- Local, slightly asymmetric myrmekites.
- Deformation lamellae in plagioclase.
- Fractures and undulose extinction in feldspar
- In quartz: undulose extinction, triple points.
- Chloritization of biotite.
- Saussurite replacement of feldspar, associated with chloritization of biotite.

Notes:

- Carlsbad twinning in feldspar, and polysynthetic twinning in plagioclase.
- Feldspar is abundant and forming eyes in the main foliation (big, fractured, K-feldspar).
- Local myrmekites associated with white mica having zircon inclusions.
- Pre-existing K-feldspar eyes are substituted by plagioclase.

Relative age diagram (blastesis-deformation tab):



Garnet-paragneiss*Sample AG19.6**Section AG19.6A**Panoramics:**Mineral assemblage:*

Garnet, quartz, feldspar, biotite, white mica, chlorite, kyanite, staurolite, zircon, oxides, apatite, epidote (allanite), rutile.

Mineral distribution:

Heterogeneous distribution of minerals.

- Large size snowball garnet rich of inclusions from large (quartz and feldspar) to fine size. The inclusions are oriented and define different zones inside the garnet; from the core toward the external part:
 - (1) Isooriented (*S1*) fine size inclusions of quartz (locally containing zircon) and feldspar with SPO, white mica with SPO coinciding with LPO, fine grain chloritoid, rutile.
 - (2) Layer rich in quartz inclusions, large to medium size, isooriented and curved from the internal part toward the external portions. The curvature of the oriented inclusions is more evident when the inclusions are smaller. The larger size quartz grains have inclusions of white mica, rutile, zircon and oriented tiny rounded inclusions (mostly fluid inclusions).
 - (3) Layer with tinier (white mica?) inclusions, rutile, quartz/feldspar.
 - (4) Zone with isooriented (*S2*) small to medium size inclusions, their orientation is at high angle to the foliation (*S3*) direction. Inclusions of: quartz/feldspar, white mica, rutile, zircon, biotite. Garnet is locally embayed on its margins (see in correspondence of pressure shadows).

Fractures are filled by chlorite (Fe-rich), biotite and feldspar.

In pressure shadows: quartz with lobate grain boundaries and cusps toward altered plagioclase crystals (albite), with substitutions of fine grain white mica and rutile; Fe-rich chlorite substitutes biotite; white mica.

Smaller size garnet crystals are also present.

- Medium size idiomorphic white mica with SPO coinciding with LPO.
- Biotite with SPO has usually a smaller size than the one of the white mica grains.
- Small to medium size ipidiomorphic quartz and feldspar crystals, inequigranular, interlobate.
- Ipidiomorphic medium size kyanite can contain biotite and zircon as inclusions. Sometimes it could be seen as skeletal grains.
- Staurolite is not common (a couple of crystals in the matrix), it can contain biotite and it is replaced by white mica.
- Apatite inside (inclusion) and outside the garnet.

Fabric:

Tectonic fabric. Lepidoblastic fabric of white mica.

Foliation:

The rock is foliated. The foliation (*S3*) is continuous and it is defined by the isoorientation of mica crystals and elongated quartz-feldspar aggregates.

The matrix mineral assemblage is constituted by garnet, quartz, biotite (replaced by chlorite), kyanite (locally replaced by quartz + white mica; growth together with biotite), white mica, rutile, feldspar; chlorite replaces biotite.

Deformation mechanisms:

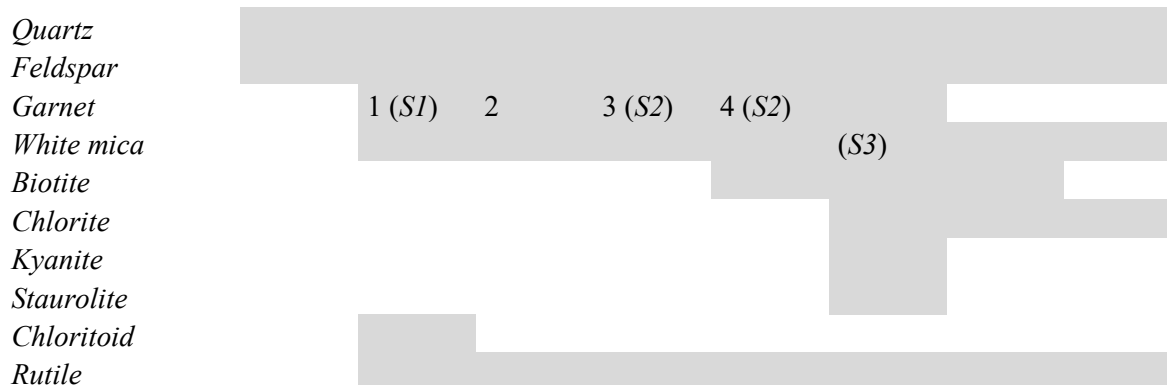
- The garnet is pre-kinematic with respect to the main amphibolite foliation *S3*. Its internal structure shows more than one accretionary phase: (1) shows *S1*, pre-kinematic respect to *S2*, (2) syn-kinematic with *S2*, (3-4) shows *S2*, pre-kinematic with respect to *S3*.
- Static recrystallization of the medium size feldspar grains included in the garnet (2).
- Dynamic recrystallization of quartz, GBM: SR, pinning; local dragging in plagioclase. Polysynthetic twins and deformation lamellae in plagioclase.
- Saussuritic alteration of albite grains in garnet pressure shadows.
- Boudinated kyanite, locally with undulose extinction, partly replaced by feldspar and biotite and white mica overgrowth.
- Fractured staurolite.
- Biotite in proximity of the garnet is replaced by chlorite.

Notes:

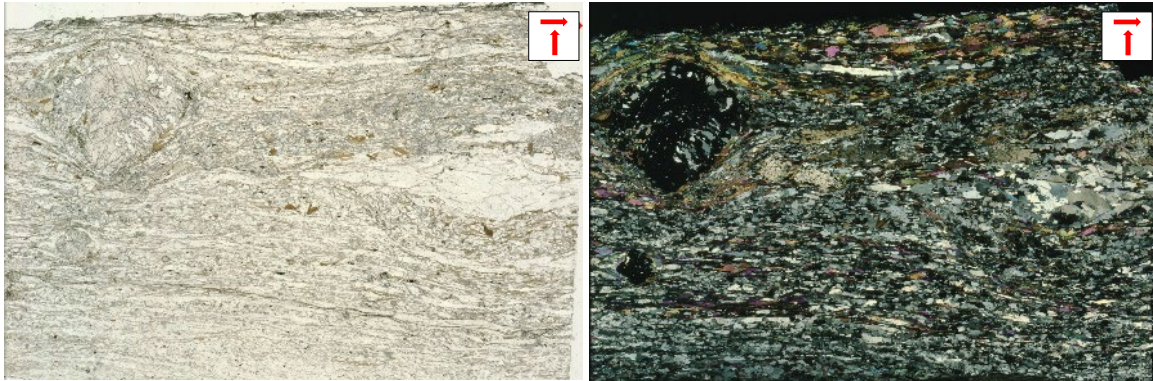
- In the most external parts of the garnet there's also chlorite as inclusion.
- Kyanite is usually close to the garnet.
- Tiny rutile and possible crocidolite inclusions in the garnet, zircon, feldspar (adularia), epidote.

Relative age diagram (blastesis-deformation tab):

(S indicates the foliation)



Section AG19.6B

Panoramics:*Mineral assemblage:*

Quartz, feldspar, garnet, white mica, biotite, kyanite, staurolite, zircon, oxides.

Mineral distribution:

Heterogeneous distribution of minerals.

- Large size snowball garnet with oriented inclusions of: quartz, white mica, biotite, rutile. Smaller idiomorphic medium-fine size garnet grains are present in the matrix.
- Kyanite in the matrix is in large idiomorphic crystals, fractured and sometimes in skeletal crystals partly substituted by biotite, feldspar, white mica. Inclusions of biotite, rutile, oxides, zircon, garnet.
- Staurolite forms medium-fine size crystals, fractured and with high relief. They are elongated in the matrix, parallel to the main foliation.
- Idiomorphic medium to fine size white mica and biotite grains usually have SPO parallel to the foliation (not always coinciding with LPO for white mica crystals: mica fish). Locally some mica grains are at high angle with respect to the principal foliation: their orientation is the same of some mica overgrowth on some kyanite crystals.
- Feldspar and quartz in the foliation are medium-fine size, interlobate, in elongated aggregates.

Fabric:

Tectonic fabric.

Foliation:

The rock is foliated. The foliation is continuous and it is defined by the SPO of white mica and biotite. The SPO of the staurolite is concordant with the foliation direction. The SPO of kyanite coincides with its LPO, and it forms an angle with respect to the foliation.

Deformation mechanisms:

- Fractured garnet. It is syn-kinematic with the foliation of the matrix.
- Kinking and undulose extinction in kyanite.
- Polysynthetic twinning in plagioclase and kinking in feldspar.
- Dynamic recrystallization of quartz, GBM: pinning. In quartz veins: undulose extinction, SR rotation.
- Static recrystallization of quartz inclusions in the garnet.
- Staurolite's fractures are at 90° to the elongation (parallel to the main foliation) of the mineral.

Notes:

- Large size idiomorphic crystals of kyanite with SPO coinciding with LPO but not oriented parallel to the foliation show isooriented inclusions of rutile, white mica, biotite parallel to the foliation. They show also kinking and undulose extinction (indicative of inter-tectonic mineral growth or rotated with the foliation).
- Myrmekitic texture at the borders of some feldspar inclusions in the garnet.

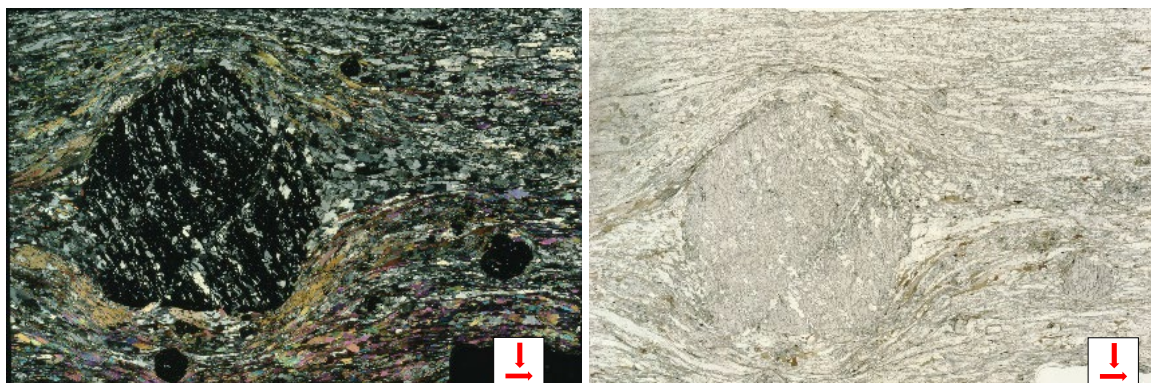
- Locally, sagenitic rutile can be seen in partially resorbed biotite.
- A couple of crystals of margarite are present in the matrix, not far from the big garnet.

Relative age diagram (blastesis-deformation tab):



Section AG19.6C

Panoramics:



Mineral assemblage:

Quartz, feldspar, garnet, kyanite, white mica, biotite, chlorite, staurolite, zircon, rutile, oxides, margarite, epidote.

Mineral distribution:

Heterogeneous distribution of minerals.

- Large size garnet crystal rich of medium-fine oriented inclusions of quartz, feldspar, rutile, white mica, biotite, zircon, and kyanite next to the garnet edges. Biotite is sometimes transformed in chlorite at the edges of the garnet or close to fractures. Garnet rim is in contact with biotite and kyanite. Local embayed garnet rim contains lobate feldspar and quartz.
- Large crystals of kyanite with inclusions of: white mica, biotite, rutile, zircon. The crystals are anhedral, sometimes skeletal. Their SPO coincides with the LPO but it's different from the foliation direction.
- Medium to fine grain ipidiomorphic white mica and biotite with SPO.
- Interlobate inequigranular quartz and feldspar aggregates.
- Rare staurolite, usually small size and ipidiomorphic, with inclusions of zircon, biotite, rutile.

Fabric:

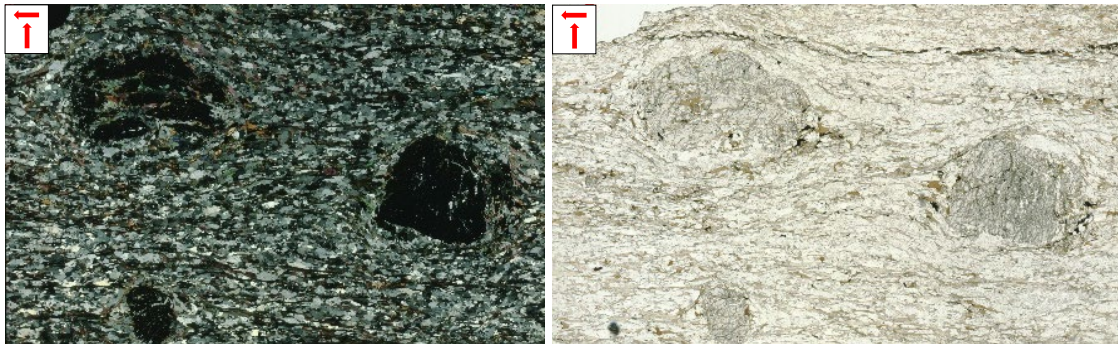
Tectonic fabric.

Foliation:

The rock is foliated. The foliation is continuous and it is defined by the preferred orientation of mica crystals and elongated quartz aggregates.

Deformation mechanisms:

- Kinking and undulose extinction of kyanite. Kyanite is deformed parallel to the foliation outside the garnet and it's substituted by white mica, biotite, feldspar.
- Kinking and undulose extinction in white mica and locally folded biotite.
- Biotite is locally substituted by chlorite.
- Deformation lamellae in plagioclase.
- Undulose extinction in quartz and GBM.
- Pre-tectonic garnet (the largest one).

Relative age diagram (blastesis-deformation tab):*Sample AV19.7**Section AV19.7C**Panoramics:**Mineral assemblage:*

Garnet, quartz, feldspar, biotite, kyanite, staurolite, white mica, oxides, zircon, apatite, chlorite, rutile.

Mineral distribution:

Heterogeneous distribution of minerals.

- Huge poikiloblastic garnet crystals with inclusions of quartz, feldspar, biotite, and tiny rutile, crocidolite, zircon. They have rounded to ellipsoidal shape, and absence of sharp boundaries. The inclusions are oriented: they can follow the foliation outside or form an angle with them. The three bigger garnet grains recognized in the thin section show different relations with the foliation:
 - (1) garnet cut by biotite and feldspar aggregates parallel to the foliation and small kyanite crystals;
 - (2) garnet with oriented inclusions of fine grain biotite and quartz/feldspar, that connect in the outer part with the foliation; the foliation is slightly deflected around the garnet;

<p>(3) oriented inclusions of quartz, feldspar, biotite are almost absent; the foliation is deflected around the garnet; the garnet is partly resorbed in correspondence of pressure shadows (note the presence of kyanite here).</p> <p>In the first case: the association of plagioclase and biotite is common, plagioclases have polysynthetic twinning and biotite grains are locally resorbed. Locally, quartz drops can be seen on larger feldspar crystals.</p> <p>Also medium-fine size garnet grains are present, with feldspar inclusions.</p> <ul style="list-style-type: none"> - Medium size biotite with SPO\equivLPO, are parallel to the main foliation. Locally they can have zircon inclusions. - Medium size feldspar and quartz aggregates in the foliation, elongated, inequigranular, interlobate. - Fractured, medium size grains of staurolite in the foliation have prismatic shape (a hexagonal basal section is also present). - Locally, leftover medium size grains of kyanite are associated to garnet (external part, in the pressure shadows of the main foliation), biotite and feldspar in the main foliation.
<p><i>Fabric:</i> Tectonic fabric. Lepidoblastic fabric of biotite crystals.</p>
<p><i>Foliation:</i> The rock is foliated. The foliation is continuous and identified by the SPO\equivLPO of biotite grains and preferred orientation of quartz/feldspar aggregates. The foliation is locally deflected around garnet porphyroblasts and it locally cuts them.</p>
<p><i>Deformation mechanisms:</i></p> <ul style="list-style-type: none"> - Kinking and deformation lamellae in plagioclase. - Kinking and fractures in staurolite. - Local kink of biotite, and resorption at the edges. - Dynamic recrystallization of quartz and feldspar. Undulose extinction of quartz, locally amoeboid shapes, window structures, dragging and pinning. - Kyanite crystals are fractured and locally reabsorbed. - Local substitution of garnet by chlorite.
<p><i>Notes:</i></p> <ul style="list-style-type: none"> - Garnet crystals are pre- to syn- tectonic. - Evidence of partial melting are resorption of biotite borders, local quartz drops and polysynthetic twinning in plagioclase. - White mica grains are found as relics in the foliation: partly resorbed and locally substituted by biotite.
<p><i>Relative age diagram (blastesis-deformation tab):</i></p> <p>Two main stages can be identified:</p> <ol style="list-style-type: none"> (1) Garnet nucleation. (2) Development of the main metamorphic foliation, associated with partial melting and garnet crystallization.

Section AV19.7E

Panoramics:*Mineral assemblage:*

Garnet, quartz, feldspar, biotite, white mica, chlorite, staurolite, epidote, chloritoid, rutile, oxides, kyanite, apatite.

Mineral distribution:

Heterogeneous distribution of minerals.

- A large poikiloblastic fractured garnet is wrapped in the foliation and partially resorbed. It has inclusions of biotite, quartz, feldspar, kyanite, white mica. Biotite inclusions are associated with feldspar, and kyanite is replaced by feldspar. The inclusions are oriented: in the outer part of the garnet they are parallel to the border but inside the mineral they are isooriented. The garnet seems to be syn-tectonic with the foliation.
- Medium to medium fine size grains of quartz and feldspar, inequigranular and interlobate aggregates in the matrix.
- Medium size biotite grains are in aggregates with the same orientation of the foliation. Sometimes they have SPO=LPO but frequently their LPO is at high angle with respect to the main foliation, locally also mica fish can be seen.
- Medium size grains of white mica in the main foliation. Locally, small size biotite grains grow on top of them.
- Medium to medium-fine size kyanite grains in the matrix are elongated in the direction of the main foliation.
- Elongated chloritoid crystals of medium size are parallel to the foliation.

Fabric:

Tectonic fabric.

Foliation:

The rock is foliated. The foliation is continuous and identified by biotite and quartz-feldspar aggregates.

Deformation mechanisms:

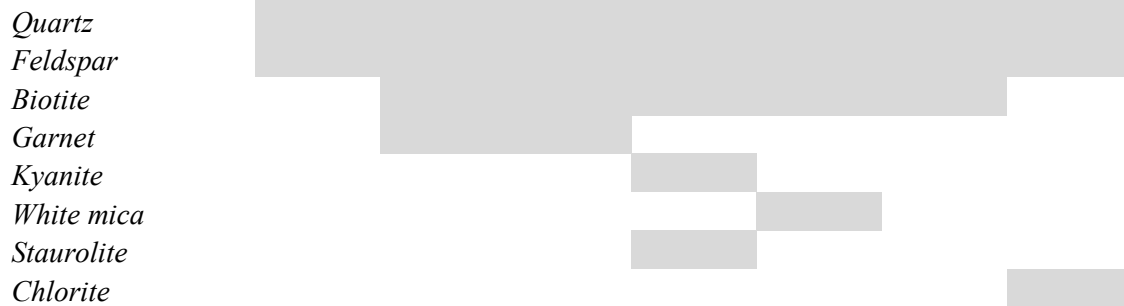
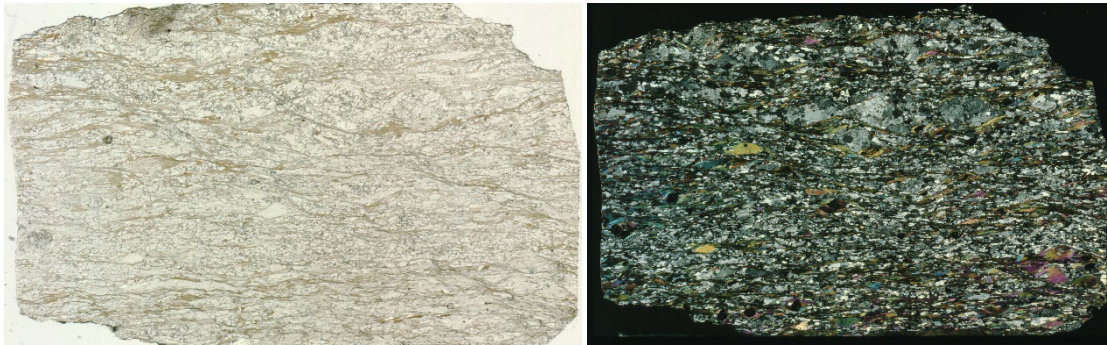
- Plagioclases show both polysynthetic and deformation twinning, fracturing and saussurite alteration.
- Undulose extinction in quartz and sub-grain rotation.
- Window structures, pinning and dragging as evidence of dynamic recrystallization in the matrix.
- Fractured and partially resorbed white mica grains in the foliation have deformation lamellae and they are kinked.
- Locally, garnet is replaced by chlorite. Chlorite also fills the fractures of the garnet.
- Twinning of kyanite inclusions in the garnet.

Foliation:

The rock is foliated. The foliation is continuous and defined by the preferred orientation of biotite and elongated quartz-feldspar aggregates.

Deformation mechanisms:

- Garnet grains are fractured and resorbed (the bigger ones resorbed at the edges and almost completely resorbed the smaller ones).
- Kyanite crystals are fractured.
- Staurolite can be substituted by feldspar.
- Chlorite substitutes biotite in the foliation.
- Kinking in feldspar.

Relative age diagram (blastesis-deformation tab):*Sample AG20.1**Panoramics:**Mineral assemblage:*

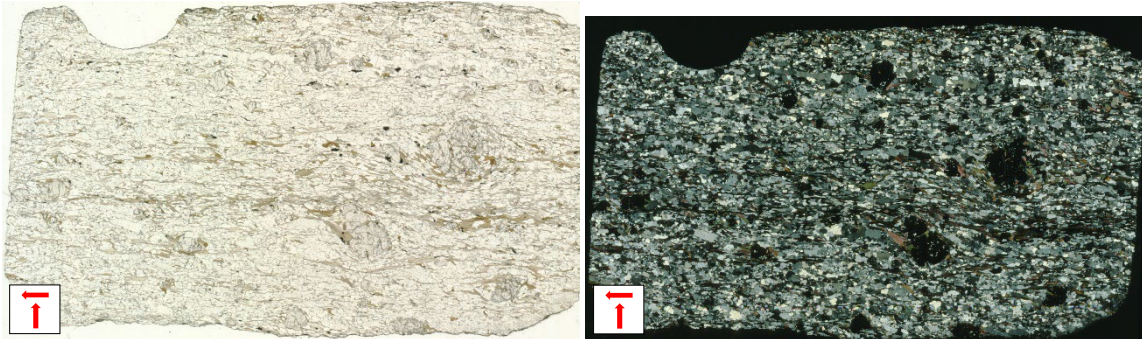
Quartz, feldspar, biotite, white mica, garnet, epidote, zircon, rutile, titanite, chlorite, Fe-oxides.

Mineral distribution:

Heterogeneous distribution of minerals.

- Quartz aggregates of fine to medium size crystals are inequigranular and interlobate, parallel to the foliation.
- Old, large to medium size, anhedral to subhedral, plagioclase grains showing polysynthetic twinning, and feldspar crystals with perthites.
- Medium size, subhedral to anhedral, fractured, garnet grains are poikilitic, with inclusions of: biotite, zircon, white mica, rutile. Inclusions at the rims usually follow the foliation, while the orientation of the inner ones can change.
- Fine grain rutile and titanite in the foliation.
- Medium to fine size idiomorphic biotite with SPO.

<ul style="list-style-type: none"> - Medium to large white mica grains are divided in: medium size mica isooriented with the foliation having LPO coinciding with SPO; and large white mica fish with LPO not coinciding with SPO, and undulose extinction. 	
<p><i>Fabric:</i> Tectonic fabric.</p>	
<p><i>Foliation:</i> The rock is foliated. The foliation is defined by the preferred orientation of biotite, white mica (the medium-size ones), and quartz aggregates, but also from the shape of anhedral garnet grains and old feldspar grains.</p>	
<p><i>Deformation mechanisms:</i></p> <ul style="list-style-type: none"> - Undulose extinction in quartz, GBM, pinning, window structures. - Partial replacement of plagioclase by saussurite and quartz. - Rutile exsolution in biotite and local chlorite replacement. - Metamictization of biotite around zircon inclusions. - White mica fish. - Locally: slight kinking of white mica. 	
<p><i>Notes:</i></p> <ul style="list-style-type: none"> - Garnet crystals are pre- to syn-kinematic. - Big mica fish can be locally substituted by feldspar and biotite. 	
<p><i>Relative age diagram (blastesis-deformation tab):</i></p> <p>The diagram shows the following sequence of events from left to right (earliest to latest):</p> <ul style="list-style-type: none"> Quartz Feldspar Biotite and White mica (White mica has a question mark) Chlorite Garnet and Titanite (Titanite has a question mark) Rutile 	

*Sample AG20.2**Section AG20.2A**Panoramics:**Mineral assemblage:*

Quartz, feldspar, biotite, garnet, chlorite, zircon, rutile, oxides, chloritoid.

Mineral distribution:

Heterogeneous distribution of minerals.

- Quartz in mostly equigranular, slightly interlobate aggregates.
- Feldspar is in medium size, anhedral grains, resorbed.
- Idiomorphic to ipidiomorphic, medium size grain biotite crystals are isooriented, usually with LPO coinciding with SPO.
- Poikilitic, ipidiomorphic, fractured garnet crystals in the foliation contain inclusions of biotite, quartz/feldspar, zircon, rutile, white mica. The inclusions can be oriented: distributed in a circle or a line following the orientation of the outside foliation of the matrix.
- Rutile in the foliation can have round quartz inclusions.
- Medium-small size elongated chloritoid in the foliation.

Fabric:

Tectonic fabric.

Foliation:

The rock is foliated. The foliation is continuous and defined by the preferred orientation of biotite, rutile, and quartz ribbons.

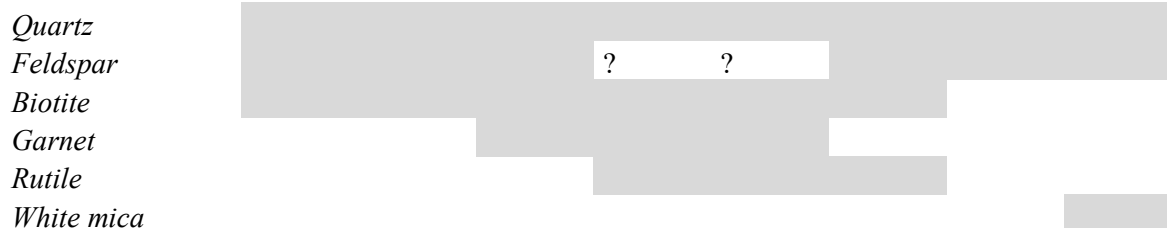
Deformation mechanisms:

- Triple points between quartz grains.
- Undulose extinction in fractured quartz, triple points.
- Undulose extinction of fractured feldspar crystals.
- Perthites in feldspar.
- Metamictization of biotite crystals around zircon inclusions.
- Partial resorption of biotite crystals that do not have LPO coinciding with LPO.
- Garnet crystals are (pre- to) syn-kinematic.
- Garnet crystals are fractured, with vein-filling made of plagioclase and biotite.
- Some garnet crystals are rich of zircon inclusions.

Notes:

- Zircon as inclusion in the matrix, but also at grain boundaries.

Relative age diagram (blastesis-deformation tab):



Section AG20.2B

Panoramics:



Mineral assemblage:

Quartz, feldspar, biotite, garnet, rutile, chlorite, zircon, epidote, oxides.

Mineral distribution:

Heterogeneous distribution of minerals.

- Idiomorphic quartz is in elongated medium-size aggregates or in small crystals forming equigranular aggregates.
- Feldspar grains are medium to medium-small size, resorbed. Finer plagioclase crystals can show polysynthetic twinning.
- Idiomorphic medium-size biotite has LPO coinciding with SPO.
- Idiomorphic garnet crystals in the foliation are poikiloblastic. The inclusions are at high angle with respect to the foliation and they comprise: zircon, rutile, quartz, epidote, biotite, chlorite. Locally the inclusions can be partly aligned with foliation wrapping the garnet grains, being parallel on one side of the mineral and discordant on the other side.
- Fine size rutile in the foliation is isooriented.

Fabric:

Tectonic fabric.

Foliation:

The rock is foliated. The foliation is continuous and defined by the isoorientation of biotite and quartz aggregates.

Deformation mechanisms:

- Undulose extinction in quartz, which can have triple points. Quartz grains are recrystallized.
- Resorption of feldspar grains, showing undulose extinction and substitution.
- Perthites and deformation lamellae in plagioclase.
- Inclusions in garnet form an angle with respect to the foliation.

Notes:

- Quartz in abundance with respect to feldspar.
- Garnet crystals are zircon-rich. The inclusions are in oriented aggregates that form an angle with the foliation of the matrix. Garnet crystals are pre- (to syn-) kinematic.
- Isoorientation of quartz aggregates indicates that dynamic recrystallization occurred before the static one (triple points and equigranular aggregates of quartz).
- Epidote as inclusion at garnet rim.
- Local tartan pattern in matrix feldspar.

Relative age diagram (blastesis-deformation tab):

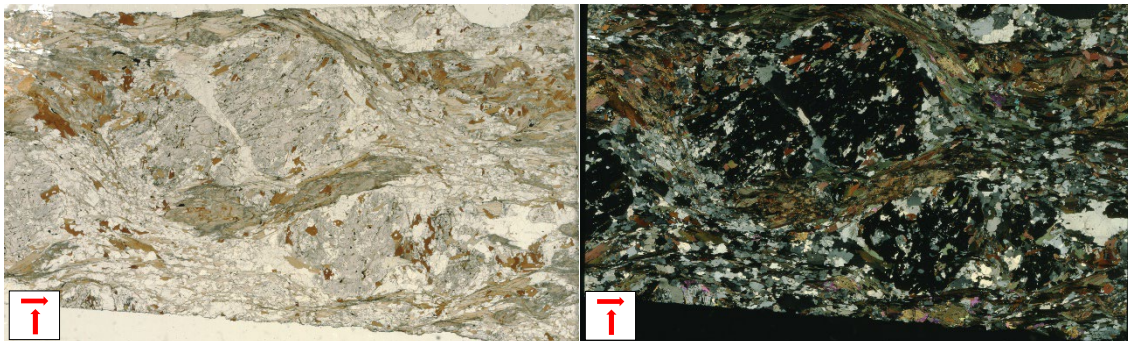
Quartz

Feldspar

Biotite

Garnet

Rutile

*Sample AS21.1**Section AS21.1A**Panoramics:**Mineral assemblage:*

Garnet, biotite, sillimanite, quartz, kyanite, feldspar, white mica, rutile, ilmenite, zircon, oxides and Fe-oxides.

Mineral distribution:

Heterogeneous distribution of minerals.

- Big garnet porphyroblasts are wrapped by the foliation of the matrix. Poikilitic, ipidiomorphic, fractured garnet grains in the foliation contain inclusions of quartz, biotite, rutile, ilmenite, titanite, opaques. The orientation of the inclusions is at high to low angle to the matrix foliation.
- Medium size biotite grains are isooriented, usually with LPO coinciding with SPO. Some grains are at high angle with respect to the main schistosity.
- Fine grainsize white mica grains are elongated in the foliation.
- Large to medium grainsize kyanite can be elongated in the foliation or at high angle.
- Thin sillimanite grains can be elongated in the foliation and occurring together with biotite, or they form nest structures in the matrix.
- Feldspar fills garnet's fractures. Matrix feldspar and quartz grains are small to medium size, anhedral.

Fabric:

Tectonic fabric. Lepidoblastic fabric of matrix biotite.

Foliation:

The rock is foliated. The foliation is continuous and defined by the isoorientation of biotite, kyanite, white mica, sillimanite.

Deformation mechanisms:

- Deformation lamellae in plagioclase.
- Metamictization of biotite around zircon inclusions.
- Local substitution of kyanite by feldspar and white mica.
- Local triple points in quartz/feldspar.
- Subgrain rotation, dragging, pinning and window structures in feldspar are evidence of dynamic recrystallization.
- Resorption of garnet edges.
- Local sagenitic rutile in biotite next to garnet.

Notes:

- Zircon in the matrix as inclusion in feldspar and biotite.
- Evidence of partial melting: drops in garnet feldspar inclusions, local polysynthetic twinning in matrix plagioclase.
- The orientation of biotite inclusions in the garnet can differ from the one of quartz/feldspar inclusions.
- The biggest garnet grains are pre-kinematic.

Relative age diagram (blastesis-deformation tab):

Quartz

Feldspar

Biotite

Garnet

Kyanite

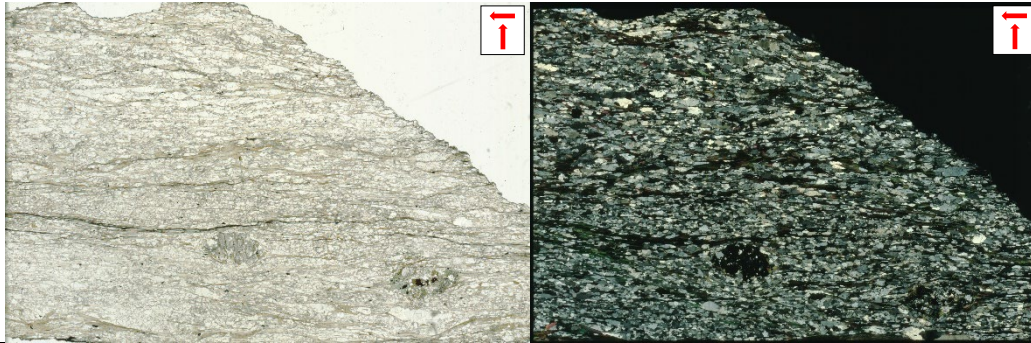
Sillimanite

Rutile

Ilmenite

White mica



*Sample OS16-006**Panoramics:**Mineral assemblage:*

Quartz, feldspar, garnet, biotite, chlorite, zircon, rutile, ilmenite, epidote, oxides and Fe-oxides.

Distribution:

Heterogeneous distribution of minerals.

- Mostly idiomorphic biotite of medium size, with SPO coinciding with LPO. With zircon's inclusions.
- Idiomorphic-subidiomorphic quartz/feldspar in elongated aggregates, inequigranular, interlobate.
- Idiomorphic medium-large size garnet crystals with inclusions of: rutile, feldspar, zircon, quartz.

Fabric:

Tectonic fabric. Lepidoblastic fabric of biotite.

Locally the medium-fine grain size chlorite crystals have a decussate fabric.

Foliation:

The rock is foliated. The foliation is continuous and it is defined by the SPO coinciding with the LPO of biotite.

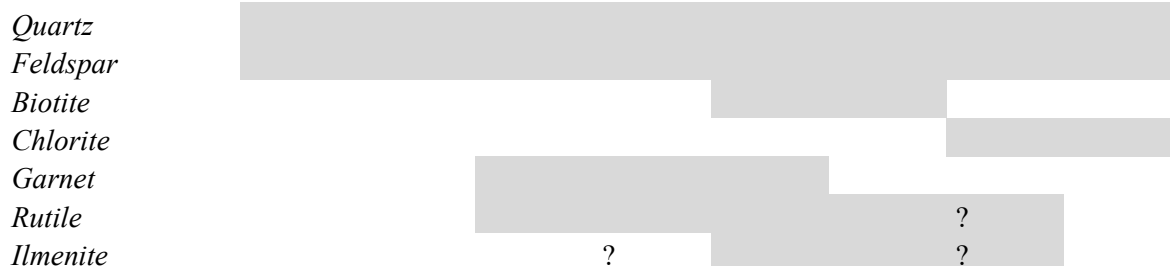
Deformation mechanisms:

- Partial transformation of biotite in chlorite.
- Metamictic aureole around zircon grains included in biotite.
- Chlorite is folded and with undulose extinction.
- Undulose extinction of quartz and dynamic recrystallization.
- Local static recrystallization of feldspar.
- Deformation lamellae and fractured feldspar.
- Biotite grains are locally substituted by chlorite: its orientation can be at high angle with respect to the main foliation or parallel to it.
- Metamictic aureole in biotite around zircon inclusions.
- Chlorite and opaques substitution of fractured garnet grains.

Notes:

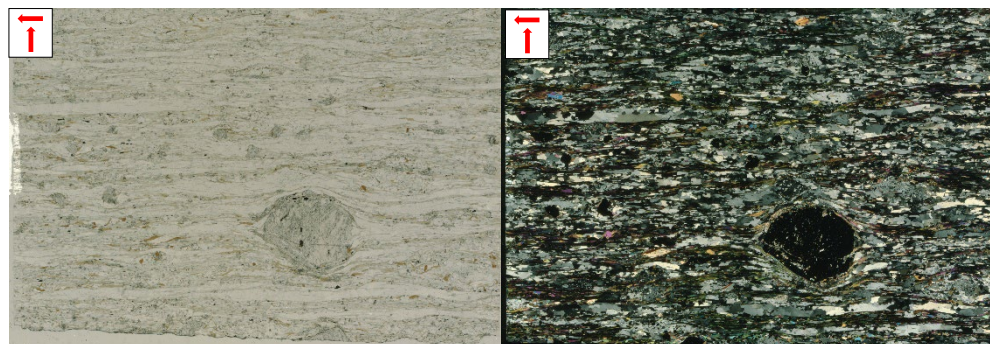
- Polysynthetic twin lamellae in plagioclase.
- Locally it's possible to see medium-fine size chlorite, sometimes folded, with SPO coinciding with LPO that is at high angle to the principal foliation.
- There's a zone with reddish Fe-oxides, rich in chlorite with decussate fabric.
- Abundant plagioclase.
- Locally fine grainsize chlorite and feldspar replace biotite.

Relative age diagram (blastesis-deformation tab):



Sample AC19.3A

Panoramics:



Mineral assemblage:

Quartz, feldspar, garnet, white mica, biotite, chlorite, kyanite, staurolite, zircon, rutile, epidote, oxides.

Distribution:

Heterogeneous distribution of minerals.

- Biotite and white mica are elongated with biotite's SPO not always coinciding with LPO. Some biotite grains are at high angle to the main foliation. Mica grainsize is from medium to medium-fine.
- Elongated quartz aggregates are in ribbons parallel to the foliation. The aggregates can be both equigranular and polygonal or inequigranular and interlobate.
- Feldspar can be in large or medium size, in elongated and subhedral to anhedral shape. Locally, pockets within the foliation are formed by large feldspar grains substituted by fine quartz "drops". In these areas also fine garnet grains, epidote, rutile and biotite with no preferential orientation are found.
Medium-fine size subhedral feldspar grains with polysynthetic twinning are elongated parallel to the foliation.
- Garnet can be of diverse size, from large to fine size. Poikiloblastic large and medium garnet crystals are wrapped by kyanite, staurolite, biotite, white mica, opaques of the main foliation. The inner foliation is at high angle with respect to the outside foliation of the rock. Garnet inclusions are zircon, rutile, white mica, feldspar, quartz, local chlorite substituting white mica.
- Poikilitic kyanite crystals have garnet and rutile inclusions. They occur together with biotite and quartz. They have SPO and LPO, however some grains are not elongated and their LPO is at high angle with respect to the principal foliation.
- Local euhedral medium-fine size staurolite is elongated in the foliation. It is often associated to biotite and kyanite, and it can be locally poikilitic (zircon inclusions).

Fabric:

Tectonitic fabric. Lepidoblastic fabric of mica.

Foliation:

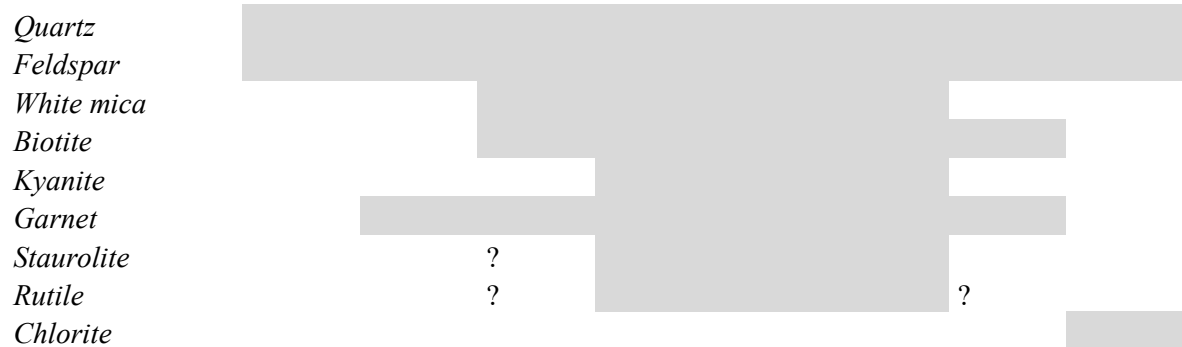
The rock is foliated. The foliation is from continuous to spaced and it is defined by quartz-feldspathic elongated domains, elongated kyanite crystals with SPO, and SPO of white mica and biotite.

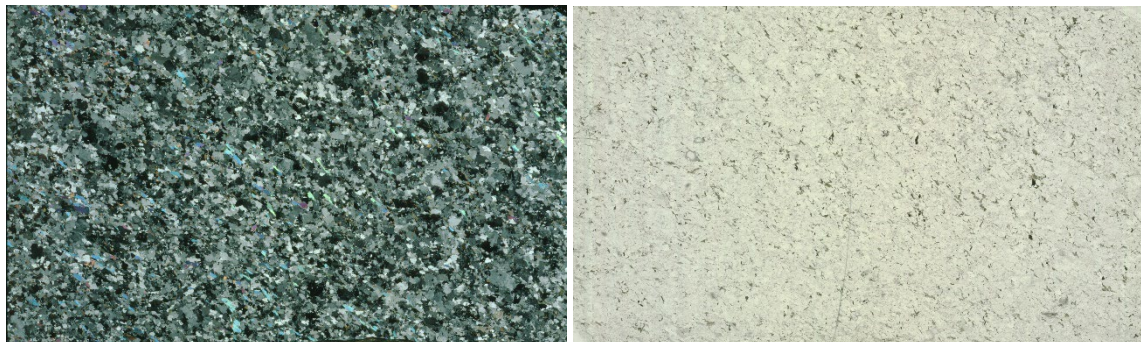
Deformation mechanisms:

- Dynamic and static recrystallization of quartz. Dragging microstructures and local window microstructures can be observed.
- Symplectites in feldspar.
- Polysynthetic twinning and deformation lamellae in plagioclase.
- Resorbed garnet, substituted by kyanite, white mica, biotite.
- Kyanite substituted by quartz.
- Local substitution of biotite with chlorite.

Notes:

- Local kyanite twinning.
- Incipient melting; local microgranites.
- Garnet crystals are in two generations: the fine size crystals within microgranitic pockets are syn-foliation, the large garnet crystals are pre-kinematic to syn-kinematic (edges).
- Biotite and white mica occur together in the foliation.

Relative age diagram (blastesis-deformation tab):

Migmatitic leucogneiss*Sample OS17-013**Section OS17-013A**Panoramics:**Mineral assemblage:*

Quartz, feldspar, white mica, biotite, chlorite, zircon, oxides, garnet, staurolite, apatite, epidote.

Mineral distribution:

Heterogeneous distribution of minerals.

- Quartz aggregates of fine to medium size grains form the matrix together with medium size feldspar grains. Quartz is often lobate or amoeboid and forms myrmekites with feldspar. Feldspar grains are ipidiomorphic, locally the bigger grains have straight edges and tartan pattern is common. Plagioclase can show polysynthetic twinning.
- Brown-greenish, medium-fine grain biotite crystals, ipidiomorphic, with SPO coinciding with LPO, are isooriented in the matrix.
- White mica crystals show high interference colors at crossed nicols, SPO coincides with LPO, parallel to the ones of biotite.
- Fine size, pinkish at 1 nicol, rounded or anhedral garnet grains can be found in the foliation.
- Staurolite grain, fine in size, elongated and fractured can be seen in the foliation.

Fabric:

Migmatitic fabric.

Foliation:

The rock is foliated. The foliation is continuous and defined by the preferred orientation of mica grains. The main foliation is defined by preferred orientation of white mica and biotite. In some places, a different orientation (direction at high angle with respect to the main foliation) is observed.

Deformation mechanisms:

- Undulose extinction in quartz, window structures, pinning, subgrain rotation, local triple points.
- Local replacement of plagioclase by feldspar monocline.
- Partial replacement of plagioclase by saussurite.
- Resorption at the edges of white mica grains.
- Local chloritization of biotite.
- Resorbed edges of white mica.

Notes:

- Staurolite is elongated parallel to the main foliation.
- Partial melting is detected from the following evidence: tartan pattern in feldspar, polysynthetic twinning in plagioclase, straight edges of big feldspar grains or cusps as result of possible melt infiltration in the rock pores.
- Myrmekites are abundant. They are an evidence of the presence of fluids in the rock pores.
- Zircon in the matrix.

Relative age diagram (blastesis-deformation tab):



Sample AV19.3

Section AV19.3-1

Panoramics:



Mineral assemblage:

Feldspar, quartz, biotite, white mica, chlorite, zircon, oxides, amphibole (green hornblende), epidote.

Mineral distribution:

Homogeneous distribution of minerals.

- In the matrix, quartz and feldspar aggregates are inequigranular, only locally seriate in shape, interlobate to amoeboid. Both minerals are idiomorphic. Feldspar grains contain tiny fractures.
- Medium-large biotite grains and small grainsize white mica grains are isooriented, usually having SPO coinciding with LPO.

Fabric:

Migmatitic fabric.

Foliation:

The rock is only locally foliated, where mica crystals are isooriented.

Deformation mechanisms:

- Undulose extinction in quartz and feldspar.
- Deformation lamellae in plagioclase. Saussurite alteration in feldspar.
- Myrmekites, locally oriented.
- Local perthites.
- Feldspar grains contain tiny fractures.
- White mica is resorbed at the edges or recrystallized in small grains.
- Sporadic amphibole is resorbed at the edges.
- Chloritization of biotite.

Notes:

- Gemination lamellae in plagioclase.
- Zircon is usually at the borders of other minerals.
- Local crystallization of clinozoisite in ipidiomorphic to idiomorphic aggregates.
- At the mesoscale, two types of biotite crystals with different colors can be recognized, probably the difference in darkness depends on their different orientation.
- Only one amphibole has been seen in the thin section.

Relative age diagram (blastesis-deformation tab):

Quartz

Feldspar

Biotite

White mica

Chlorite

Amphibole

*Section AV19.3-2**Panoramics:**Mineral assemblage:*

Feldspar, quartz, white mica, biotite, chlorite, zircon, oxides, epidote.

Mineral distribution:

Homogeneous distribution of minerals.

- Feldspar aggregates are inequigranular, interlobate. Locally amoeboid. The biggest grains are idiomorphic to ipidiomorphic.
- Medium-fine size biotite and thin white mica are isooriented.

Fabric:

Migmatitic fabric.

Foliation:

The rock is foliated. The foliation is continuous and defined by isooriented mica aggregates.

Deformation mechanisms:

- Undulose extinction of fractured feldspar grains.
- Myrmekites.
- Resorption of white mica.

Notes:

- Polysynthetic twinning in plagioclase.
- Epidote can have zircon inclusions.

Relative age diagram (blastesis-deformation tab):

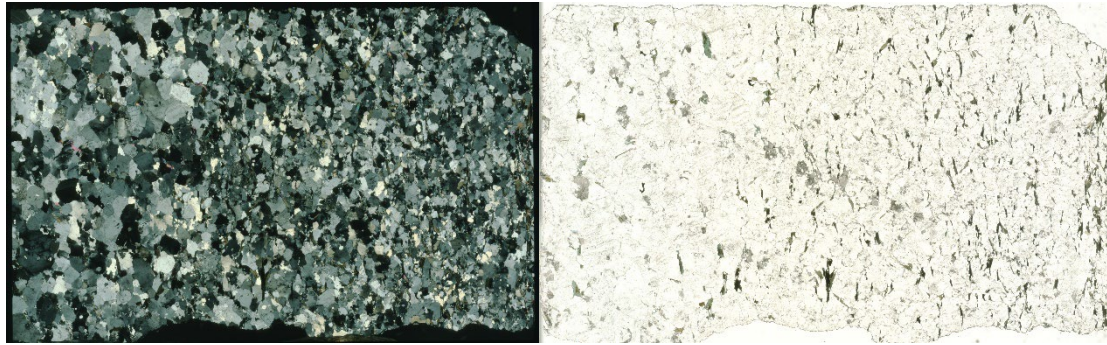
Quartz

Feldspar

Biotite

White mica

Chlorite

*Sample AV19.4**Section AV19.4-1**Panoramics:**Mineral assemblage:*

Feldspar, quartz, biotite, white mica, chlorite, zircon, oxides, Fe-oxides, apatite.

Mineral distribution:

Heterogeneous distribution of minerals.

- Feldspar is in subidiomorphic, large grainsize crystals. The shape of the aggregates is interlobate and changes from inequigranular to locally seriate.
- Medium to small grainsize biotite crystals have SPO not always coinciding with LPO (local mica fishes).

Fabric:

Migmatitic fabric.

Foliation:

The rock is foliated. The foliation is continuous and defined by isooriented mica crystals. Biotite crystals have two orientations at ca. 120° difference one from the other. White mica is associated to biotite.

Deformation mechanisms:

- Undulose extinction, fractures, and saussuritic alteration of feldspar.
- Abundant myrmekites.

Notes:

- Local tartan pattern in feldspar.
- Sagenitic rutile in chloritized biotite.
- Epidote can have zircon inclusions.

- Zircon is both within grains and at the interface between crystals.

Relative age diagram (blastesis-deformation tab):

Quartz

Feldspar

Biotite

White mica

Chlorite



Section AV19.4-2

Panoramics:



Mineral assemblage:

Feldspar, quartz, white mica, biotite, chlorite, zircon, oxides, epidote.

Mineral distribution:

Homogeneous distribution of minerals.

- Large idiomorphic feldspar crystals form locally equigranular polygonal to interlobate aggregates.
- Medium size biotite grains with LPO coinciding with LPO in the matrix are locally associated with small grainsize white mica grains.

Fabric:

Magmatic fabric.

Foliation:

The rock is slightly foliated, with isooriented mica in the matrix.

Deformation mechanisms:

- Undulose extinction of feldspar, fractures and perthites.
- Deformation lamellae in plagioclase.
- Dissolution of white mica.
- Myrmekites.
- Local sagenitic rutile on a chloritized biotite.

Notes:

- Abundant polysynthetic twinning in plagioclase.
- Zircon is within crystals.
- Locally there's a residue of white mica in large feldspar grains.

Relative age diagram (blastesis-deformation tab):

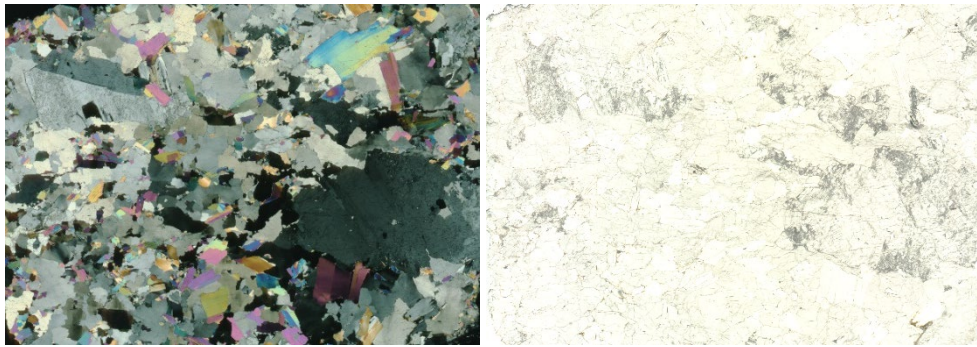
Quartz
Feldspar
Biotite
White mica
Chlorite



Granitic dikes

Sample AV21-001

Panoramics:



Mineral assemblage:

Feldspar, white mica, quartz, garnet, zircon.

Mineral distribution:

Homogeneous distribution of minerals.

- Large feldspar grains can have idiomorphic to ipidiomorphic shape. Locally, polysynthetic twinning in plagioclase and Carlsbad twinning in K-feldspar can be seen.
- Large white mica crystals with high interference colors have different LPO. Sometimes they have small to medium size quartz inclusions.

Fabric:

Magmatic fabric.

Foliation:

The rock is not foliated.

Deformation mechanisms:

- Saussurite alteration of feldspar.
- Partial resorption at the edges of white mica and at the borders of quartz inclusions.

Notes:

- Quartz is less abundant, almost absent.
- Garnet has been seen only as a medium-size crystal grown at the edge of a big feldspar crystal, together with residual quartz crystallized in the interstitial space between different feldspar crystals.
- Probably the melt residual was silica-rich.

Relative age diagram (blastesis-deformation tab):

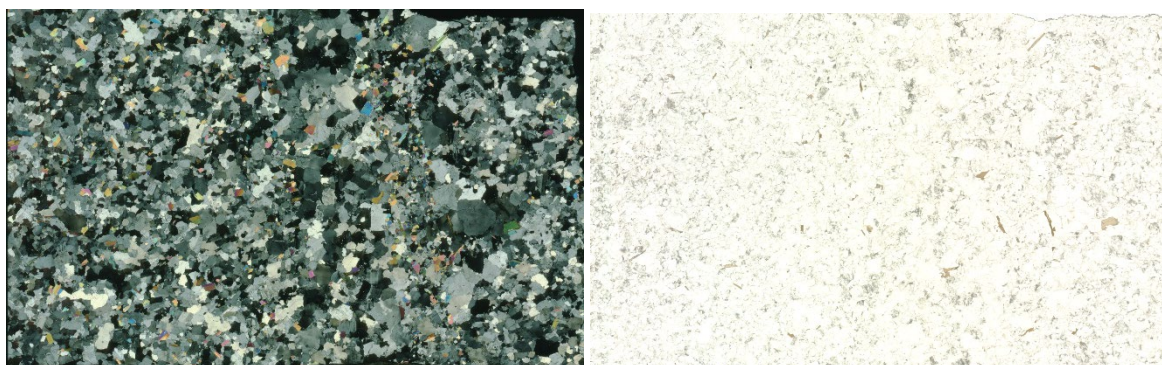
Feldspar
White mica
Quartz
Garnet



Sample AV21-002

Section AV21-002A

Panoramics:



Mineral assemblage:

Feldspar, quartz, white mica, biotite, chlorite, zircon, rutile, oxides, garnet.

Mineral distribution:

Homogeneous distribution of minerals.

- Large feldspar crystals have idiomorphic shape.
- Quartz medium-size crystals are subjected to GBM, hence forming also window structures and a lobate crystal shape. Quartz is also responsible for “pore-filling”, probably as a product of residual melts.
- White mica grains are medium to medium-fine size, with idiomorphic to ipidiomorphic shape. They are both oriented parallel to the base or to the c-axis, in the latter case the LPO is usually coinciding with SPO.
- Fine to medium-fine, anhedral to ipidiomorphic biotite grains do not have a specific preferred orientation.
- Medium-size euhedral fractured garnet has feldspar inclusions.

Fabric:

Magmatic fabric.

Foliation:

The rock is not foliated.

Deformation mechanisms:

- Deformation lamellae in plagioclase.
- Myrmekites.
- Saussurite alteration in feldspar.
- Substitution of biotite by chlorite and plagioclase.
- Thin sagenitic rutile can be spotted at biotite’s edges.
- Local slight kinking of white mica.
- Loss of elements at mica edges and partial resorption, locally leading to a skeletal structure.

Notes:

- Locally, plagioclase may show old polysynthetic twinning.
- Melt residuum was probably silica-rich. Evidence for this are: quartz filling the interstices between feldspar grains, and resorption of white mica.

Relative age diagram (blastesis-deformation tab):

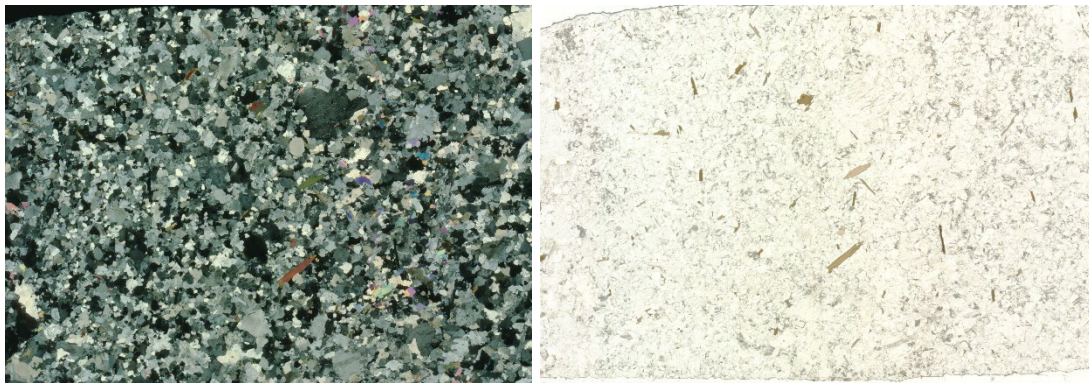
Feldspar

Quartz

White mica

Biotite

Chlorite

*Section AV21-002B**Panoramics:**Mineral assemblage:*

Feldspar, quartz, biotite, white mica, zircon, epidote, chlorite, rutile, oxides.

Mineral distribution:

Homogeneous distribution of minerals.

- Feldspar medium-size grains are idiomorphic, sometimes geminated.
- Lobate, fine to medium size quartz crystals grow on the feldspar crystals.
- White mica is usually idiomorphic and locally idiomorphic, with high interference colors and without a preferred orientation in the rock.
- Biotite is less abundant, its size is medium to fine, and just locally it can be substituted by chlorite.

Fabric:

Magmatic fabric.

Foliation:

The rock is not foliated.

Deformation mechanisms:

- Saussuritic alteration of feldspar.
- Deformation lamellae in plagioclase.
- Sometimes feldspar grains are micro-fractured.
- Undulose extinction in feldspar.
- Pseudo-coronitic textures can be seen around some feldspar grains.
- Local myrmekites.

- Resorption at biotite's edges, and local crystallization of very fine grains of sagenitic rutile.
- Sometimes, white mica crystals have fringes at their terminations, usually parallel to their orientation, probably due to resorption.
- In few cases, little portions of large white mica crystals are kinked.

Notes:

- Local Carlsbad twinning in K-feldspar, polysynthetic twinning and growth zonation in idiomorphic plagioclase.
- Triple points formed by feldspar grains are indicative of the magmatic origin.

Relative age diagram (blastesis-deformation tab):

Feldspar
Quartz
White mica
Biotite



Appendix H

MICROPROBE ANALYSES AND GEOETHERMOBAROMETRIC CALCULATIONS (CHAPTER 4)

This appendix is available online at: <https://zenodo.org/record/8399771>.

All data related to Microprobe analyses and geothermometric estimates presented in *Chapter 4* have been uploaded onto the general-purpose open-access repository Zenodo: <https://zenodo.org/record/8399771>. In this page we briefly describe the contents of each file.

Microprobe analyses

The folder *Microprobe analyses* contains Excel tables with the results of all the chemical analyses performed using the Electron MicroProbe Analyzer. Each Excel file corresponds to a specific sample. Within each Excel file, there is a list of analyses divided per profile (e.g., profile *D10*, *D14*, etc.) and mineral (garnet, biotite, plagioclase, white mica as “grt”, “bt”, “pl”, “wm”). In the Excel sheets, below the list of analyses, there is also a plot which displays the composition of each point analyzed on the specific mineral (e.g., Grossular-Pyrope-Almandine (Grs-Py-Alm) triplot for garnet compositions).

As we mentioned in the main text, for all samples we analyzed the most external diffusion profile of our garnet rims which describes the Alpine history. Therefore, for some samples we considered only part of the profile measured at the microprobe. The considered points are highlighted in yellow in the Excel spreadsheets.

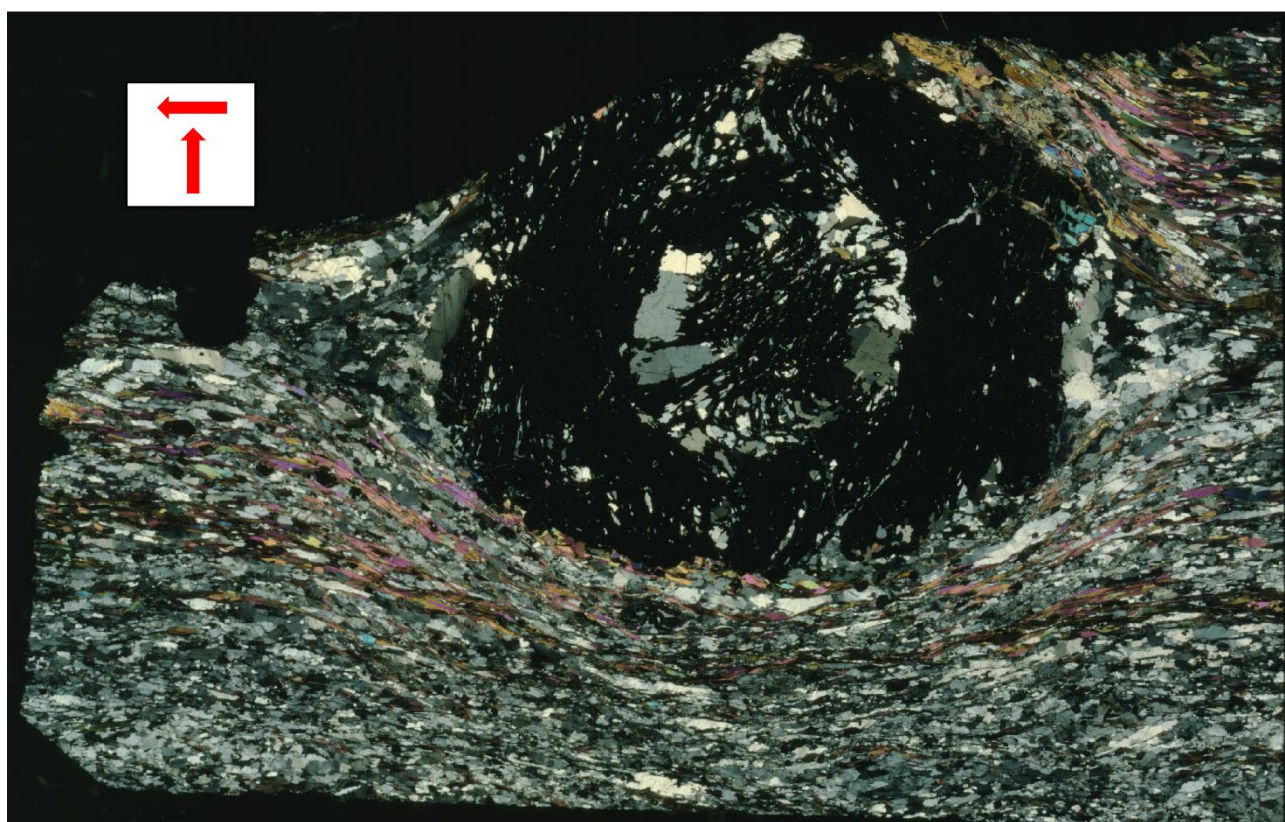
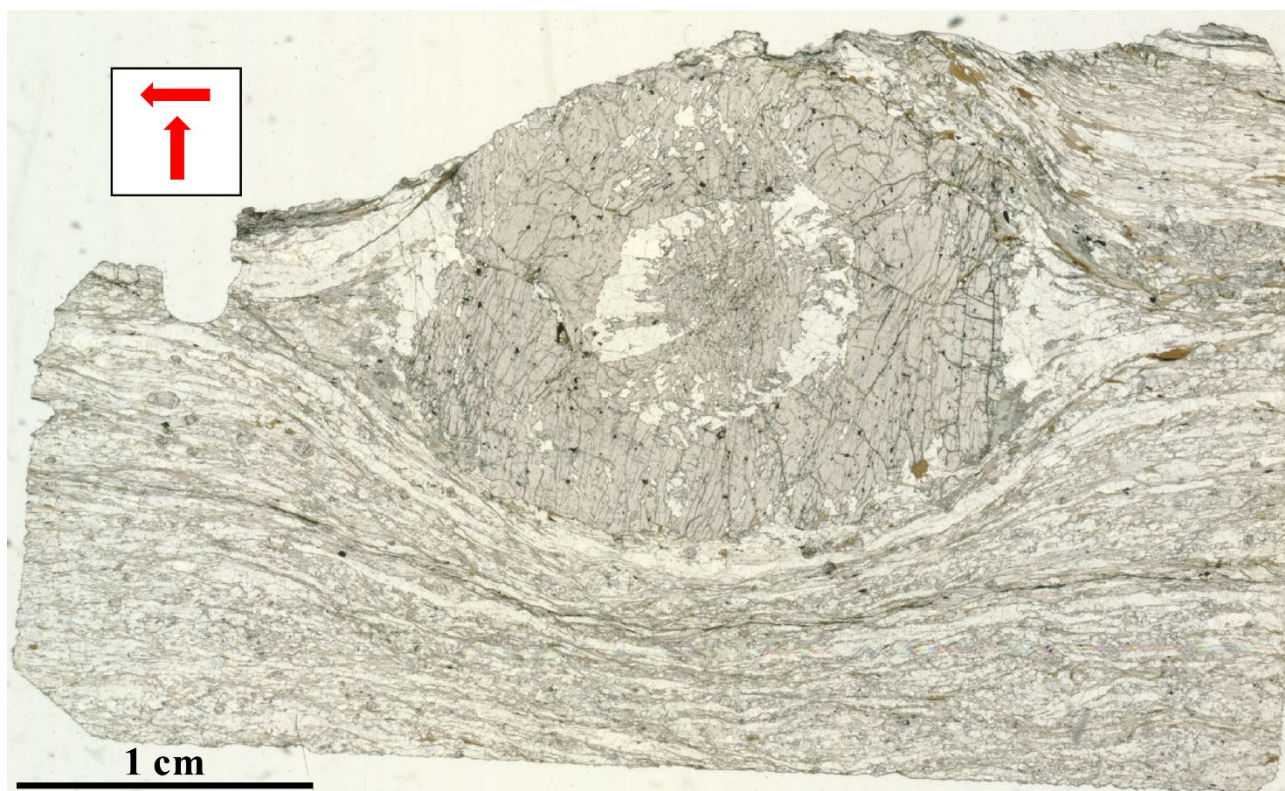
Geothermobarometry

The file *GeoTB.xlsx* is an Excel file containing representative mineral compositions and the geothermometers and geobarometers applied for the calculation of temperature and pressure (T and P) conditions of “outer rims” and “inner rims”. The applied thermometers are garnet-biotite (Holdaway, 2000) and garnet-phengite (Caddick & Thompson, 2008). The applied barometers are garnet-aluminosilicate-quartz-plagioclase (GASP; Caddick & Thompson, 2008) and phengite (Caddick & Thompson, 2008).

Appendix I

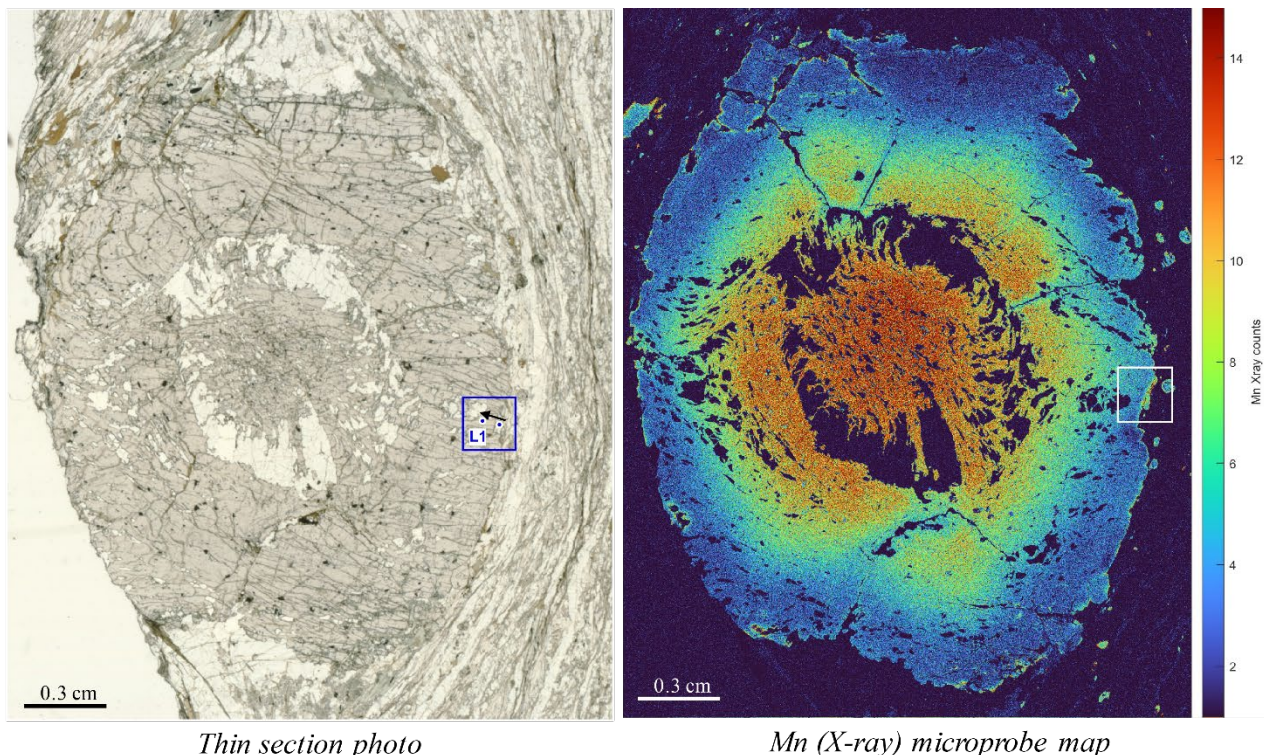
MICROPROBE CHEMICAL PROFILES AND RESULTS OF DIFFUSION MODELLING IN GARNET (CHAPTER 4)

Sample AG19.6A – thin section



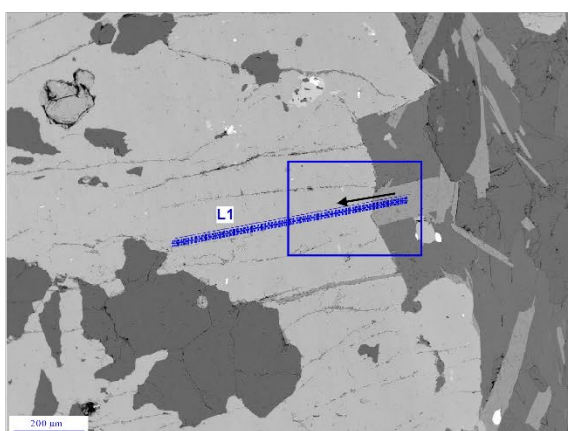
Sample AG19.6A – thin section

Profile L1

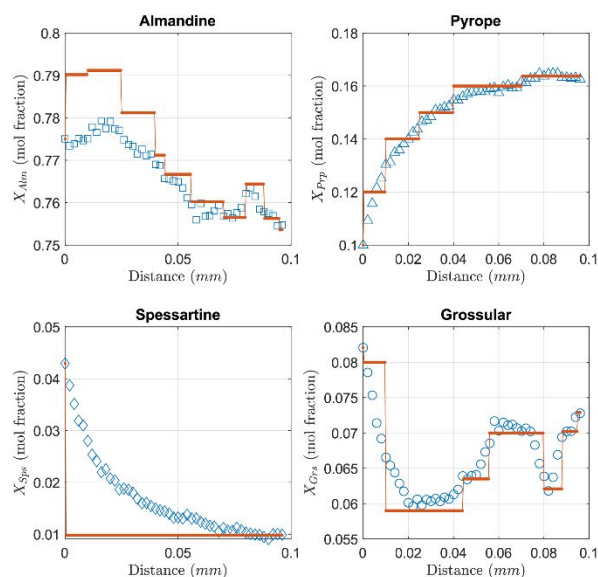


Thin section photo

Mn (X-ray) microprobe map



Microprobe photo



Measured profiles (blue symbols) and initial conditions (red lines) for garnet diffusion modelling with GDIF

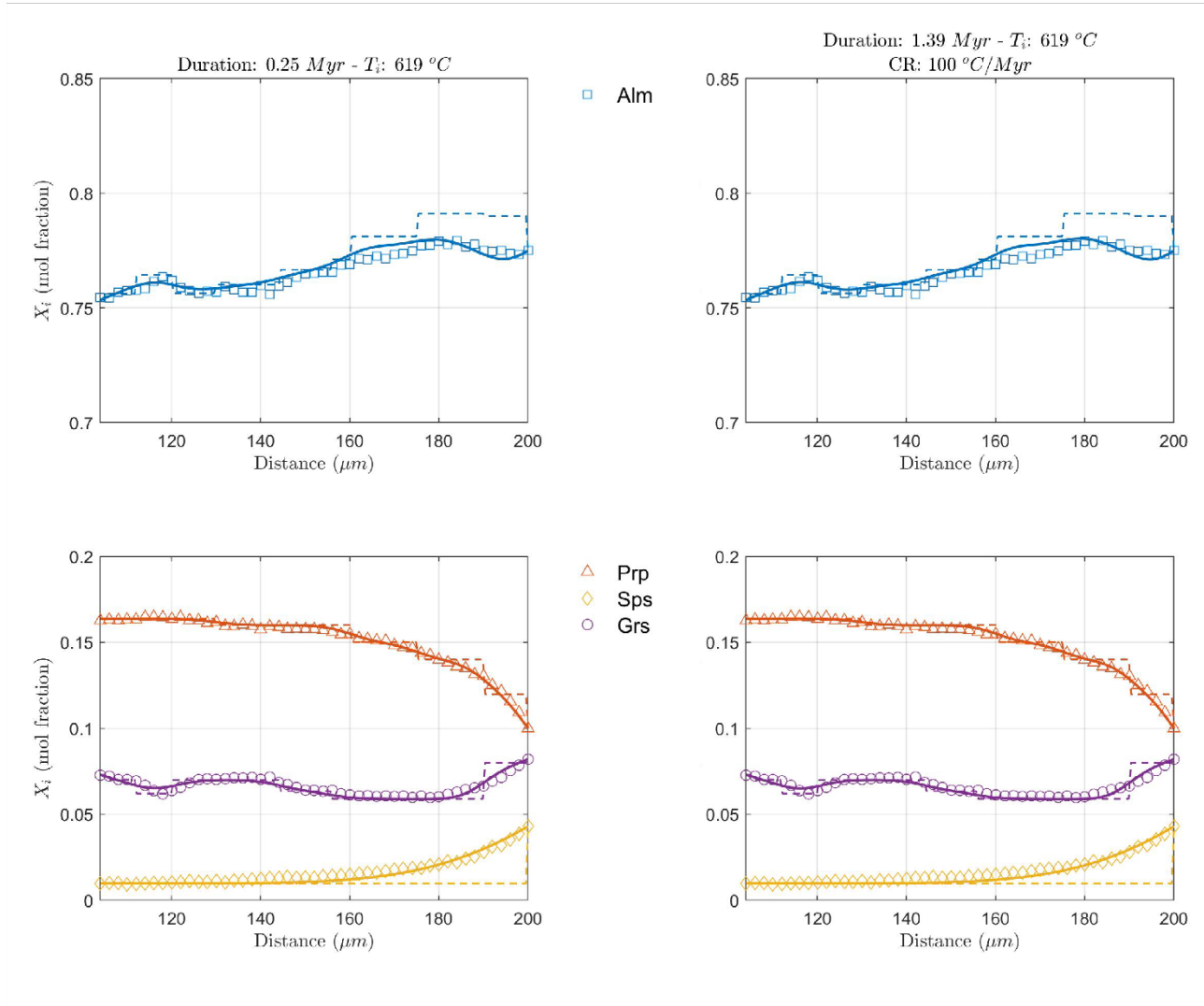
In the figures above is indicated the location of profile L1 on the thin section photos and microprobe X-ray map. The black arrows point from the first to the last point of the measured profiles. The microprobe profiles and fitting step-like functions are shown on the right. Note that only the first measured portion (garnet rim) of the profile has been considered for calculation. The relevant microprobe analyses are highlighted in yellow in the Excel table of *Appendix H* available online (folder *Microprobe analyses - Analyses_AG19.6A.xlsx*).

Sample AG19.6A – thin section

Profile L1 – rim

CASE 1:
Constant temperature

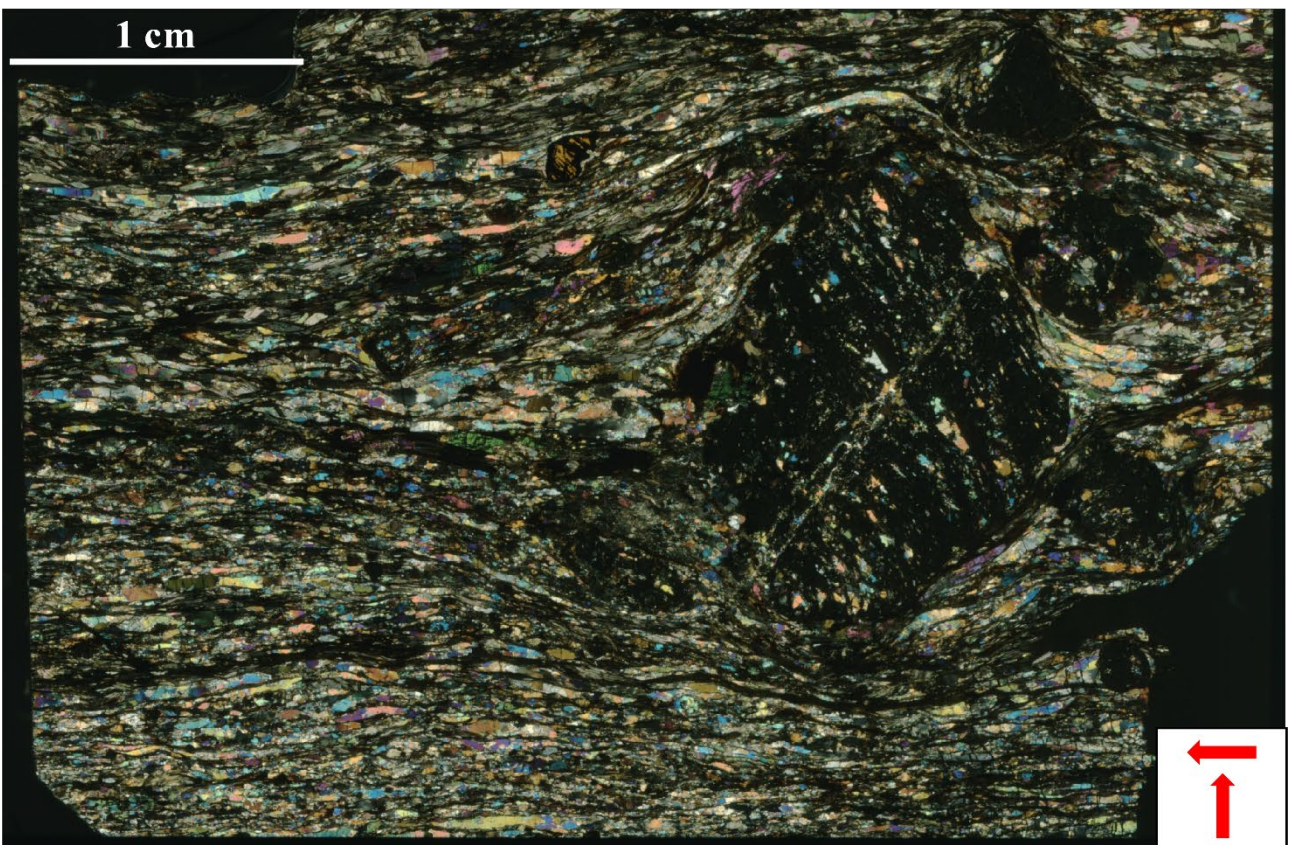
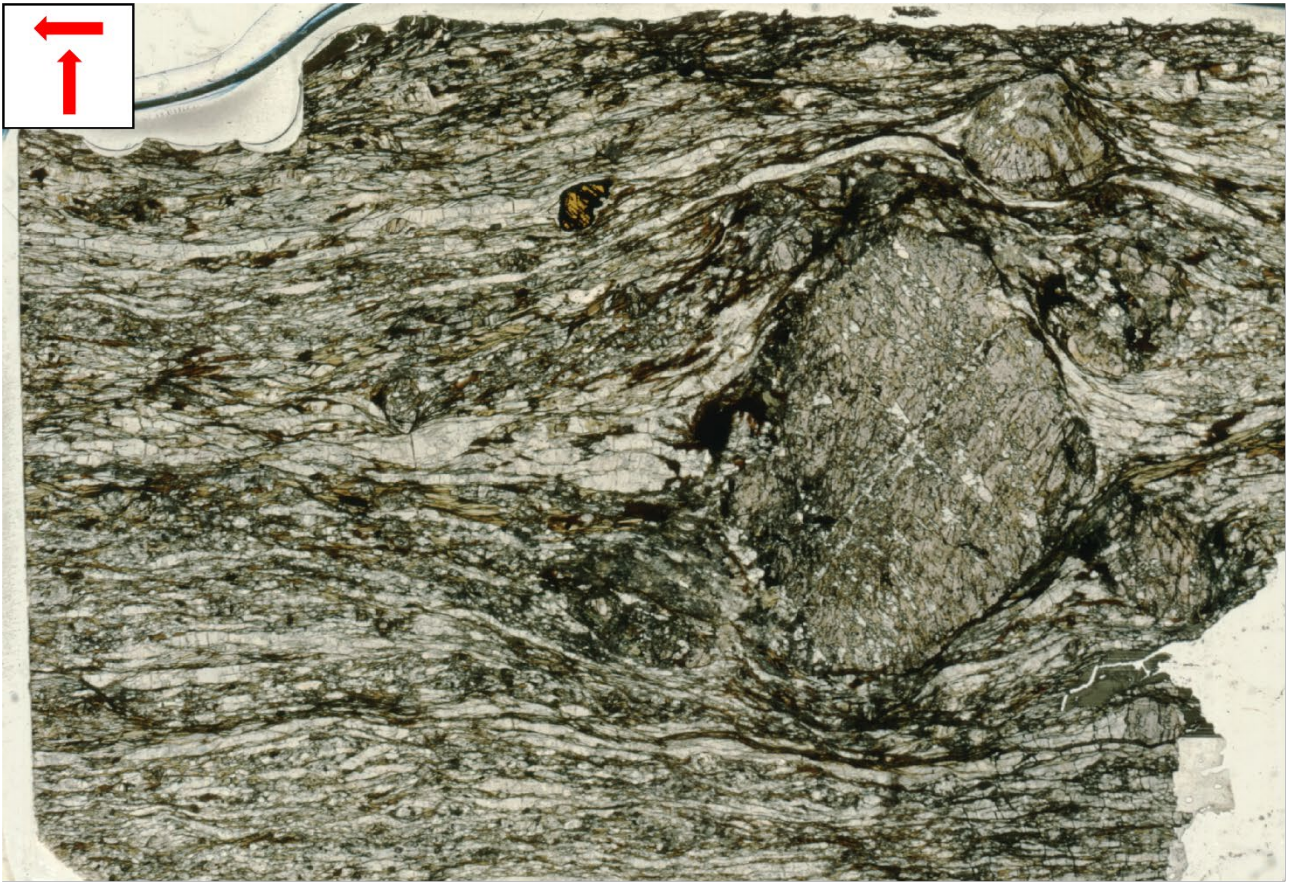
CASE 2:
Cooling history



Results of garnet diffusion modelling

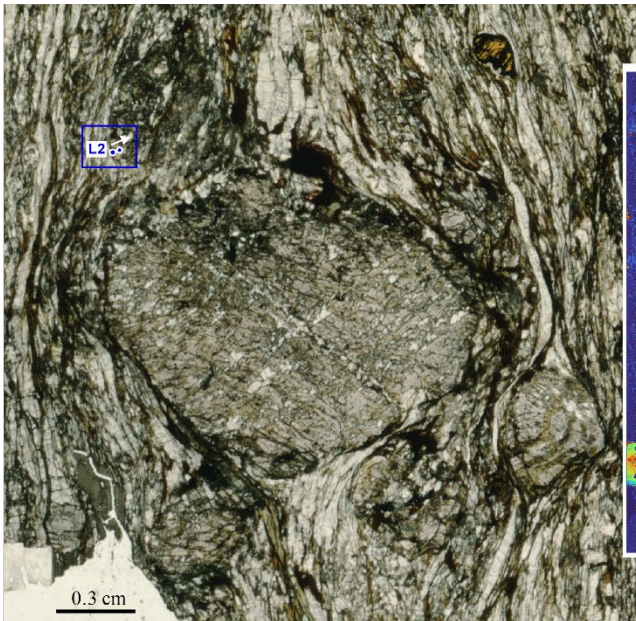
Microprobe profiles are indicated with colored symbols, initial conditions for garnet diffusion modelling with GDIFF with dashed lines, and diffusion results with thick colored lines.

Sample AG19.6C – thick section

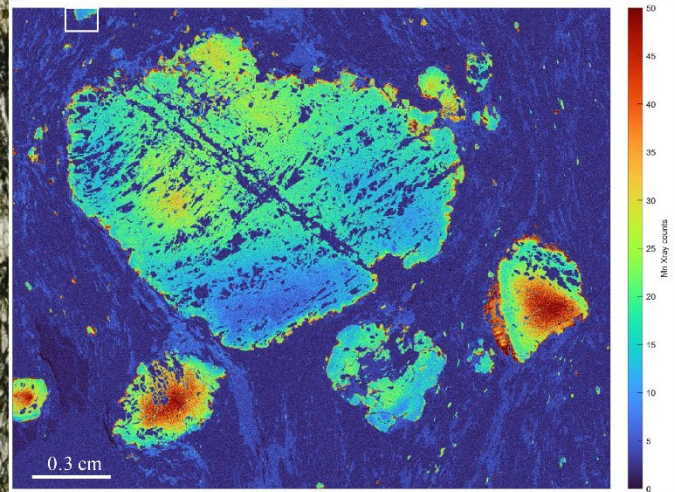


Sample AG19.6C – thick section

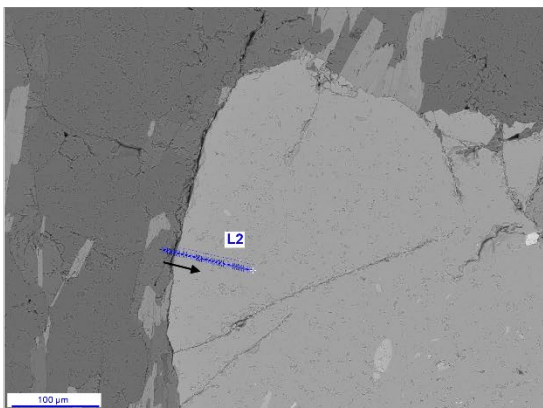
Profile L2



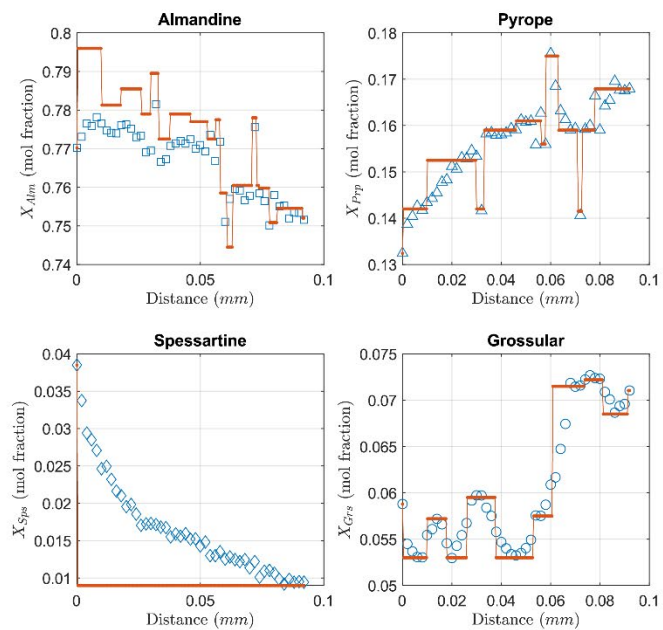
Thick section photo



Mn (X-ray) microprobe map



Microprobe photo



Measured profiles (blue symbols) and initial conditions (red lines) for garnet diffusion modelling with GDIFF

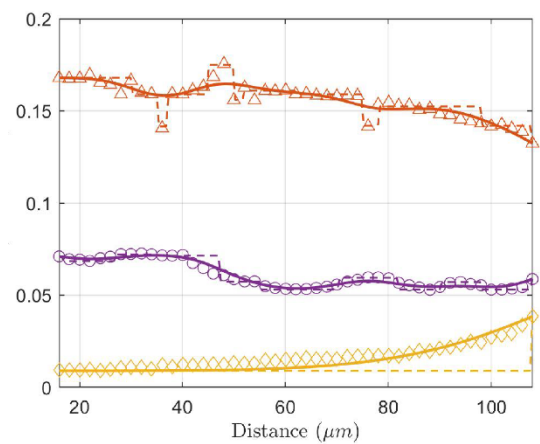
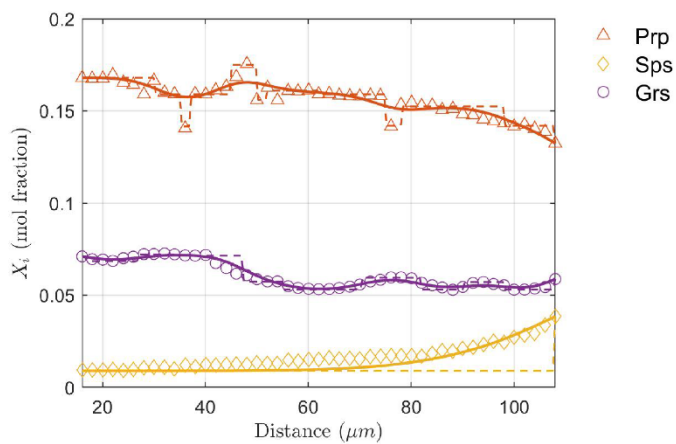
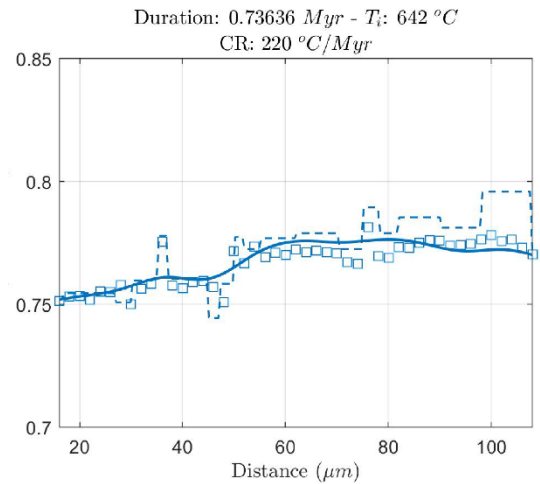
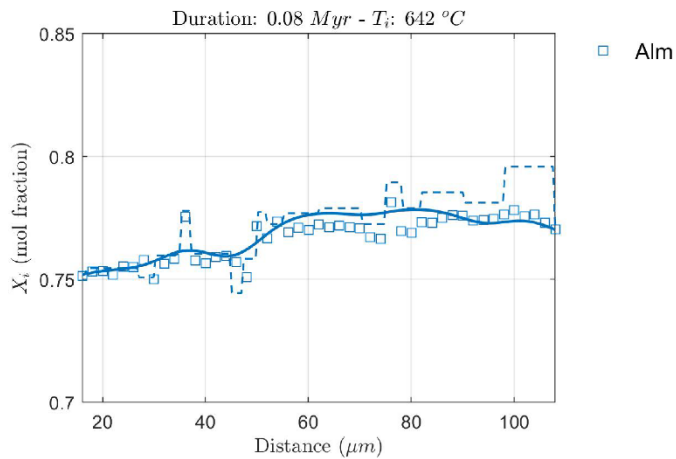
In the figures above is indicated the location of profile L2 on the thick section photos and microprobe X-ray map. The black and white arrows point from the first to the last point of the measured profiles. The microprobe profiles and fitting step-like functions are shown on the right. The relevant microprobe analyses are in Appendix H (online folder *Microprobe analyses - Analyses_AG19.6C.xlsx*).

Sample AG19.6C – thick section

Profile L2

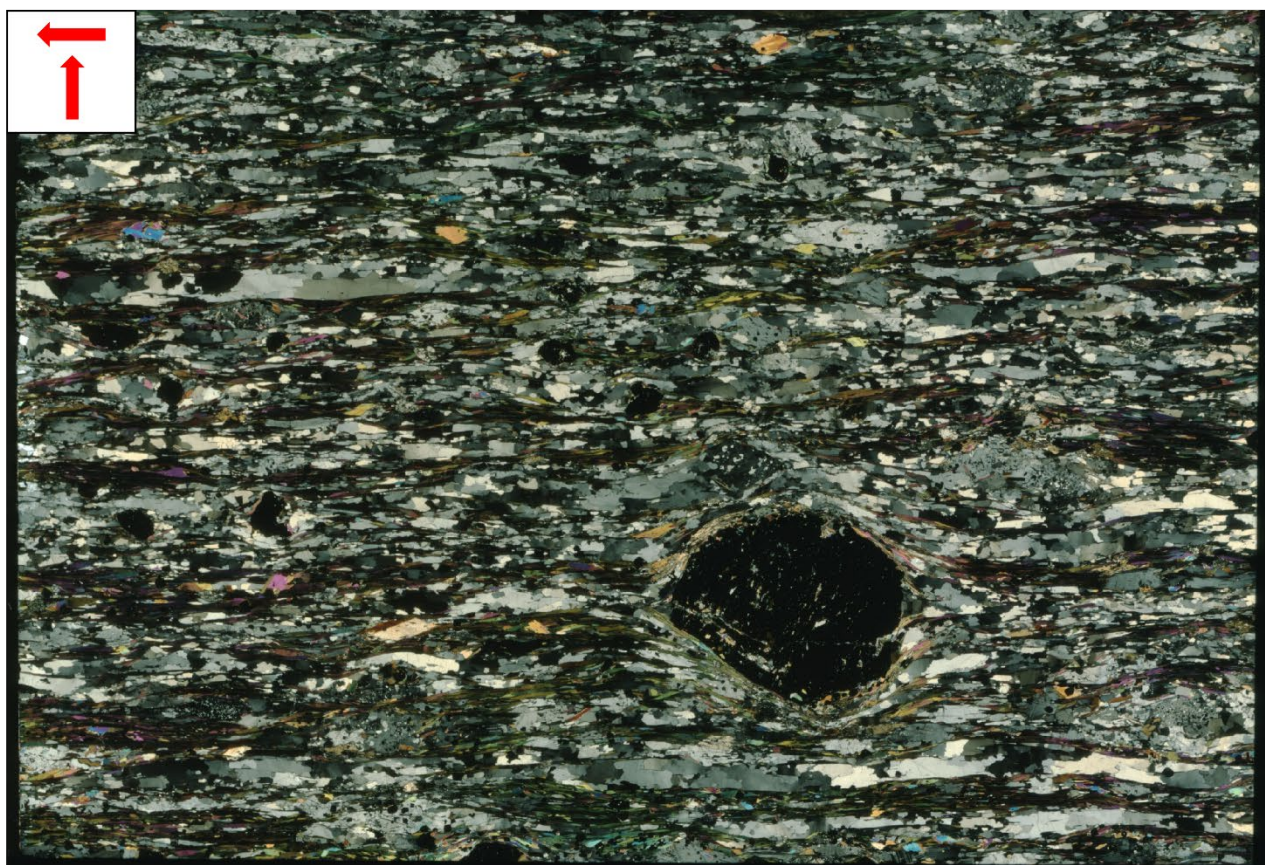
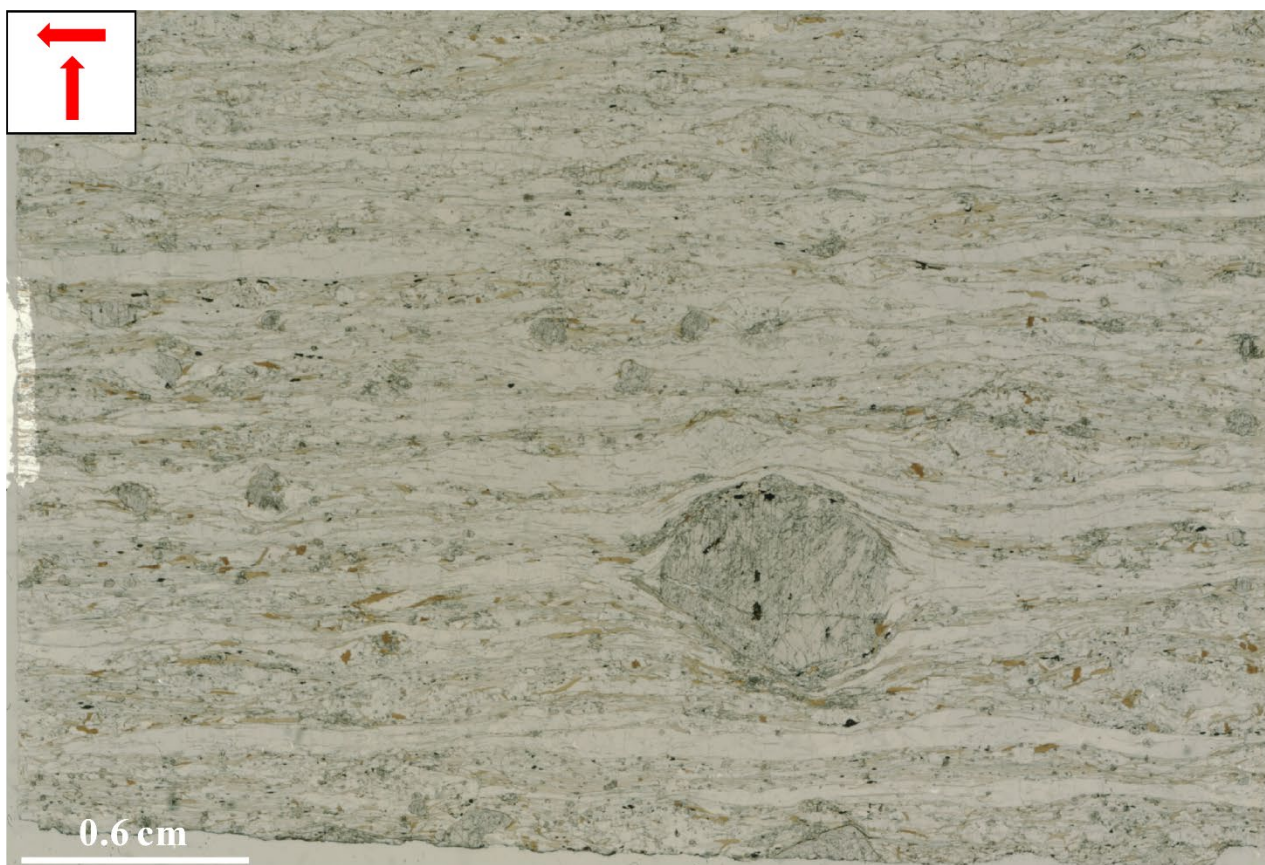
CASE 1:
Constant temperature

CASE 2:
Cooling history

**Results of garnet diffusion modelling**

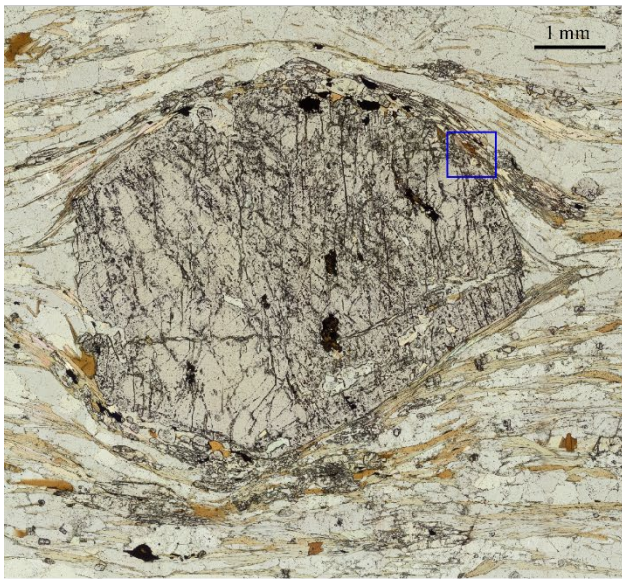
Microprobe profiles are indicated with colored symbols, initial conditions for garnet diffusion modelling with GDIFF with dashed lines, and diffusion results with thick colored lines.

Sample AC19.3A – thin section

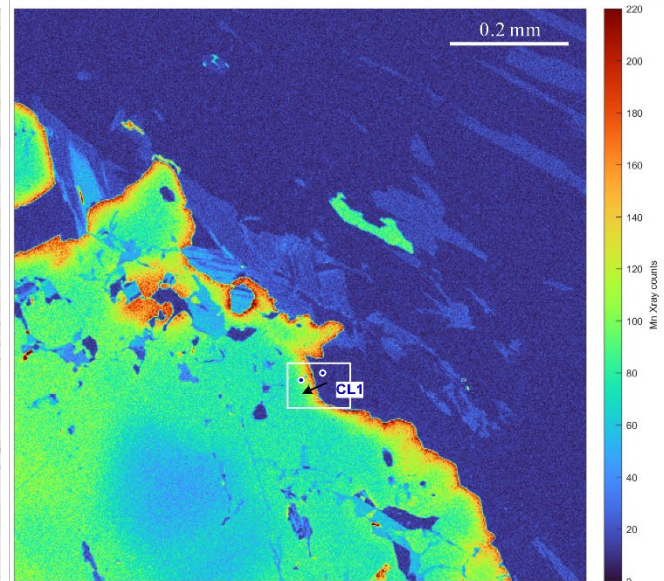


Sample AC19.3A – thin section

Profile CL1

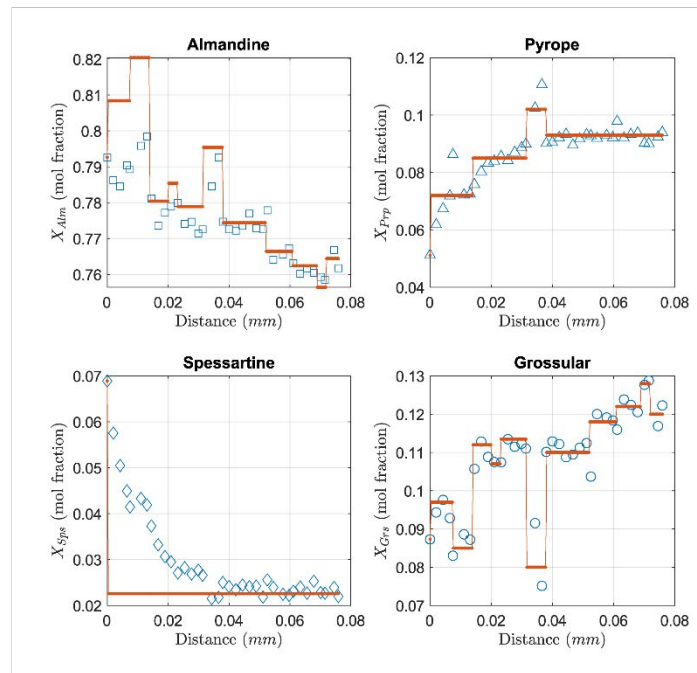


Thin section photo



Mn (X-ray) microprobe map

In the figures above is indicated the location of profile CL1 on the thin section photo and microprobe X-ray map. The black arrow points from the first to the last point of the measured profiles. The microprobe profiles and fitting step-like functions are shown on the right. The relevant microprobe analyses are in *Appendix H* (online folder *Microprobe analyses - Analyses_AC19.3A.xlsx*).



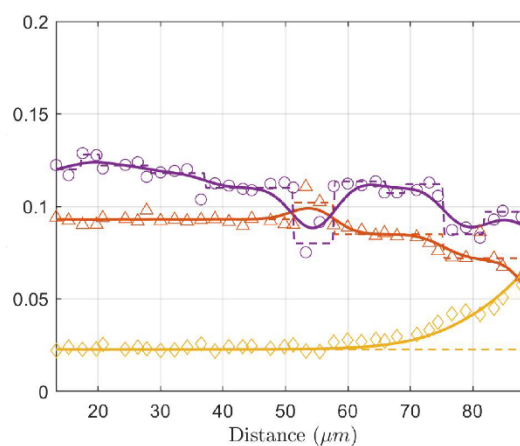
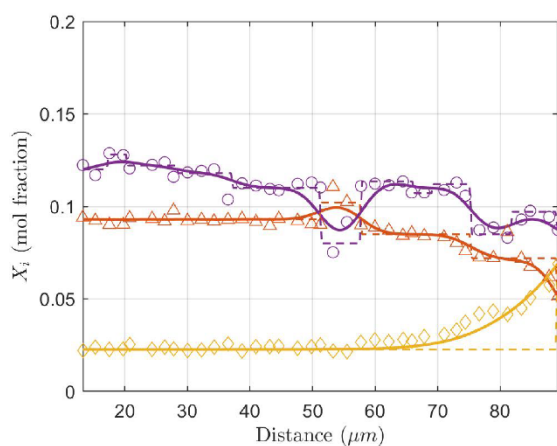
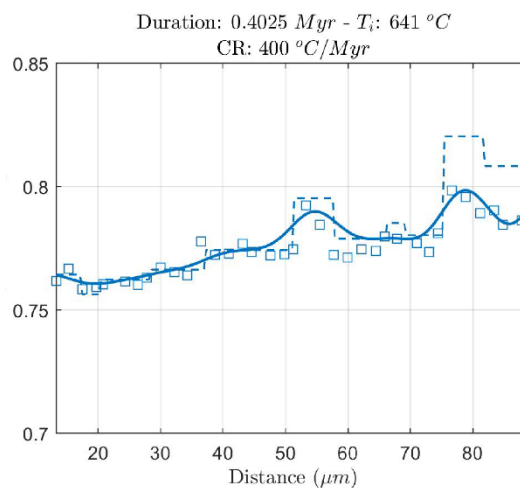
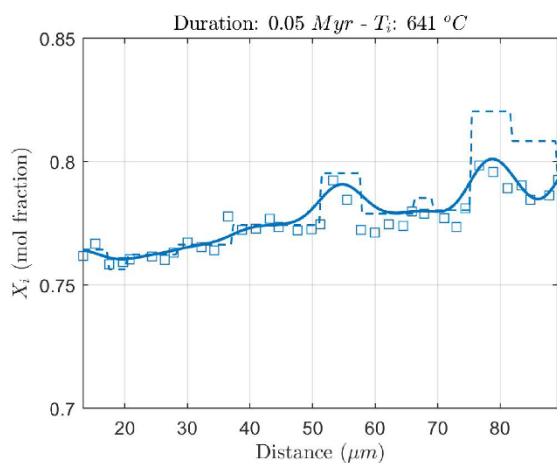
Measured profiles (blue symbols) and initial conditions (red lines) for garnet diffusion modelling with GDIFF.

Sample AC19.3A – thin section

Profile CL1

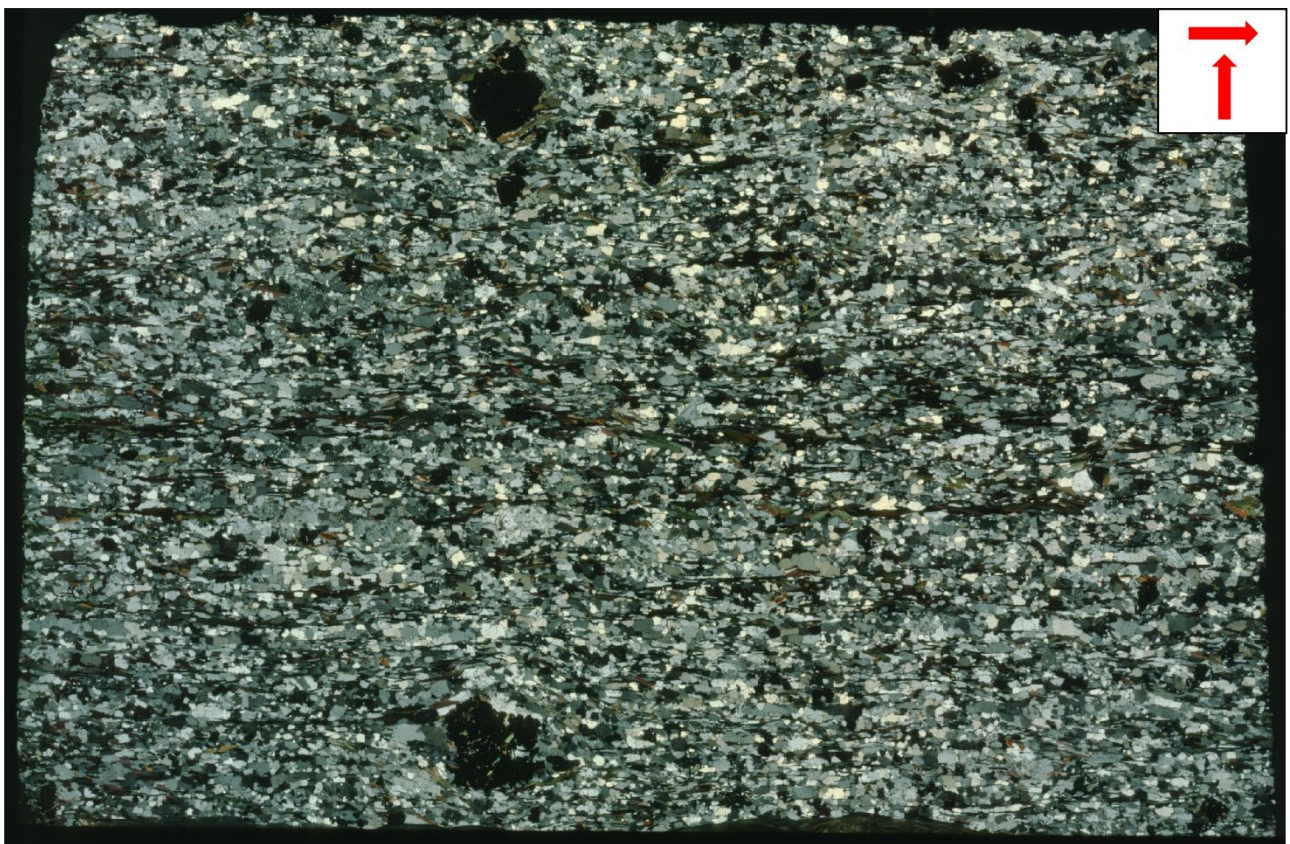
CASE 1:
Constant temperature

CASE 2:
Cooling history

**Results of garnet diffusion modelling**

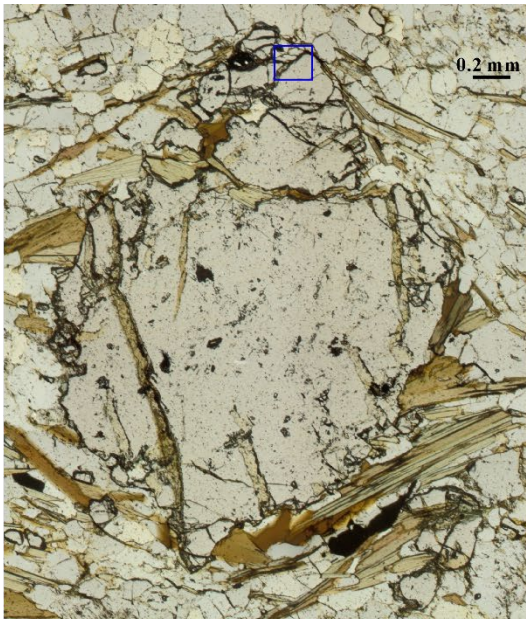
Microprobe profiles are indicated with colored symbols, initial conditions for garnet diffusion modelling with GDIFF with dashed lines, and diffusion results with thick colored lines.

Sample AG20.2B – thin section

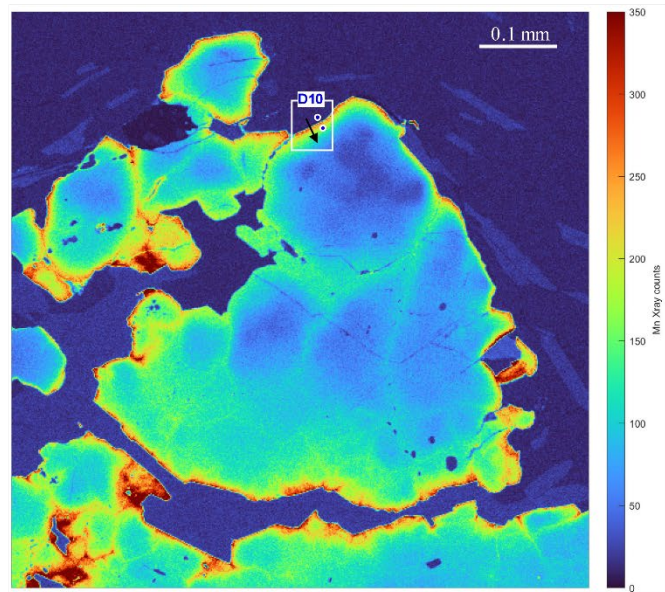


Sample AG20.2B – thin section

Profile D10

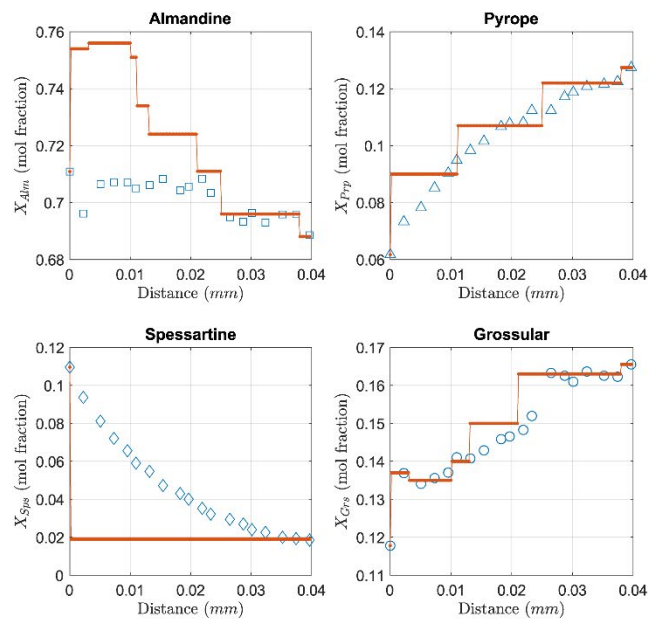


Thin section photo



Mn (X-ray) microprobe map

In the figures above is indicated the location of profile D10 on the thin section photo and microprobe X-ray map. The black arrow points from the first to the last point of the measured profiles. The microprobe profiles and fitting step-like functions are shown on the right. The relevant microprobe analyses are in *Appendix H* (online folder *Microprobe analyses - Analyses_AG20.2B.xlsx*).



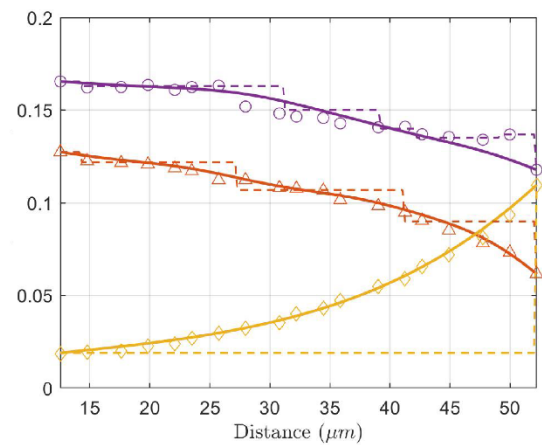
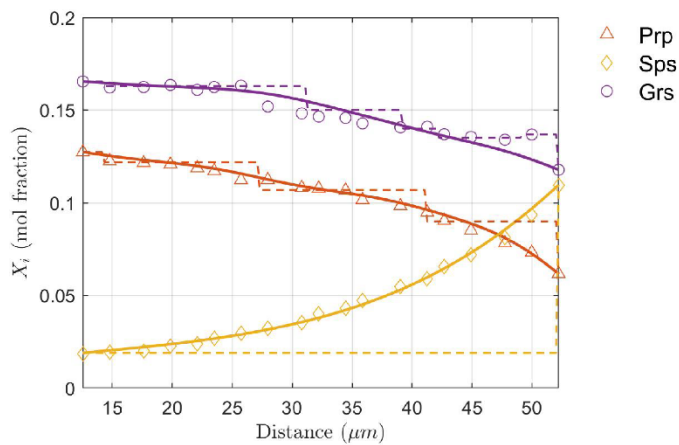
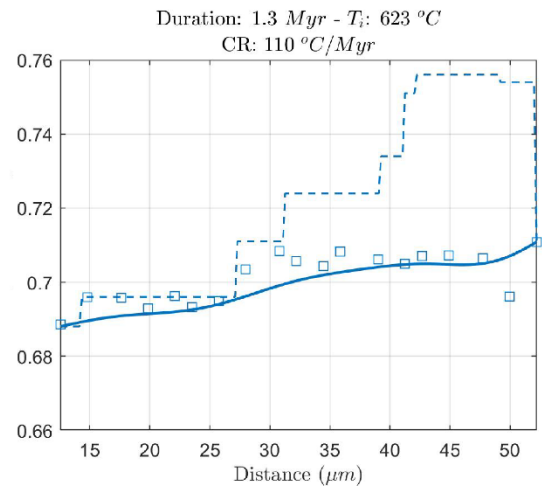
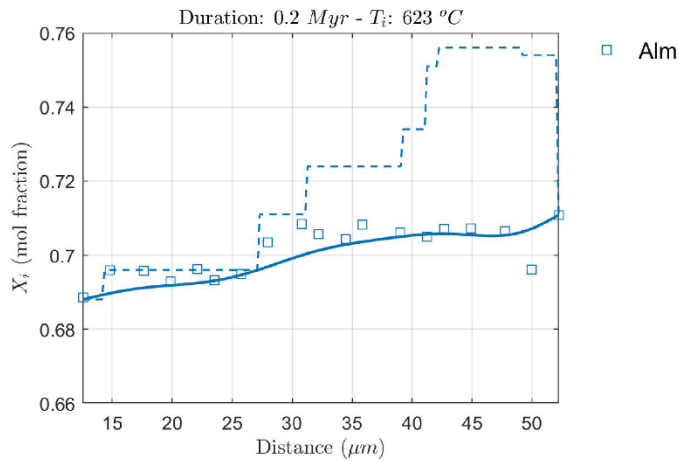
Measured profiles (blue symbols) and initial conditions (red lines) for garnet diffusion modelling with GDIFF.

Sample AG20.2B – thin section

Profile D10

CASE 1:
Constant temperature

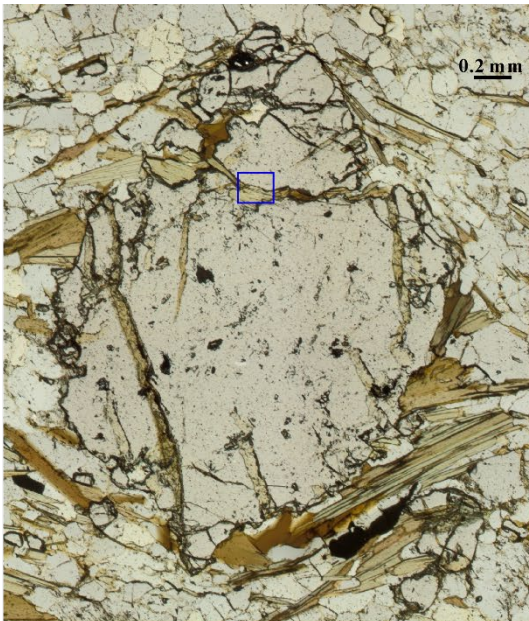
CASE 2:
Cooling history

**Results of garnet diffusion modelling**

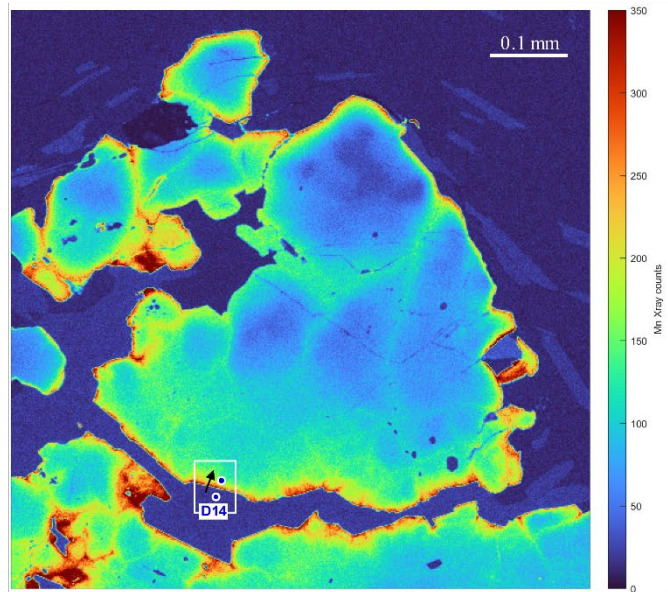
Microprobe profiles are indicated with colored symbols, initial conditions for garnet diffusion modelling with GDIFF with dashed lines, and diffusion results with thick colored lines.

Sample AG20.2B – thin section

Profile D14

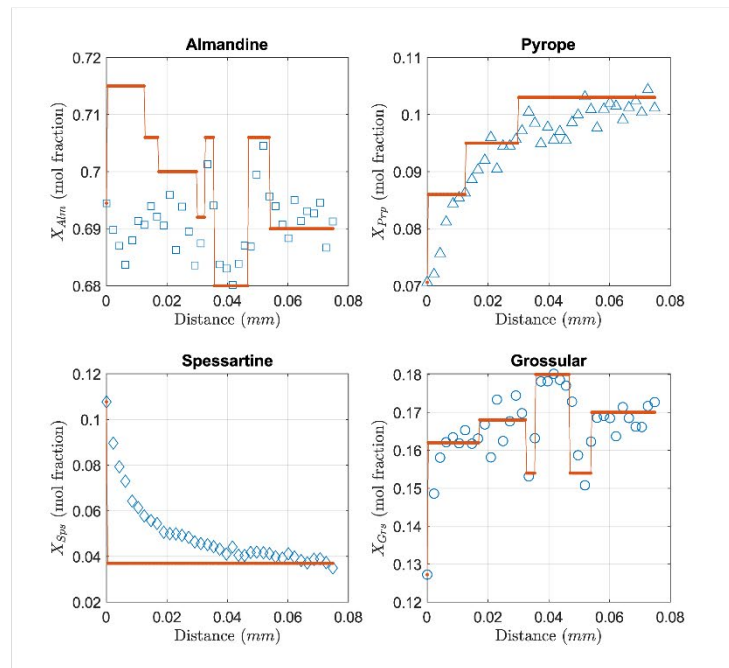


Thin section photo



Mn (X-ray) microprobe map

In the figures above is indicated the location of profile D14 on the thin section photo and microprobe X-ray map. The black arrow points from the first to the last point of the measured profiles. The microprobe profiles and fitting step-like functions are shown on the right. The relevant microprobe analyses are in *Appendix H* (online folder *Microprobe analyses - Analyses_AG20.2B.xlsx*).



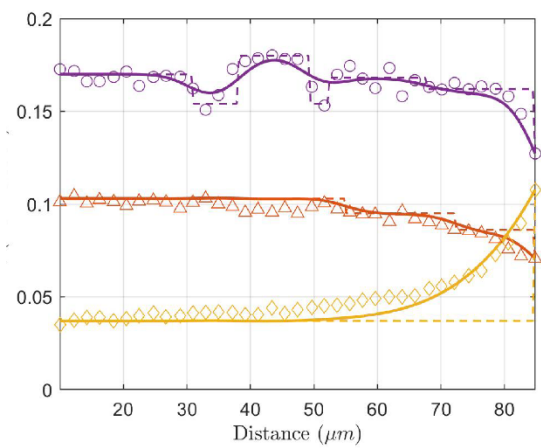
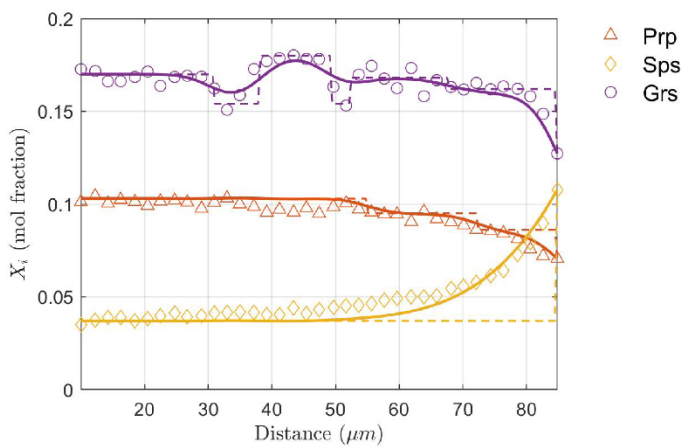
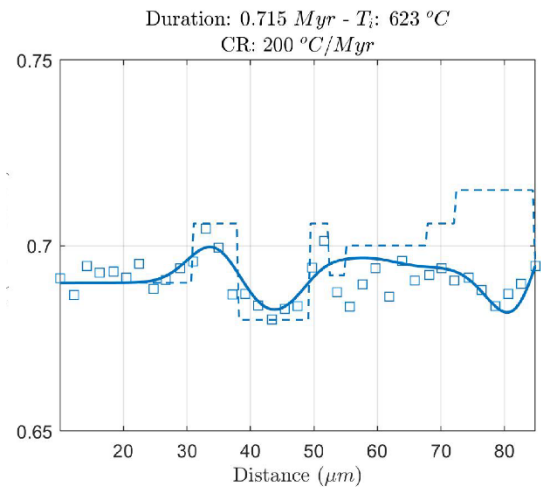
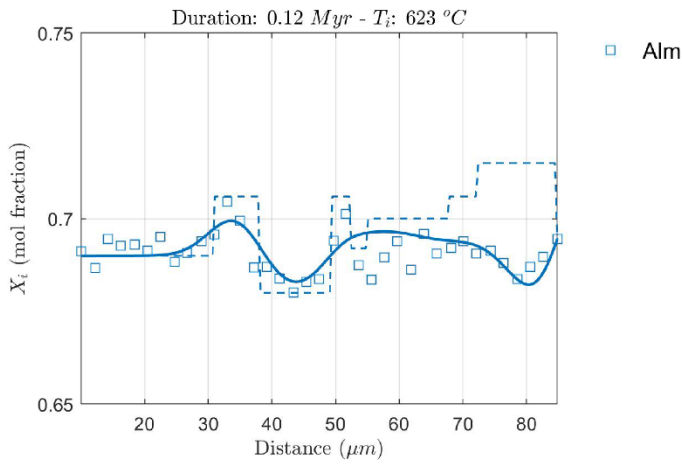
Measured profiles (blue symbols) and initial conditions (red lines) for garnet diffusion modelling with GDIFF.

Sample AG20.2B – thin section

Profile D14

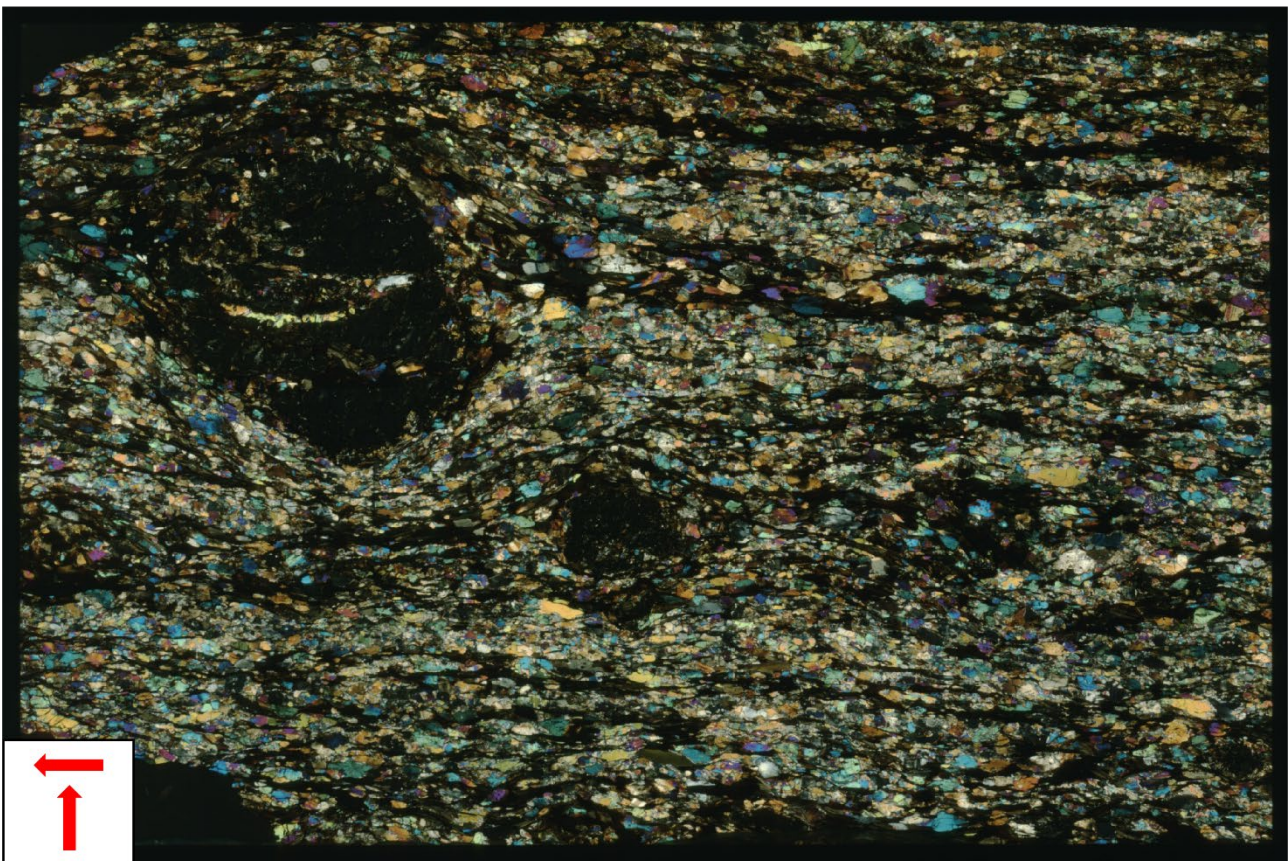
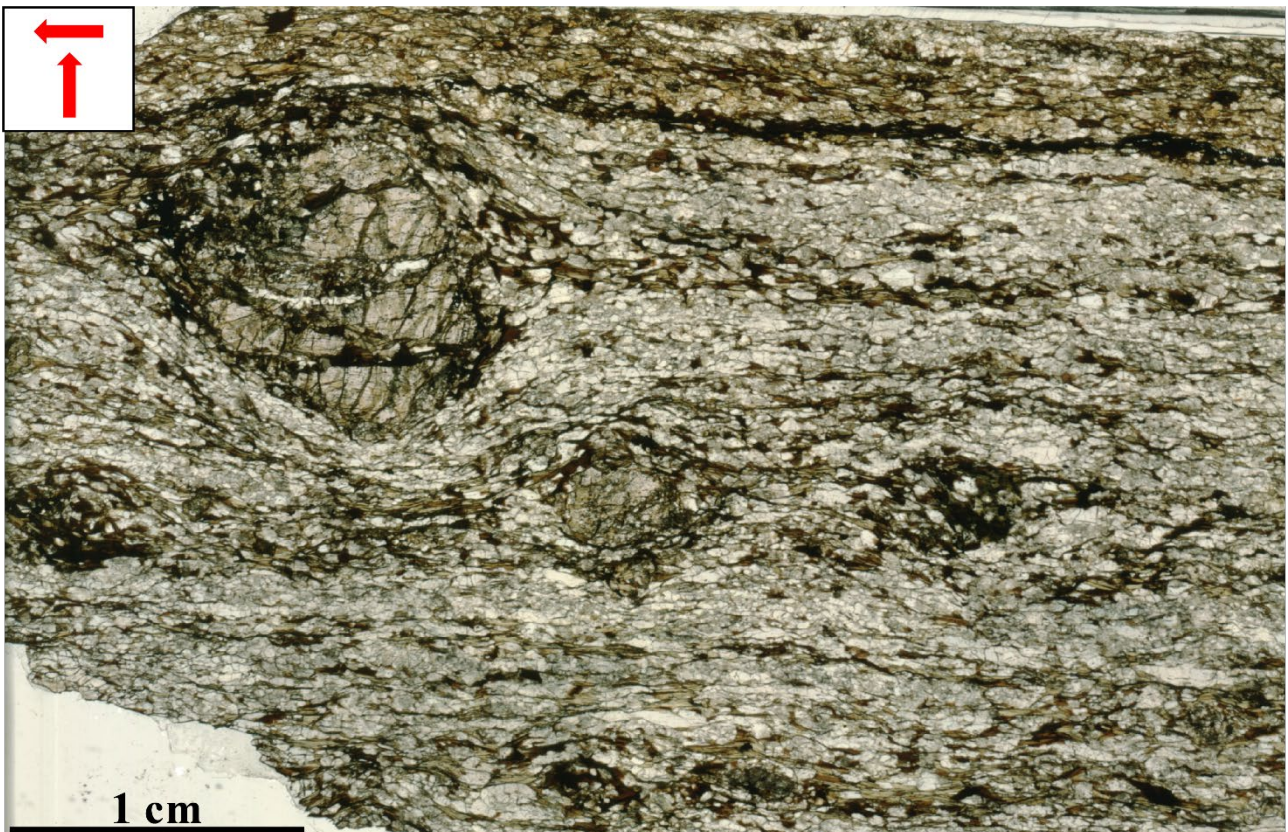
CASE 1:
Constant temperature

CASE 2:
Cooling history

**Results of garnet diffusion modelling**

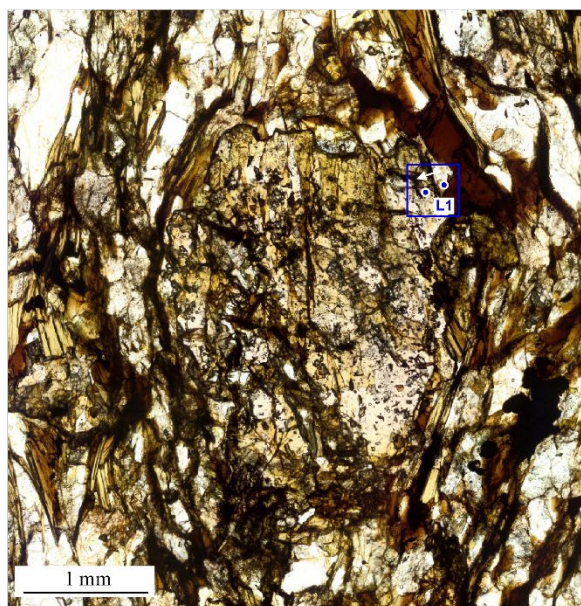
Microprobe profiles are indicated with colored symbols, initial conditions for garnet diffusion modelling with GDIFF with dashed lines, and diffusion results with thick colored lines.

Sample AV19.7C – thick section

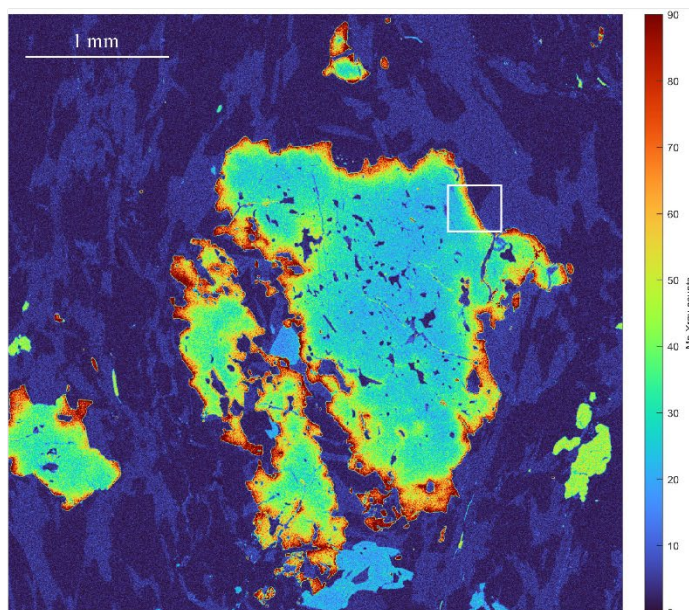


Sample AV19.7C – thick section

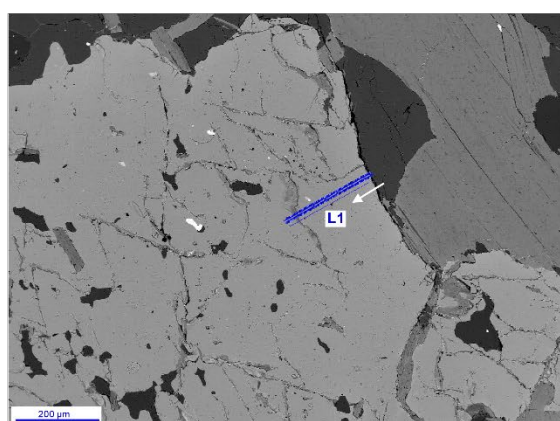
Profile L1



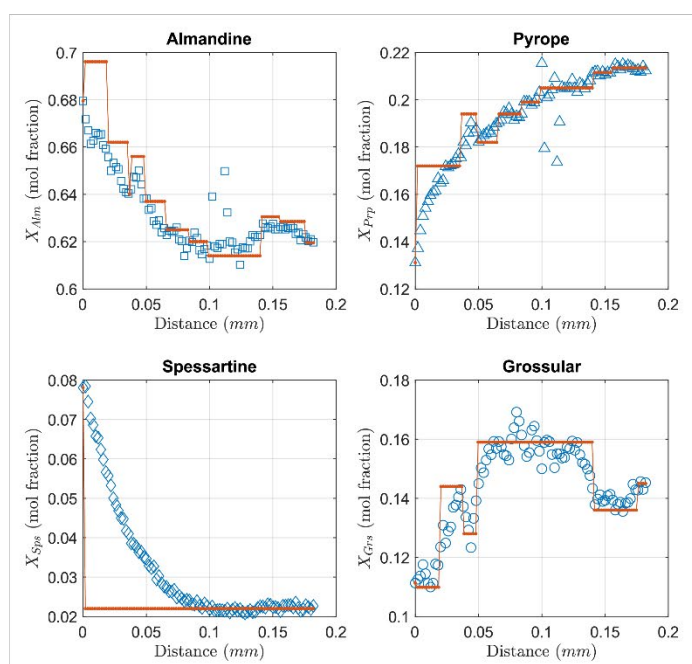
Thick section photo



Mn (X-ray) microprobe map



Microprobe photo



Measured profiles (blue symbols) and initial conditions (red lines) for garnet diffusion modelling with GDIF.

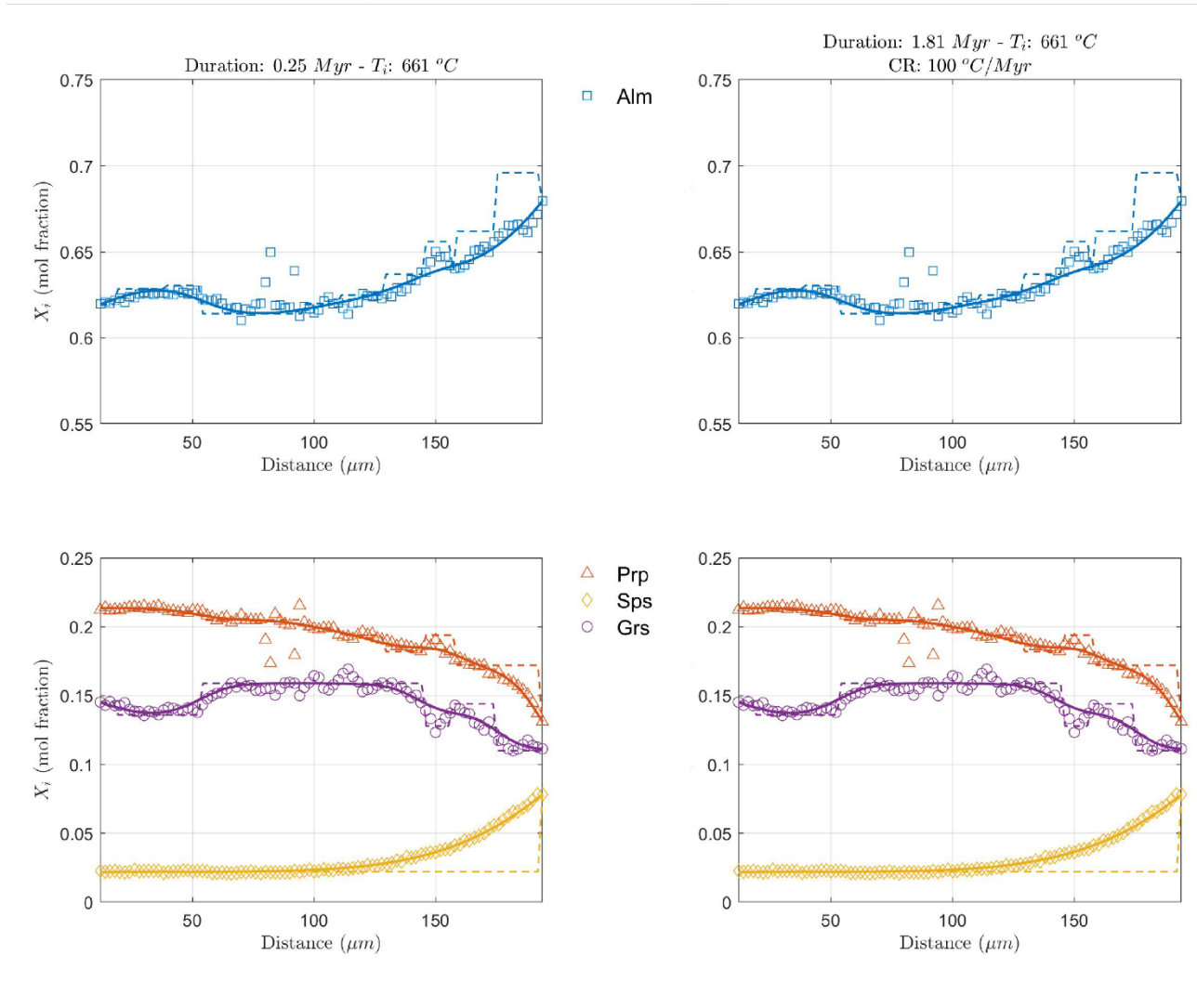
In the figures above is indicated the location of profile L1 on the thick section photos and microprobe X-ray map. The white arrows point from the first to the last point of the measured profiles. The microprobe profiles and fitting step-like functions are shown on the right. The considered microprobe analyses are highlighted in yellow in the Excel table of *Appendix H* available online (folder *Microprobe analyses - Analyses_AV19.7.xlsx*).

Sample AV19.7C – thick section

Profile L1

CASE 1:
Constant temperature

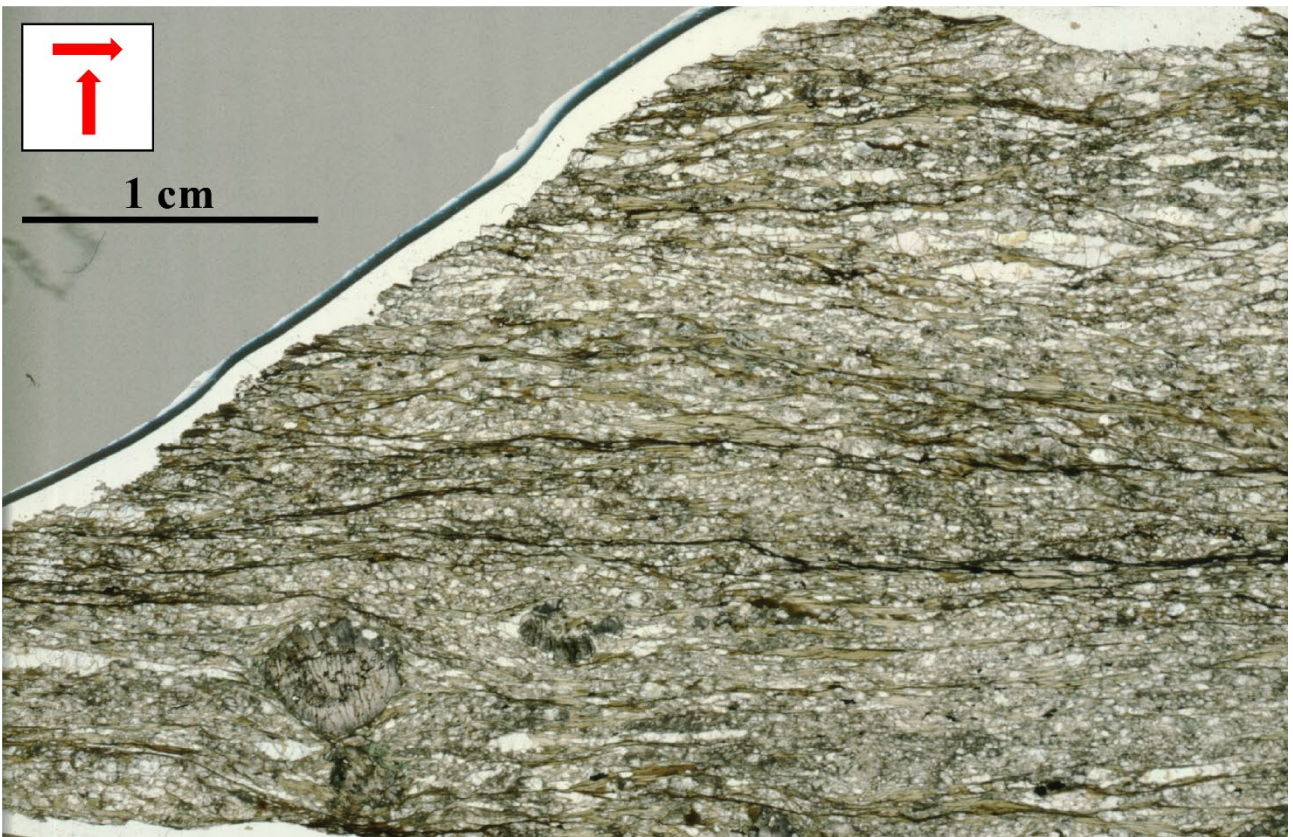
CASE 2:
Cooling history



Results of garnet diffusion modelling

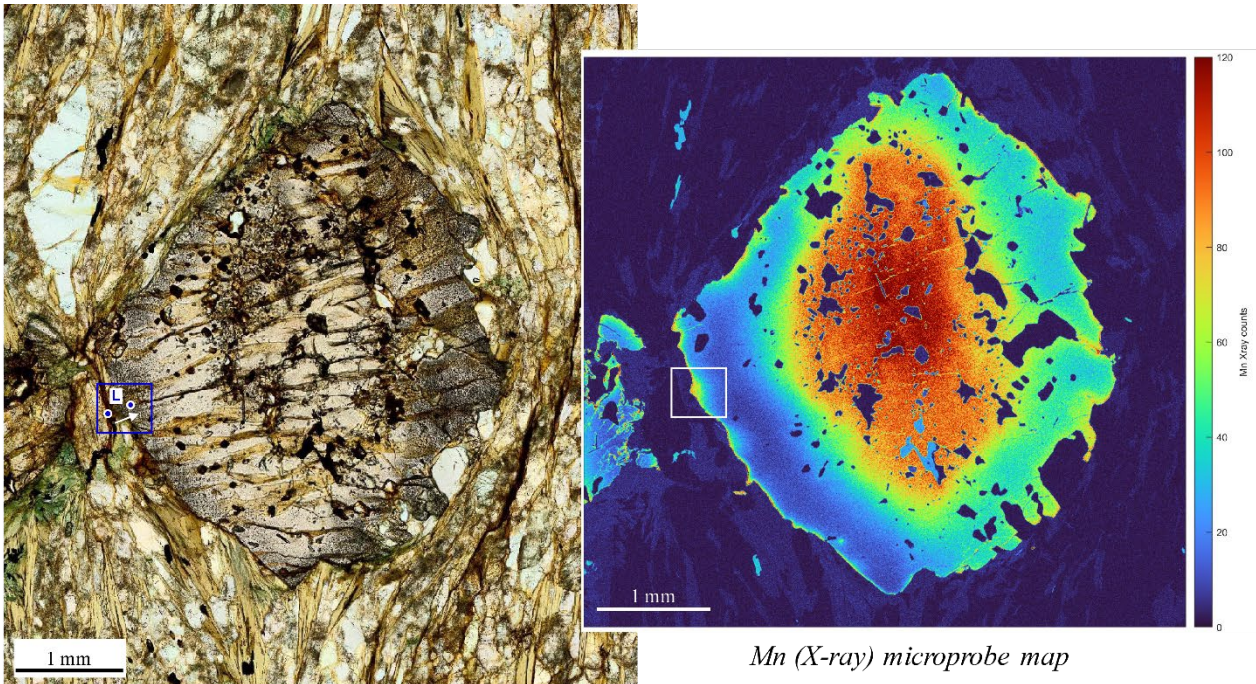
Microprobe profiles are indicated with colored symbols, initial conditions for garnet diffusion modelling with GDIFF with dashed lines, and diffusion results with thick colored lines.

Sample OS16-006 – thick section

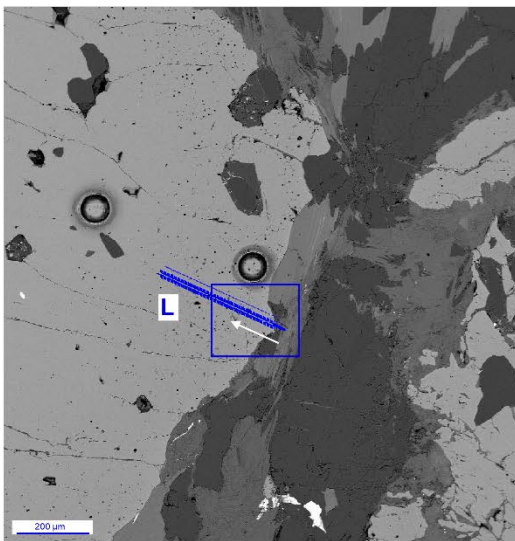


Sample OS16-006 – thick section

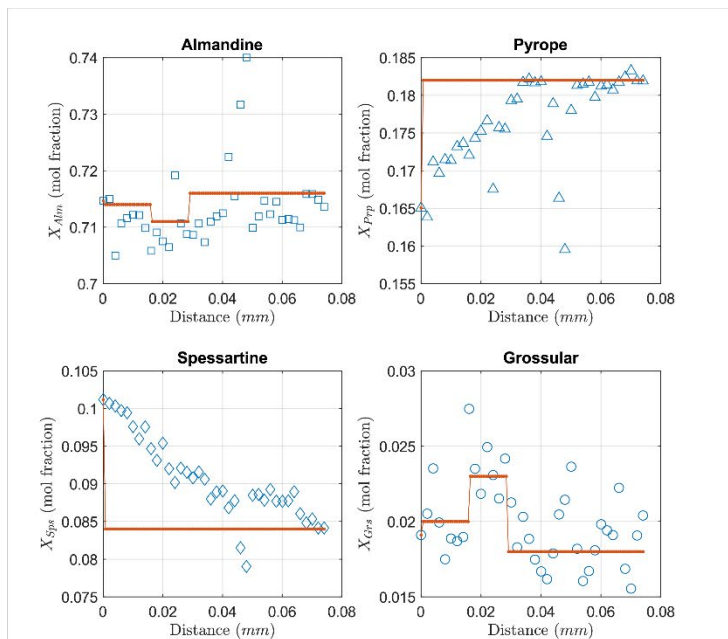
Profile L



Thick section photo



Microprobe photo



Measured profiles (blue symbols) and initial conditions (red lines) for garnet diffusion modelling with GDIFF.

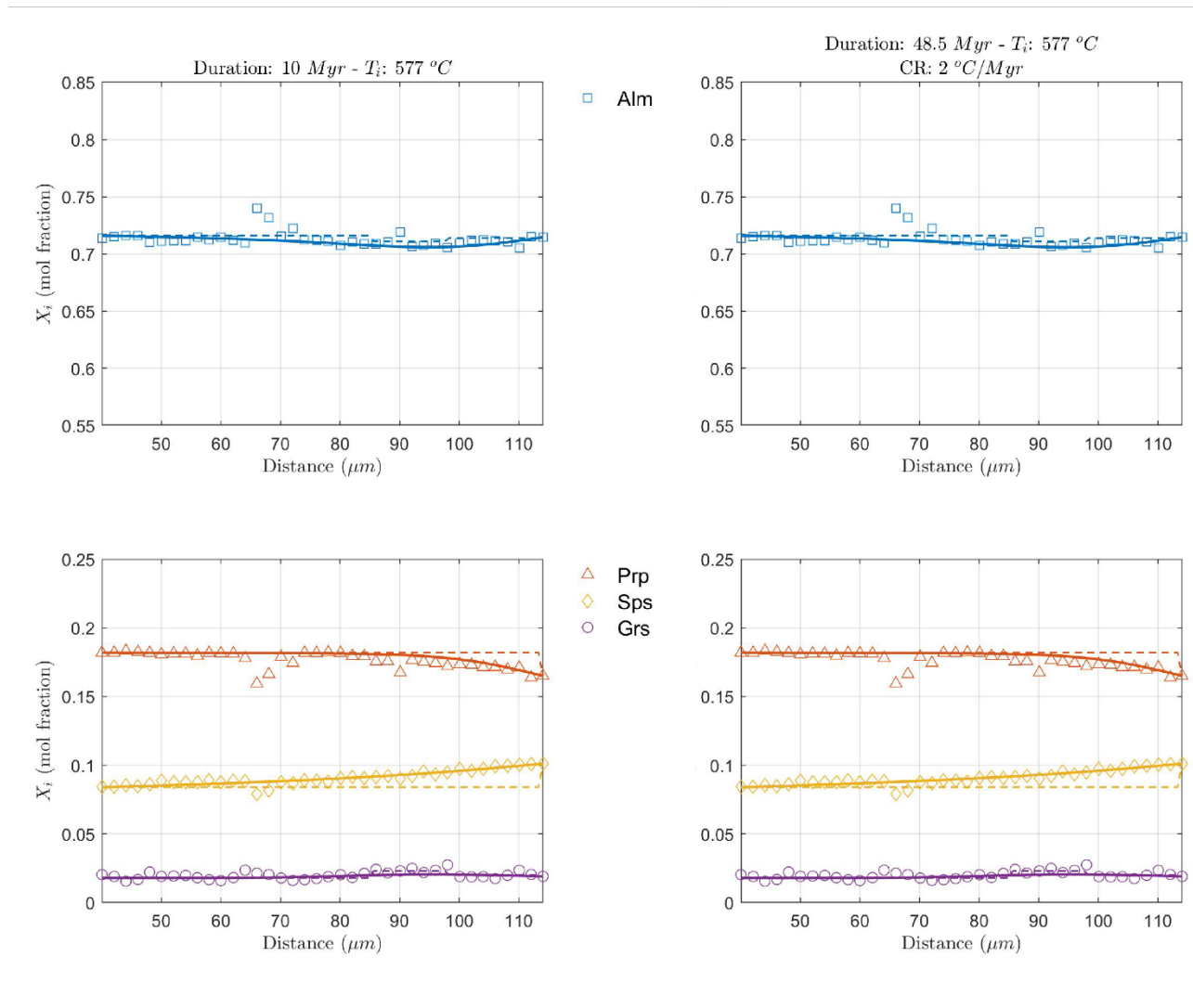
In the figures above is indicated the location of profile L on the thick section photos and microprobe X-ray map. The white arrows point from the first to the last point of the measured profiles. The microprobe profiles and fitting step-like functions are shown on the right. Note that only the first measured portion (garnet rim) of the profile has been considered for calculation. The relevant microprobe analyses are highlighted in yellow in the Excel table of Appendix H available online (folder *Microprobe analyses - Analyses_OS16-006.xlsx*).

Sample OS16-006 – thick section

Profile L

CASE 1:
Constant temperature

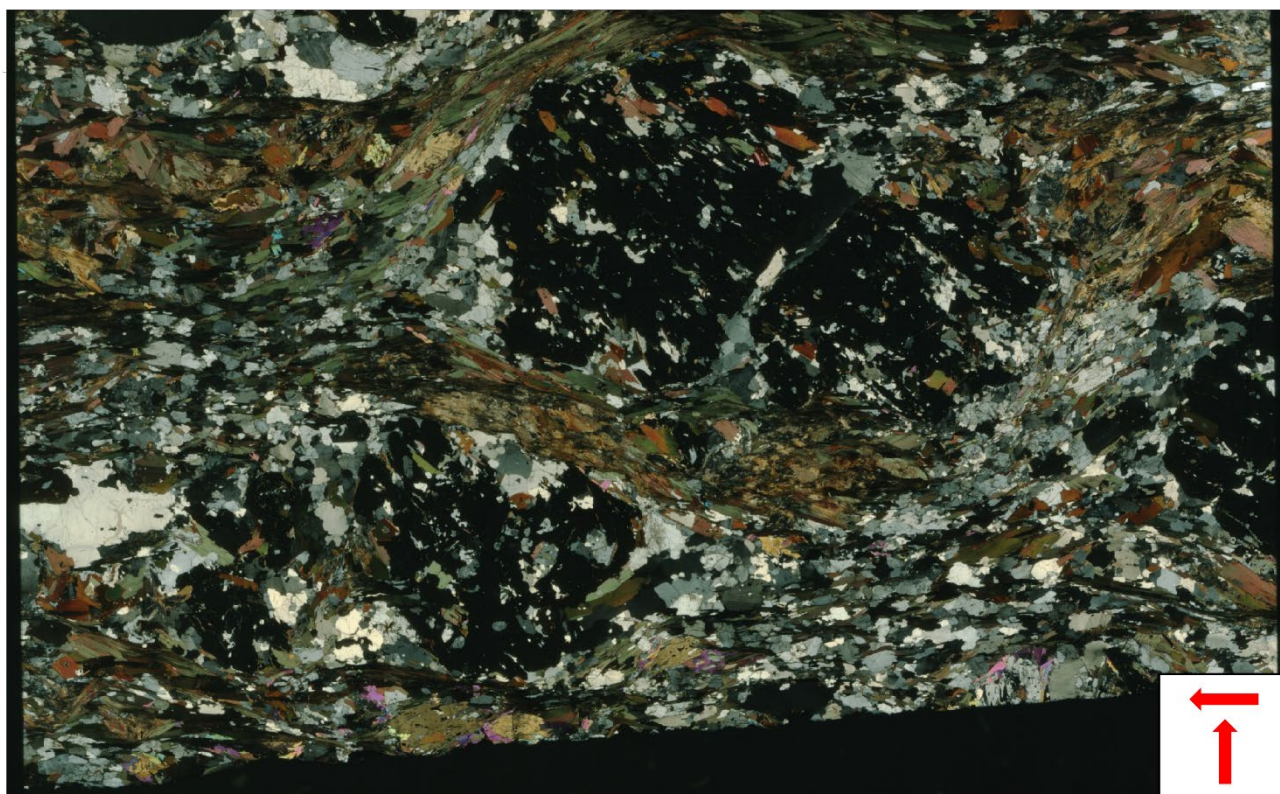
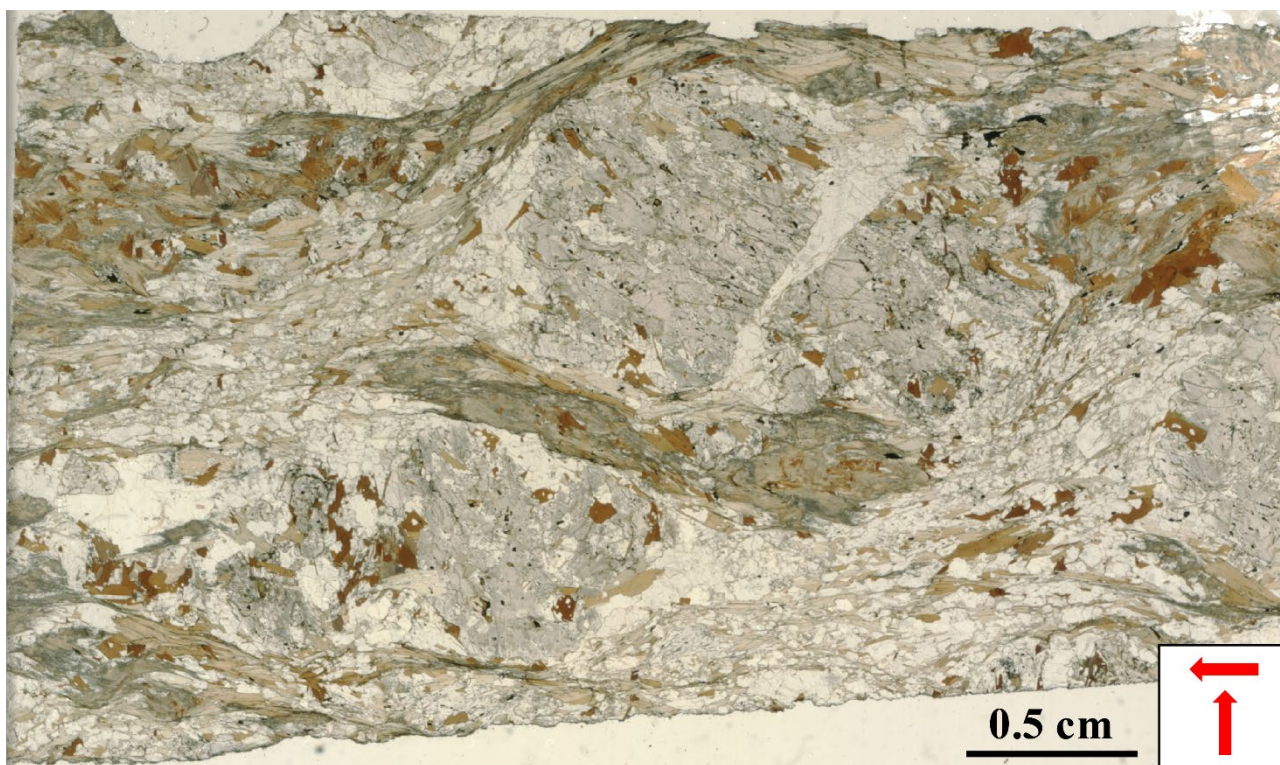
CASE 2:
Cooling history



Results of garnet diffusion modelling

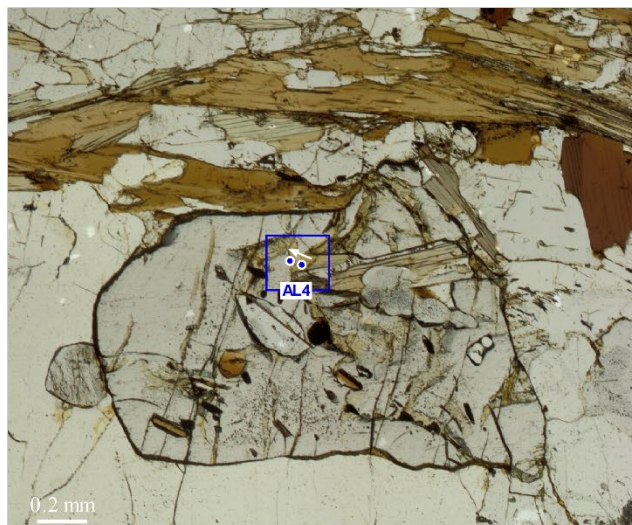
Microprobe profiles are indicated with colored symbols, initial conditions for garnet diffusion modelling with GDIFF with dashed lines, and diffusion results with thick colored lines.

Sample AS21.1A – thin section

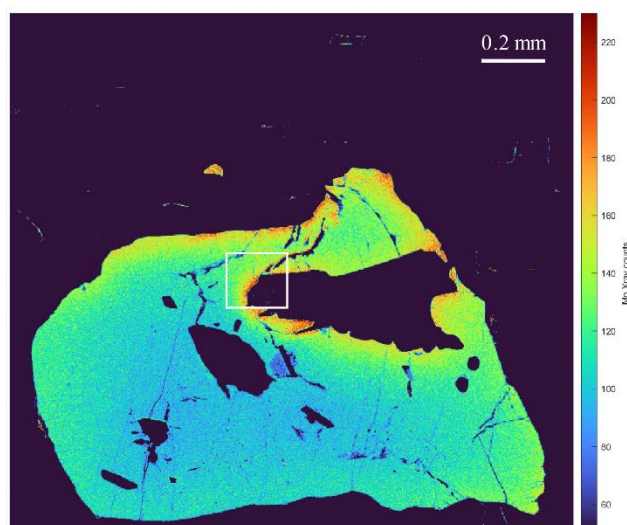


Sample AS21.1A – thin section

Profile AL4

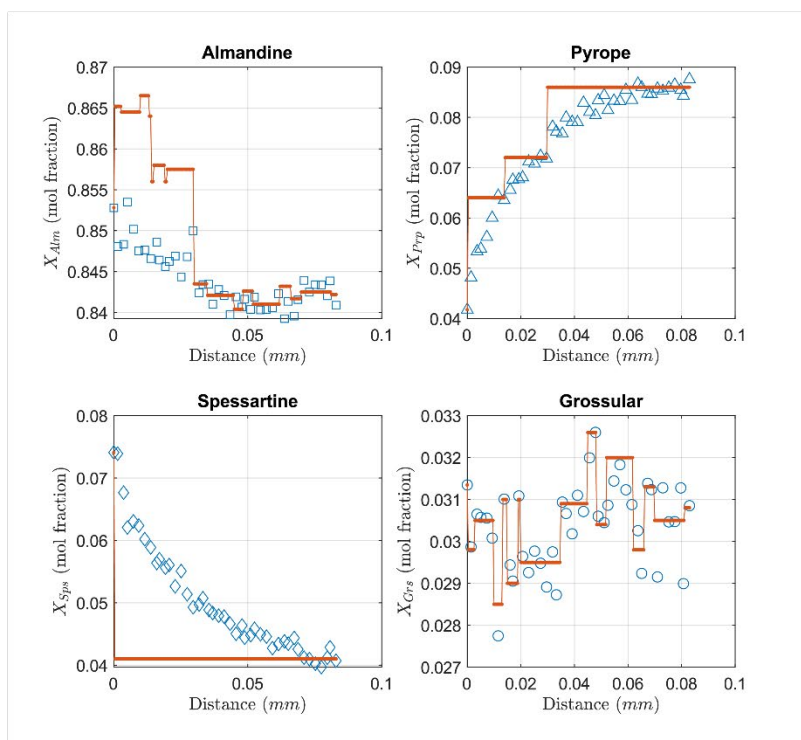


Thin section photo



Mn (X-ray) microprobe map

In the figures above is indicated the location of profile AL4 on the thin section photo and microprobe X-ray map. The white arrow points from the first to the last point of the measured profiles. The microprobe profiles and fitting step-like functions are shown on the right. The relevant microprobe analyses are in *Appendix H* (online folder *Microprobe analyses - Analyses_AS21.1A.xlsx*).



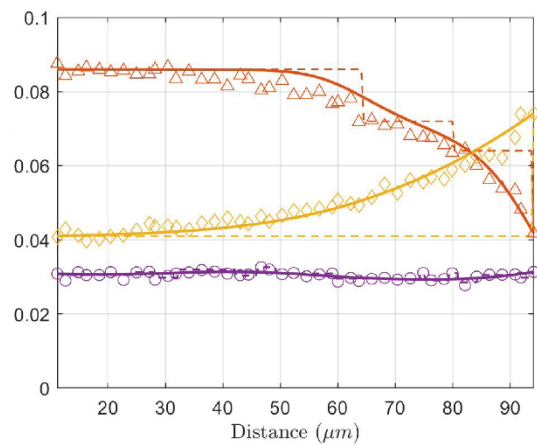
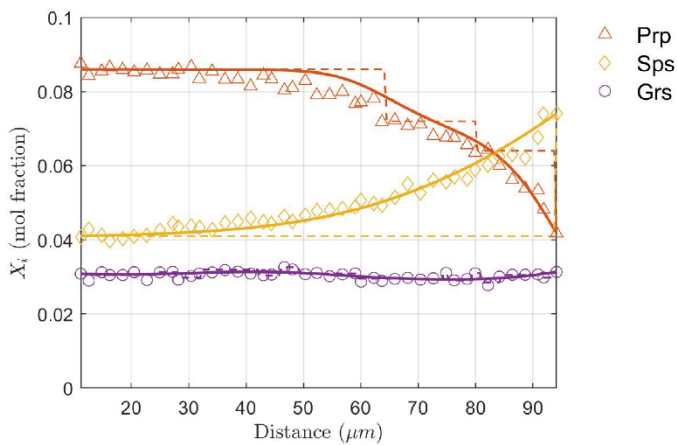
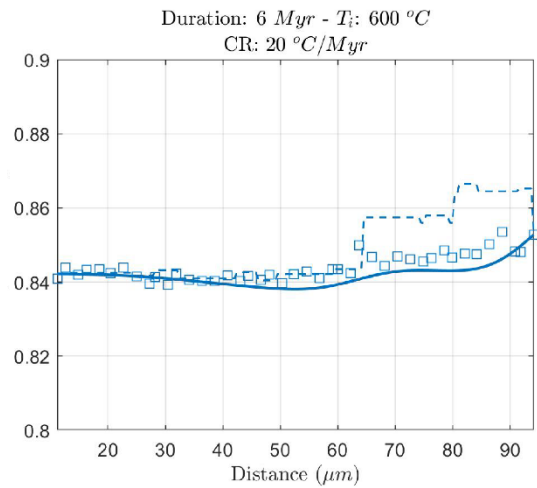
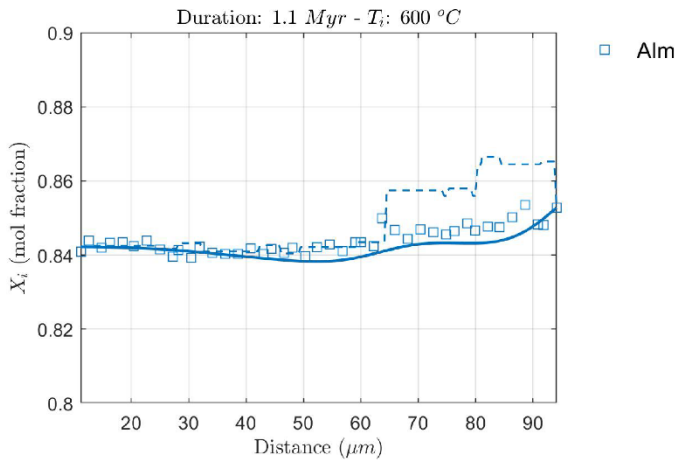
Measured profiles (blue symbols) and initial conditions (red lines) for garnet diffusion modelling with GDIFF.

Sample AS21.1A – thin section

Profile AL4

CASE 1:
Constant temperature

CASE 2:
Cooling history

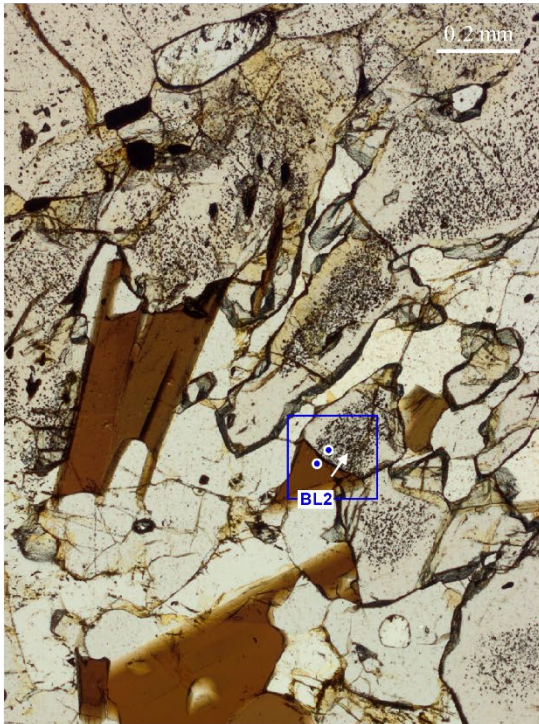


Results of garnet diffusion modelling

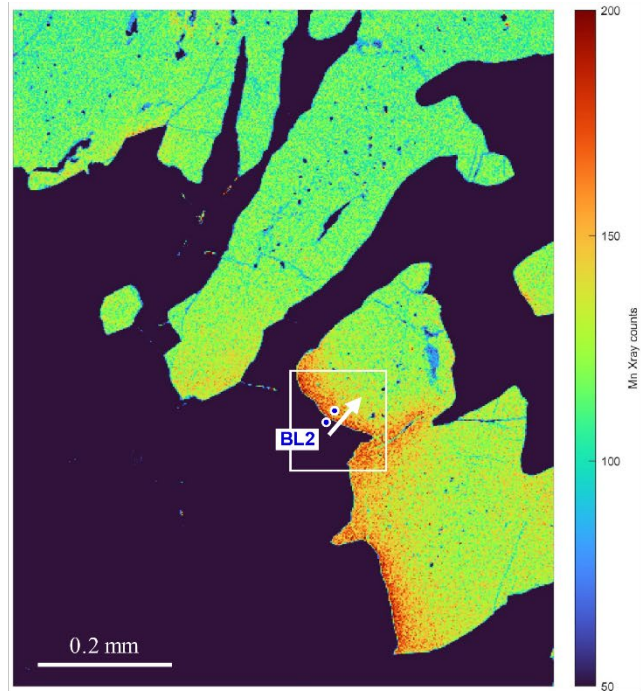
Microprobe profiles are indicated with colored symbols, initial conditions for garnet diffusion modelling with GDIFF with dashed lines, and diffusion results with thick colored lines.

Sample AS21.1A – thin section

Profile BL2

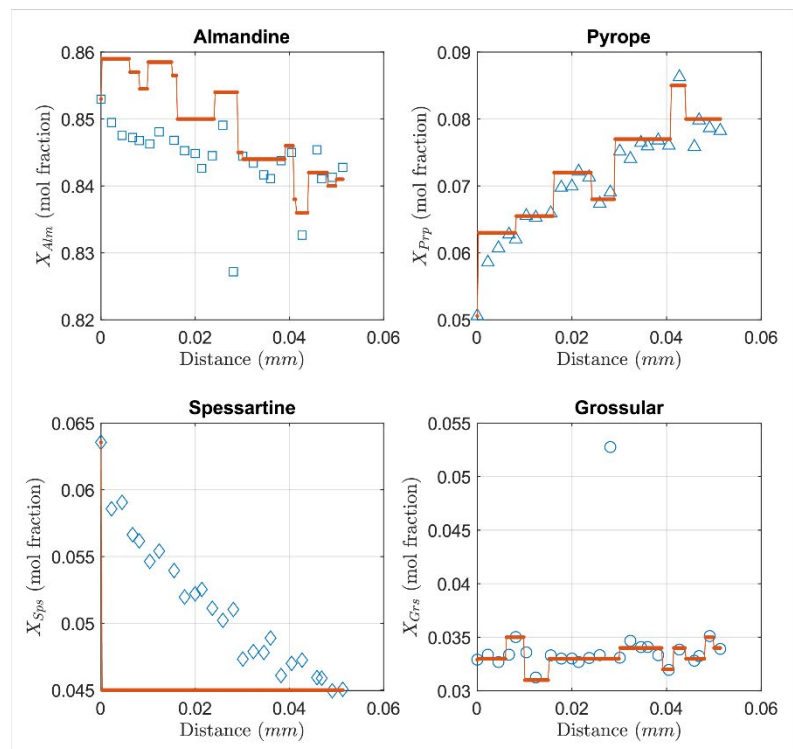


Thick section photo



Mn (X-ray) microprobe map

In the figures above is indicated the location of profile BL2 on the thin section photo and microprobe X-ray map. The white arrows point from the first to the last point of the measured profiles. The microprobe profiles and fitting step-like functions are shown on the right. The relevant microprobe analyses are in *Appendix H* (online folder *Microprobe analyses - Analyses_AS21.1A.xlsx*).



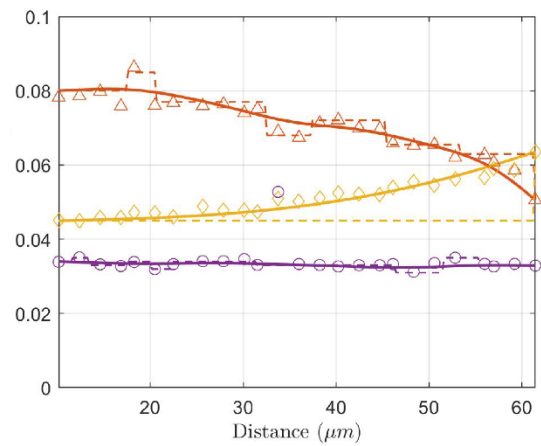
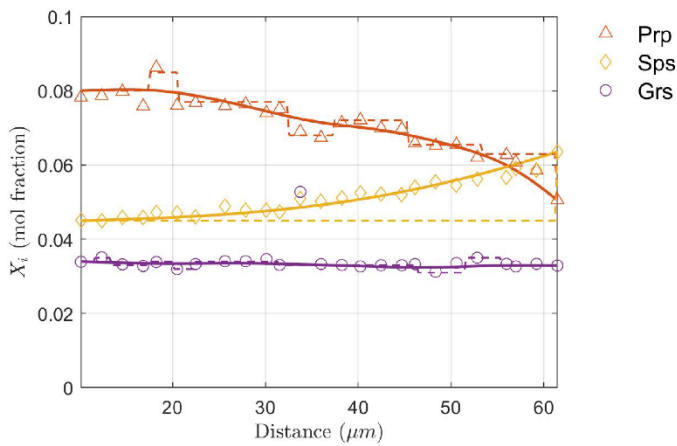
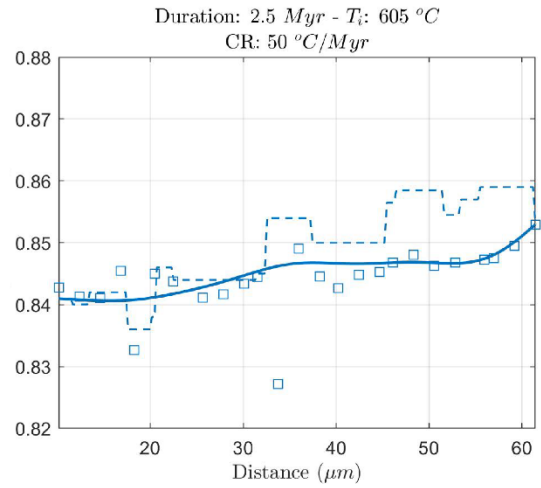
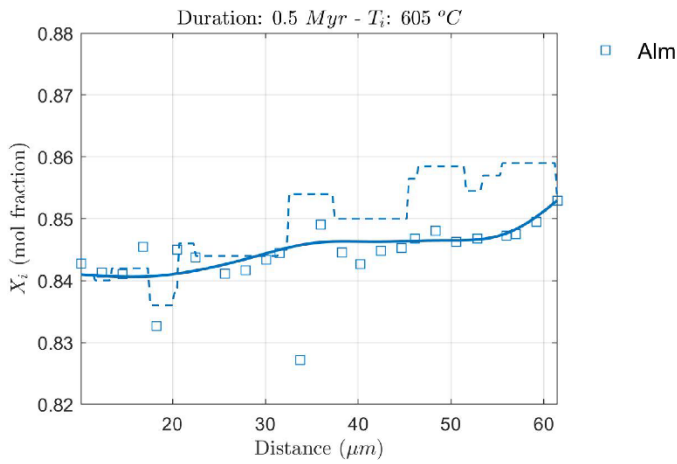
Measured profiles (blue symbols) and initial conditions (red lines) for garnet diffusion modelling with GDIFF.

Sample AS21.1A – thin section

Profile BL2

CASE 1:
Constant temperature

CASE 2:
Cooling history



Results of garnet diffusion modelling

Microprobe profiles are indicated with colored symbols, initial conditions for garnet diffusion modelling with GDIFF with dashed lines, and diffusion results with thick colored lines.

Appendix J

CODE FOR 1D THERMAL MODELS AND NUMERICAL MODEL RESULTS (CHAPTER 4)

This appendix is available online at: <https://zenodo.org/record/8399771>.

The Matlab scripts related to the one-dimensional thermal numerical models described in *Chapter 4* have been uploaded onto the general-purpose open-access repository Zenodo in the folder *Code_thermal models*: <https://zenodo.org/record/8399771>.

Here follows the main code *Tsolve.m*.

Matlab code for 1D thermal models simulating regional exhumation

```
clear,clc,figure(1),clf
%Physical Parameters
L      =      40000;    %Domain height
k      =      3;      %thermal conductivity
rCp    =      3000*1000; %Heat capacity times density
rg     =      3000*10; %Lithostatic gradient
Hr     =      0.5*1e-6; %Radiogenic heat production
Qs     =      60*1e-3; %Surface Heat flux
Edot_mm =      1;    %Erosion rate in mm/yr
y_mark = [5000:5000:L,L]; %Initial position of markers
Tsurf  =      0;    %Surface Temperature
%Numerical Parameters
ny     =      200;    %Numerical resolution
CFL    =      0.2;    %Condizione di Courant-Friedrichs-Lewy
nout   =      500;    %Plot every nout steps/store path every nout
%Preprocessing
yr2sec =      60*60*24*365; %how many secs in 1 year
Edot   = Edot_mm*1e-3/yr2sec; %recalculate erosion
dy     =      L/(ny-1); %Calculate dx
y      =      0:dy:L; %Domain
dt1    =      dy^2/(k/rCp)*CFL; %Timestep for diffusion
dt2    =      dy/Edot*CFL; %Timestep for Erosion
dt     =      min(dt1,dt2); %Choose the minimum
Edot_m =      Edot*ones(size(y_mark));
%Initial conditions
T      =      Tsurf+(Qs/k)*y-0.5*Hr/k*y.^2;
T0     =      T;
qflux0 = -Qs+Hr*y;
%Start time iterations
t      =      0;
i      =      0;
itp    =      0;
Lstop  =      0;
while Lstop==0
    i      =      i+1;
    t      =      t+dt;
    Told   =      T;
    T(2:end-1) = Told(2:end-1) + dt*(k/rCp*diff(diff(Told))/dy/dy ...
        +Hr/rCp);
    T(1:end-1) = T(1:end-1) + dt*Edot*diff(T)/dy;
    T(1)      =      Tsurf;
    T(end)    =      -(qflux0(end)*dy)/k+T(end-1);
    y_mark    =      y_mark -Edot_m*dt;
    P_mark    =      rg*y_mark;
    T_mark    =      interp1(y,T,y_mark,'linear',Tsurf);
    Qsurf     =      k*(T(2)-T(1))/dy*1e3;%Value in mW/m2
    Edot_m(y_mark<0)=0;
    if Edot_m(end)==0
```

```

    Lstop=1;
end
if mod(i,nout)==1
    itp      = itp+1;
    FSS      = 12;
    LWW      = 1.2;
    %Monitor path
    y_path(itp,:) = y_mark;
    P_path(itp,:) = P_mark;
    T_path(itp,:) = T_mark;
    t_path(itp,:) = t*ones(size(P_mark));
    %Visualization
    figure(1),clf
    subplot(121)
    plot(T0,-y/1e3,T,-y/1e3,'LineWidth',LWW),grid on
    title(['t (Myr): ',num2str(t/yr2sec/1e6)])
    xlabel('T (^oC)','FontSize',FSS)
    ylabel('y (km)','FontSize',FSS)
    axis([0 900 -40 0])
    set(gca,'FontSize',FSS*0.8,'LineWidth',LWW*0.8)
    subplot(122)
    plot(T_path,-y_path/1E3,'LineWidth',LWW),grid on%,hold on
    title(['Qs (mW/m^2): ',num2str(Qsurf)])
    xlabel('T (^oC)','FontSize',FSS)
    ylabel('y (km)','FontSize',FSS)
    axis([0 900 -40 0])
    set(gca,'FontSize',FSS*0.8,'LineWidth',LWW*0.8)
    drawnow
end
end

FSS      = 12;
LWW      = 1.2;

%Visualization
subplot(121)
plot(T0,-y/1e3,T,-y/1e3,'LineWidth',LWW),grid on
title(['t (Myr): ',num2str(t/yr2sec/1e6)])
xlabel('T (^oC)','FontSize',FSS)
ylabel('y (km)','FontSize',FSS)
axis([0 900 -40 0])
set(gca,'FontSize',FSS*0.8,'LineWidth',LWW*0.8)
subplot(122)
plot(T_path,-y_path/1E3,'LineWidth',LWW),grid on
title(['Qs (mW/m^2): ',num2str(Qsurf)])
xlabel('T (^oC)','FontSize',FSS)
ylabel('y (km)','FontSize',FSS)
axis([0 900 -40 0])
set(gca,'FontSize',FSS*0.8,'LineWidth',LWW*0.8)

%Postprocess cooling rates
CR = -diff(T_path,1,1)./diff(t_path,1,1);
CR = [CR]*yr2sec*1e6; %just to keep the same size in last point
TCR= 0.5*(T_path(2:end,:)+T_path(1:end-1,:));
Yp = 0.5*(y_path(2:end,:)+y_path(1:end-1,:));
Pp = 0.5*(P_path(2:end,:)+P_path(1:end-1,:));

figure(2),clf
subplot(221)
plot(T_path,-y_path/1E3,'LineWidth',LWW),hold on
plot(T0,-y/1e3,'--','Color',[0 0 0 0.8],'LineWidth',LWW)

```

```

plot(T,-y/1e3,'--','Color',[0 0 0 0.4],'LineWidth',LWW),hold off
hold off
grid on
xlabel('$T$ $(^{\circ}C)$','FontSize',FSS,'Interpreter','latex')
ylabel('$y$ $(km)$','FontSize',FSS,'Interpreter','latex')
axis([0 800 -40 0])
axis square
title('A')
text(50,-35,['\$Q_s^{\{final\}}: \$ ',num2str(round(Qsurf)), ...
' \$ (mW/m^2)$'],'Color',[0 0 0 0.8],'Rotation',0,'FontSize',...
FSS*0.9,'Interpreter','latex')
text(200,-15,['initial'],'Color',[0 0 0 0.8],'Rotation',-48,'FontSize',...
FSS,'Interpreter','latex')
text(400,-7.5,['final'],'Color',[0 0 0 0.4],'Rotation',-35,'FontSize',...
FSS,'Interpreter','latex')
set(gca,'FontSize',FSS*0.8,'LineWidth',LWW*0.8)

subplot(222)
plot(T_path,P_path/1E9,'LineWidth',LWW),grid on,hold on
plot_reactions(LWW,0.85),hold on
axis square
xlabel('$T$ $(^{\circ}C)$','FontSize',FSS,'Interpreter','latex')
ylabel('$P$ $(GPa)$','FontSize',FSS,'Interpreter','latex')
axis([0 800 0 1.5])
hold off
title('B')
set(gca,'FontSize',FSS*0.8,'LineWidth',LWW*0.8)

subplot(223)
plot(Pp/1e9,CR,'LineWidth',LWW),grid on
xlabel('$P$ $(GPa)$','FontSize',FSS,'Interpreter','latex')
ylabel('$CR$ $(^{\circ}C/Myr)$','FontSize',FSS,'Interpreter','latex')
axis([0 1.5 -10 50])
axis square
title('C')
set(gca,'FontSize',FSS*0.8,'LineWidth',LWW*0.8)
%-----
subplot(224)
plot(TCR,CR,'LineWidth',LWW),grid on
axis([50 800 -10 50])
xlabel('$T$ $(^{\circ}C)$','FontSize',FSS,'Interpreter','latex')
ylabel('$CR$ $(^{\circ}C/Myr)$','FontSize',FSS,'Interpreter','latex')
axis square
title('D')
set(gca,'FontSize',FSS*0.8,'LineWidth',LWW*0.8)
%-----

set(gcf,'Position', [[663 230 882 722]])
stringg = ['print -dpng Results_f4_',num2str(round(Edot_mm)),...
'.png -r300'];eval(stringg);

%% new figure
figure(3),clf

subplot(121)
plot(Pp/1e9,CR,'LineWidth',LWW),grid on
xlabel('$P$ $(GPa)$','FontSize',FSS,'Interpreter','latex')
ylabel('$CR$ $(^{\circ}C/Myr)$','FontSize',FSS,'Interpreter','latex')
axis([0 1.5 -10 500])
set(gca,'FontSize',FSS*0.8,'LineWidth',LWW*0.8)

```

```
%-----  
subplot(122)  
plot(TCR,CR, 'LineWidth',LWW),grid on  
axis([50 800 -10 500])  
xlabel('$T$ $(^{\circ}C)$', 'FontSize',FSS, 'Interpreter', 'latex')  
ylabel('$CR$ $(^{\circ}C/Myr)$', 'FontSize',FSS, 'Interpreter', 'latex')  
set(gca, 'FontSize',FSS*0.8, 'LineWidth',LWW*0.8)  
set(gcf, 'Position', [672.6000 423.8000 751.2000 471.2000])  
  
stringg = ['print -dpng Results_f6_', num2str(round(Edot_mm)), ...  
          '.png -r300'];eval(stringg);
```

Results of 1D thermal models for regional exhumation

The results of one-dimensional thermal models are displayed in the following *figures J.1* and *J.2*. An online version of these figures is available in the Zenodo repository (*T_models.pdf*).

A movie of the simulation showing the movement of single rock markers and the related change in geotherm configuration (as in *panel A* in *figures J.1* and *J.2*) for 1 mm/yr exhumation velocity has also been uploaded in the repository with the name *Movie_thermal.avi*.

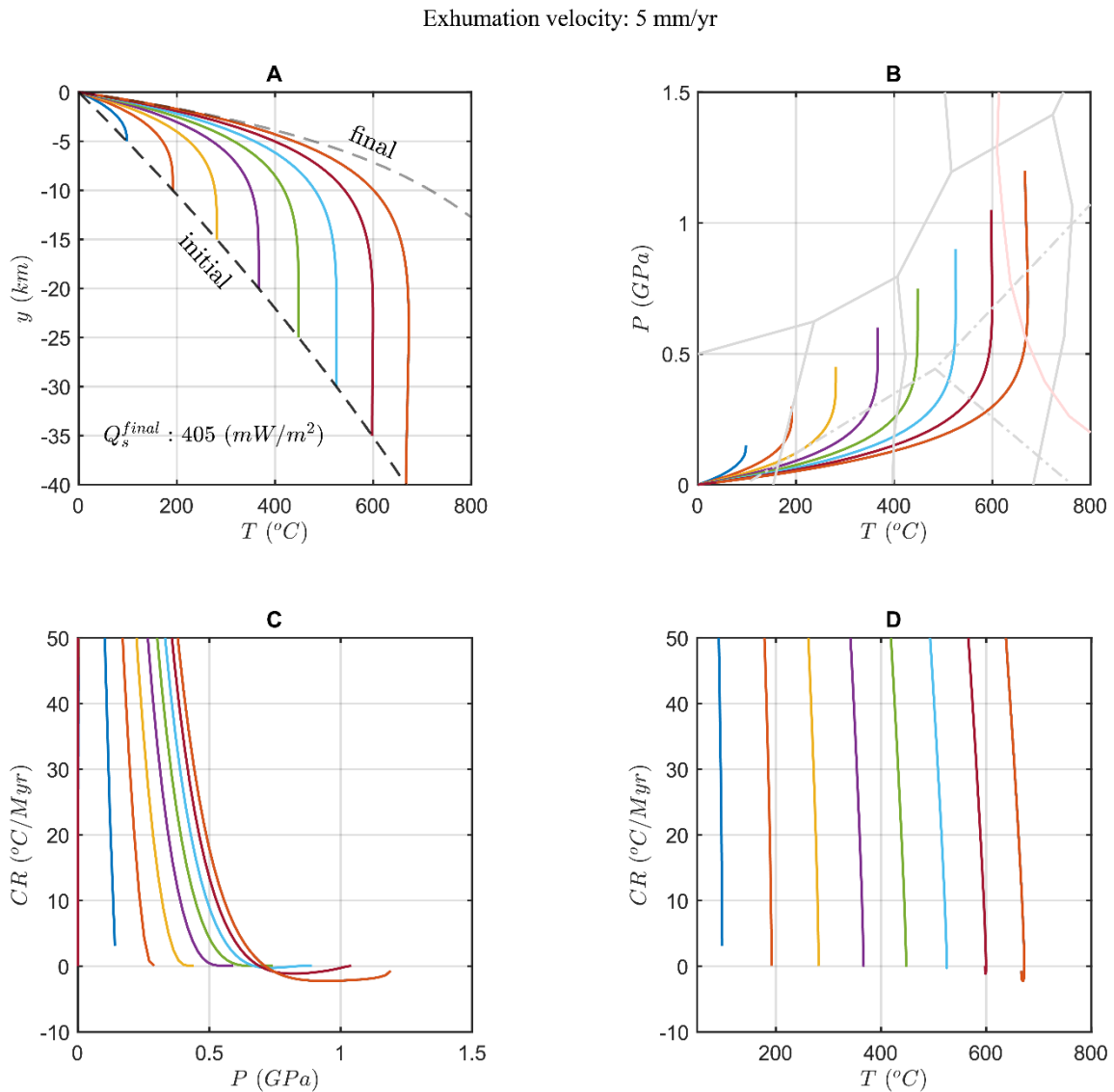


Figure J.1. 1D thermal model results for an exhumation velocity of 5 mm/yr. See Chapter 4 for further details.

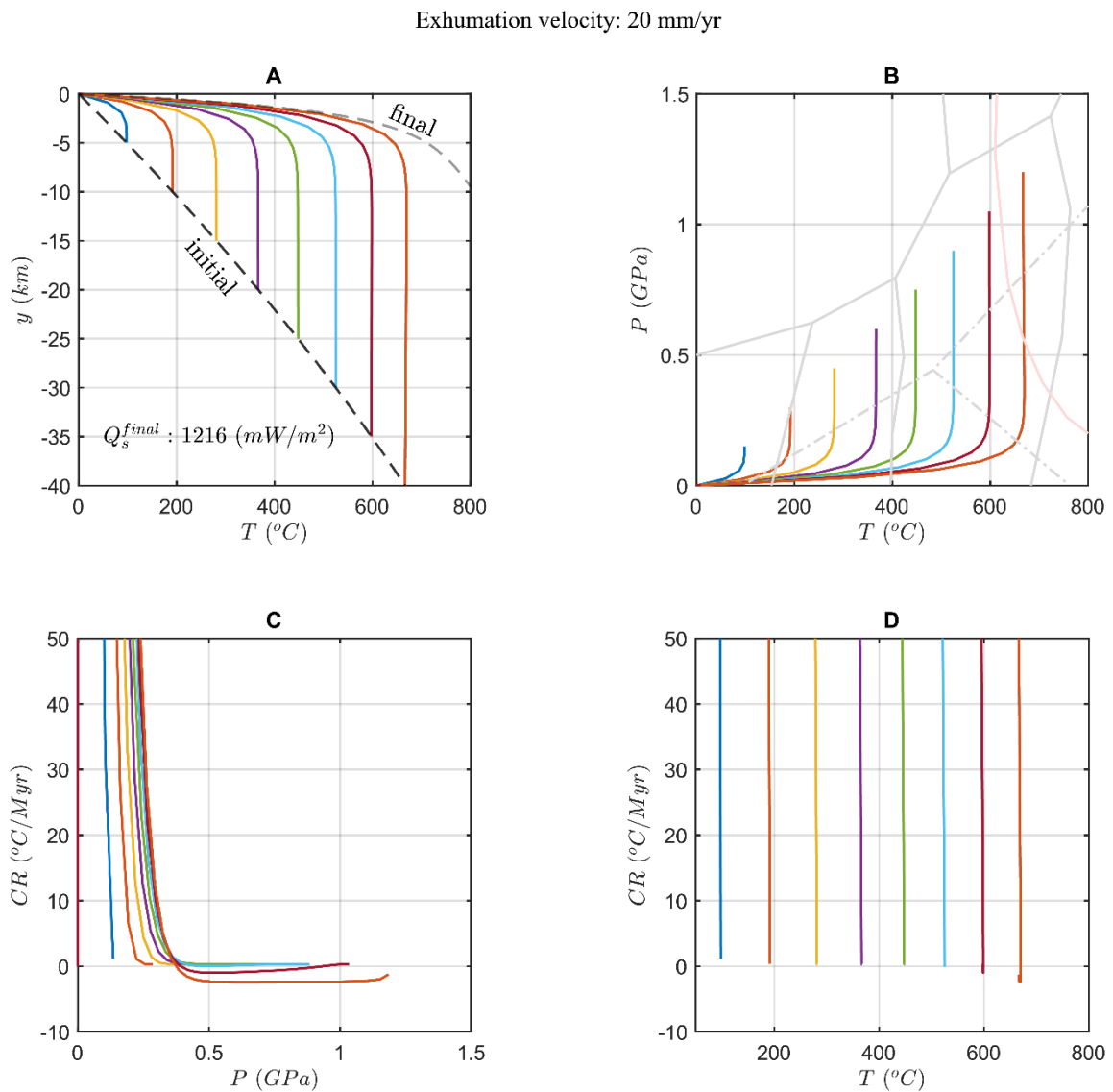


Figure J.2. 1D thermal model results for an exhumation velocity of 20 mm/yr. See Chapter 4 for further details.

Bibliography

- Ague, J. J., & Baxter, E. F. (2007). Brief thermal pulses during mountain building recorded by Sr diffusion in apatite and multicomponent diffusion in garnet. *Earth and Planetary Science Letters*, 261(3–4), 500–516. <https://doi.org/10.1016/j.epsl.2007.07.017>
- Ague, J. J., & Carlson, W. D. (2013). Metamorphism as garnet sees it: the kinetics of nucleation and growth, equilibration, and diffusional relaxation. *Elements*, 9(6), 439–445. <https://doi.org/10.2113/gselements.9.6.439>
- Allaz, J., Maeder, X., Vannay, J. C., & Steck, A. (2005). Formation of aluminosilicate-bearing quartz veins in the Simano nappe (Central Alps): Structural, thermobarometric and oxygen isotope constraints. *Schweizerische Mineralogische Und Petrographische Mitteilungen*, 85(2–3), 191–214. <https://doi.org/10.5169/seals-1660>
- Allmendinger, R. W., Cardozo, N., & Fisher, D. M. (2011). Structural geology algorithms: Vectors and tensors. *Cambridge University Press*.
- Alsop, G. I., & Holdsworth, R. E. (2007). Flow perturbation folding in shear zones. *Geological Society Special Publication*, 272, 75–101. <https://doi.org/10.1144/GSL.SP.2007.272.01.06>
- Barrow, G. (1893). On an Intrusion of Muscovite-biotite Gneiss in the South-eastern Highlands of Scotland, and its accompanying Metamorphism. *Quarterly Journal of the Geological Society*, 49(1–4), 330–358. <https://doi.org/10.1144/gsl.jgs.1893.049.01-04.52>
- Barrow, G. (1912). On the geology of Lower Dee-side and the southern Highland Border. *Proceedings of the Geologists' Association*, 23(5), 274–290. [https://doi.org/10.1016/s0016-7878\(12\)80018-6](https://doi.org/10.1016/s0016-7878(12)80018-6)
- Becker, H. (1993). Garnet peridotite and eclogite Sm-Nd mineral ages from the Lepontine dome (Swiss Alps): New evidence for Eocene high-pressure metamorphism in the central Alps. *Geology*, 21(7), 599–602. [https://doi.org/10.1130/0091-7613\(1993\)021<0599:GPAESN>2.3.CO;2](https://doi.org/10.1130/0091-7613(1993)021<0599:GPAESN>2.3.CO;2)
- Beltrán-Triviño, A., Winkler, W., & Von Quadt, A. (2013). Tracing Alpine sediment sources through laser ablation U-Pb dating and Hf-isotopes of detrital zircons. *Sedimentology*, 60(1), 197–224. <https://doi.org/10.1111/sed.12006>
- Beltrando, M., Compagnoni, R., & Lombardo, B. (2010). (Ultra-) High-pressure metamorphism and orogenesis: an Alpine perspective. *Gondwana Research*, 18(1), 147–166. <https://doi.org/10.1016/j.gr.2010.01.009>

- Berg, C. A., Carlson, W. D., & Connelly, J. N. (2013). Strain rates at high temporal resolution from curved inclusion trails in garnet, Passo del Sole, Central Swiss Alps. *Journal of Metamorphic Geology*, 31(3), 243–262. <https://doi.org/10.1111/jmg.12017>
- Berger, A., Burri, T., Alt-Epping, P., & Engi, M. (2008). Tectonically controlled fluid flow and water-assisted melting in the middle crust: an example from the Central Alps. *Lithos*, 102(3–4), 598–615. <https://doi.org/10.1016/j.lithos.2007.07.027>
- Berger, A., Mercolli, I., & Engi, M. (2005). The central Lepontine Alps: Notes accompanying the tectonic and petrographic map sheet Sopra Ceneri (1:100'000). *Schweizerische Mineralogische Und Petrographische Mitteilungen*, 85(2–3), 109–146.
- Berger, A., Schmid, S. M., Engi, M., Bousquet, R., & Wiederkehr, M. (2011). Mechanisms of mass and heat transport during Barrovian metamorphism: A discussion based on field evidence from the Central Alps (Switzerland/northern Italy). *Tectonics*, 30(1), TC1007. <https://doi.org/10.1029/2009TC002622>
- Bindeman, I. N., & Melnik, O. E. (2016). Zircon survival, rebirth and recycling during crustal melting, magma crystallization, and mixing based on numerical modelling. *Journal of Petrology*, 57(3), 437–460. <https://doi.org/10.1093/petrology/egw013>
- Black, L. P., Kamo, S. L., Allen, C. M., Davis, D. W., Aleinikoff, J. N., Valley, J. W., Mundil, R., Campbell, I. H., Korsch, R. J., & Williams, I. S. (2004). Improved ²⁰⁶Pb/²³⁸U microprobe geochronology by the monitoring of a trace-element-related matrix effect; SHRIMP, ID-TIMS, ELA-ICP-MS and oxygen isotope documentation for a series of zircon standards. *Chemical Geology*, 205(1–2), 115–140. <https://doi.org/10.1016/j.chemgeo.2004.01.003>
- Boekhout, F., Spikings, R., Sempere, T., Chiaradia, M., Ulianov, A., & Schaltegger, U. (2012). Mesozoic arc magmatism along the southern Peruvian margin during Gondwana breakup and dispersal. *Lithos*, 146–147, 48–64. <https://doi.org/10.1016/j.lithos.2012.04.015>
- Boston, K. R., Rubatto, D., Hermann, J., Engi, M., & Amelin, Y. (2017). Geochronology of accessory allanite and monazite in the Barrovian metamorphic sequence of the Central Alps, Switzerland. *Lithos*, 286, 502–518. <https://doi.org/10.1016/j.lithos.2017.06.025>
- Bousquet, R., Goffé, B., Henry, P., Le Pichon, X., & Chopin, C. (1997). Kinematic, thermal and petrological model of the Central Alps: Lepontine metamorphism in the upper crust and eclogitisation of the lower crust. *Tectonophysics*, 273(1–2), 105–127. [https://doi.org/10.1016/S0040-1951\(96\)00290-9](https://doi.org/10.1016/S0040-1951(96)00290-9)

- Bousquet, R., Oberhänsli, R., Goffé, B., Wiederkehr, M., Koller, F., Schmid, S. M., Schuster, R., Engi, M., Berger, A., & Martinotti, G. (2008). Metamorphism of metasediments at the scale of an orogen: A key to the Tertiary geodynamic evolution of the Alps. *Geological Society Special Publication*, 298(1), 393–411. <https://doi.org/10.1144/SP298.18>
- Bousquet, R., Oberhänsli, R., Schmid, S. M., Berger, A., Wiederkehr, M., Robert, C., Möller, A., Rosenberg, C., Koller, F., Molli, G., & Zeilinger, G. (2012). Metamorphic framework of the Alps. CCGM/CGMW. <http://www.geodynamps.eu>
- Braun, J., Chéry, J., Poliakov, A., Mainprice, D., Vauchez, A., Tomassi, A., & Daignières, M. (1999). A simple parameterization of strain localization in the ductile regime due to grain size reduction: A case study for olivine. *Journal of Geophysical Research: Solid Earth*, 104(B11), 25167–25181. <https://doi.org/10.1029/1999JB900214>
- Braun, J., Van der Beek, P., & Batt, G. (2006). Quantitative Thermochronology: Numerical Methods for the Interpretation of Thermochronological Data. *Cambridge University Press, Cambridge*. <https://doi.org/10.1017/CBO9780511616433>
- Brinkman, H. C. (1951). Heat effects in capillary flow. *Applied Scientific Research*, A2(1), 120–124. <https://doi.org/10.1007/bf00411976>
- Brouwer, F. M., Burri, T., Engi, M., & Berger, A. (2005). Eclogite relics in the Central Alps: PT-evolution, Lu-Hf ages and implications for formation of tectonic mélange zones. *Schweizerische Mineralogische Und Petrographische Mitteilungen*, 85(2–3), 147–174.
- Brouwer, F. M., & Engi, M. (2005). Staurolite and other aluminous phases in alpine eclogite from the central Swiss Alps: Analysis of domain evolution. *Canadian Mineralogist*, 43(1), 105–128. <https://doi.org/10.2113/gscanmin.43.1.105>
- Brouwer, F. M., Van de Zedde, D. M. A., Wortel, M. J. R., & Vissers, R. L. M. (2004). Late-orogenic heating during exhumation: Alpine PTt trajectories and thermomechanical models. *Earth and Planetary Science Letters*, 220(1–2), 185–199. [https://doi.org/10.1016/S0012-821X\(04\)00050-0](https://doi.org/10.1016/S0012-821X(04)00050-0)
- Brown, M. (2014). The contribution of metamorphic petrology to understanding lithosphere evolution and geodynamics. *Geoscience Frontiers*, 5(4), 553–569. <https://doi.org/10.1016/j.gsf.2014.02.005>
- Brun, J. P., & Cobbold, P. R. (1980). Strain heating and thermal softening in continental shear zones: a review. *Journal of Structural Geology*, 2(1-2), 149–158. [https://doi.org/10.1016/0191-8141\(80\)90045-0](https://doi.org/10.1016/0191-8141(80)90045-0)

- Buchmann, H. (1953). *Geologie und Petrographie des oberen Maggia-Tales zwischen Fusio und Broglio im NW-Tessin: inauguraldissertation*. Basler Berichthaus.
- Burg, J. P., & Gerya, T. V. (2005). The role of viscous heating in Barrovian metamorphism of collisional orogens: Thermomechanical models and application to the Lepontine Dome in the Central Alps. *Journal of Metamorphic Geology*, 23(2), 75–95.
<https://doi.org/10.1111/j.1525-1314.2005.00563.x>
- Burg, J. P., Kaus, B. J. P., & Podladchikov, Y. Y. (2004). Dome structures in collisional orogens: mechanical investigation of the gravity/compression interplay, in: D. L. Whitney, C. Teysier, & C. S. Siddoway (Eds.), *Gneiss domes in orogeny*. *Geological Society of America, Boulder, Colorado* (pp. 47-66).
- Burg, J. P., & Moulas, E. (2022). Cooling-rate constraints from metapelites across two inverted metamorphic sequences of the Alpine-Himalayan belt; evidence for viscous heating. *Journal of Structural Geology*, 156, 104536. <https://doi.org/10.1016/j.jsg.2022.104536>
- Burg, J. P., & Schmalholz, S. M. (2008). Viscous heating allows thrusting to overcome crustal-scale buckling: Numerical investigation with application to the Himalayan syntaxes. *Earth and Planetary Science Letters*, 274(1–2), 189–203. <https://doi.org/10.1016/j.epsl.2008.07.022>
- Burov, E., Jolivet, L., Le Pourhiet, L., & Poliakov, A. (2001). A thermomechanical model of exhumation of high pressure (HP) and ultra-high pressure (UHP) metamorphic rocks in Alpine-type collision belts. *Tectonophysics*, 342(1-2), 113-136.
[https://doi.org/10.1016/S0040-1951\(01\)00158-5](https://doi.org/10.1016/S0040-1951(01)00158-5)
- Burri, T., Berger, A., & Engi, M. (2005). Tertiary migmatites in the Central Alps: Regional distribution, field relations, conditions of formation and tectonic implications. *Schweizerische Mineralogische Und Petrographische Mitteilungen*, 85(2–3), 215–232.
- Bussien, D., Bussy, F., Magna, T., & Masson, H. (2011). Timing of Palaeozoic magmatism in the Maggia and Sambuco nappes and paleogeographic implications (Central Lepontine Alps). *Swiss Journal of Geosciences*, 104(1), 1–29. <https://doi.org/10.1007/s00015-010-0049-6>
- Caddick, M.J., Konopásek, J., & Thompson, A.B. (2010). Preservation of garnet growth zoning and the duration of prograde metamorphism. *Journal of Petrology* 51(11), 2327–2347.
<https://doi.org/10.1093/petrology/egq059>
- Caddick, M. J., & Thompson, A. B. (2008) Quantifying the tectono-metamorphic evolution of pelitic rocks from a wide range of tectonic settings: mineral compositions in equilibrium. *Contributions to Mineralogy and Petrology* 156, 177–195. <https://doi.org/10.1007/s00410-008-0280-6>

- Camacho, A., Lee, J. K. W., Hensen, B. J., & Braun, J. (2005). Short-lived orogenic cycles and the eclogitization of cold crust by spasmodic hot fluids. *Nature*, *435*(7046), 1191–1196. <https://doi.org/10.1038/nature03643>
- Candioti, L. G., Duretz, T., Moulas, E., & Schmalholz, S. M. (2021). Buoyancy versus shear forces in building orogenic wedges. *Solid Earth*, *12*(8), 1749–1775. <https://doi.org/10.5194/se-12-1749-2021>
- Candioti, L. G., Duretz, T., & Schmalholz, S. M. (2022). Horizontal force required for subduction initiation at passive margins with constraints from slab detachment. *Frontiers in Earth Science*, *10*, 785418. <https://doi.org/10.3389/feart.2022.785418>
- Casasopra, S. (1940). Studio petrografico dello gneiss granitico Leventina: Valle Riviera e Valle Leventina (Canton Ticino) (Doctoral dissertation, ETH Zurich).
- Cavargna-Sani, M., Epard, J. L., Bussy, F., & Ulianov, A. (2014a). Basement lithostratigraphy of the Adula nappe: Implications for Palaeozoic evolution and Alpine kinematics. *International Journal of Earth Sciences*, *103*(1), 61–82. <https://doi.org/10.1007/s00531-013-0941-1>
- Cavargna-Sani, M., Epard, J. L., & Steck, A. (2014b). Structure, geometry and kinematics of the northern Adula nappe (Central Alps). *Swiss Journal of Geosciences*, *107*(2–3), 135–156. <https://doi.org/10.1007/s00015-014-0175-7>
- Cermak, V., & Rybach, L. (1982). 4.1. 1 Introductory remarks: 4.1 Thermal conductivity and specific heat of minerals and rocks. Subvolume A, 305–310.
- Chakraborty, S. (2006). Diffusion modeling as a tool for constraining timescales of evolution of metamorphic rocks. *Mineralogy and Petrology*, *88*, 7–27. <https://doi.org/10.1007/s00710-006-0152-6>
- Chemenda, A. I., Mattauer, M., & Bokun, A. N. (1996). Continental subduction and a mechanism for exhumation of high-pressure metamorphic rocks: new modelling and field data from Oman. *Earth and Planetary Science Letters*, *143*(1–4), 173–182. [https://doi.org/10.1016/0012-821x\(96\)00123-9](https://doi.org/10.1016/0012-821x(96)00123-9)
- Chu, X., Ague, J. J., Tian, M., Baxter, E. F., Rumble III, D., & Chamberlain, C. P. (2018). Testing for rapid thermal pulses in the crust by modeling garnet growth–diffusion–resorption profiles in a UHT metamorphic ‘Hot Spot’, New Hampshire, USA. *Journal of Petrology*, *59*(10), 1939–1964. <https://doi.org/10.1093/petrology/egy085>

- Cioldi, S. (2017). Thermal evolution of crustal-scale thrust zones in three collisional mountain regions: geospeedometry of inverted metamorphic gradients (Doctoral dissertation, ETH Zurich).
- Codoni, A. G. (1981). Geologia e petrografia del Pizzo di Claro (Doctoral dissertation, Zurich University).
- Corvò, S., Maino, M., Langone, A., Schenker, F. L., Piazzolo, S., Casini, L., & Seno, S. (2021). Local variations of metamorphic record from compositionally heterogeneous rocks (Cima di Gagnone, Central Alps): Inferences on exhumation processes of (U)HP–HT rocks. *Lithos*, 390–391, 106126. <https://doi.org/10.1016/j.lithos.2021.106126>
- Corvò, S., Maino, M., Langone, A., Schenker F. L., Tagliaferri, A., Perozzo, M., Casini, L., & Seno, S. (in review) Monazite and zircon U-(Th-)Pb dating reveal multiple episodes of HT metamorphism in the Cima Lunga unit (Central Alps): implications for the exhumation of high-pressure rocks.
- Coward, M., & Dietrich, D. (1989). Alpine tectonics — An overview. *Geological Society, London, Special Publications*, 45(1), 1–29. <https://doi.org/10.1144/gsl.sp.1989.045.01.01>
- Cygan, R. T., & Lasaga, A. C. (1985). Self-diffusion of magnesium in garnet at 750 degrees to 900 degrees C. *American Journal of Science*, 285(4), 328-350. <https://doi.org/10.2475/ajs.285.4.328>
- Dale, J., & Holland, T. J. B. (2003). Geothermobarometry, P–T paths and metamorphic field gradients of high-pressure rocks from the Adula Nappe, Central Alps. *Journal of Metamorphic Geology*, 21(8), 813-829. <https://doi.org/10.1046/j.1525-1314.2003.00483.x>
- Dal Vesco, E. (1953). Genesi e metamorfosi delle rocce basiche e ultrabasiche nell'ambiente mesozonale dell'orogene pennidico: studio geologico-petrografico della Catena Gaggio-Basal (Cantone Ticino). Doctoral dissertation, ETH Zurich.
- Debelmas, J., & Lemoine, M. (1970). The western Alps: Palaeogeography and structure. *Earth-Science Reviews*, 6(4), 221–256. [https://doi.org/10.1016/0012-8252\(70\)90079-6](https://doi.org/10.1016/0012-8252(70)90079-6)
- Della Torre, F., Maggini, L., Bonzanigo, L., Hunziker, J. C., & Joss, M. G. (2015). Foglio 1291 Bosco/Gurin. *Atlante Geologico Della Svizzera*, 1:25000.
- Deutsch, A., & Steiger, R. H. (1985). Hornblende K-Ar ages and the climax of Tertiary metamorphism in the Lepontine Alps (south-central Switzerland): an old problem reassessed. *Earth and Planetary Science Letters*, 72(2-3), 175-89. [https://doi.org/10.1016/0012-821X\(85\)90004-4](https://doi.org/10.1016/0012-821X(85)90004-4)

- Dewey, J. F. (2005). Orogeny can be very short. *Proceedings of the National Academy of Sciences of the United States of America*, 102(43), 15286–15293. <https://doi.org/10.1073/pnas.0505516102>
- Dewey, J. F., Helman, M. L., Knott, S. D., Turco, E., & Hutton, D. H. W. (1989). Kinematics of the western Mediterranean. *Geological Society Special Publication*, 45(45), 265–283. <https://doi.org/10.1144/GSL.SP.1989.045.01.15>
- Dobrzhinetskaya, L., Green, H. W., & Wang, S. (1996). Alpe Arami: A peridotite massif from depths of more than 300 kilometers. *Science*, 271(5257), 1841–1845. <https://doi.org/10.1126/science.271.5257.1841>
- Duprat-Oualid, S., Yamato, P., & Schmalholz, S. M. (2015). A dimensional analysis to quantify the thermal budget around lithospheric-scale shear zones. *Terra Nova*, 27(3), 163–168. <https://doi.org/10.1111/ter.12144>
- Duretz, T., Schmalholz, S. M., & Podladchikov, Y. Y. (2015). Shear heating-induced strain localization across the scales. *Philosophical Magazine*, 95(28–30), 3192–3207. <https://doi.org/10.1080/14786435.2015.1054327>
- Dutch, R., & Hand, M. (2010). Retention of Sm–Nd isotopic ages in garnets subjected to high-grade thermal reworking: implications for diffusion rates of major and rare earth elements and the Sm–Nd closure temperature in garnet. *Contributions to Mineralogy and Petrology* 159, 93–112. <https://doi.org/10.1007/s00410-009-0418-1>
- Engi, M., Berger, A., & Roselle, G. T. (2001). Role of the tectonic accretion channel in collisional orogeny. *Geology*, 29(12), 1143–1146. [https://doi.org/10.1130/0091-7613\(2001\)029<1143:ROTTAC>2.0.CO;2](https://doi.org/10.1130/0091-7613(2001)029<1143:ROTTAC>2.0.CO;2)
- England, P. C., & Holland, T. J. (1979). Archimedes and the Tauern eclogites: the role of buoyancy in the preservation of exotic eclogite blocks. *Earth and Planetary Science Letters*, 44(2), 287–294. [https://doi.org/10.1016/0012-821X\(79\)90177-8](https://doi.org/10.1016/0012-821X(79)90177-8)
- England, P. C., & Molnar, P. (1993). The interpretation of inverted metamorphic isograds using simple physical calculations. *Tectonics*, 12(1), 145–157. <https://doi.org/10.1029/92tc00850>
- England, P. C., & Smye, A. J. (2022). Metamorphism and deformation on subduction interfaces: 1. Physical framework. *Geochemistry, Geophysics, Geosystems*, 24, e2022GC010644. <https://doi.org/10.1029/2022GC010644>

- England, P. C., & Thompson, A. B. (1984). Pressure-temperature-time paths of regional metamorphism I. Heat transfer during the evolution of regions of thickened continental crust. *Journal of Petrology*, 25(4), 894–928. <https://doi.org/10.1093/petrology/25.4.894>
- Etchecopar, A. (1977). A plane kinematic model of progressive deformation in a polycrystalline aggregate. *Tectonophysics*, 39(1–3), 121–139. [https://doi.org/10.1016/0040-1951\(77\)90092-0](https://doi.org/10.1016/0040-1951(77)90092-0)
- Evans, B. W., & Trommsdorff, V. (1978). Petrogenesis of garnet lherzolite, Cima di Gagnone, Lepontine Alps. *Earth and Planetary Science Letters*, 40(3), 333–348. [https://doi.org/10.1016/0012-821x\(78\)90158-9](https://doi.org/10.1016/0012-821x(78)90158-9)
- Evans, B. W., Trommsdorff, V., & Richter, W. (1979). Petrology of an eclogite-metarodingite suite at Cima di Gagnone, Ticino, Switzerland. *American Mineralogist*, 64(1–2), 15–31.
- Finch, M. A., Weinberg, R. F., & Hunter, N. J. R. (2016). Water loss and the origin of thick ultramylonites. *Geology*, 44, 599–602. <http://dx.doi.org/10.1130/G37972.1>
- Fleitout, L., & Froidevaux, C. (1980). Thermal and mechanical evolution of shear zones. *Journal of Structural Geology*, 2(1–2), 159–164. [https://doi.org/10.1016/0191-8141\(80\)90046-2](https://doi.org/10.1016/0191-8141(80)90046-2)
- Florence, & F.P., & Spear, F.S. (1995). Intergranular diffusion kinetics of Fe and Mg during retrograde metamorphism of a pelitic gneiss from the Adirondack Mountains. *Earth and Planetary Science Letters* 134, 329–340. [https://doi.org/10.1016/0012-821X\(95\)00129-Z](https://doi.org/10.1016/0012-821X(95)00129-Z)
- Foley, M. L., Putlitz, B., Baumgartner, L. P., Renda, E. M., Ulianov, A., Siron, G., & Chiaradia, M. (2023). Identifying crustal contributions in the Patagonian Chon Aike Silicic Large Igneous Province. *Contributions to Mineralogy and Petrology*, 178(11), 80.
- Fossen, H. (2016). Structural geology. *Cambridge university press*.
- Fossen, H., & Cavalcante, G. C. G. (2017). Shear zones—A review. *Earth-Science Reviews*, 171, 434–455. <https://doi.org/10.1016/j.earscirev.2017.05.002>
- Fox, M., Herman, F., Kissling, E., & Willett, S. D. (2015). Rapid exhumation in the Western Alps driven by slab detachment and glacial erosion. *Geology*, 43(5), 379–382. <https://doi.org/10.1130/G36411.1>
- Frey, M. (1969). Die Metamorphose des Keupers von Tafeljura bis zum Lukmanier-Gebiet (Doctoral dissertation).
- Frey, M., Desmons, J., & Neubauer, F. (1999). The new metamorphic map of the Alps. *Schweizerische Mineralogische und Petrographische Mitteilungen*, 79, 1–230.

- Frey, M., & Ferreiro Mählmann, R. (1999). Alpine metamorphism of the Central Alps. *Schweizerische Mineralogische Und Petrographische Mitteilungen*, 79(1), 135–154.
- Froitzheim, N., Pleuger, J., Roller, S., & Nagel, T. (2003). Exhumation of high-and ultrahigh-pressure metamorphic rocks by slab extraction. *Geology*, 31(10), 925–928.
<https://doi.org/10.1130/G19748.1>
- Froitzheim, N., Schmid, S. M., & Frey, M. (1996). Mesozoic paleogeography and the timing of eclogite-facies metamorphism in the Alps: A working hypothesis. *Eclogae Geologicae Helvetiae*, 89(1), 81.
- Fu, B., Page, F. Z., Cavosie, A. J., Fournelle, J., Kita, N. T., Lackey, J. S., Wilde, S. A., & Valley, J. W. (2008). Ti-in-zircon thermometry: Applications and limitations. *Contributions to Mineralogy and Petrology*, 156(2), 197–215. <https://doi.org/10.1007/s00410-008-0281-5>
- Galli, A., Le Bayon, B., Schmidt, M. W., Burg, J. P., Caddick, M. J., & Reusser, E. (2011). Granulites and charnockites of the Gruf Complex: evidence for Permian ultra-high temperature metamorphism in the Central Alps. *Lithos*, 124(1–2), 17–45.
<https://doi.org/10.1016/j.lithos.2010.08.003>
- Galli, A., Le Bayon, B., Schmidt, M. W., Burg, J. P., Reusser, E., Sergeev, S. A., & Larionov, A. (2012). U-Pb zircon dating of the Gruf Complex: Disclosing the late Variscan granulitic lower crust of Europe stranded in the Central Alps. *Contributions to Mineralogy and Petrology*, 163(2), 353–378. <https://doi.org/10.1007/s00410-011-0676-6>
- Gebauer, D. (1994). A P-T-t path for some high-pressure ultramafic/mafic rock associations and their felsic country-rocks based on SHRIMP-dating of magmatic and metamorphic zircon domains. Example: Central Swiss Alps. In *Abstracts of the 8th International Conference on Geochronology, Cosmochronology and Isotope Geology. ICOG 8, Berkeley, USA, 5. – 11. 6. 1994, U. S. Geological Survey circular 1107, 109, 1994.* & in *Extended Abstract Version for 16th General Meeting of IMA, Pisa, Italy, Sept. 4-9, 1994, Abstract volume: 139-140.*
- Gebauer, D. (1996). A P-T-t path for an (ultra?-) high-pressure ultramafic/mafic rock-association and its felsic country-rocks based on SHRIMP-dating of magmatic and metamorphic zircon domains. Example: Alpe Arami (Central Swiss Alps). In *Earth Processes Reading the Isotopic Code, Geophysical Monograph*, 95, 307–329. American Geophysical Union.
- Gebauer, D. (1999). Alpine geochronology of the Central and Western Alps: New constraints for a complex geodynamic evolution. *Schweizerische Mineralogische Und Petrographische Mitteilungen*, 79(1), 191–208.

- Geisler, T., Rashwan, A. A., Rahn, M. K. W., Poller, U., Zwingmann, H., Pidgeon, R. T., Schleicher, H., & Tomaschek, F. (2003). Low-temperature hydrothermal alteration of natural metamict zircons from the Eastern Desert, Egypt. *Mineralogical Magazine*, 67(3), 485–508. <https://doi.org/10.1180/0026461036730112>
- Geisler, T., Schaltegger, U., & Tomaschek, F. (2007). Re-equilibration of zircon in aqueous fluids and melts. *Elements*, 3(1), 43–50. <https://doi.org/10.2113/gselements.3.1.43>
- Gieré, R., Rumble, D., Günther, D., Connolly, J., & Caddick, M. J. (2011). Correlation of growth and breakdown of major and accessory minerals in metapelites from Campolungo, Central Alps. *Journal of Petrology*, 52(12), 2293–2334. <https://doi.org/10.1093/petrology/egr043>
- Gisler, C., Hochuli, P. A., Ramseyer, K., Bläsi, H., & Schlunegger, F. (2007). Sedimentological and palynological constraints on the basal Triassic sequence in Central Switzerland. *Swiss Journal of Geosciences*, 100(2), 263–272. <https://doi.org/10.1007/s00015-007-1225-1>
- Gouffon, Y. (editor) (in review). Tectonic map of Switzerland 1:500.000 – Explicatory notes. *swisstopo*.
- Gregory, C. J., Buick, I. S., Hermann, J., & Rubatto, D. (2009). Mineral-scale trace element and U–Th–Pb age constraints on metamorphism and melting during the Petermann Orogeny (central Australia). *Journal of Petrology*, 50(2), 251–287. <https://doi.org/10.1093/petrology/egn077>
- Gregory, C. J., Rubatto, D., Hermann, J., Berger, A., & Engi, M. (2012). Allanite behaviour during incipient melting in the southern Central Alps. *Geochimica et Cosmochimica Acta*, 84, 433–458. <https://doi.org/10.1016/j.gca.2012.01.020>
- Grond, R., Wahl, F., & Pfiffner, M. (1995). Mehrphasige alpine Deformation und Metamorphose in der nördlichen Cima-Lunga- Einheit, Zentralalpen (Schweiz) = Polyphase Alpine deformation and metamorphism in the northern Cima Lunga unit, Central Alps (Switzerland). *Schweizerische Mineralogische Und Petrographische Mitteilungen*, 75, 371–386.
- Grujic, D., & Mancktelow, N. S. (1996). Structure of the northern Maggia and Lebendun Nappes, Central Alps, Switzerland. *Eclogae Geologicae Helvetiae*, 89(1), 461–504.
- Gueydan, F., Leroy, Y. M., Jolivet, L., & Agard, P. (2003). Analysis of continental midcrustal strain localization induced by microfracturing and reaction-softening. *Journal of Geophysical Research: Solid Earth*, 108(B2). <https://doi.org/10.1029/2001JB000611>

- Günthert, A. W., Stern, W. B., & Schwander, H. (1996). The polycyclic evolution of the Penninic Maggia nappe, Central Alps: A summary report. *Schweizerische Mineralogische Und Petrographische Mitteilungen*, 76(1), 1–22.
- Hacker, B. R., Kelemen, P. B., & Behn, M. D. (2015). Continental lower crust. *Annual Review of Earth and Planetary Sciences*, 43, 167–205.
<https://doi.org/10.1146/annurev-earth-050212-124117>
- Hallett, B. W., & Spear, F. S. (2011). Insight into the cooling history of the Valhalla complex, British Columbia. *Lithos*, 125(1–2), 809–824. <https://doi.org/10.1016/j.lithos.2011.05.002>
- Handy, M. R., Schmid, M. S., Bousquet, R., Kissling, E., & Bernoulli, D. (2010). Reconciling plate-tectonic reconstructions of Alpine Tethys with the geological-geophysical record of spreading and subduction in the Alps. *Earth-Science Reviews*, 102(3–4), 121–158.
<https://doi.org/10.1016/j.earscirev.2010.06.002>
- Handy, M. R., Ustaszewski, K., & Kissling, E. (2015). Reconstructing the Alps–Carpathians–Dinarides as a key to understanding switches in subduction polarity, slab gaps and surface motion. *International Journal of Earth Sciences*, 104(1), 1–26.
<https://doi.org/10.1007/s00531-014-1060-3>
- Hänny, R., Grauert, B., & Soptratanova, G. (1975). Paleozoic migmatites affected by high-grade tertiary metamorphism in the central Alps (Valle Bodengo, Italy). *Contributions to Mineralogy and Petrology*, 51, 173–96. <https://doi.org/10.1007/BF00372078>
- Harley, S. L., Kelly, N. M., & Möller, A. (2007). Zircon behaviour and the thermal histories of mountain chains. *Elements*, 3(1), 25–30. <https://doi.org/10.2113/gselements.3.1.25>
- Hartz, E. H., & Podladchikov, Y. Y. (2008). Toasting the jelly sandwich: The effect of shear heating on lithospheric geotherms and strength. *Geology*, 36(4), 331–334.
<https://doi.org/10.1130/G24424A.1>
- Hasterok, D., & Webb, J. (2017). On the radiogenic heat production of igneous rocks. *Geoscience Frontiers*, 8(5), 919–940. <https://doi.org/10.1016/j.gsf.2017.03.006>
- Heinrich, C. A. (1982). Kyanite-eclogite to amphibolite facies evolution of hydrous mafic and pelitic rocks, Adula nappe, Central Alps. *Contributions to Mineralogy and Petrology*, 81(1), 30–38.
<https://doi.org/10.1007/BF00371156>

- Heinrich, C. A. (1986). Eclogite facies regional metamorphism of hydrous mafic rocks in the Central Alpine Adula Nappe. *Journal of Petrology*, 27(1), 123–154.
<https://doi.org/10.1093/petrology/27.1.123>
- Herman, F., Copeland, P., Avouac, J. P., Bollinger, L., Mahéo, G., Le Fort, P., Rai, S., Foster, D., Pêcher, A., Stüwe, K., & Henry, P. (2010). Exhumation, crustal deformation, and thermal structure of the Nepal Himalaya derived from the inversion of thermochronological and thermobarometric data and modeling of the topography. *Journal of Geophysical Research: Solid Earth*, 115(B6). <https://doi.org/10.1029/2008JB006126>
- Hermann, J., Rubatto, D., & Trommsdorff, V. (2006). Sub-solidus Oligocene zircon formation in garnet peridotite during fast decompression and fluid infiltration (Duria, Central Alps). *Mineralogy and Petrology*, 88(1), 181–206. <https://doi.org/10.1007/s00710-006-0155-3>
- Herwartz, D., Nagel, T. J., Münker, C., Scherer, E. E., & Froitzheim, N. (2011). Tracing two orogenic cycles in one eclogite sample by Lu-Hf garnet chronometry. *Nature Geoscience*, 4(3), 178–183. <https://doi.org/10.1038/ngeo1060>
- Herwegh, M., Berger, A., Baumberger, R., Wehrens, P., & Kissling, E. (2017). Large-Scale Crustal-Block-Extrusion During Late Alpine Collision. *Scientific Reports*, 7(1), 1–10. <https://doi.org/10.1038/s41598-017-00440-0>
- Hilley, G. E., Bürgmann, R., Zhang, P. Z., & Molnar, P. (2005). Bayesian inference of plastosphere viscosities near the Kunlun Fault, northern Tibet. *Geophysical Research Letters*, 32, L01302. <https://doi.org/10.1029/2004GL021658>
- Holdaway, M. J. (2000). Application of new experimental and garnet Margules data to the garnet-biotite geothermometer. *American mineralogist*, 85(7-8), 881–892. <https://doi.org/10.2138/am-2000-0701>
- Horstwood, M. S., Košler, J., Gehrels, G., Jackson, S. E., McLean, N. M., Paton, C., Pearson, N. J., Sircombe, K., Sylvester, P., Vermeesch, P., Bowring, J. F., Condon, D. J., & Schoene, B. (2016). Community-derived standards for LA-ICP-MS U-(Th-) Pb geochronology—Uncertainty propagation, age interpretation and data reporting. *Geostandards and Geoanalytical Research*, 40(3), 311–332.
- Hoskin, P. W. O. (2005). Trace-element composition of hydrothermal zircon and the alteration of Hadean zircon from the Jack Hills, Australia. *Geochimica et Cosmochimica Acta*, 69(3), 637–648. <https://doi.org/10.1016/j.gca.2004.07.006>

- Hoskin, P. W. O., & Black, L. P. (2000). Metamorphic zircon formation by solid-state recrystallization of protolith igneous zircon. *Journal of Metamorphic Geology*, *18*(4), 423–439. <https://doi.org/10.1046/j.1525-1314.2000.00266.x>
- Hoskin, P. W. O., & Schaltegger, U. (2003). The composition of zircon and igneous and metamorphic petrogenesis. In Hancher J. & Hoskin P. (Eds.). *Zircon, Reviews in mineralogy and geochemistry*, (Vol. 53, pp. 27–62). <https://doi.org/10.1515/9781501509322-005>
- Huber, M., Ramsay, J., & Simpson, C. (1980). Deformation in the Maggia and Antigorio nappes, Lepontine Alps. *Eclogae Geologicae Helvetiae*, *73*, 2, 593–606.
- Huerta, A. D., Royden, L. H., & Hodges, K. V. (1998). The thermal structure of collisional orogens as a response to accretion, erosion, and radiogenic heating. *Journal of Geophysical Research*, *103*(7), 15287–15302. <https://doi.org/10.1029/98jb00593>
- Huerta, A. D., Royden, L. H., & Hodges, K. V. (1999). The effects of accretion, erosion and radiogenic heat on the metamorphic evolution of collisional orogens. *Journal of Metamorphic Geology*, *17*(4), 349–366. <https://doi.org/10.1046/j.1525-1314.1999.00204.x>
- Hunziker, J. C. (1970). Polymetamorphism in the Monte Rosa, western Alps. *Eclogae Geologicae Helvetiae*, *63*, 151–61.
- Hurford, A. J. (1986). Cooling and uplift patterns in the Lepontine Alps South Central Switzerland and an age of vertical movement on the Insubric fault line. *Contributions to Mineralogy and Petrology*, *92*(4), 413–427. <https://doi.org/10.1007/BF00374424>
- Jackson, S. (2008). LAMTRACE data reduction software for LA-ICP-MS. In *Laser Ablation ICP-MS in the Earth Sciences: Current Practices and Outstanding Issues*. *Mineralogical Association of Canada*, *40*, 305–307.
- Jäger, E. (1973). Die Alpine Orogenese im Lichte der Radiometrischen Alterbestimmung. *Eclogae Geologicae Helvetiae*, *66*, 11–21.
- Jamieson, R. A., Beaumont, C., Fullsack, P., & Lee, B. (1998). Barrovian regional metamorphism: where's the heat? *Geological Society Special Publication*, *138*(1), 23–51. <https://doi.org/10.1144/GSL.SP.1996.138.01.03>
- Janots, E., Engi, M., Berger, A., Allaz, J., Schwarz, J., & Spandler, C. (2008). Prograde metamorphic sequence of REE minerals in pelitic rocks of the Central Alps: implications for allanite–monazite–xenotime phase relations from 250 to 610 °C. *Journal of Metamorphic Geology*, *26*(5), 509–526. <https://doi.org/10.1111/j.1525-1314.2008.00774.x>

- Janots, E., Engi, M., Rubatto, D., Berger, A., Gregory, C., & Rahn, M. (2009). Metamorphic rates in collisional orogeny from in situ allanite and monazite dating. *Geology*, *37*(1), 11–14. <https://doi.org/10.1130/g25192a.1>
- Jenny, H. (1923). Über Bau und Entstehung der penninischen Decken. *Eclogae Geologicae Helvetiae*, *5*.
- Ji, S., Jiang, Z., Rybacki, E., Wirth, R., Prior, D., & Xia, B. (2004). Strain softening and microstructural evolution of anorthite aggregates and quartz–anorthite layered composites deformed in torsion. *Earth and Planetary Science Letters*, *222*, 377–390. <http://dx.doi.org/10.1016/j.epsl.2004.03.021>
- Jochum, K. P., Weis, U., Stoll, B., Kuzmin, D., Yang, Q., Raczek, I., Jacob, D. E., Stracke, A., Birbaum, K., Frick, D. A., Günther, D., & Enzweiler, J. (2011). Determination of reference values for NIST SRM 610-617 glasses following ISO guidelines. *Geostandards and Geoanalytical Research*, *35*(4), 397–429. <https://doi.org/10.1111/j.1751-908X.2011.00120.x>
- Kidder, S. B., Herman, F., Saleeby, J., Avouac, J. P., Ducea, M. N., & Chapman, A. (2013). Shear heating not a cause of inverted metamorphism. *Geology*, *41*(8), 899–902. <https://doi.org/10.1130/G34289.1>
- Kincaid, C., & Silver, P. (1996). The role of viscous dissipation in the orogenic process. *Earth and Planetary Science Letters*, *142*, 271–288. [https://doi.org/10.1016/0012-821X\(96\)00116-1](https://doi.org/10.1016/0012-821X(96)00116-1)
- Kiss, D., Podladchikov, Y. Y., Duretz, T., & Schmalholz, S. M. (2019). Spontaneous generation of ductile shear zones by thermal softening: Localization criterion, 1D to 3D modelling and application to the lithosphere. *Earth and Planetary Science Letters*, *519*, 284–296. <https://doi.org/10.1016/j.epsl.2019.05.026>
- Klaper, E. M. (1982). Deformation und Metamorphose in der nördlichen Maggia-zone. *Schweizerische Mineralogische und Petrographische Mitteilungen*, *62*, 47-76.
- Klein, C., Hurlbut, C. S., Dana, J. D., & Mineraloge, G. (1993). *Manual of mineralogy* (Vol. 394). Wiley.
- Klötzli, U., Klötzli, E., Günes, Z., & Kosler, J. (2009). Accuracy of laser ablation U-Pb zircon dating: Results from a test using five different reference zircons. *Geostandards and Geoanalytical Research*, *33*(1), 5-15.

- Kohn, M. J. (2014). 4.7 - Geochemical Zoning in Metamorphic Minerals. In *Treatise on Geochemistry: Second Edition (2nd ed., Vol. 4)*. Elsevier Ltd.
<https://doi.org/10.1016/B978-0-08-095975-7.00305-3>
- Kohn, M.J., & Spear, F. (2000). Retrograde net transfer reaction insurance for pressure-temperature estimates. *Geology* 28, 1127–1130.
[https://doi.org/10.1130/0091-7613\(2000\)28<1127:RNTRIF>2.0.CO;2](https://doi.org/10.1130/0091-7613(2000)28<1127:RNTRIF>2.0.CO;2)
- Köppel, V., & Grünenfelder, M., (1975). Concordant U–Pb ages of monazite and xenotime from the Central Alps and the timing of high temperature Alpine metamorphism, a preliminary report. *Schweizerische Mineralogische und Petrographische Mitteilungen*, 55, 129–132.
- Köppel, V., & Grünenfelder, M. (1978). The significance of monazite U-Pb ages: examples from the Lepontine area of the Swiss Alps. In *Fourth International Conference, Geochronology, Cosmochronology, Isotope Geology*, 226-227.
- Köppel, V., Günthert, A., & Grünenfelder, M. (1981). Patterns of U-Pb zircon and monazite ages in polymetamorphic units of the Swiss Central Alps. *Schweizerische Mineralogische Und Petrographische Mitteilungen*, 61, 97–119.
- Leloup, P. H., Ricard, Y., Battaglia, J., & Lacassin, R. (1999). Shear heating in continental strike-slip shear zones: Model and field examples. *Geophysical Journal International*, 136(1), 19–40.
<https://doi.org/10.1046/j.1365-246X.1999.00683.x>
- Li, X., Long, W., Li, Q., Liu, Y., Zheng, Y., Yang, Y., Chamberlain, K. R., Wan, D., Guo, C., & Wang, X. (2010). Penglai zircon megacrysts: a potential new working reference material for microbeam determination of Hf–O isotopes and U–Pb age. *Geostandards and Geoanalytical Research*, 34(2), 117–134. <https://doi.org/10.1111/j.1751-908x.2010.00036.x>
- Liati, A., Gebauer, D., & Fanning, M. (2000). U-Pb SHRIMP dating of zircon from the Novate granite (Bergell, Central Alps): Evidence for Oligocene-Miocene magmatism, Jurassic/Cretaceous continental rifting and opening of the Valais trough. *Schweizerische Mineralogische Und Petrographische Mitteilungen*, 80(3), 305–316.
- Liati, A., Gebauer, D., & Fanning, C. M. (2009). Geochronological evolution of HP metamorphic rocks of the Adula nappe, Central Alps, in pre-Alpine and Alpine subduction cycles. *Journal of the Geological Society*, 166(4), 797–810. <https://doi.org/10.1144/0016-76492008-033>
- Longerich, H. P., Jackson, S. E., & Günther, D. (1996). Inter-laboratory note. Laser ablation inductively coupled plasma mass spectrometric transient signal data acquisition and analyte concentration calculation. *Journal of Analytical Atomic Spectrometry*, 11(9), 899–904.

- Maino, M., Adamuszek, M., Schenker, F. L., Seno, S., & Dabrowski, M. (2021). Sheath fold development around deformable inclusions: Integration of field-analysis (Cima Lunga unit, Central Alps) and 3D numerical models. *Journal of Structural Geology*, *144*, 104255. <https://doi.org/10.1016/j.jsg.2020.104255>
- Maino, M., Casini, L., Boschi, C., Di Giulio, A., Setti, M., & Seno, S. (2020). Time-Dependent heat budget of a thrust from geological records and numerical experiments. *Journal of Geophysical Research: Solid Earth*, *125*(3), 1–24. <https://doi.org/10.1029/2019JB018940>
- Maino, M., Casini, L., Ceriani, A., Decarlis, A., Di Giulio, A., Seno, S., Setti, M., & Stuart, F. M. (2015). Dating shallow thrusts with zircon (U-Th)/He thermochronometry — The shear heating connection. *Geology*, *43*(6), 495–498. <https://doi.org/10.1130/G36492.1>
- Mako, C. A., & Caddick, M. J. (2018). Quantifying magnitudes of shear heating in metamorphic systems. *Tectonophysics*, *744*, 499–517. <https://doi.org/10.1016/j.tecto.2018.07.003>
- Malusà, M. G., Faccenna, C., Baldwin, S. L., Fitzgerald, P. G., Rossetti, F., Balestrieri, M. L., Danišik, M., Ellero, A., Ottria, G., & Piromallo, C. (2015). Contrasting styles of (U) HP rock exhumation along the Cenozoic Adria-Europe plate boundary (Western Alps, Calabria, Corsica). *Geochemistry, Geophysics, Geosystems*, *16*(6), 1786–1824. <https://doi.org/10.1002/2015GC005767>
- Malusà, M. G., Villa, I. M., Vezzoli, G., & Garzanti, E. (2011). Detrital geochronology of unroofing magmatic complexes and the slow erosion of Oligocene volcanoes in the Alps. *Earth and Planetary Science Letters*, *301*(1–2), 324–336. <https://doi.org/10.1016/j.epsl.2010.11.019>
- Mancktelow, N. S., & Pennacchioni, G. (2004). The influence of grain boundary fluids on the microstructure of quartz-feldspar mylonites. *Journal of Structural Geology*, *26*(1), 47–69. [https://doi.org/10.1016/S0191-8141\(03\)00081-6](https://doi.org/10.1016/S0191-8141(03)00081-6)
- Maxelon, M., & Mancktelow, N. S. (2005). Three-dimensional geometry and tectonostratigraphy of the Pennine zone, Central Alps, Switzerland and Northern Italy. *Earth-Science Reviews*, *71*(3–4), 171–227. <https://doi.org/10.1016/j.earscirev.2005.01.003>
- McDonough, W. F., & Sun, S. S. (1995). The composition of the Earth. *Chemical Geology*, *120*(3–4), 223–253. [https://doi.org/10.1016/0009-2541\(94\)00140-4](https://doi.org/10.1016/0009-2541(94)00140-4)
- Merle, O., Cobbold, P. R., & Schmid, S. M. (1989). Tertiary kinematics in the Lepontine dome. *Geological Society Special Publication*, *45*(1), 113–134. <https://doi.org/10.1144/GSL.SP.1989.045.01.06>

- Meyre, C., De Capitani, C., Zack, T., & Frey, M. (1999). Petrology of high-pressure metapelites from the Adula Nappe (Central Alps, Switzerland). *Journal of Petrology*, 40(1), 199–213. <https://doi.org/10.1093/petroj/40.1.199>
- Meyre, C., Marquer, D., Schmid, S. M., & Ciancaleoni, L. (1998). Syn-orogenic extension along the Forcola fault: Correlation of Alpine deformations in the Tambo and Adula nappes (Eastern Penninic Alps). *Eclogae Geologicae Helvetiae*, 91(3), 409–420.
- Miyashiro, A. (2012). *Metamorphism and metamorphic belts*. Springer Science & Business Media.
- Molnar, P., & England, P. (1990). Temperatures, heat flux, and frictional stress near major thrust faults. *Journal of Geophysical Research*, 95(B4), 4833–4856. <https://doi.org/10.1029/JB095iB04p04833>
- Monié, P. (1985). La méthode ^{39}Ar - ^{40}Ar appliquée au métamorphisme alpin dans le massif du Mont Rose (Alpes occidentales). Chronologie détaillée depuis 110 Ma. *Eclogae Geologicae Helvetiae*, 78, 487-516.
- Moulas, E. (2023). GDIFF: a Finite Difference code for the calculation of multicomponent diffusion in garnet (v 1.2). *Zenodo*. <https://doi.org/10.5281/zenodo.8224137>
- Moulas, E., Schmalholz, S. M., Podladchikov, Y., Tajčmanová, L., Kostopoulos, D., & Baumgartner, L. (2019). Relation between mean stress, thermodynamic, and lithostatic pressure. *Journal of Metamorphic Geology*, 37(1), 1–14. <https://doi.org/10.1111/jmg.12446>
- Nabelek, P. I., Whittington, A. G., & Hofmeister, A. M. (2010). Strain heating as a mechanism for partial melting and ultrahigh temperature metamorphism in convergent orogens: Implications of temperature-dependent thermal diffusivity and rheology. *Journal of Geophysical Research*, 115(12), 1–17. <https://doi.org/10.1029/2010JB007727>
- Nagel, T. J. (2008). Tertiary subduction, collision and exhumation recorded in the Adula nappe, central Alps. *Geological Society, London, Special Publications*, 298(1), 365–392. <https://doi.org/10.1144/sp298.17>
- Nagel, T. J., De Capitani, C., & Frey, M. (2002a). Isograds and P-T evolution in the eastern Lepontine Alps (Graubünden, Switzerland). *Journal of Metamorphic Geology*, 20(3), 309–324. <https://doi.org/10.1046/j.1525-1314.2002.00368.x>
- Nagel, T., De Capitani, C., Frey, M., Froitzheim, N., Stunitz, H., & Schmid, S. M. (2002b). Structural and metamorphic evolution during rapid exhumation in the Lepontine dome (southern Simano and Adula nappes, Central Alps, Switzerland). *Eclogae Geologicae Helvetiae*, 95(3), 301–321.

- Newman, J., Lamb, W. M., Drury, M. R., & Vissers, R. L. (1999). Deformation processes in a peridotite shear zone: reaction-softening by an H₂O-deficient, continuous net transfer reaction. *Tectonophysics*, 303(1–4), 193–222. [https://doi.org/10.1016/S0040-1951\(98\)00259-5](https://doi.org/10.1016/S0040-1951(98)00259-5)
- Nimis, P., & Trommsdorff, V. (2001). Revised thermobarometry of Alpe Arami and other garnet peridotites from the Central Alps. *Journal of Petrology*, 42(1), 103–115. <https://doi.org/10.1093/petrology/42.1.103>
- Oliot, E., Goncalves, P., & Marquer, D. (2010). Role of plagioclase and reaction softening in a metagranite shear zone at mid-crustal conditions (Gotthard Massif, Swiss Central Alps). *J. Metamorph. Geol.* 28, 849–871. <http://dx.doi.org/10.1111/j.1525-1314.2010.00897.x>
- Oxburgh, E. R., & Turcotte, D. L. (1974). Thermal gradients and regional metamorphism in overthrust terrains with special reference to the eastern Alps. *Schweizerische Mineralogische Und Petrographische Mitteilungen*, 54, 641–662.
- Paquin, J., & Altherr, R. (2001). New constraints on the P-T evolution of the Alpe Arami garnet peridotite body (Central Alps, Switzerland). *Journal of Petrology*, 42(6), 1137–1140. <https://doi.org/10.1093/petrology/42.6.1119>
- Passchier, C. W., & Trouw, R. A. J. (2005). *Microtectonics* (2nd ed., p. 366). Springer.
- Paterson, S. R., Vernon, R. H., & Tobisch, O. T. (1989). A review of criteria for the identification of magmatic and tectonic foliations in granitoids. *Journal of Structural Geology*, 11(3), 349–363. [https://doi.org/10.1016/0191-8141\(89\)90074-6](https://doi.org/10.1016/0191-8141(89)90074-6)
- Pfeifer, H.-R. (1981). A model for fluids in metamorphosed ultramafic rocks III. Mass transfer under amphibolite facies conditions in olivine-enstatite rocks of the Central Alps, Switzerland. *Bulletin de Minéralogie*, 104(6), 834–847. <https://doi.org/10.3406/bulmi.1981.7533>
- Pfeifer, H.-R. (1987). A model for fluids in metamorphosed ultramafic rocks: IV. Metasomatic veins in metaharzburgites of Cima di Gagnone, Valle Verzasca, Switzerland. In *Chemical transport in metasomatic processes* (pp. 591–632). Springer.
- Pfiffner, M. A. (1999). Genese der Hochdruckmetamorphen ozeanischen Abfolge des Cima Lunga-Einheit (Zentralalpen). In *Diss. ETH* (Vol. 13011). ETHZ.
- Pfiffner, M., & Trommsdorff, V. (1997). Evidence for high-pressure metamorphosed ophicarbonatite rocks, Cima di Gagnone, Central Alps. *Terra Nova Abstract Supplement*, 1, 26.

- Pfiffner, M., & Trommsdorff, V. (1998). The high-pressure ultramafic-mafic-carbonate suite of Cima Lunga-Adula, Central Alps: Excursions to Cima di Gagnone and Alpe Arami. *Schweizerische Mineralogische Und Petrographische Mitteilungen*, 78(2), 337–354.
- Piccoli, F., Lanari, P., Hermann, J., & Pettke, T. (2021). Deep subduction, melting, and fast cooling of metapelites from the Cima Lunga Unit, Central Alps. *Journal of Metamorphic Geology*, 40(1), 121–143. <https://doi.org/10.1111/jmg.12621>
- Platt, J. P. (1986). Dynamics of orogenic wedges and the uplift of high-pressure metamorphic rocks. *Geological society of America bulletin*, 97(9), 1037-1053. [https://doi.org/10.1130/0016-7606\(1986\)97%3C1037:DOOWAT%3E2.0.CO;2](https://doi.org/10.1130/0016-7606(1986)97%3C1037:DOOWAT%3E2.0.CO;2)
- Platt, J. P. (2015). Influence of shear heating on microstructurally defined plate boundary shear zones. *Journal of Structural Geology*, 79, 80–89. <https://doi.org/10.1016/j.jsg.2015.07.009>
- Platt, J. P., & Behr, W. M. (2011). Grainsize evolution in ductile shear zones: Implications for strain localization and the strength of the lithosphere. *Journal of Structural Geology*, 33(4), 537–550. <https://doi.org/10.1016/j.jsg.2011.01.018>
- Pleuger, J., & Podladchikov, Y. Y. (2014). A purely structural restoration of the NFP20-East cross section and potential tectonic overpressure in the Adula nappe (central Alps). *Tectonics*, 33(5), 656–685. <https://doi.org/10.1002/2013TC003409>
- Preiswerk, H. (1918). Geologische Beschreibung der Lepontinischen Alpen, zweiter Teil: oberes Tessin- und Maggiagebiet. *Beiträge Zur Geologischen Karte Der Schweiz*, 26.
- Ramsay, J. G. (1980). Shear zone geometry: a review. *Journal of structural geology*, 2(1–2), 83–99. [https://doi.org/10.1016/0191-8141\(80\)90038-3](https://doi.org/10.1016/0191-8141(80)90038-3)
- Reverdatto, V. V., & Polyansky, O. P. (2004). Modelling of the thermal history of metamorphic zoning in the Connemara region (western Ireland). *Tectonophysics*, 379, 77–91. <https://doi.org/10.1016/j.tecto.2003.10.005>
- Ring, U., & Glodny, J. (2021). The importance of tangential motion in the Central Alps: Kinematic analysis and RbSr dating of mylonitic rocks from the Pennine nappes in the eastern Central Alps. *Earth-Science Reviews*, 218, 103644. <https://doi.org/10.1016/j.earscirev.2021.103644>
- Rosenbaum, G., & Lister, G. S. (2005). The Western Alps from the Jurassic to Oligocene: Spatio-temporal constraints and evolutionary reconstructions. *Earth-Science Reviews*, 69(3–4), 281–306. <https://doi.org/10.1016/j.earscirev.2004.10.001>

- Rosenberg, C. L., Bellahsen, N., Rabaute, A., & Girault, J. B. (2021). Distribution, style, amount of collisional shortening, and their link to Barrovian metamorphism in the European Alps. *Earth-Science Reviews*, 222, 103774. <https://doi.org/10.1016/j.earscirev.2021.103774>
- Rosenberg, C. L., & Kissling, E. (2013). Three-dimensional insight into Central-Alpine collision: Lower-plate or upper-plate indentation? *Geology*, 41(12), 1219–1222. <https://doi.org/10.1130/G34584.1>
- Ryan, P. D., & Dewey, J. F. (2019). The sources of metamorphic heat during collisional orogeny: the Barrovian enigma. *Canadian Journal of Earth Sciences*, 56(12), 1309–1317. <https://doi.org/10.1139/cjes-2018-0182>
- Rubatto, D. (2002). Zircon trace element geochemistry: Partitioning with garnet and the link between U–Pb ages and metamorphism. *Chemical Geology*, 184(1–2), 123–138. [https://doi.org/10.1016/s0009-2541\(01\)00355-2](https://doi.org/10.1016/s0009-2541(01)00355-2)
- Rubatto, D., & Hermann, J. (2007). Experimental zircon/melt and zircon/garnet trace element partitioning and implications for the geochronology of crustal rocks. *Chemical Geology*, 241(1–2), 38–61. <https://doi.org/10.1016/j.chemgeo.2007.01.027>
- Rubatto, D., Hermann, J., Berger, A., & Engi, M. (2009). Protracted fluid-induced melting during Barrovian metamorphism in the Central Alps. *Contributions to Mineralogy and Petrology*, 158(6), 703–722. <https://doi.org/10.1007/s00410-009-0406-5>
- Ruiz, M., Schaltegger, U., Gaynor, S. P., Chiaradia, M., Abrecht, J., Gisler, C., Giovanoli, F., & Wiederkehr, M. (2022). Reassessing the intrusive tempo and magma genesis of the late Variscan Aar batholith: U–Pb geochronology, trace element and initial Hf isotope composition of zircon. *Swiss Journal of Geosciences*, 115(1), 1–24.
- Rutter, E. H., & Brodie, K. H. (1988). The role of tectonic grain size reduction in the rheological stratification of the lithosphere. *Geologische Rundschau*, 77, 295–307. <https://doi.org/10.1007/BF01848691>
- Rütti, R. (2001). Tectono-metamorphic evolution of the Simano-Adula nappe boundary, Central Alps, Switzerland. *Schweizerische Mineralogische Und Petrographische Mitteilungen*, 81(1), 115–129.
- Rütti, R. (2003). The tectono-metamorphic evolution of the northwestern Simano Nappe (Central Alps, Switzerland) (Doctoral dissertation, ETH Zurich).

- Rütti, R., Marquer, D., & Thompson, A. B. (2008). Tertiary tectono-metamorphic evolution of the European margin during Alpine collision: Example of the Leventina Nappe (Central Alps, Switzerland). *Swiss Journal of Geosciences*, *101*(Suppl. 1), 157–171.
<https://doi.org/10.1007/s00015-008-1278-9>
- Rütti, R., Maxelon, M., & Mancktelow, N. S. (2005). Structure and kinematics of the northern Simano Nappe, Central Alps, Switzerland. *Eclogae Geologicae Helvetiae*, *98*(1), 63–81.
<https://doi.org/10.1007/s00015-005-1148-7>
- Sandmann, S., Nagel, T. J., Herwartz, D., Fonseca, R. O. C., Kurzwski, R. M., Münker, C., & Froitzheim, N. (2014). Lu–Hf garnet systematics of a polymetamorphic basement unit: New evidence for coherent exhumation of the Adula Nappe (Central Alps) from eclogite-facies conditions. *Contributions to Mineralogy and Petrology*, *168*(5), 1–21.
<https://doi.org/10.1007/s00410-014-1075-6>
- Sawyer, E. W. (2008). *Atlas of migmatites* (Vol. 9, p. 371). The Canadian Mineralogist Special Publication, NRC Research Press.
- Scambelluri, M., Pettke, T., Rampone, E., Godard, M., & Reusser, E. (2014). Petrology and trace element budgets of high-pressure peridotites indicate subduction dehydration of serpentinized mantle (Cima di Gagnone, Central Alps, Switzerland). *Journal of Petrology*, *55*(3), 459–498.
<https://doi.org/10.1093/petrology/egt068>
- Schaltegger, U., Gebauer, D., & Von Quadt, A. (2002). The mafic-ultramafic rock association of Loderio-Biasca (lower Pennine nappes, Ticino, Switzerland): Cambrian oceanic magmatism and its bearing on early Paleozoic paleogeography. *Chemical Geology*, *186*(3–4), 265–279.
[https://doi.org/10.1016/S0009-2541\(02\)00005-0](https://doi.org/10.1016/S0009-2541(02)00005-0)
- Schaltegger, U., Wotzlaw, J. F., Ovtcharova, M., Chiaradia, M., & Spikings, R. (2014). Mass spectrometry in Earth sciences: the precise and accurate measurement of time. *Chimia*, *68*(3), 124–128.
- Schenker, F. L. (2013). Thermo-mechanical evolution of the Pelagonian Gneiss Dome (Greece): Insights from numerical modeling and new geological and geochronological data (Doctoral dissertation, ETH Zurich).
- Schenker, F. L., Gerya, T., & Burg, J. P. (2012). Bimodal behavior of extended continental lithosphere: Modeling insight and application to thermal history of migmatitic core complexes. *Tectonophysics*, *579*, 88–103. <https://doi.org/10.1016/j.tecto.2012.07.002>

- Schenker, F. L., Schmalholz, S. M., Moulas, E., Pleuger, J., Baumgartner, L. P., Podladchikov, Y. Y., Vrijmoed, J., Buchs, N., & Müntener, O. (2015). Current challenges for explaining (ultra)high-pressure tectonism in the Pennine domain of the Central and Western Alps. *Journal of Metamorphic Geology*, 33(8), 869–886. <https://doi.org/10.1111/jmg.12143>
- Schlunegger, F., & Kissling, E. (2015). Slab rollback orogeny in the Alps and evolution of the Swiss Molasse basin. *Nature Communications*, 6(1), 8605. <https://doi.org/10.1038/ncomms9605>
- Schlunegger, F., & Willett, S. (1999). Spatial and temporal variations in exhumation of the central Swiss Alps and implications for exhumation mechanisms. *Geological Society, London, Special Publications*, 154(1), 157–179. <https://doi.org/10.1144/GSL.SP.1999.154.01.07>
- Schmalholz, S. M., & Duretz, T. (2015). Shear zone and nappe formation by thermal softening, related stress and temperature evolution, and application to the Alps. *Journal of Metamorphic Geology*, 33(8), 887–908. <https://doi.org/10.1111/jmg.12137>
- Schmalholz, S. M., Duretz, T., Schenker, F. L., & Podladchikov, Y. Y. (2014). Kinematics and dynamics of tectonic nappes: 2-D numerical modelling and implications for high and ultra-high pressure tectonism in the Western Alps. *Tectonophysics*, 631(C), 160–175. <https://doi.org/10.1016/j.tecto.2014.05.018>
- Schmalholz, S. M., & Podladchikov, Y. Y. (2013). Tectonic overpressure in weak crustal-scale shear zones and implications for the exhumation of high-pressure rocks. *Geophysical Research Letters*, 40(10), 1984–1988. <https://doi.org/10.1002/grl.50417>
- Schmalholz, S. M., & Schenker, F. L. (2016). Exhumation of the Dora Maira ultrahigh-pressure unit by buoyant uprising within a low-viscosity mantle oblique-slip shear zone. *Terra Nova*, 28(5), 348–355. <https://doi.org/10.1111/ter.12227>
- Schmid, S. M., Fügenschuh, B., Kissling, E., & Schuster, R. (2004). Tectonic map and overall architecture of the Alpine orogen. *Eclogae Geologicae Helvetiae*, 97(1), 93–117. <https://doi.org/10.1007/s00015-004-1113-x>
- Schmid, S. M., Pfiffner, O. A., Froitzheim, N., Schönborn, G., & Kissling, E. (1996). Geophysical-geological transect and tectonic evolution of the Swiss-Italian Alps. *Tectonics*, 15(5), 1036–1064. <https://doi.org/10.1029/96tc00433>
- Schmid, S. M., Rück, P., & Schreurs, G. (1990). The significance of the Schams nappes for the reconstruction of the paleotectonic and orogenic evolution of the Penninic zone along the NFP-20 East traverse (Grisons, eastern Switzerland). *Mémoires de la Société géologique de France (1833)*, 156, 263–287.

- Schorn, S., Diener, J. F., Powell, R., & Stüwe, K. (2018). Thermal buffering in the orogenic crust. *Geology*, *46*(7), 643–646. <https://doi.org/10.1130/G40246.1>
- Sharma, R. S. (1969). On banded gneisses and migmatites from Lavertezzo and Rozzera (Val Verzasca, Ticino). *Schweizerische Mineralogische Und Petrographische Mitteilungen*, *49*, 199–276.
- Siiivola, J., & Schmid, R., 2007. A Systematic Nomenclature for Metamorphic Rocks 12. List of Mineral Abbreviations. *Recommendations by the IUGS Subcommittee on the Systematics of Metamorphic Rocks*.
- Sláma, J., Košler, J., Condon, D. J., Crowley, J. L., Gerdes, A., Hanchar, J. M., Horstwood, M. S. A., Morris, G. A., Nasdala, L., & Norberg, N. (2008). Plešovice zircon—A new natural reference material for U–Pb and Hf isotopic microanalysis. *Chemical Geology*, *249*(1–2), 1–35. <https://doi.org/10.1016/j.chemgeo.2007.11.005>
- Smit, M. A., Scherer, E. E., & Mezger, K. (2013). Lu–Hf and Sm–Nd garnet geochronology: chronometric closure and implications for dating petrological processes. *Earth and Planetary Science Letters*, *381*, 222–233. <https://doi.org/10.1016/j.epsl.2013.08.046>
- Smye, A. J., & England, P. C. (2022). Metamorphism and deformation on subduction interfaces: 2. Petrological and tectonic implications. *Geochemistry, Geophysics, Geosystems*, *24*(1), e2022GC010645. <https://doi.org/10.1029/2022GC010645>
- Souche, A., Medvedev, S., Andersen, T. B., & Dabrowski, M. (2013). Shear heating in extensional detachments: Implications for the thermal history of the Devonian basins of W Norway. *Tectonophysics*, *608*, 1073–1085. <https://doi.org/10.1016/j.tecto.2013.07.005>
- Spear, F. S. (1993). Metamorphic phase equilibria and pressure-temperature-time paths. *Mineralogical Society of America Monograph*, *799*, 352–356.
- Spear, F. S., & Florence, F. P. (1992). Thermobarometry in granulites: pitfalls and new approaches. *Precambrian Research*, *55*(1–4), 209–241. [https://doi.org/10.1016/0301-9268\(92\)90025-J](https://doi.org/10.1016/0301-9268(92)90025-J)
- Stampfli, G. M., Mosar, J., Marquer, D., Marchant, R., Baudin, T., & Borel, G. (1998). Subduction and obduction processes in the Swiss Alps. *Tectonophysics*, *296*(1–2), 159–204. [https://doi.org/10.1016/S0040-1951\(98\)00142-5](https://doi.org/10.1016/S0040-1951(98)00142-5)
- Steck, A. (1998). The Maggia cross-fold: An enigmatic structure of the lower Penninic nappes of the Lepontine Alps. *Eclogae Geologicae Helvetiae*, *91*, 333–343.

- Steck, A., Della Torre, F., Keller, F., Pfeifer, H. R., Hunziker, J., & Masson, H. (2013). Tectonics of the Lepontine Alps: Ductile thrusting and folding in the deepest tectonic levels of the Central Alps. *Swiss Journal of Geosciences*, *106*(3), 427–450.
<https://doi.org/10.1007/s00015-013-0135-7>
- Steck, A., Epard, J. L., & Masson, H. (2019). The Maggia nappe: An extruding sheath fold basement nappe in the Lepontine gneiss dome of the Central Alps. *International Journal of Earth Sciences*, *108*(8), 2429–2442. <https://doi.org/10.1007/s00531-019-01771-1>
- Steck, A., & Hunziker, J. (1994). The Tertiary structural and thermal evolution of the Central Alps—Compressional and extensional structures in an orogenic belt. *Tectonophysics*, *238*(1–4), 229–254. [https://doi.org/10.1016/0040-1951\(94\)90058-2](https://doi.org/10.1016/0040-1951(94)90058-2)
- Steffen, K., Selverstone, J., & Brearley, A. (2001). Episodic weakening and strengthening during synmetamorphic deformation in a deep-crustal shear zone in the Alps. *Geological Society, London, Special Publications*, *186*, 141–156. <https://doi.org/10.1144/GSL.SP.2001.186.01.09>
- Steiger, R. H. (1983). Isotopic dating of metamorphic events in the central Alps. *Terra Cognita*, *3*, p. 140.
- Steiger, R. H., & Bucher, I. (1978). Are Rb-Sr biotite ages in the central Alps necessarily cooling ages? In *Fourth International Conference, Geochronology, Cosmochronology, Isotope Geology*, U.S. Geological Survey, Open file report, 414-415.
- Steiner, H. (1984). Radiometrische alterbestimmungen an gesteinen der Maggia-decke (Penninikum der Zentralalpen). *Schweizerische Mineralogische Und Petrographische Mitteilungen*, *64*(1–2), 227–259.
- Steinitz, G., & Jäger, E. (1981). Rb-Sr and K-Ar studies on rocks from the Suretta nappe, eastern Switzerland. *Schweizerische Mineralogische und Petrographische Mitteilungen*, *61*, 121-31.
- Stipp, M., Stünitz, H., Heilbronner, R., & Schmid, S. M. (2002). The eastern Tonale fault zone: A “natural laboratory” for crystal plastic deformation of quartz over a temperature range from 250 to 700 °C. *Journal of Structural Geology*, *24*(12), 1861–1884.
[https://doi.org/10.1016/s0191-8141\(02\)00035-4](https://doi.org/10.1016/s0191-8141(02)00035-4)
- Stöckhert, B., & Gerya, T. V. (2005). Pre-collisional high pressure metamorphism and nappe tectonics at active continental margins: A numerical simulation. *Terra Nova*, *17*(2), 102–110.
<https://doi.org/10.1111/j.1365-3121.2004.00589.x>

- Stüwe, K. (1998). Heat sources of Cretaceous metamorphism in the Eastern Alps – a discussion. *Tectonophysics*, 287, 251–269. [https://doi.org/10.1016/S0040-1951\(98\)80072-3](https://doi.org/10.1016/S0040-1951(98)80072-3)
- Stüwe, K. (2002). Geodynamics of the Lithosphere. *Berlin, Springer* (pp. 449). <https://doi.org/10.1007/978-3-662-04980-8>
- Stüwe, K., & Ehlers, K. (1998). Distinguishing Cooling Histories using Thermometry: Interpretations of Cooling Curves with some Examples from the Glein-Koralpe Region and the Central Swiss Alps. *Mitteilungen der Österreichischen Geologischen Gesellschaft*, 89, 201–212.
- Swiss National Map n°1273 – Biasca (1:25.000). *swisstopo*.
- Swiss National Map n°1293 – Osogna (1:25.000). *swisstopo*.
- Swiss National Map n°1294 – Grono (1:25.000). *swisstopo*.
- Tagliaferri, A., Schenker, F. L., Ulianov, A., Maino, M., & Schmalholz, S. M. (2023). Implications of new geological mapping and U-Pb zircon dating for the Barrovian tectono-metamorphic evolution of the Lepontine dome (Central European Alps). *Geochemistry, Geophysics, Geosystems*, 24, e2022GC010772. <https://doi.org/10.1029/2022GC010772>
- Tajčmanová, L., Manzotti, P., & Alvaro, M. (2021). Under pressure: High-pressure metamorphism in the Alps. *Elements*, 17(1), 17–22. <https://doi.org/10.2138/GSELEMENTS.17.1.17>
- Teipel, U., Eichhorn, R., Loth, G., Rohrmüller, J., Höll, R., & Kennedy, A. (2004). U-Pb SHRIMP and Nd isotopic data from the western Bohemian massif (Bayerischer Wald, Germany): Implications for upper Vendian and lower Ordovician magmatism. *International Journal of Earth Sciences*, 93(5), 782–801. <https://doi.org/10.1007/s00531-004-0419-2>
- Theune, U. (2023). Ternary Plots. *MATLAB Central File Exchange*. Retrieved September 13, 2023. <https://www.mathworks.com/matlabcentral/fileexchange/7210-ternary-plots>
- Thielmann, M., Rozel, A., Kaus, B. J. P., & Ricard, Y. (2015). Intermediate-depth earthquake generation and shear zone formation caused by grain size reduction and shear heating. *Geology*, 43(9), 791–794. <https://doi.org/10.1130/G36864.1>
- Thigpen, J. R., Ashley, K. T., & Law, R. D. (2017). Evaluating kinematic displacement rate effects on transient thermal processes in thrust belts using coupled thermomechanical finite-element models. *Geological Society of America, Memoirs*, 213, 1–23.

- Thigpen, J. R., Ashley, K. T., Mako, C., Law, R. D., & Spencer, B. (2021). Interplay between crustal-scale thrusting, high metamorphic heating rates, and the development of inverted thermal-metamorphic gradients: Numerical models and examples from the Caledonides of Northern Scotland. *Tectonics*, *40*(11), 1–24. <https://doi.org/10.1029/2021TC006716>
- Thompson, A. B., & England, P. C. (1984). Pressure—temperature—time paths of regional metamorphism II. Their inference and interpretation using mineral assemblages in metamorphic rocks. *Journal of Petrology*, *25*(4), 929–955. <https://doi.org/10.1093/petrology/25.4.929>
- Thompson, A. B., & Ridley, J. R. (1987). Pressure—temperature—time (P—T—t) histories of orogenic belts. *Philosophical Transactions of the Royal Society of London - Series A: Mathematical and Physical Sciences*, *321*(1557), 27–45.
- Tilley, C. E. (1925). A preliminary survey of metamorphic zones in the southern Highlands of Scotland. *Quarterly Journal of the Geological Society*, *81*(1–4), 100–112. <https://doi.org/10.1144/gsl.jgs.1925.081.01-04.05>
- Todd, C. S., & Engi, M. (1997). Metamorphic field gradients in the Central Alps. *Journal of Metamorphic Geology*, *15*(4), 513–530. <https://doi.org/10.1111/j.1525-1314.1997.00038.x>
- Tracy, R. J., Robinson, P., & Thompson, A. B. (1976). Garnet composition and zoning in the determination of temperature and pressure of metamorphism, central Massachusetts. *American Mineralogist* *61*, 762–775.
- Trail, D., Watson, E. B., & Tailby, N. D. (2012). Ce and Eu anomalies in zircon as proxies for the oxidation state of magmas. *Geochimica et Cosmochimica Acta*, *97*, 70–87. <https://doi.org/10.1016/j.gca.2012.08.032>
- Trommsdorff, V. (1974). Alpine metamorphism of peridotitic rocks. *Schweizerische Mineralogische Und Petrographische Mitteilungen*, *54*, 333–352.
- Trommsdorff, V. (1990). Metamorphism and tectonics in the Central Alps: The Alpine lithospheric mélange of Cima Lunga and Adula. *Memorie Della Società Geologica Italiana*, *45*, 39–49.
- Trommsdorff, V., Hermann, J., Müntener, O., Pfiffner, M., & Risold, A. C. (2000). Geodynamic cycles of subcontinental lithosphere in the Central Alps and the Arami enigma. *Journal of Geodynamics*, *30*(1–2), 77–92. [https://doi.org/10.1016/S0264-3707\(99\)00028-9](https://doi.org/10.1016/S0264-3707(99)00028-9)
- Trümpy, R. (1973). The timing of orogenic events in the Central Alps. *Gravity and tectonics*, 287, 301.

- Tumiati, S., Zanchetta, S., Pellegrino, L., Ferrario, C., Casartelli, S., & Malaspina, N. (2018). Granulite-facies overprint in garnet peridotites and kyanite eclogites of Monte Duria (Central Alps, Italy): Clues from srilankite- and sapphirine-bearing symplectites. *Journal of Petrology*, 59(1), 115–152. <https://doi.org/10.1093/petrology/egy021>
- Turcotte, D. L., & Schubert, G. (2014). *Geodynamics* (3rd ed.). Cambridge University Press.
- Ulianov, A., Müntener, O., Schaltegger, U., & Bussy, F. (2012). The data treatment dependent variability of U-Pb zircon ages obtained using mono-collector, sector field, laser ablation ICP-MS. *Journal of Analytical and Atomic Spectrometry*, 27(4), 663–676. <https://doi.org/10.1039/c2ja10358c>
- Ulianov, A., Müntener, O., & Schaltegger, U. (2015). The ICPMS signal as a Poisson process: a review of basic concepts. *Journal of Analytical Atomic Spectrometry*, 30(6), 1297–1321.
- Vance, J. A. (1961). Polysynthetic twinning in plagioclase. *American Mineralogist*, 46(9–10), 1097–1119.
- Vaughan-Hammon, J. D., Candiotti, L. G., Duretz, T., & Schmalholz, S. M. (2022). Metamorphic facies distribution in the Western Alps predicted by petrological–thermomechanical models of syn-convergent exhumation. *Geochemistry, Geophysics, Geosystems*, 23(8), e2021GC009898. <https://doi.org/10.1029/2021GC009898>
- Vavra, G., Schmid, R., & Gebauer, D. (1999). Internal morphology, habit and U-Th-Pb microanalysis of amphibolite-to-granulite facies zircons: Geochronology of the Ivrea Zone (Southern Alps). *Contributions to Mineralogy and Petrology*, 134(4), 380–404. <https://doi.org/10.1007/s004100050492>
- Vermeesch, P. (2018). IsoplotR: A free and open toolbox for geochronology. *Geoscience Frontiers*, 9(5), 1479–1493. <https://doi.org/10.1016/j.gsf.2018.04.001>
- Viete, D. R. (2008). The nature and origin of regional metamorphism: observations from the Barrovian metamorphic series of Scotland.
- Viete, D. R., Hermann, J., Lister, G. S., & Stenhouse, I. R. (2011). The nature and origin of the Barrovian metamorphism, Scotland: diffusion length scales in garnet and inferred thermal time scales. *Journal of the Geological Society*, 168(1), 115–132. <https://doi.org/10.1144/0016-76492009-087>
- Von Blanckenburg, F., & Davies, J. H. (1995). Slab breakoff: A model for syncollisional magmatism and tectonics in the Alps. *Tectonics*, 14, 120–131. <https://doi.org/10.1029/94TC02051>

- Vonlanthen, P., Gerald, J. D. F., Rubatto, D., & Hermann, J. (2012). Recrystallization rims in zircon (Valle d'Arbedo, Switzerland): An integrated cathodoluminescence, LA-ICP-MS, SHRIMP, and TEM study. *American Mineralogist*, *97*(2–3), 369–377.
<https://doi.org/10.2138/am.2012.3854>
- Wenk, E. (1955). Eine Strukturkarte der Tessiner Alpen. *Schweizerische Mineralogische Und Petrographische Mitteilungen*, *35*, 311–319.
- Wenk, E., & Keller, F. (1969). Isograde in Amphibolitserien der Zentralalpen. *Schweizerische Mineralogische Und Petrographische Mitteilungen*, *49*, 157–198.
- Weyer, S., Jarick, J., & Mezger, K. (1999). Quantitative temperature-time information from retrograde diffusion zoning in garnet: constraints for the P–T–t history of the Central Black Forest, Germany. *Journal of Metamorphic Geology* *17*, 449–461.
<https://doi.org/10.1046/j.1525-1314.1999.00207.x>
- Wiederkehr, M. (2009). From subduction to collision: a combined metamorphic, structural and geochronological study of polymetamorphic metasediments at the NE edge of the Lepontine dome (Swiss central Alps), Ph.D. thesis, Univ. Basel, Basel.
http://edoc.unibas.ch/diss/DissB_8635
- Wiederkehr, M., Bousquet, R., Schmid, S. M., & Berger, A. (2008). From subduction to collision: Thermal overprint of HP/LT meta-sediments in the north-eastern Lepontine Dome (Swiss Alps) and consequences regarding the tectono-metamorphic evolution of the Alpine orogenic wedge. *Swiss Journal of Geosciences*, *101*(Suppl. 1), 127–155.
<https://doi.org/10.1007/s00015-008-1289-6>
- Wiederkehr, M., Bousquet, R., Ziemann, M. A., Berger, A., & Schmid, S. M. (2011). 3-D assessment of peak-metamorphic conditions by Raman spectroscopy of carbonaceous material: An example from the margin of the Lepontine dome (Swiss Central Alps). *International Journal of Earth Sciences*, *100*(5), 1029–1063. <https://doi.org/10.1007/s00531-010-0622-2>
- Wiederkehr, M., Sudo, M., Bousquet, R., Berger, A., & Schmid, S. M. (2009). Alpine orogenic evolution from subduction to collisional thermal overprint: The $^{40}\text{Ar}/^{39}\text{Ar}$ age constraints from the Valaisan Ocean, central Alps. *Tectonics*, *28*(6), TC6009.
<https://doi.org/10.1029/2009TC002496>
- Winter, J. D. (2013). *Principles of igneous and metamorphic petrology*. Pearson Education.

- Wölfler, A., Wolff, R., Hampel, A., Hetzel, R., & Dunkl, I. (2023). Phases of enhanced exhumation during the Cretaceous and Cenozoic orogenies in the Eastern European Alps: New insights from thermochronological data and thermokinematic modeling. *Tectonics*, *42*, e2022TC007698. <https://doi.org/10.1029/2022TC007698>
- Yakymchuk, C., Kirkland, C. L., & Clark, C. (2018). Th/U ratios in metamorphic zircon. *Journal of Metamorphic Geology*, *36*(6), 715–737. <https://doi.org/10.1111/jmg.12307>
- Yuen, D. A., Fleitout, L., Schubert, G., & Froidevaux, C. (1978). Shear deformation zones along major transform faults and subducting slabs. *Geophysical Journal of the Royal Astronomical Society*, *54*(1), 93–119. <https://doi.org/10.1111/j.1365-246X.1978.tb06758.x>
- Zanchetta, S., Garzanti, E., Doglioni, C., & Zanchi, A. (2012). The Alps in the Cretaceous: A doubly vergent pre-collisional orogen. *Terra Nova*, *24*(5), 351–356. <https://doi.org/10.1111/j.1365-3121.2012.01071.x>

Curriculum vitae

ALESSIA TAGLIAFERRI



Alessia Tagliaferri

PhD candidate in geology

PROFILE

ORCID: orcid.org/0000-0002-2016-0330

Google Scholar: [Alessia Tagliaferri - Google Scholar](#)

LinkedIn : www.linkedin.com/in/alessia-tagliaferri-826430a0

Researchgate: <https://www.researchgate.net/profile/Alessia-Tagliaferri>

LANGUAGES

Italian: mother language – English: fluent – French: fluent –
German: beginner

CONTACT

+41 798919570

alessia.tagliaferri@supsi.ch

Lugano (CH)

FORMATION

2019 – 2023
Mendrisio (CH)

Scuola Universitaria Professionale della Svizzera Italiana (SUPSI)
PhD student in geology

2019 – 2023
Lausanne (CH)

Université de Lausanne (UNIL)
PhD student in geology

2013–2019
Milano (IT)

Università degli Studi di Milano Statale (UNIMI)
Student in Earth Sciences

2008–2013
Lecco (IT)

Liceo Scientifico G. B. Grassi Lecco
Student

UNIVERSITY DEGREE

2016–2019
Milano (IT)

Università degli Studi di Milano Statale (UNIMI)
Master Degree in Earth Sciences

Thesis title: Rilevamento geologico e analisi strutturale multiscale del basamento Varisico e delle metacoperture post-Varisiche, Laghi del Frisson; Massiccio dell'Argentera, Alpi Marittime (*Geological Fieldwork and Multiscale Structural Analysis of Variscan Basement and Post-Variscan Meta-covers, Frisson Lakes; Argentera Massif, Maritime Alps*). Supervision of Prof. Maria Iole Spalla and Prof. Michele Zucali.

2013–2016
Milano (IT)

Università degli Studi di Milano Statale (UNIMI)
Bachelor Degree in Earth Sciences

Thesis title: Correzione topografica e anomalie di gravità nel Tirreno meridionale (*Topographic Correction and Gravity Anomalies in the Southern Tyrrhenian Sea*). Supervision of Prof. Anna Maria Marotta.

ACADEMIC EXPERIENCE

2019 – 2023
Switzerland (CH)

Scuola Universitaria Professionale della Svizzera Italiana (SUPSI)
Université de Lausanne (UNIL)
PhD student in geology
Supervision of Dr. Filippo Luca Schenker and Prof. Stefan Markus Schmalholz.

EXPERIENCE OUTSIDE ACADEMIA

2017–2018
(4 months)
Milano (IT)

Traineeship (UNIMI)
Schlumberger Srl

- Building of a sound static 3D geologic model (based on seismic sections) with Petrel software.
- Teamwork in the Oil&Gas Industry.

COMPETENCES

- **Fieldwork and geological mapping :**

Fieldwork and geological survey at scale 1:2.000 to produce geological-structural maps at scale 1:4.000. Fieldwork and geological survey at scale 1:10.000 for swisstopo to produce the Swiss National Maps 1:25.000. Data elaboration in QGIS, ArcMap, ArcGIS Pro and utilization of geodata from swisstopo. Use of vector and raster data, DEM, hillshade; digitalization of points, lines, areas; georeferencing; working with table datasets. Realization of geological sections.

- **Structural geology :**

Multiscale structural analysis: measure of faults, foliation, lineation, fractures, veins in the field (meso-scale) and study of their relationship with the overall geology of a studied area (macro-scale); deformation mechanisms at the thin section scale (micro-scale) and relation to mineral blastesis.

Basics of statistical structural analysis: use of WinTensor (basic user) and Stereonet softwares.

- **Geochemistry :**

Electron Probe Micro-Analyser (EPMA) to obtain the composition in oxides of mineral phases under the form of point, line, or map analyses.

Laser Ablation Inductively-Coupled Plasma Mass Spectrometry (LA-ICP-MS) to analyze trace element composition in minerals.

- **Petrology :**

Knowledge of metamorphic petrology and application of thermobarometric estimates. Use of different geothermometers and geobarometers, and Perple_X.

- **Geochronology :**

U-Pb dating on zircon crystals with LA-ICP-MS and SwissSIMS ion probe to assess the absolute age of metamorphic rocks.

Use of Scanning Electron Microscope (SEM) to produce images in cathodoluminescence (and related analysis of zircon internal textures as preparation for zircon dating).

Use of Lamtrace software and IsoplotR for U-Pb data treatment.

- **Numerical modelling :**

Thermo-kinematic numerical modelling with Matlab.

Basic knowledge of Fortran Programming Language and Generic Mapping Tools (GMT).

- **Scientific communication :**

Attending to scientific conferences and presentation of my work (oral and poster presentation).

- **Other Software :**

Adobe suite; Microsoft Office 365; Mendeley; XMapTools; Petrel; Octave.

AWARDS

- 2023 – Lausanne (CH) Bourse doctorale Société Académique Vaudoise
- 2023 – Wien (AT) OSPP (Outstanding Student and PhD candidate Presentation)
Award EGU General Assembly 2023
- 2023 Humboldt Post-Doc fellowship (starting in June 2024)

SCIENTIFIC COLLABORATIONS

Ongoing:

Tagliaferri, A., Moulas, E., Schenker, F. L., Schmalholz, S. M. – Scuola universitaria professionale della Svizzera italiana (SUPSI), Université de Lausanne (UNIL), Johannes Gutenberg Universität Mainz (JGU)

Tagliaferri, A., Schenker, F. L., Maino, M., Corvò, S. – Scuola universitaria professionale della Svizzera italiana (SUPSI), Université de Lausanne (UNIL), Università di Pavia (UNIPV)

Tagliaferri, A., Pigazzi, E., Schenker, F. L., Tartarotti, P. – Scuola universitaria professionale della Svizzera italiana (SUPSI), Université de Lausanne (UNIL), Università degli Studi di Milano Statale (UNIMI)

Finished:

Tagliaferri, A., Fassmer, K. – Scuola universitaria professionale della Svizzera italiana (SUPSI), Université de Lausanne (UNIL), Universität Innsbruck

SCIENTIFIC PUBLICATIONS

Publications with peer review process:

Tagliaferri, A.*, Schenker, F. L., Ulianov, A., Maino, M., & Schmalholz, S. M. (2023). Implications of new geological mapping and U-Pb zircon dating for the Barrovian tectono-metamorphic evolution of the Lepontine dome (Central European Alps). *Geochemistry, Geophysics, Geosystems*, 24, e2022GC010772. <https://doi.org/10.1029/2022GC010772>

Publications under review for peer review journals:

Tagliaferri, A.*, Moulas, E., Schmalholz, S. M., & Schenker, F. L. (in review). Fast and spatially heterogeneous cooling rates at amphibolite-facies conditions reveal the significance of local heat sources: a case study from the Lepontine Alps (Switzerland). *American Journal of Science*.

Corvò, S.*, Maino, M., Langone, A., Schenker F. L., **Tagliaferri, A.**, Perozzo, M., Casini, L., & Seno, S. (in review). Monazite and zircon U-(Th-)Pb dating reveal multiple episodes of HT metamorphism in the Cima Lunga unit (Central Alps): implications for the exhumation of high-pressure rocks. *International Journal of Geosciences*.

SCIENTIFIC CONFERENCES

Tagliaferri, A.*, Moulas, E., Schmalholz, S. M., Schenker, F. L. (2023). Garnet multi-component diffusion modelling reveals local heat sources affecting the cooling history of the Lepontine dome. 21st Swiss Geoscience Meeting 2023, Mendrisio.

Pigazzi, E.*, Morandi, S., **Tagliaferri, A.**, Arrigoni, F., Schenker, F. L., Tartarotti, P. (2023). An analysis of the peak-temperature recorded by the meta-sedimentary covers of the Central Alps using Raman spectroscopy. 21st Swiss Geoscience Meeting 2023, Mendrisio.

Maino, M.*, Corvò, S., Schenker, F. L., Perozzo, M., **Tagliaferri, A.**, Seno, S., & Langone, A. (2023). Deformation-induced changes in the metamorphic record along rheologically contrasted boundaries: inferences from Cima di Gagnone (Cima Lunga unit, Central Alps). 21st Swiss Geoscience Meeting 2023, Mendrisio.

Tagliaferri, A.*, Moulas, E., Schmalholz, S. M., & Schenker, F. L. (2023). Revealing the cooling history of the Lepontine dome: insights from garnet multicomponent-diffusion modeling. GSA connects 2023, 15th-18th October 2023, Pittsburgh, Pennsylvania.

<https://gsa.confex.com/gsa/2023AM/meetingapp.cgi/Paper/392463>

In Geological Society of America Abstracts with Programs. Vol. 55, No. 6, 2023. doi: 10.1130/abs/2023AM-392463.

Schenker, F. L.* , **Tagliaferri, A.**, Maino, M., Perozzo, M., Castelletti, C., Giacomazzi, D., Vandelli, A., Wennubst, R., Gouffon, Y., & Ambrosi, C. (2023) Dynamics of a crustal-scale shear zone in the Central European Alps. GSA connects 2023, 15th-18th October 2023, Pittsburgh, Pennsylvania.

<https://gsa.confex.com/gsa/2023AM/meetingapp.cgi/Paper/392493>

In Geological Society of America Abstracts with Programs. Vol. 55, No. 6, 2023. doi: 10.1130/abs/2023AM-392493.

Tagliaferri, A.*, Moulas, E., Schmalholz, S. M., & Schenker, F. L. (2023). Garnet compositional re-adjustment: cooling rate constraint in metapelites from the Lepontine dome (Central European Alps) (No. EGU23-9052). Copernicus Meetings. In Abstract proceedings EGU General Assembly 2023.

Schenker, F. L.* , Maino, M., **Tagliaferri, A.**, Perozzo, M., Castelletti, C., Giacomazzi, D., Vandelli, A., Wennubst, R., Gouffon, Y., & Ambrosi, C. (2022) 3D reconstruction of the sole shear zone of the Adula nappe and its repercussion on the Alpine regional geology. 20th Swiss Geoscience Meeting 2022, Lausanne.

Tagliaferri, A.*, Schenker, F. L., Schmalholz, S. M. & Ulianov, A. (2022) Geological mapping and U-Pb dating of detrital and magmatic zircon crystals in the Lepontine dome (Central European Alps). 20th Swiss Geoscience Meeting 2022, Lausanne.

Tagliaferri, A.*, Schenker, F. L., Schmalholz, S. M., Ulianov, A. & Seno S. (2022) Investigating the time of deformation and heat transfer in the Lepontine Dome (Central European Alps). Congresso della Società Geologica Italiana 2022, Torino.

Tagliaferri, A.*, Schenker, F. L., Schmalholz, S. M., Ulianov, A. & Seno S. (2022) LA-ICP-MS U-Pb dating on zircons from the Lepontine Dome (Central European Alps). EGU General Assembly 2022, Wien.

Tagliaferri, A.*, Schenker, F. L., Schmalholz, S. M. & Ulianov, A. (2021) LA-ICPMS U-Pb dating on zircons from the Lepontine Dome (Central European Alps). 19th Swiss Geoscience Meeting 2021, Genève.

Tagliaferri, A.*, Schenker, F. L., Schmalholz, S. M. & Ulianov, A. (2021) LA-ICPMS U-Pb dating on zircons from the Lepontine Dome (Central European Alps). DPMS Meeting 2021, Programme doctoral en Sciences des Minéraux (CUSO : Conférence Universitaire de Suisse Occidentale), Fribourg.

Tagliaferri, A.*, Schmalholz, S. M. & Schenker, F. L. (2021) Investigating heat transfer through the Lepontine Dome (Central European Alps) with a combined petrological, structural, dating and modelling approach. EGU General Assembly 2021, Wien.

Tagliaferri, A.*, Schenker, F. L., Schmalholz, S. M. & Seno, S. (2020) A thermo-kinematic model to investigate heat transfer through the nappes of the Lepontine Dome. 18th Swiss Geoscience Meeting Swiss Geoscience Meeting 2020, Zurich.

Schenker, F. L.*, Wennubst, R., **Tagliaferri, A.**, Maino, M., Peyresaubes, D., De Pedrini, A., Vandelli, A., Gouffon, Y. & Ambrosi, C. (2020) The anatomy of the basal shear zone of the High-Pressure Adula nappe and its repercussion on the Alpine regional geology. 18th Swiss Geoscience Meeting Swiss Geoscience Meeting 2020, Zurich.

Tagliaferri, A.*, Schenker, F. L., Schmalholz, S. M., & Seno, S. (2020) Heat transfer through the nappes of the Lepontine Dome. EGU General Assembly 2020, Wien.

Tagliaferri, A.*, Corti L., Spalla M. I., & Zucali M. (2019) Multiscale structural analysis of the Variscan Basement and Permo-Mesozoic covers, at Frisson Lakes (Argentera Massif, Maritime Alps). 17th Swiss Geoscience Meeting 2019, Fribourg.

Schenker, F. L.*, **Tagliaferri, A.**, Ambrosi, C., Scapozza, C., Czerski, D., Maino, M. & Gouffon, Y. (2019) The tectonics of the Simano, Cima-Lunga, Adula and Maggia nappes in the southern Lepontine dome. 17th Swiss Geoscience Meeting 2019, Fribourg.

* = Corresponding author

As of December 2023.

Scuola universitaria professionale
della Svizzera italiana
SUPSI
Dipartimento ambiente costruzioni e design
Istituto scienze della Terra

Unil
UNIL | Université de Lausanne

FNSNF
SWISS NATIONAL SCIENCE FOUNDATION

